Transport Characteristics of Selected Dyes Through Track-Etched Multiporous Pet Membranes

Seçilmiş Boyar Maddelerin İz Aşındırılmış Çoklu Gözenekli Pet Membanlardan Taşınım Özellikleri

Research Article

Dila Kaya and Kaan Keçeci*
İstanbul Medeniyet University, Department of Chemistry, Üsküdar, İstanbul, Turkey.

ABSTRACT

We have investigated the transport properties of track-etched poly(ethylene terephthalate) (PET) membranes in order to pursue possible applications for effective separation and sensing purposes. We have obtained cylindrical and conical nanopores on PET membranes using symmetrical and asymmetrical track-etch methods, respectively. We have used the fabricated nanopores for the transport of charged dye molecules. Effect of applied potential, temperature and pore geometry was shown for crystal violet dye. We have also investigated the transport of methyl orange and shown negatively charged carboxylate groups on the PET nanopore walls along with applied potential enhanced the selective transport of cations. The temperature and the conical geometry were also found to promote the transport of cations.

Key Words
track-etched nanopore; mass transport; PET membrane; crystal violet; methyl orange.

ÖZ

Etkin ayırma ve algılama sağlayabilecek uygulamaların elde edilebilmesi amacıyla iz-aşındırılmış poli (etilen tereftalat) (PET) membranlardan taşınım özellikleri araştırılmıştır. Simetrik ve asimetrik iz-aşındırma yöntemleri ile PET membranlarda silindirik ve konik nanogözenekler oluşturulmuştur. Elde edilen nanogözenekler yüklü boyar maddelerin taşınımı amacıyla kullanılmıştır. Kristal Viyole boyar maddesi için potansiyel, sıcaklık ve gözenek geometrisinin taşınıma etkileri incelenmiştir. Metil Oranj boyar maddesinin taşınımı da ayrıca incelenmiş ve PET nanogözeneklerinin duvarında bulunan negatif yüklü karboksil grupları ve uygulanan potansiyelin katyonların seçici taşınımını arttırdığı gösterilmiştir. Sıcaklık ve konik geometrinin de katyonların taşınımını arttırdığı bulunmuştur.

Anahtar Kelimeler
iz-aşındırılmış nanogözenek; kütle taşınımı; PET membran; kristal viyole, metil oranj.

Article History: Received: Oct 20, 2017; Revised: Dec 06, 2017; Accepted: Dec 06, 2017; Available Online: Feb 20, 2018.

DOI: 10.15671/HJBC.2018.209

Correspondence to: K. Keçeci; Istanbul Medeniyet University, Department of Chemistry, Uskudar, Istanbul, Turkey.
Tel: +90 216 280 3464 Fax: +90 216 280 3464 E-Mail: kaan.kececi@medeniyet.edu.tr

INTRODUCTION

Nanoporous (or nanochannelle) structures formed in solid materials are used in various separation techniques and sensing applications for biomolecules [1-3]. These structures/materials, can be biological or synthetic, and can be prepared to including single or multiple nanopores [4]. While single nanoporous materials are used for determination and detection at molecular level, studies based on selective transport of analytes from multiple nanopore membranes can also be performed.

Biological nanoporous structures are usually obtained with ion channels isolated from bacteria (eg, α-hemolysin, maltoporin) inserted into lipid bilayer [5,6]. Biological nanopores are not resistant to factors such as pH, temperature, ion concentration and potential, which entails the production of these structures synthetically [7]. The desired attributes for nanopores are that they are low cost, reproducible, chemically and thermally robust and stable. For this reason, synthetic nanoporous materials have been developed in order to overcome the disadvantages of biological nanopores. Some of the methods used to obtain these materials are nanopipettes [8], electron beam lithography [9,10], laser melting [11], and ion beam shaping [12,13]. In addition to these techniques, track-etching method, which is an easy method yielding reproducible sized pores with desired geometries, is often preferred [14-17]. Application areas of synthetic nanopores that can be obtained as a result of the development of synthetic methods include biomolecule characterization [18,19], desalination [20], determination of DNA sequences [19,21] and molecular separation [22].

Transport from multiporous membranes has also high potential for biomedical applications [23]. Nanoporous membranes produced with desired pore size, density and thickness are alternatives for controlled release of pharmacological agents [24]. However, in order to use a membrane in such technologies, the selectivity or molecular flux of the nanoporous structure must be able to match the application in demand. It is also desired that the process of obtaining nanoporous membranes is economical and reproducible. For all these reasons, extensive research is needed on analyte transport from nanoporous membranes.

One of the most frequently used nanoporous materials is anodic aluminum oxide (AAO) membranes [25,26]. The geometry of the nanopores can be controlled by changing the conditions of the anodization process. However, the thickness of AAO membranes leads to very low molecular flow and transport rate making them unsuitable for most processes. Cylindrical nanopores can also be obtained by controlling various advanced technologies such as the use of focused ion beams in silicon (Si) and silicon nitride (SiN) membranes [27]. Although these membranes are thermally and chemically stable, the process of forming nanopores is quite expensive. Similarly, nanopores created on graphene are often used for purposes such as DNA analysis [19]. The greatest advantage of these membranes is their high durability, despite being very thin [28]. However, preparation of films from these expensive materials and subsequent processing of pores in these films are not economically feasible because special equipment is required. Therefore, in order to obtain nanoporous membranes, techniques such as track-etching which is both economically viable and enable effective separation and transport, can be preferred.

Charles Martin and his co-workers have published a series of papers on molecular transport using gold nanotubules obtained from track-etched polymer (polycarbonate-PC) membranes [29-33]. In order to control the surface properties and enable easier functionalization, they have performed electroless gold deposition onto the pore walls and modified the surface with functional groups using thiol chemistry. These functionalized gold nanotubules made it possible to enhance the selectivity and permeability of the membranes for certain analytes depending on their charge and size. Some examples on surface functionalization of polymer nanochannels for enhanced transport rates and selectivity include changing the surface charge by adding L-cysteine on the surface and therefore making it ion-permselective [29]; functionalizing with various groups such as polymers, organic acids etc. for discriminating different molecules [34] and functionalizing the pore surface of polyimide (PI) membrane with ethylenediamine, making it selective towards anions [35].

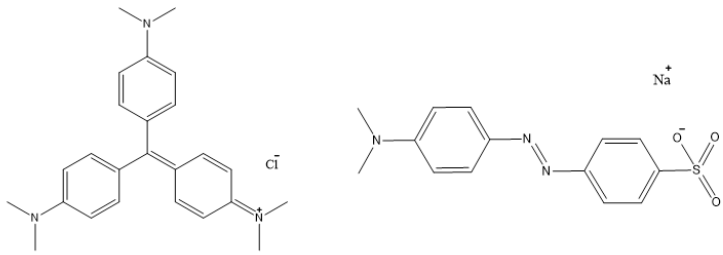

Figure 1. A: Crystal Violet (Triarylmethane dye, M: 407.99 g/mol); B: Methyl Orange (Azo dye, M: 327.33 g/mol).

Studies on analyte transport from multiporous polymers can either focus on surface functionalization of the nanopore in order to enhance the transport rate of the analyte or taking advantage of the already negatively charged wall of PET membrane which possess negative carboxyl ($-COO^-$) groups at neutral pH due to track-etching process [36].

In this work, we have prepared cylindirical and conical nanopores on PET membranes using track-etch method and investigated the transport characteristics of charged analytes through these membranes. The primary reasons for choosing PET membrane for the mass transport experiments were that it is easily track-etched (without the need of high temperatures or additional chemicals), mechanically robust, stable in extreme conditions of pH and temperature with a slightly negative surface charge density. The effects of applied potential, pore geometry and temperature were studied and the use of track-etched membanes for selective and effective transport of the analytes were shown.

MATERIALS and METHODS

Experimental

Poly(ethylene terephthalate) (PET) membranes (3 cm diameter, 12 μm thickness) were obtained from Gesellshaft für Schwerionenforschung (GSI, Darmstadt-Germany). The membranes were irradiated with heavy ions (i.e., Au ion, 11.4 MeV) at various ion densities even down to 1 ion/membrane.

This was succeeded by defocusing the ion beam and using a metal mask with a 0.1 mm diameter aperture with a shutter system which shuts down the ion beam as the single ion passage was detected. All the membranes were exposed to UV irradiation (254 nm) to saturate the damages in tracks. All solutions were prepared from deionized water (Millipore Direct-Q 5, Millipore Co.). Formic acid (HCOOH), sodium hydroxide (NaOH), crystal violet ($C_{25}H_{30}ClN_3$) (Figure 1A), methyl orange ($C_{14}H_{14}N_3NaO_3S$) (Figure 1B) and potassium chloride (KCl) were purchased from Sigma Aldrich. All the chemicals were used as received without further purification.

Fabrication of Nanopores

PET membranes were treated with long-wave UV irradiation overnight in order to sensitize the tracks, increase the track etching rate and make the pores more homogeneous in size. Cylindrical nanopores were obtained on PET membranes using track- etch method. With this purpose, batch etching was performed in which the track membranes were suspended in a beaker filled with etching solution (9 M NaOH) for a predetermined time at room temperature. Afterwards, the membrane was kept in a beaker filled with stopping solution (1 M HCOOH) for 30 minutes and finally the membrane was washed with di-water to remove possible residues from the membrane surface.

Conically shaped nanopores were obtained using a previously discussed asymmetric chemical etching technique [37]. Shortly, the membrane was mounted between the two halves of a conductivity cell with UV-treated side of the membrane facing the alkaline etching solution (9 M NaOH) and the other side facing the stopping solution (1 M HCOOH and 1 M KCl). Platinium (Pt) electrodes were immersed into each cell and 1 V transmembrane potential was applied to monitor the breakthrough moment (Keithley 6487 picoammeter/voltage source, Cleveland, OH, USA). After the etching process, etching solution was replaced with stopping solution for neutralization. Then, both cells were

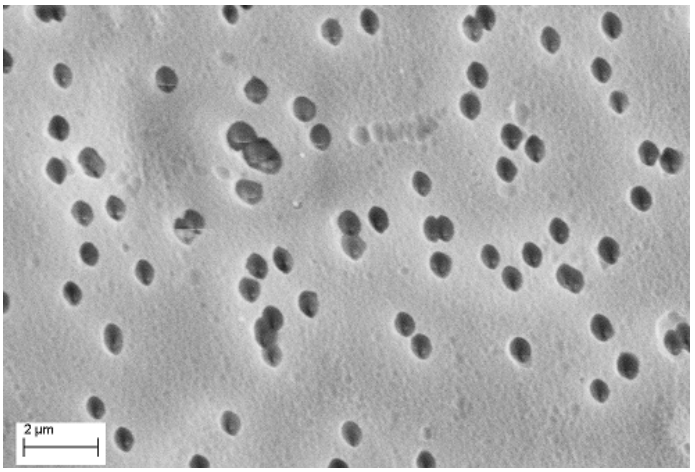

Figure 2. SEM image of multiporous PET etched for 2 hours.

rinsed with di-water to remove possible residues from the membrane surface. In the end, conically shaped nanopore was obtained with two different sized openings called base (large opening) and tip (small opening). The large opening of the nanopore (d_{base}) was directly determined from SEM images of multipore membranes while electrochemical measurements were performed for the calculation of small opening (d_{tip}) of the conical membrane. With this purpose, both halves of the conductivity cell were filled with electrolyte solution (i.e., 1 M KCl, 10 mM PBS buffer at pH = 7) while the single nanopore membrane was mounted between these cells. Ag/AgCl electrodes were used and potential was stepped between -1 V and +1 V. The resistance of the nanopore (R) is proportional to the conductivity of solution (ρ) the length of nanopore (l, thickness of the membrane), d_{base} and d_{tip} as given in Equation 1. R value was the reciprocal of the slope of I-V curve obtained from the electrochemical measurement and the tip diameter was calculated using Equation 1 (Conductivity measurements were carried out with a Mettler Toledo FE 30 conductivity meter).

$$R = \frac{4\rho l}{\pi d_{tip} d_{base}} \quad (1)$$

Mass Transfer Experiments

The membranes were mounted between the two halves of an H-cell to investigate the transport properties of charged analytes. The cell volumes were 5 mL with an effective permeation area of 0.3 cm^2. The feed half-cell was filled with the known concentration of the analyte in phosphate buffer (10 mM, pH = 7) and the permeate half-cell contained only pure buffer solution. Phosphate buffer at pH 7 was selected because at neutral pH, nanopore surface charge of PET membrane is negative because of $-COO^-$ groups on its pore walls [38], crystal violet is positively charged and methyl orange is negatively charged ($pK_{a,MO}$= 3.47; $pK_{a,CV}$= 9.4). Both halves of the cell were continuously stirred with a magnetic stirrer (~1050 rpm). Samples were collected from the permeate cell at regular time intervals and the concentration of the analyte was determined using a UV-Vis spectrophotometer (Shimadzu-2600). A linear calibration curve of analytes of known concentrations was used for the spectrophotometric calculations.

RESULTS and DISCUSSION

Pore diameters of cylindrical pores and base diameters of the conical nanopores were obtained from the SEM images of multipore membranes (10^9 nanopores/cm^2). SEM image of a multipore PET membrane etched for 2 hours is given in Figure 2 with a calculated base diameter value of 533±47 nm. An average of 20 pores were used to calculate the diameters with Image-J software and standard deviation values were taken into account.

A linear relationship was observed between etching time and pore diameter (Figure 3). The bulk etching rate, which equals the slope of the obtained linear plot, was found as 4.5±0.2 $nm.min^{-1}$. This linear relationship enabled reproducible production of nanopores with desired diameters.

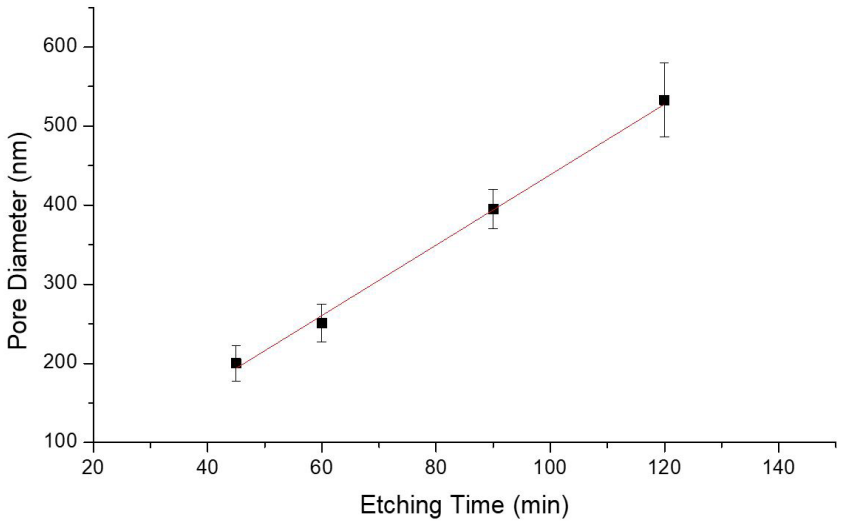

Figure 3. Pore diameter as a function of etching time.

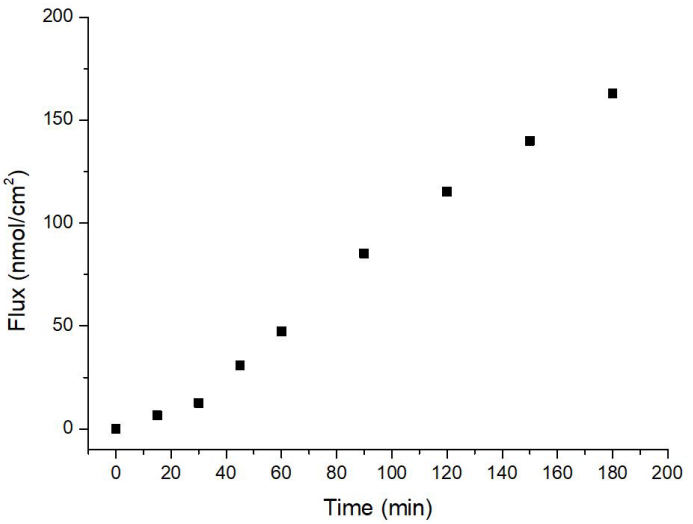

Figure 4. Permeation of CV^+ through 25±1 nm nanopores (Pore density: 10^9 pore/cm^2).

Permeation of the Analytes

Permeation of CV^+ through the nanoporous membrane was conducted using a multiporous (10^9 pore.cm^{-2}) PET membrane with a pore diameter of 25 ± 1 nm. The transport of the positively charged dye was continued for three hours and the transported amount of the analyte (per cm^2) increased linearly. Figure 4 shows the linear relationship of molecular flux and time with an R^2 value of 0.990. The permeation rate was calculated from the slope of the obtained line, which yielded the amount of analyte transferred per unit time.

Effect of Potential on Analyte Transport Rate

In order to investigate the potential dependency of molecular transport, an electric field was applied. Anode was immersed in the feed cell and cathode was immersed in the permeate cell in order to promote the transport rate of CV^+. The flux data for the transport of CV^+ through the PET membrane with different applied voltages is presented in Figure 5. The promotive effect of potential on flux can be seen in Figure 5, that as the potential was increased, the flux of CV^+ gave a direct correlation as expected. This correlation can be explained by the contributing forces to the transport (i.e., electro-osmosis, electrophoresis) of the analyte. When there is no electric field applied, the transport is only due to diffusion from feed cell to the permeate cell because of the concentration gradient; however, as a certain potential is applied, electrophoretic and electro-osmotic forces also contribute to the transport, driving the positively charged analyte to thecounter electrode (i.e., cathode side).

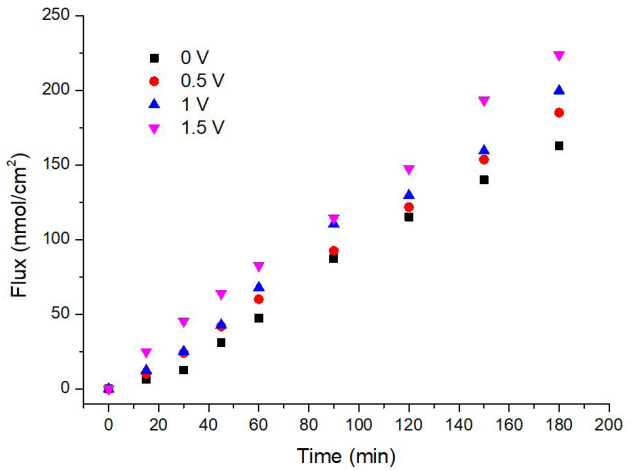

Figure 5. CV^+ flux under various applied potentials.

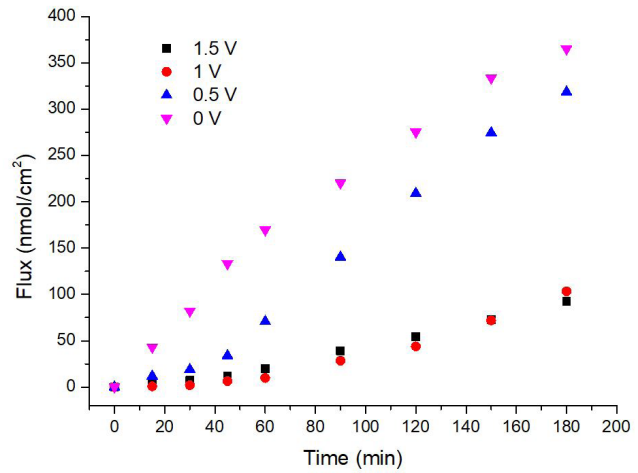

Figure 6. MO^- flux under various potentials.

In order to compare the nanopore selectivity towards oppositely charged analytes, MO^- was transported through the same membrane under various potentials. The effect of potential on MO^- flux was the opposite of CV+ and is shown in Figure 6. The negatively charged analyte is driven to the anode (the feed cell) electrophoretically under applied potential which decreases the overall molecular flux of MO^-.

The plots between molecular flux and time were all linear with R^2 values over 0.990 and 0.938 for CV^+ and MO^-, respectively. Transport rates (nmol. $cm^{-2}min^{-1}$) were calculated from the slope of these linear plots. In order to inspect the selectivity of the membrane towards the positively charged analyte CV^+, selectivity coefficients which are defined as the ratio of transport rates of the analytes were calculated using Equation 2. The obtained values are presented in Table 1.

The results indicated that with the increasing potential, the membrane became selective towards the positively charged analyte CV^+. When no potential was applied, MO^- was transported with a higher rate than that of CV^+ which contradicts with the argument of PET being selective towards

$$\alpha = \frac{Rate\left(CV^+\right)}{Rate\left(MO^-\right)} \quad (2)$$

positively charged analytes. But in our case, the analytes differ in molecular volume and structure so that the net charge of the molecule is not the only contributing factor to the permeation rate. MO^- which is an azo dye has a molecular volume of 257 $Å^3$ whereas the triarylmethane dye, CV^+ has a molecular volume of 378 $Å^3$.

Table 1. Selectivity coefficients with respect to applied potential.

Potential (V)	Rate (nmol.cm^{-2}.min^{-1})		Selectivity (α)
	MO^-	CV^+	
0	2.03	0.99	0.49
0.5	1.92	1.05	0.55
1	0.57	1.12	1.97
1.5	0.53	1.22	2.30

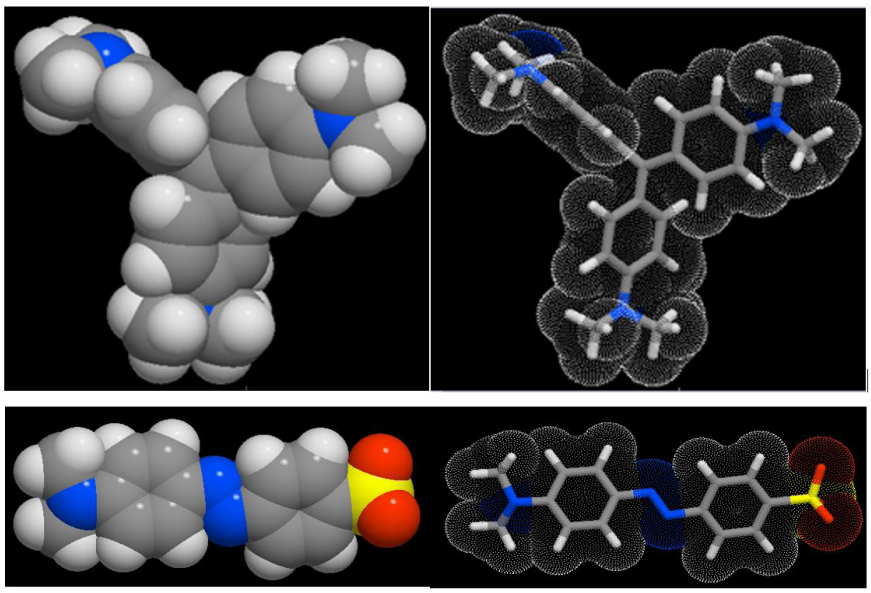

Figure 7. Molecular structures of CV^+ and MO^- (Produced using Molinspiration Cheminformatics Software [39].

This difference in molecular volume, and the linear structure of MO^- (shown in Figure 7) enhances its transport rate. Therefore without any applied potential, its transport rate is higher than CV^+ despite having a negative charge. But as the potential is increased, electrokinetic phenomena (i.e. electrophoretic and electro-osmotic forces) have a significant impact on transport selectivity towards positively charged analyte, CV^+.

Effect of Temperature on Analyte Transport Rate

Another parameter of interest on transport rate was temperature. The transport of CV^+ through 25 ± 1 nm pore membrane was carried on under 1.5 V potential and four different temperature values. According to the obtained results, transport rate increased from 1.22 to 7.23 nmol.cm^{-2}.min^{-1} as a function of temperature which was raised from 298 K to 328 K, respectively (Figure 8). This behavior indicated that the transport of the CV^+ has an endothermic nature and favored higher temperatures (due to the positive dependence of diffusion coefficient to temperature). Arrhenius equation can be used to explain the temperature dependence of diffusion coefficient (Equation 3); where D is the diffusion coefficient, D_0 is the diffusion coefficient at infinite temperature, E_a is the activation energy, T is the absolute temperature and k is the Boltzmann constant.

Effect of Pore Geometry on Analyte Transport Rate

In order to investigate the effect pore geometry on the transport rate of the analyte, multiporous PET membranes with conical geometries were fabricated and subsequently used for the transport of CV^+. The prepared nanopores

$$D = D_0 e^{-\frac{E_a}{kT}} \quad (3)$$

had tip openings of 25 nm for comparison with cylindrical ones. This was achieved through a second etching step developed by Wharton et. al. [40]. Shortly, after the first step of etching, a more dilute etching solution (2 M NaOH) was introduced in both half cells and under a transmembrane potential of 1 V. This second step

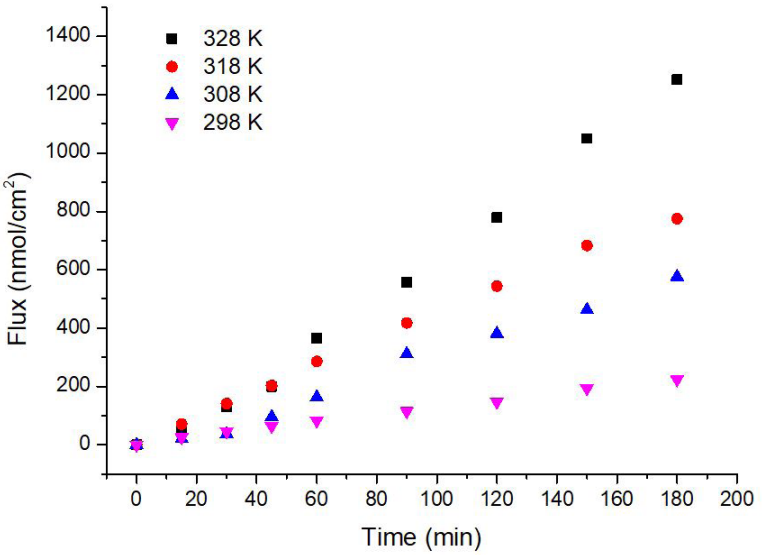

Figure 8. Temperature dependence of CV^+ flux.

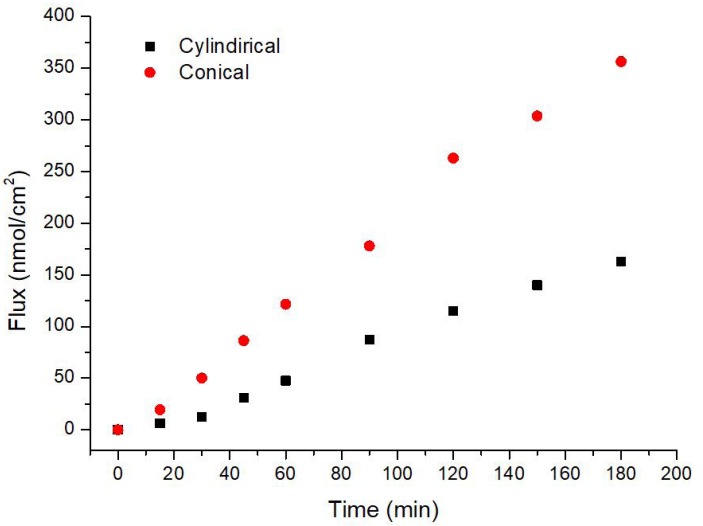

Figure 9. CV^+ flux through pores with different geometries.

of etching was stopped when the pore reached the desired size by monitoring the current values and once again the etching solution was replaced with the stopping solution content to terminate further widening of the pore. Thereafter, the half cells were rinsed with water and the membrane was then used for the experiments.

Analyte was added to the tip side of the membrane and the transport of CV^+ through the membrane was performed. The dependence of CV^+ flux to nanopore geometry is shown in Figure 9. It is obvious that the transport rate significantly increased when the nanopores have conical geometry. The trapping zone, which is formed near the nanopores' tip entrance, was shown to have a positive effect on the transport of charged analyte doubling its molecular flux. The effects of nanopore geometry on the sensing phenomena have been widely researched especially for single nanopores and it was shown that the ionic current is directly affected by the pore's resistance which is related to the pore's geometry [41]. Furthermore, the promotive effect of conical geometry was previously reported for multipore asymmetrical nanopores for the transport of charged analytes as well [42]. Further investigations were performed to analyze the effect of geometry on

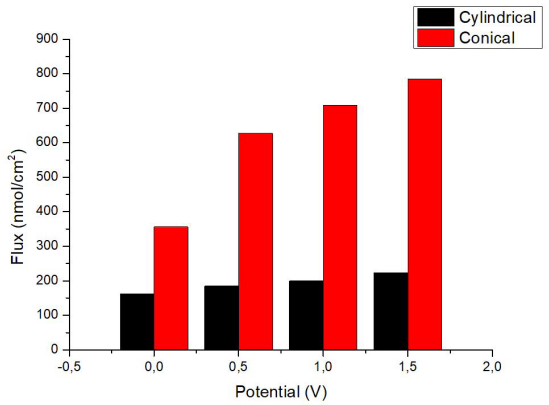

Figure 10. CV^+ flux through pores with different geometries at various potentials.

the molecular flux at varying potentials (Figure 10). Once more it was shown that the potential has a promoting effect on CV^+ transport because applying a potential entails electrophoretic forces that enhance the transport of positively charged analyte. It was also found that the increase in the flux was more significant for conically shaped pores than that of cylindrical ones.

Conclusion

In conclusion, we have demonstrated the effect of potential, pore geometry and temperature (etc.) on the transport phenomenon by the transport rate of charged dye molecules across a track-etched polymeric membrane. We have shown here that the nanoporous membranes can be used as molecular sieves, can show transport selectivity, and can be used both for anions and cations. Applying potential across the membrane has promoted the transport of CV^+ but decreased the transport of MO^-, thus increased the membrane selectivity towards positively charged analyte. The studies on the geometry of nanopore showed that the transport of CV^+ was faster using a conical nanopore. In addition, high temperature was also found to enhance the flux of CV^+. The nanopore diameter and its geometry can be arranged, so, these membranes are applicable for model studies and for fundamental investigation of how the transport phenomena occur. We are pursuing possible applications of track-etched polymer membranes in chemical and bio-separations and sensors. For such applications, flux or throughput across the membrane is an important issue and these membranes perhaps hold promise for the development of highly selective membranes for chemical separations and sensors.

Acknowledgements

This work is performed at the Laboratory of Natural Sciences, Istanbul Medeniyet University.

References

1. H. Hatori, H. Takagi, Y. Yamada, Gas separation properties of molecular sieving carbon membranes with nanopore channels, Carbon, 42 (2004) 1169-1173.
2. S.G. Lemay, Nanopore-based biosensors: the interface between ionics and electronics, ACS nano, 3 (2009) 775-779.
3. A.S. Prabhu, T.Z.N. Jubery, K.J. Freedman, R. Mulero, P. Dutta, M.J. Kim, Chemically modified solid state nanopores for high throughput nanoparticle separation, J. Phys. Condens. Matter, 22 (2010) 454107.
4. S.B. Lee, D.T. Mitchell, L. Trofin, T.K. Nevanen, H. Söderlund, C.R. Martin, Antibody-based bio-nanotube membranes for enantiomeric drug separations, Science, 296 (2002) 2198-2200.
5. J. Kasianowicz, E. Brandin, D. Branton, D.W. Deamer, Characterization of individual polynucleotide molecules using a membrane channel, Proc. Natl. Acad. Sci. U.S.A., 93 (1996) 13770-13773.
6. S.M. Bezrukov, M. Winterhalter, Examining noise sources at the single-molecule level: 1/f noise of an open maltoporin channel, PRL, 85 (2000) 202.
7. C. Dekker, Solid-state nanopores, Nat. Nanotechnol., 2 (2007) 209-215.
8. K.K. Hu, Y.X. Wang, H.J. Cai, M.V. Mirkin, Y. Gao, G. Friedman, Y. Gogotsi, Open Carbon Nanopipettes as Resistive-Pulse Sensors, Rectification Sensors, and Electrochemical Nanoprobes, Anal. Chem., 86 (2014) 8897-8901.

9. H.M. Kim, M.H. Lee, K.B. Kim, Theoretical and experimental study of nanopore drilling by a focused electron beam in transmission electron microscopy, Nanotechnology, 22 (2011) 275303.
10. A.G. Ahmadi, S. Nair, Geometry of nanopore devices fabricated by electron beam lithography: Simulations and experimental comparisons, Microelectron. Eng., 112 (2013) 149-156.
11. N.L. Kazanskiy, S.P. Murzin, Y.L. Osetrov, V.I. Tregub, Synthesis of nanoporous structures in metallic materials under laser action, Opt. Lasers Eng., 49 (2011) 1264-1267.
12. N. Patterson, D. Adams, V. Hodges, M. Vasile, J. Michael, P. Kotula, Controlled fabrication of nanopores using a direct focused ion beam approach with back face particle detection, Nanotechnology, 19 (2008) 235304.
13. J. He, L. Lin, P. Zhang, S. Lindsay, Identification of DNA basepairing via tunnel-current decay, Nano Lett., 7 (2007) 3854-3858.
14. P.Y. Apel, Y.E. Korchev, Z. Siwy, R. Spohr, M. Yoshida, Diode-like single-ion track membrane prepared by electro-stopping, Nucl. Instrum. Methods Phys. Res. B., 184 (2001) 337-346.
15. P.Y. Apel, I.V. Blonskaya, O.L. Orelovitch, B.A. Sartowska, R. Spohr, Asymmetric ion track nanopores for sensor technology. Reconstruction of pore profile from conductometric measurements, Nanotechnology, 23 (2012) 225503
16. V. Chavan, C. Agarwal, A.K. Pandey, J.P. Nair, P. Surendran, P.C. Kalsi, A. Goswami, Controlled development of pores in polyethylene terepthalate sheet by room temperature chemical etching method, J. Memb. Sci., 471 (2014) 185-191.
17. A. Kocer, L. Tauk, P. Dejardin, Nanopore sensors: From hybrid to abiotic systems, Biosens. Bioelectron., 38 (2012) 1-10.
18. A. Mara, Z. Siwy, C. Trautmann, J. Wan, F. Kamme, An Asymmetric Polymer Nanopore for Single Molecule Detection, Nano Lett., 4 (2004) 497-501.
19. C.A. Merchant, K. Healy, M. Wanunu, V. Ray, N. Peterman, J. Bartel, M.D. Fischbein, K. Venta, Z. Luo, A.C. Johnson, DNA translocation through graphene nanopores, Nano Lett., 10 (2010) 2915-2921.
20. D. Cohen-Tanugi, J.C. Grossman, Water desalination across nanoporous graphene, Nano Lett., 12 (2012) 3602-3608.
21. H. Bayley, Are we there yet ? Comment on "Nanopores: A journey towards DNA sequencing" by Meni Wanunu, Phys. Life Rev., 9 (2012) 161-163.
22. T.C. Kuo, L.A. Sloan, J.V. Sweedler, P.W. Bohn, Manipulating molecular transport through nanoporous membranes by control of electrokinetic flow: effect of surface charge density and Debye length, Langmuir, 17 (2001) 6298-6303.
23. S.P. Adiga, C. Jin, L.A. Curtiss, N.A. Monteiro-Riviere, R.J. Narayan, Nanoporous membranes for medical and biological applications, Wiley Interdiscip. Rev. Nanomed. Nanobiotechnol., 1 (2009) 568-581.
24. T.A. Desai, S. Sharma, R.J. Walczak, A. Boiarski, M. Cohen, J. Shapiro, T. West, K. Melnik, C. Cosentino, P.M. Sinha, Nanoporous implants for controlled drug delivery, BioMEMS and Biomedical Nanotechnology Volume III, Springer, Berlin, Germany, 2006.
25. S. Kipke, G. Schmid, Nanoporous alumina membranes as diffusion controlling systems, Adv. Funct. Mater., 14 (2004) 1184-1188.
26. L. Velleman, G. Triani, P.J. Evans, J.G. Shapter, D. Losic, Structural and chemical modification of porous alumina membranes, Microporous Mesoporous Mater., 126 (2009) 87-94.
27. C.J. Lo, T. Aref, A. Bezryadin, Fabrication of symmetric sub-5 nm nanopores using focused ion and electron beams, Nanotechnology, 17 (2006) 3264.
28. G.F. Schneider, S.W. Kowalczyk, V.E. Calado, G. Pandraud, H.W. Zandbergen, L.M. Vandersypen, C. Dekker, DNA translocation through graphene nanopores, Nano Lett., 10 (2010) 3163-3167.
29. S.B. Lee, C.R. Martin, pH-Switchable, ion-permselective gold nanotubule membrane based on chemisorbed cysteine, Anal. Chem., 73 (2001) 768-775.
30. K.B. Jirage, J.C. Hulteen, C.R. Martin, Nanotubule-based molecular-filtration membranes, Science, 278 (1997) 655-658.
31. S.B. Lee, C.R. Martin, Electromodulated molecular transport in gold-nanotube membranes, J. Am. Chem. Soc., 124 (2002) 11850-11851.
32. K.B. Jirage, J.C. Hulteen, C.R. Martin, Effect of thiol chemisorption on the transport properties of gold nanotubule membranes, Anal. Chem., 71 (1999) 4913-4918.
33. S. Yu, S.B. Lee, C.R. Martin, Electrophoretic protein transport in gold nanotube membranes, Anal. Chem., 75 (2003) 1239-1244.
34. E.N. Savariar, K. Krishnamoorthy, S. Thayumanavan, Molecular discrimination inside polymer nanotubules, Nat. Nanotechnol., 3 (2008) 112-117.
35. M. Ali, B. Yameen, R. Neumann, W. Ensinger, W. Knoll, O. Azzaroni, Biosensing and supramolecular bioconjugation in single conical polymer nanochannels, facile incorporation of biorecognition elements into nanoconfined geometries, J. Am. Chem. Soc., 130 (2008) 16351-16357.
36. Q.H. Nguyen, M. Ali, V. Bayer, R. Neumann, W. Ensinger, Charge-selective transport of organic and protein analytes through synthetic nanochannels, Nanotechnology, 21 (2010) 365701.
37. K. Kececi, N. San, D. Kaya, Nanopore detection of double stranded DNA using a track-etched polycarbonate membrane, Talanta, 144 (2015) 268-274.
38. Z. Siwy, P. Apel, D. Baur, D.D. Dobrev, Y.E. Korchev, R. Neumann, R. Spohr, C. Trautmann, K.O. Voss, Preparation of synthetic nanopores with transport properties analogous to biological channels, Surf. Sci., 532 (2003) 1061-1066.
39. Molinspiration Cheminformatics Software. 2001, Molinspiration: Nova Ulica, SK-900 26 Slovensky Grob, Slovak Republic.
40. J.E. Wharton, P. Jin, L.T. Sexton, L.P. Horne, S.A. Sherrill, W.K. Mino, C.R. Martin, A method for reproducibly preparing synthetic nanopores for resistive-pulse biosensors, Small, 3 (2007) 1424-1430.

41. D. Kaya, A. Dinler, N. San, K. Kececi, Effect of Pore Geometry on Resistive-Pulse Sensing of DNA Using Track-Etched PET Nanopore Membrane, Electrochim. Acta, 202 (2016) 157-165.

42. Q.H. Nguyen, M. Ali, S. Nasir, W. Ensinger, Transport properties of track-etched membranes having variable effective pore-lengths, Nanotechnology, 26 (2015) 485502.

Determination of Acidic Dissociation Constants of Chlorthalidone and Terbutaline in Water Using DFT and Ab Initio Methods

DFT ve Başlangıç Yöntemlerini Kullanılarak Klortalidon ve Terbütalinin Asidik Ayrışma Sabitlerinin Belirlenmesi

Research Article

Farhoush Kiani[1]* and Ali Rajabalinezhad[2]

[1]Department of Chemistry, Faculty of Science, Ayatollah Amoli Branch, Islamic Azad University, Amol, Iran.

[2]Department of NanoChemical Engineering, Faculty of Nanotechnology, Semnan University, Semnan, Iran.

ABSTRACT

In the present study, pK_a values of both drug called Chlorthalidone and Terbutaline were determined in aqueous solution. For this purpose, the B3LYP calculation with the 6-31+G(d) basis set was utilized. The reactions and equilibria that possess a high hydrogen-band-donor capability and constitute the indispensable theoretical basis to calculate the acidity constants of Chlorthalidone and Terbutaline, are shown. To analyze the formation of intermolecular hydrogen bonds between the existent species and water molecules, Tomasi's method was used. In this way, it was determined that in alkaline aqueous solutions the cation, anion, and neutral species of Chlorthalidone and Terbutaline are solvated with one, two, three, and four molecules of water, respectively. To proceed, the calculated pK_a were compared with the experimental values, which there is comparable agreement between them. The resulting data illustrated that the method was likely to be useful for the prediction of pKa values in aqueous solution.

Key Words

chlorthalidone, terbutaline, acidic dissociation constant, intermolecular hydrogen bond.

ÖZ

Bu çalışmada klortalidon ve terbütalin ilaçlarının pK_a değerleri sulu çözeltileri içinde hesaplanmıştır. B3LYP hesaplamaları ile 6-31+G(d) temel setinden faydalanmak amaçlanmıştır. Hidrojen bağı verici özelliği yüksek olan ve aynı zamanda klortalidon ve terbütalin için asitlik sabitlerinin hesaplanmasında teorik açıdan vazgeçilmez olan denge ve tepkimeler gösterilmiştir. Var olan türler ve su molekülleri arasındaki hidrojen bağı oluşumlarını analiz etmek için Tomasi yöntemi kullanılmıştır. Böylece klortalidon ve terbütalinin alkali su çözeltisi içerisindeki katyon, anyon ve nötr oluşumlarının, sırasıyla bir, iki, üç ve dört su molekülüyle çözünebildiği saptanmıştır. Sonraki adımda hesaplanan pK_a değerleri deneysel sonuçlarla karşılaştırılmış ve kabul edilebilir bir örtüşme görülmüştür. Elde edilen veriler uygulanan tekniğin sulu çözeltilerde pK_a tahminlerinde kullanışlı bir seçenek olacağını göstermektedir.

Anahtar Kelimeler

klortalidon, terbütalin, asidik ayrılma sabiti, moleküllerarası hidrojen bağı.

Article History: Received: Oct 10, 2015; Revised: Dec 12, 2016; Accepted: Dec 10, 2017; Available Online: Feb 20, 2018.

DOI: 10.15671/HJBC.2018.210

Correspondence to: F. Kiani; Department of Chemistry, Faculty of Science, Islamic Azad University, Amol, Iran.

Tel: + +98 01143217076 Fax: ++98 01143217120 E-Mail: farhoush_kiani@yahoo.com

INTRODUCTION

The ability to deliver therapeutic agents to a sick in a pulsatile or staggered release profile has been a major target in drug delivery research over the last two decades. In ancient pharmacy system, due to non-real prescription of drug dose, high amount of drug consume without any profit in cardiovascular system and mean tissues till reach to point of effect and may be cause for side effects during its path. The technology can allow target delivery of drugs to different areas of the body. Therefore, drug delivery technology (DDT) is increasingly important as a component of drug development. A key issue in drug delivery system is to maximize the drug access to specific sites, and to be able to control the release of drugs, in order to maintain a desired drug concentration level for long periods of time without reaching a toxic level or dropping below the minimum effective level [1].

Using nanotechnology, it may be possible to achieve (1) improved delivery of poorly water-soluble drugs; (2) targeted delivery of drugs in a cell- or tissue specific manner; (3) transcytosis of drugs across tight epithelial and endothelial barriers; (4) delivery of large macromolecule drugs to intracellular sites of action; (5) co-delivery of two or more drugs or therapeutic modality for combination therapy; (6) visualization of sites of drug delivery by combining therapeutic agents with imaging modalities; and (7) real-time read on the in vivo efficacy of a therapeutic agent [2].

Diuretics are a wonderful group of compounds. There are several classes of diuretics, but all diuretics enhance the excretion of water from bodies [3]. Thiazides are a type of diuretics often used to treat hypertension and edema that these thiazides were developed during the 1950s. Although they lower blood pressure effectively, the mechanisms have confused researchers [4]. Hypertension causes devastating action all over the time. Hypertension increases to the workload of the heart and arteries. It can mar the blood vessels of the brain, heart, and kidneys. Therefore is used from Chlorthalidone (CTD) to treat hypertension [5]. Although CTD does not have a thiazidic construction, it presents the same effects of the thiazidic diuretics. It reduces the amount of water in the body by raising the flow of urine, which helps to lower arterial pressure [6]. Relievers are medicines which are specifically designed to relieve asthma symptoms by relaxing the muscle cells that surround the airways. This allows the airways to open so that air can pass more easily in and out of the lungs. Nowadays reliever medications come in two types: short-acting and long-acting. Terbutaline is in the class of Short-acting reliever medications which it can be specifically used to treat asthma symptoms. Terbutaline works as bronchodilators. In severe asthma, bronchodilators are usually given intravenously or by inhalation [7-9].

Many drug compounds include at least one acidic and/or basic functionality, and the ionization state of these groups play a large role in determining the physiochemical properties of a compound. The pKa for a compound creates a means of specifying the extent of ionization of the compound at any solution pH. Information of a compound's pKa value plays a main role in the expansion of drug delivery formulations [10,11].

Aqueous pKa values are especially useful due to their environmental and pharmacological applications, because it governs solubility, absorption, distribution, metabolism and elimination [12,13]. In recent years a number of methods employed for pKa measurements based on solubility [14], potentiometric titration [15], spectrophotometry [16], HPLC [17] and, most recently, on capillary electrophoresis (CE) [18] and Liquid chromatography (LC) [19]. On the other hand, the theoretical prediction of pKa values using quantum chemical methods has attracted a great extent of interest. So now, pKa values can be predicted by computational methods on the basis of molecular structure, applying various quantum theoretical techniques. The pKa can be calculated from the energy of the following reaction:

$$AH \xleftrightarrow{\Delta G} A + H \quad (1)$$

Using the relation:

$$pK_a = \Delta G/2.303RT \quad (2)$$

ΔG is the free energy of reaction obtained by taking the difference of the molecular free energies of the products from the reactant [20-24].

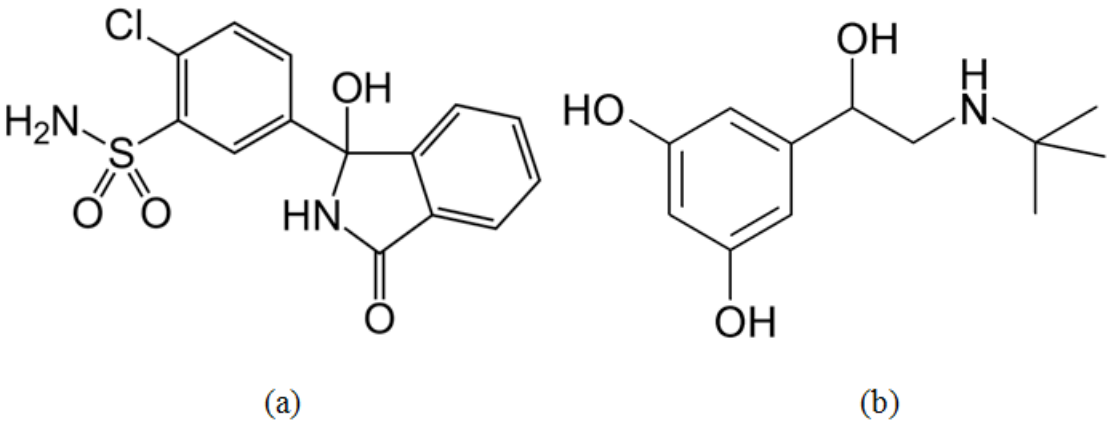

Figure 1. The structures of the (a) Chlorthalidone and (b) Terbutaline for carrying out the calculations.

Polarizable continuum models (PCM) by Tomasi and coworkers have been applied to compute free energy differences for cations, neutral compounds, and their anions. It is one of the most used and reliable continuum solvation methods [25]. On the basis of solvation free energies, the pKa values were obtained for the compounds in question by using thermodynamic equations, involving the combined experimental and computed data [26].

The increasing popularity of quantum mechanical (QM) methods for the calculation of drug design is due to the first principle nature of QM, which should provide the highest accuracy. It is an understatement to say that the density functional theory (DFT) has strongly influenced the evolution of quantum chemistry during the past 15 years; the term "revolutionalized" is perhaps more appropriate. Based on the famous Hohenberg and Kohn theorems [27], DFT provided a sound basis for the development of computational strategies for obtaining information about the energetics, structure, and properties of (atoms and) molecules at much lower costs than traditional ab initio wave function techniques. In DFT methods, Becke's three parameters exchange functional (B3) [28,29] incorporated with gradient-corrected correlation functional of Lee, Yang and Parr (LYP) [30] by implementing the split-valence polarized 6-31+G(d) basis set [31,32] have been used for the calculation of molecular structure optimization.

This article refers to the influence of factors such as the Self-Consistent Reaction Field (SCRF) model applied, choice of a particular thermodynamic equation, atomic radii used to build a cavity in the solvent (water), optimization of geometry in water, inclusion of electron correlation, and the dimension of the basis set on the solvation free energies and on the calculated pK_a values. In this study, pKa values of Chlorthalidone and Terbutaline were specified in aqueous solution by an ab initio method and at a temperature of 25°C. To explain the acidic dissociation constants obtained, we investigated the molecular conformations and solute-solvent interactions of the cation, anion, and neutral species of Chlorthalidone and Terbutaline using ab initio and density functional theory (DFT) methods.

Computational Methods

All the theoretical computations were performed using CS Chem3D version 5.0 and Gaussian 98 program package [33,34]. The initial geometry and different conformers of Chlorthalidone and Terbutaline (see Figure 1) were built with the help of the mentioned softwares by the semi empirical PM3 method. All the initial geometries and solvated molecules in water were optimized with the Gaussian 98 program packages using the B3LYP/6-31+G(d) methods and the default convergence criteria. The polarized continuum model (PCM) which is the ideal conceptual framework to describe solvent effects on all species involved in the selected ionization reaction, was used [35]. Furthermore, to shed light on the experimental pKa values of these drugs in water, several conformers were tested by the excel program, but some of the conformers were

Table 1. Calculated Total Energy Using the Tomasi method at the B3LYP/6-31+G(d) Level of Theory for Cationic, Neutral, and Anionic Species of Chlorthalidone and Terbutaline, at 298.15 K[a].

		$G_o$sol	$G_o$sol/molecule			$G_o$sol	$G_o$sol/molecule
N	**solvated species**	**(Hartree)**	**(kj.mol^{-1})**	**N**	**solvated species**	**(Hartree)**	
		Terbutaline				**Chlorthalidone**	
0	H_3L^+	-1968207.194	-749.650498	0	$H_2L_2^+$	-4751467.721	-1809.738403
1	H_3L^+	-1084452.038	-826.0919	1	$H_2L_2^+$	-2476091.022	-1886.186448
2	H_3L^+	-789866.9489	-902.53326	2	$H_2L_2^+$	-1717630.22	-1962.632319
3	H_3L^+	-642574.2365	-978.974364	3	$H_2L_2^+$	-1338398.294	-2039.075868
4	H_3L^+	-554199.8598	-1055.41785	4	$H_2L_2^+$	-1110858.844	-2115.518855
0	H_2L	-1966966.495	-749.177941	0	HL^+	-4750391.962	-1809.328668
1	H_2L	-1083830.825	-825.618685	1	HL^+	-2475542.398	-1885.768528
2	H_2L	-789452.666	-902.059884	2	HL^+	-1717261.775	-1962.211319
3	H_2L	-642270.5384	-978.511674	3	HL^+	-1338127.711	-2038.663629
4	H_2L	-553956.9623	-1054.955276	4	HL^+	-1110638.577	-2115.099379
0	HL^-	-1965727.829	-748.706158	0	L	-4749309.665	-1808.916443
1	HL^-	-1083222.626	-825.155384	1	L	-2475001.995	-1885.356871
2	HL^-	-789052.2712	-901.602377	2	L	-1716898.167	-1961.795847
3	HL^-	-641961.374	-978.040656	3	L	-1337856.169	-2038.24993
4	HL^-	-553711.9538	-1054.488682	4	L	-1110423.029	-2114.688888
0	L_2^-	-1964472.16	-748.227899			Water [26]	
1	L_2^-	-1082592.883	-824.675671		H_3O^+	-2.0180 · 105	-7.6862 · 101
2	L_2^-	-788633.1749	-901.123501		$H_3O^+(H_2O)$	-2.0124 · 105	-1.5330 · 102
3	L_2^-	-641649.1213	-977.564933		$H_3O^+(H_2O)_2$	-2.0105 · 105	-2.2973 · 102
4	L_2^-	-553461.3892	-1054.011507		H_2O	-2.0068 · 105	-7.6434 · 101
					$(H_2O)_2$	-2.0068 · 105	-1.5287 · 102
					OH^-	-1.9941 · 105	-7.5952 · 101
					$OH^-(H_2O)$	-2.0006 · 105	-1.5240 · 102
					$OH^-(H_2O)_2$	-2.0028 · 105	-2.2885 · 102
					$OH^-(H_2O)_3$	-2.0039 · 105	-3.0529 · 102
					$OH^-(H_2O)_4$	-2.0044 · 105	-3.8173 · 102

[a]N: total number of solvation water molecules; Gsolo , total free energy in solution; Gsolo/molecule, total energy of solvated species per water molecule; $H_2L_2^+$ and H_3L^+ and H_L^+ , cation species; L and H_2L, neutral; HL^- and L_2^-, anion species.

not considered further because the estimated error in its acidic dissociation constants was unacceptable. Finally, we selected the solvation of the species by means of intermolecular hydrogen bonds (IHBs) that involve one molecule of the mentioned species and some molecules of water (see Table 1).

RESULT and DISCUSSION

Fully protonated Chlorthalidone and Terbutaline have two acid groups and three acid groups, respectively. For Chlorthalidone, a proton can be lost from either of the two groups to give different ionized species: the loss of a proton from the first ammonium group (NH_3^+) is most probable and from the second ammonium group (NH_2^+) least probable. Therefore, this concept of microscopic ionization constants k_1 and k_2 may be used, where k_1 involving the first ammonium group proton is [36]:

$$k_1=[H^+][C_{14}H_8ClNH_2NH_2^+O_4S]/[C_{14}H_8ClNH_3^+NH_2O_4S] \quad (3)$$

And k_2 involving the second ammonium proton (NH_2^+) is:

It can be displayed that for a dibasic acid (Chlorthalidone) the first ionization constant K_1 is

$$k_2=[H^+][C_{14}H_8ClNH_3^+NHO_4S/[C_{14}H_8ClNH_3^+NH_2^+O_4S] \quad (4)$$

the sum $k_1 + k_2$ and the second ionization constant K_2 is $(k_{12}\cdot k_{21})/(k_{12}+k_{21})$, where the subscript 12 specifies loss of proton 2 following loss of proton 1 and subscript 21 denotes loss of proton 1 following loss of proton 2.

In the case of Terbutaline, eight differently protonated microspecies exist in solution and 12 microconstants are necessary to describe the system (Figure 2) [37].

Based on an earlier work by Taka´cs-Nova´k et al., it is proposed a three-step protonation scheme which is shown in Figure 3 with all free protons omitted for clarity [38].

It must be noted that the chemical interpretation of the changes can be determined by NMR spectroscopy exactly [39-41].

Considering the microconstants of two drugs, various reactions including cationic, zwitterion and anionic species were checked, but some of the reactions were not considered further because the estimated error in its dissociation constants was unacceptable. In the long run, the models selected for the considered system and the computed values of the dissociation constants for Chlorthalidone and Terbutaline are listed in Table 2.

The acidic dissociation constants of Chlorthalidone and Terbutaline have been determined using the CE method [42]. In the case of Terbutaline, UV spectroscopy is less suitable for the demonstration of partitioning of the neutral form because here the uncharged species has the same spectrum as that of the cation form. Of course, potentiometry and spectroscopic methods are highly sensitive and as such are suitable for studying chemical equilibria solutions.

Solvent-Solute Interactions:
Ionic Product of Water

For an ionization reaction in pure water or an aqueous solution, in which a water molecule, loses the nucleus of one of its hydrogen atoms to become a hydroxide ion (OH^-). The hydrogen nucleus (H^+) protonates other water molecules to form hydronium (H_3O^+), immediately.

$$2H_2O \leftrightarrow H_3O^+ + OH^- \quad (5)$$

Applying law of mass action at equilibrium, the value of dissociation constant (K) can be expressed as follows:

$$K = [H_3O^+]\,[OH^-]/[H_2O]^2 \quad (6)$$

Since dissociation takes place to a very small extent, the concentration of undissociated water molecules ($[H_2O]$); can be regarded as constant.

$$K_w = [H_3O^+][OH^-] \quad (7)$$

K_w is a constant at a given temperature and is known as ionic product of water. Equations 5 and 7 are frequently used in studies of acid-base equilibria in aqueous media [43]. It must be noted

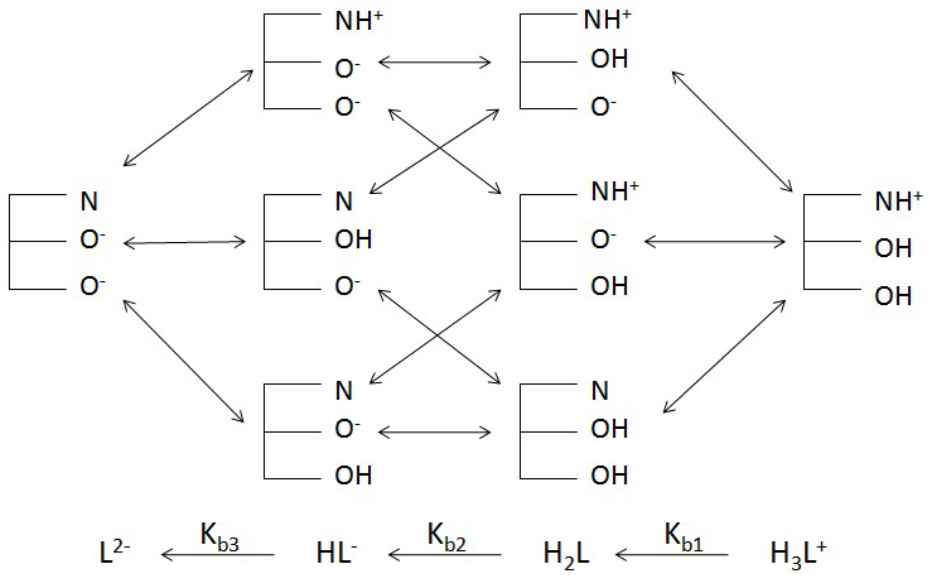

Figure 2. Protonation of Terbutaline.

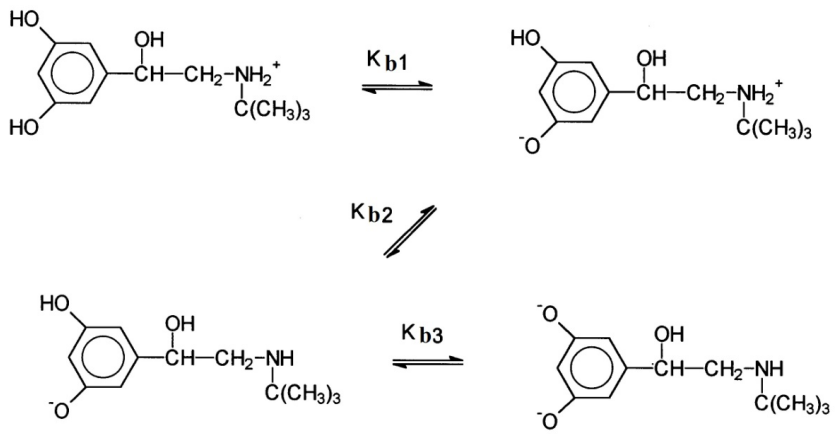

Figure 3. Suggested protonation scheme of Terbutaline.

that the solvation of anions is effective in protic solvents where hydrogen bonds can be formed between the proton of the solvent and the lone pairs of electrons of the anion. The total energies of the single and solvated OH- ion have been computed in water at the B3LYP/6-31+G(d) level of theory, using Tomasi's model. Considering the structures of the hydroxyl ion solvated with one water and also two water molecules together, it can be concluded that the IHBs between the OH^- ion and the water molecules of solvation belong to the class of moderate or strong H bonds. The calculated total energy values confirm a in significant decrease of the total energy of the OH^- ion when its solvation increases [44,45].

According to the above content and to provide a more acceptable illustration of the protolysis of water, the reaction has been shown as follows:

$$3H_2O \leftrightarrow H_3O^+ + OH^-(H_2O) \quad (8)$$

The above reaction assumes that both H+ and OH^- ions are hydrated with one water molecule. Also, indicating with KN1 the equilibrium constant of the reaction of Equation 8 and considering the equations 5 and 7, it is inferred that [46]:

$$K_w = K_{N1}[H_2O] \quad (9)$$

Table 2. Values of pK_a for the Protonation of Chlorthalidone and Terbutaline Obtained Using the Tomasi method at the B3LYP/6-31+G(d) Level of Theory, at 298.15 K[a].

Species	Selected equations	pK_a (Calculated)	pK_a (Experimental)	Ref
Chlorthalidone	$H_2L^{+2}(H_2O) + H_2O \longleftrightarrow HL^{+}(H_2O) + H_3O^{+}$	9.26	8.98 (I = 0.05)	[42]
	$HL^{+}(H_2O) + 2H_2O \longleftrightarrow L(H_2O)_2 + H_3O^{+}$	10.96	10.82 (I = 0.05)	[42]
	$H_3L^{+} + 2H_2O \longleftrightarrow H_2L(H_2O) + H_3O^{+}$	8.85	8.79 (I = 0.05)	[42]
Terbutaline	$H_2L + 2H_2O \longleftrightarrow HL^{-}(H_2O) + H_3O^{+}$	9.93	9.54 (I = 0.05)	[42]
	$HL^{-} + 2H_2O \longleftrightarrow L^{2-}(H_2O) + H_3O^{+}$	10.88	10.47 (I = 0.05)	[42]

As regards, $[H_2O]$ is the molar concentration of water; K_{N1} (at 298.15 K) was calculated as follows:

$$K_{N1} = K_w/[H_2O] = 1.831x10^{-16} \quad (10)$$

With a similar trend, K_{N2} and K_{N3} (at 298.15 K) were calculated as follows:

$$4H_2O \leftrightarrow H_3O^{+} + OH^{-}(H_2O)_2 \quad (11)$$

$$5H_2O \leftrightarrow H_3O^{+} + OH^{-}(H_2O)_3 \quad (12)$$

The selected reaction considers that OH^{-} ions are hydrated with two water and three molecules, respectively.

$$K_w = K_{N2}[H_2O]^2 \quad (13)$$

$$K_w = KN_3[H_2O]_3 \quad (14)$$

As a result :

$$K_{N2} = K_w/[H_2O]^2 = 3.3226x10^{-18} \quad (15)$$

$$K_{N3} = K_w/[H_2O]_3 = 6.4149x10^{-20} \quad (16)$$

Similarly, the total energies of the single and solvated Chlorthalidone (cationic, neutral) and Terbutaline (cationic, zwitterion, and anionic) species were calculated in water at the B3LYP/6-31+G(d) level of the theory, using Tomasi's model. Table 1 summarizes the variations of the total energy ($kJ.mol^{-1}$) of the species per water molecule as a function of the total number of solvation water molecules. Figure 4 and Table 1 show the marked increase of the total energies of cations when the solvation increases.

The data show that the water, exerting its hydrogen-bond donor (HBD) capability, forms IHBs with the Chlorthalidone and Terbutaline species [47]. These hydrogen bonds can be classified as strong, moderate, and weak, according to their lengths, angles, and energies [45].

First Ionization Constant of Chlorthalidone and Terbutaline

It was chosen that in alkaline solutions Chlorthalidone suffers a reaction of partial neutralization as follows:

$$H_2L^{+2}(H_2O) + OH^{-}(H_2O) \leftrightarrow HL^{+}(H_2O) + 3H_2O \; K_{c1} \quad [17]$$

$$H_3L^{+} + OH^{-}(H_2O)_3 \leftrightarrow H_2L(H_2O) + 3H_2O \qquad K_{d1} \quad [18]$$

In Reaction 17, $H_2L^{+}2(H_2O)$ is the Chlorthalidone cation (+2) solvated with one water molecule, and $HL^{+}(H_2O)$ represents the cation (+1) solvated with one water molecule. In Reaction 18, H_3L^{+} is the Terbutaline cation, and $H_2L(H_2O)$ represents the Terbutaline zwitterion solvated with one water molecule. The earlier reaction is characterized by equilibrium constants (K_{CI}) and (K_{DI}), which were theoretically obtained.

By incorporating Equations (11) and (17) and also (12) and (18), was obtained the reaction of Equations (19) and (20), which define the first ionization constant of Chlorthalidone (K_{al}) and Terbutaline (K_{bl}):

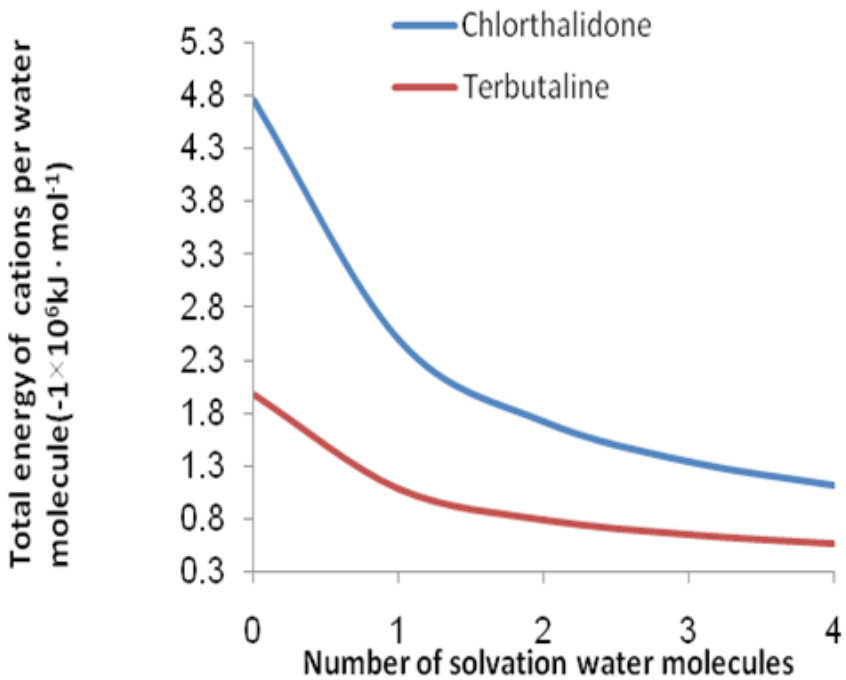

Figure 4. Plot of the total energy (kJ · mol^{-1}) of solvated Chlorthalidone and Terbutaline cations.

$$H_2L^+2(H_2O) + H_2O \leftrightarrow HL^+(H_2O) + H_3O^+ \quad (19)$$
$$H_3L^+ + 2H_2O \leftrightarrow H_2L(H_2O) + H_3O^+ \quad (20)$$

It is obvious that:

$$K_{al} = K_{C1}xK_{N2} \quad (21)$$
$$K_{bl} = K_{D1}xK_{N3} \quad (22)$$

The Previous equations were applied to determine theoretically the value of the first ionization constant of Chlorthalidone and Terbutaline in water. Table 3 and 4 summarize the optimized values of molecular properties of the $H_2L^+2(H_2O)$ cation (Figure 5a), $OH^-(H_2O)_2$ ion, and the HL^+ (H^2O) cation (Figure 5b) for Chlorthalidone, and also the H_3L^+ cation (Figure 5d) , $OH^-(H_2O)_3$ ion, and the H_2L (H_2O) zwitterion (Figure 5e) for Terbutaline obtained at the B3LYP/6-31+G(d) level of theory with Tomasi's method in water at 298.15 K.

Evidently, the formation of the Chlorthalidone cation (+1) implies that the electronic density of the N22 atom decreases notably (in absolute value) with respect to the N22 atom of the Chlorthalidone cation (+2) (Table 3). Also, the formation of the Terbutaline zwitterion implies that the electronic density of the N10 atom increases notably (in absolute value) with respect to the N10 atom of the Terbutaline cation as shown Table 4. It can be observed that the p_{K1} value (Chlorthalidone and Terbutaline) theoretically calculated (pK_1= 9.26 and 8.85) is relatively comparable with the experimentally determined pKa (pK_{al}= 8.98 and 8.79) [42].

Second Ionization Constant of Chlorthalidone and Terbutaline

It was chosen that the $HL^+(H_2O)$ cation (for Chlorthalidone) and the H_2L zwitterion (for Terbutaline) suffer a total neutralization as follows:

$$HL^+(H_2O)+OH^-(H_2O)_2 \leftrightarrow L(H_2O)_2+2H_2O \quad K_{c2} \quad (23)$$

$$H_2L^+OH^-(H_2O)_3 \leftrightarrow HL^-(H_2O)+3H_2O \quad K_{c2} \quad (24)$$

In this Reaction 23, $L(H_2O)_2$ is the neutral Chlorthalidone solvated with two water molecules.

Table 3. Calculated Structural Magnitudes Using Tomasi's method at the B3LYP/6-31+G(d) Level of Theory for the Cations, Neutral Molecule of Chlorthalidone at 298.15 K[a].

species	calculated magnitudes		
Chlorthalidone	**H_2L^{+2}**	**HL^{+}**	**L**
K_{C1}	5.47139×10+26		
K_{C2}		2.7487×10+28	
K_{a1}	1819784793		
K_{a2}		91422675850	
a_0	5.66	5.53	5.61
qN9	-0.869781	-0.881671	-0.350277
qN22	-1.235729	-1.033625	-1.002692
qO10	-0.452519	-	-
qO11	-0.662984	-0.462837	-0.726303
qO12	-	-0.64038	-0.655234
qO20	-0.414597	-0.612895	-0.536961
qO21	-0.519032	-0.690307	-0.76932
qO34	-	-	-1.100298
qO35	-	-1.081889	-
qO36	-1.055022	-	-
qO37	-	-	-1.091448
qH27	0.560659	-	-
qH28	0.571317	0.575024	0.571452
qH29	0.573757	0.562625	-
qH30	-	0.564973	-
qH33	-	0.524151	0.513411
qH35	0.624499	-	-
qH36	-	0.545505	-
qH39	-	-	0.560644
dH35O36	1.63926	-	-
dN22H36	-	1.89488	-
dH33O34	-	-	1.97168
dO21H35	-	-	1.98381
dH28O37	-	-	2.05303
AN22H35O36	176.5741	-	-
AN22H33O35	-	157.74426	-
AN9H28O37	-	-	134.23199
AO34H33O21	-	-	141.77624
AN22H33O34	-	-	155.04642

Table 3. Calculated Structural Magnitudes Using Tomasi's method at the B3LYP/6-31+G(d) Level of Theory for the Cations, Neutral Molecule of Chlorthalidone at 298.15 K[a] (continue).

D-C4C3C2C1	-32.052136	-31.606238	-32.178525
D-C5C4C3C2	-0.239757	-0.089232	-0.181981
D-C6C2C1C5	-69.202169	-69.097333	-64.074964
D-C7C6C2C1	29.643695	28.928289	28.239304
D-C8C5C4C3	-176.253668	-176.957027	-176.707388
D-N9C8C5C4	178.512585	-175.352583	-177.842982
D-C10C7C6C2	178.579414	-179.589697	-
D-O11C10C7C6	2.339733	-2.906465	-
D-C10N9C8C5	-	-	-5.804318
D-O11C10N9C8	-	-	-176.288169
D-O12C8C5C4	64.176803	71.92783	69.227345
D-C13C1C8C5	149.243109	140.682767	154.143681
D-C14C13C1C8	178.424588	178.561283	177.096798
D-C15C14C13C1	-0.860136	-0.391354	0.290698
D-C16C15C14C13	-0.758667	-0.565803	0.01348
D-C17C1C13C14	1.562234	0.815243	-0.644875
D-CL18C16C15C14	-179.676325	-179.565976	179.267007
D-S19C17C11C13	173.238183	177.083055	-
D-O20S19C17C1	-126.540082	-120.788711	-122.934802
D-O21S19C17C1	15.942181	8.98578	7.64642
D-N22S19C17C1	124.290736	122.849115	119.724121
D-H23C1C13C14	-178.236375	-	-
D-H24C2C1C13	168.844385	-	-
D-H23C1C17C16	-	178.546553	-179.642006
D-H24C2C1C17	-	28.341488	20.469946
D-H25C3C2C1	148.253578	148.047655	147.303637
D-H26C4C3C2	-179.641099	179.293498	178.918952
D-H27N6C2C1	-150.836406	-150.655141	-151.549369
D-H28N9C8C5	-120.810473	-129.784592	-176.90843
D-H29N9C8C5	119.791579	111.185705	-
D-H30O12C8C5	15.657391	12.077779	-
D-H31C14C13C1	178.358033	179.139532	-
D-H32C15C14C13	179.615518	179.709326	-
D-H29O12C8C5	-	-	-61.203366
D-H30C14C13C1	-	-	-179.685702

Table 3. Calculated Structural Magnitudes Using Tomasi's method at the B3LYP/6-31+G(d) Level of Theory for the Cations, Neutral Molecule of Chlorthalidone at 298.15 K[a] (continue).

D-H31C15C14C13	-	-	179.972921
H32N22S19C17	-	-	107.333167
D-H33N22S19C17	52.2896	113.893199	-125.427425
D-H34N22S19C17	-70.679558	-118.787314	-
D-H35N22S19C17	169.97626	113.819214	-
D-O36N22S19C17	168.047124	-	-
D-H37O36N22S19	143.97334	-	-
D-H38O36N22S19	-37.820899	-	-
D-H36O35N22S19	-	8.348871	-
D-H37O35N22S19	-	128.319656	-
D-O34O21S19C17	-	-	120.891683
D-H35O34O21S19	-	-	167.46884
D-H36O34O21S19	-	-	112.052863
D-O37O11C10N9	-	-	1.572607
D-H38O37O11C10	-	-	126.991671
D-H39O37O11C10	-	-	179.277537

[a] K_{C1} and K_{C2}, equilibrium constants of equations; K_{a1} and K_{a2}, first and second acidic dissociation constants of species in water; D, dihedral angle between the indicated atoms (Å); a_0, bohr radius (Å); q, total atomic charge (Muliken) (au); r, bond lengths between the indicated atoms; d, distance of the IHB between the indicated atoms (Å); A, H-bond angles (°).

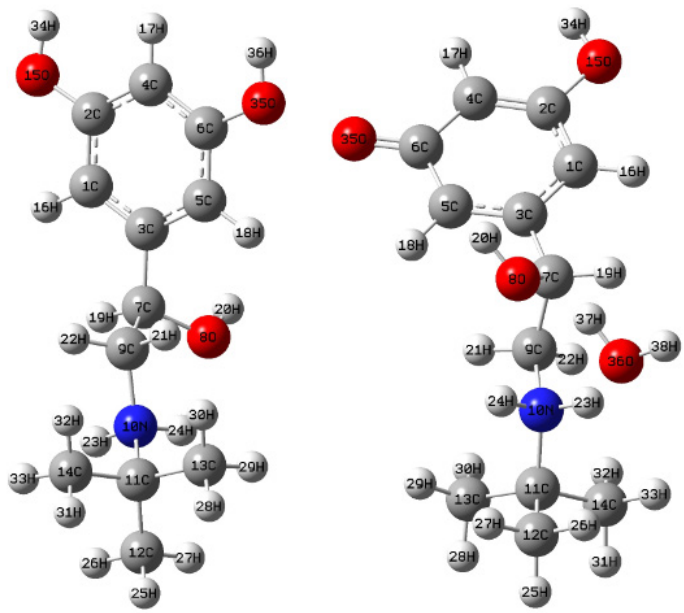

Figure 5. Calculated structure for the Chlorthalidone cations (a) and (b), natural Chlorthalidone (c), Terbutaline cation (d), and Terbutaline zwitterion (e), at the B3LYP/6-31+G(d) level of theory and using Tomasi's method in water at 298.15 K.

Also, in reaction 24, $HL^-(H_2O)$ represents the Terbutaline anion solvated with one water molecule. By incorporating Equations (11) and (23) as well as (12) and (24), were obtained the reaction of Equations (25) and (26):

$$HL^+(H_2O) + 2H_20 \leftrightarrow L(H_2O)_2 + H_3O^+ \qquad K_{a2} \qquad (25)$$

$$H_2L^+2H_2O \leftrightarrow HL^-(H_2O) + 3H_3O^+ \qquad K_{b2} \qquad (26)$$

The equilibrium constant K_{a2} and K_{b2} that characterizes the above reactions, are as follows:

$$K_{a2} = K_{C2} \times K_{N2} \qquad (27)$$

$$K_{b2} = K_{D2} \times K_{N3} \qquad (28)$$

These equations were used to determine theoretically the value of the second ionization constant of Chlorthalidone and Terbutaline in water. Table 3 and 4 summarize the optimized values of molecular properties of the neutral Chlorthalidone (Figure 5c), and also the H_2L zwitterion, $OH^-(H_2O)_3$ ion, and $HL^-(H_2O)$ anion molecule (Figure 6) for Terbutaline obtained at the B3LYP/6-31+G(d) level of theory with Tomasi's method in water at 298.15 K. Evidently, the formation of the neutral Chlorthalidone implies that the electronic density of the N9 atom decreases notably (in absolute value) with respect to the N9 atom of the Chlorthalidone cation (+1), as shown Table 3. Also, the formation of the Terbutaline anion implies that the electronic density of the N10 atom decreases notably (in absolute value) with respect to the N10 atom of the Terbutaline zwitterion (Table 4).

It can be observed that the p_{K2} value (Chlorthalidone and Terbutaline) theoretically calculated (p_{K2} = 10.96 and 9.93) is relatively comparable with the experimentally determined pKa (pK_{a2} = 10.82 and 9.54) [42].

Third Ionization Constant of Terbutaline

Also, it is selected that the HL^- anion suffers a total neutralization process as follows:

$$HL^- + OH^-(H_2O)_3 \leftrightarrow L^{2-}(H_2O) + 3H_2O \qquad (29)$$

In the above reaction, L^{-2} represents the second anion of Terbutaline. The reaction described in Eq. (25) is characterized by another equilibrium constant, K_{C3}, which was also theoretically determined. By combining Equations (12) and (29), the Third ionization reaction of Terbutaline was obtained:

$$HL^- + 2H_2O \leftrightarrow L^{2-}(H_2O) + H_3O^+ \qquad (30)$$

The third ionization constant (K_{a3}) that characterizes the above reaction is associated with constants K_{C3} and K_{N3} by Equation 31:

$$K_{a3} = K_{c3} \times K_{N3} \qquad (31)$$

The above equation was used to determine theoretically the value of the third ionization constant of Terbutaline in water. Table 4 summarizes the optimized values of molecular properties of the HL- anion (Figure 7), $OH^-(H_2O)_3$ ion, and $L^{2-}(H_2O)$ anion molecule (Figure 7) obtained at the B3LYP/6-31+G(d) level of theory with Tomasi's method in water at 298.15 K. Obviously, the formation of the Terbutaline anion (L^{2-}) implies that the electronic density of the O33 atom increases notably (in absolute value) with respect to the O34 atom of the Terbutaline anion (HL^-) (Table 4).

It can be observed that the pK_{b2} value theoretically calculated (pK_{b3}= 10.88) is relatively comparable with the experimentally determined p_{Kb} (pK_{b3}= 10.45) [42].

The molecule of water originated from the acid-base reaction, together with the hydration water molecule of the Chlorthalidone and Terbutaline, and these are the molecules of water that interact with the Chlorthalidone and Terbutaline molecules by means of IHBs. Figure 5a shows that the distance and bond angle formed by the involved atoms (H35O36, O36H35N22) in the IHB are 1.63926 Å and 176.57410, respectively. According to ref 45 and 48, The IHB of this cation is moderate. Similarly, the IHB of the Chlorthalidone cation (+1), the neutral Chlorthalidone and zwitterion of Terbutaline belongs to the moderate closely to weak. Also, the IHB of the anions of Terbutaline belongs to the moderate closely to strong, as shown in Tables 3 and 4. Finally, it must be noted that IHB data can be use in the design of benefit and economical nanodrugs

Table 4. Calculated Structural Magnitudes Using Tomasi's method at the B3LYP/6-31+G(d) Level of Theory for the Cations, Neutral Molecule of Terbutaline at 298.15 K.

Species	**Calculated Magnitudes**					
Terbutaline	**H_3L^+**	**$H_2L(H_2O)$**	**H_2L**	**$HL^-(H_2O)$**	**HL^-**	**$L^{-2}(H_2O)$**
K_{D1}	1.10203×10+28	-	-	-	-	-
K_{D2}	-	-	1.31883×10+29	-	-	-
K_{D3}	-	-	-	-	1.18412×10+30	-
K_{b1}	706940668	-	-	-	-	-
K_{b2}	8460184083	-	-	-	-	-
K_{b3}	75960017400	-	-	-	-	-
a_0	4.83	5.24	5.21	5.25	4.94	5.08
A036H37O8	-	140.01703	-	-	-	-
AN10H23O36	-	141.8248	-	-	-	-
A035H37O34	-	-	-	171.22513	-	-
A034H36O15	-	-	-	-	-	178.26984
d08H37	-	1.903	-	-	-	-
d036H23	-	1.91285	-	-	-	-
d034H37	-	-	-	1.69809	-	-
d015H36	-	-	-	-	-	1.60425
qN10	-0.728662	-0.786153	-0.73998	-0.398989	-0.46447	-0.467017
q08	-0.773568	-0.834024	-0.72149	-0.752051	-0.80841	-0.813892
qO15	-0.780143	-0.795078	-0.79112	-0.791939	-0.796125	-1.014998
qO33	-	-	-	-	-	-0.980297
qO34	-	-	-	-0.959339	-0.93215	-1.125891
qO35	-	-0.920977	-0.92307	-1.114995	-	-
qO36	-	-1.12687	-	-	-	-
	-0.789211	-	-	-	-	-
D-C4C2C1C3	0.43675	0.715758	0.524039	0.428692	0.728914	1.227871
D-C5C3C1C2	-0.343587	-0.480222	-0.3195	-0.273286	-0.440616	-0.993797
D-C6C5C3C1	-0.114031	-0.107579	-0.20194	-0.340209	-	-
D-C6C4C2C1	-	-	-	-	-0.326334	-0.76845
D-C7C3C1C2	178.755146	-179.6147	-179.74	-179.8691	-179.9317	-179.45804
D-O8C7C3C1	137.429313	124.83565	123.741	124.27799	124.8866	126.488056
D-C9C7C3C1	-105.749265	-115.5787	-117.795	-111.994	-113.4004	-112.55841
D-N10C9C7C3	-171.570301	-163.7614	-163.32	168.75447	-173.2636	-172.09556
D-C11N10C9C7	166.91148	-171.3762	161.0855	179.58776	-93.94761	-94.268028
D-C12C11N10C9	176.524133	-172.7705	175.966	176.76981	171.9442	171.220353
D-C13C11N10C9	-64.652973	-53.34922	-65.1655	-65.84131	-71.05039	-71.889549
D-C14C11N10C9	57.327208	68.472449	56.61855	56.922857	51.71159	50.87956
D-O15C2C1C3	-179.921752	-179.7674	-179.844	179.87817	-179.9048	-179.55796

Table 4. Calculated Structural Magnitudes Using Tomasi's method at the B3LYP/6-31+G(d) Level of Theory for the Cations, Neutral Molecule of Terbutaline at 298.15 K (continue).

D-H16C1C3C5	178.858907	178.17527	178.0466	-178.4323	-	177.061977
D-H16C1C2C4	-	-	-	-	-177.8487	-
D-H17C4C2C1	179.497525	179.99705	-179.964	179.7405	179.8799	179.656523
D-H18C5C3C1	-178.65648	178.33117	178.7774	178.57563	177.7021	175.267853
D-H19C7C3C1	14.716872	5.790718	4.028713	6.779443	8.227176	9.719289
D-H20O8C7C3	-48.881118	-0.535404	3.566009	3.791477	10.40072	9.379499
D-H21C9C7C3	-54.130222	-45.23875	-46.2391	-71.26685	-52.49135	-51.589765
D-H22C9C7C3	68.106797	76.037769	76.18596	44.472684	62.64193	63.73312
D-H23N10C9C7	-68.955213	-44.02643	-73.3176	-55.81476	33.70633	31.454611
D-H24N10C9C7	43.420651	65.345162	38.22395	-	-	-
D-H24C12C11N10	-	-	-	178.67598	176.7455	176.886624
D-H25C12C11N10	179.358828	65.345162	179.3902	-61.66615	-63.52368	-63.3316
D-H26C12C11N10	-61.875869	-58.68381	-61.6162	57.897276	56.17431	56.176564
D-H27C12C11N10	60.478921	62.624266	60.22582	-	-	-
D-H27C13C11N10	-	-	-	-172.7262	-176.2895	-176.28462
D-H28C13C11N10	-174.13763	-174.4564	-174.796	-52.56811	-55.90301	-55.763377
D-H29C13C11N10	-55.723089	-55.75045	-56.0816	67.594404	63.92951	63.832794
D-H30C13C11N10	67.326907	66.400544	66.23309	-	-	-
D-H30C14C11N10	-	-	-	177.35701	177.467	178.05327
D-H31C14C11N10	174.905789	175.60185	175.9323	-62.58781	-62.79616	-61.839087
D-H32C14C11N10	-66.353409	-65.43026	-65.0011	57.508329	57.41653	57.853294
D-H33C14C11N10	56.456058	56.886217	57.14056	-	-	-
D-H33O15C2C1	-	-	-	-178.655	-178.8565	-
D-H34O15C2C1	-178.511186	-178.8125	-178.569	-	-	-
D-O35C6C5C3	-179.662513	179.65356	179.6185	-	-	-
D-H36O35C6C5	178.908676	-	-	-	-	-
D-O36O8C7C3	-	-158.8168	-	-	-	-
D-H37O36O8C7	-	129.12879	-	-	-	-
D-H38O36O8C7	-	89.603925	-	-	-	-
D-O34C6C4C2	-	-	-	-179.6065	-179.8231	-
D-O35O34C6C4	-	-	-	170.67133	-	-
D-H36O35O34C6	-	-	-	-103.5901	-	-
D-H37O35O34C6	-	-	-	64.627751	-	-
D-O33C6C4C2	-	-	-	-	-	-179.21227
D-O34O15C2C1	-	-	-	-	-	-179.51738
D-H35O34O15C2	-	-	-	-	-	0.580446
D-H36O34O15C2	-	-	-	-	-	-171.85203

[a] K_{D1}, K_{D2} and K_{D3}, equilibrium constants of equations; K_{b1}, K_{b2} and K_{b3}, acidic dissociation constants of species in water; D, dihedral angle between the indicated atoms (Å); a_0, Bohr radius (Å); q, total atomic charge (Muliken) (au); r, bond lengths between the indicated atoms; d, distance of the IHB between the indicated atoms (Å); A, H-bond angles (°).

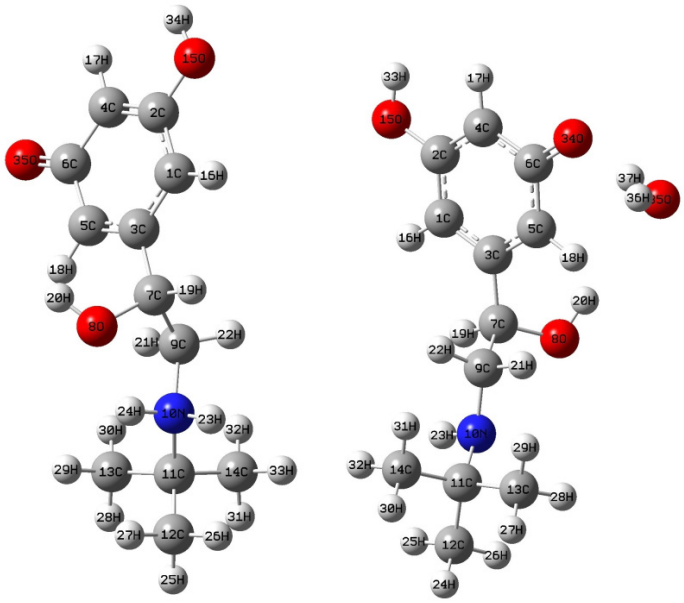

Figure 6. Calculated structure for (a) the Terbutaline anion (H_2L) and (b) the Terbutaline zwitterion ($HL^-(H_2O)$), at the B3LYP/6-31+G(d) level of theory and using Tomasi's method in water at 298.15 K.

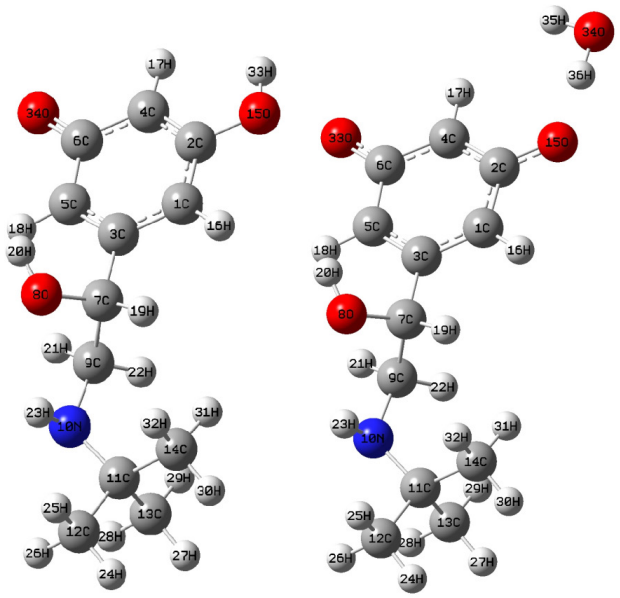

Figure 7. Calculated structure for the Terbutaline anions, at the B3LYP/6-31+G(d) level of theory and using Tomasi's method in water at 298.15 K.

that are very useful in the treatment of disease.

CONCLUSIONS

In this study, we showed the possibility of a theoretical method that uses pH values to determine the ionization constants of Chlorthalidone and Terbutaline. Also, the autoprotolysis constants calculated with an acceptable degree of accuracy. With this purpose, we selected various acid-base reactions that take into account the solvation of the hydrogen, hydroxyl ions, and other cations or anions in protic solvents such as water, which possess a high hydrogen-bond-donor capability. The calculations performed at the B3LYP/6-31+G(d) levels of theory using Tomasi's method allowed us to prove that cations, neutral molecules, and anions form IHBs with some molecules of water. The autoprotolysis constants theoretically show a suitable agreement with the autoprotolysis constants experimentally determined by the CE

method.

ACKNOWLEDGMENT

Thanks are gratefully extended to the Faculty of Chemistry, Semnan University and Islamic Azad University, Ayatollah Amoli Branch for their valuable helps with this work.

References

1. D.G. Arkfield, E. Rubenstein, Quest for the Holy Grail to cure arthrithis and osteoporosis: emphasis on bone drug delivery systems, Adv. Drug. Deliver. Rev., 57 (2005) 939-944.
2. M.O. Emeje, I.C. Obidike, E.I. Akpabio, S.I. Ofoefule, Toxicology and pharmaceutical science, Recent Advances in Novel Drug Carrier Systems, InTech, Turkey, 2012.
3. R.W. Matthew, R. Agarwal, Heart disease and stroke statistics, Am. Heart Assoc., 59 (2012) 1089-1095.
4. D.H. Ellison, J. Loffing, Thiazide effects and side effects: insights from molecular genetics, Am. Heart Assoc., 54 (2009) 196-202.
5. Sica DA, Resistant hypertension: diagnosis, evaluation, and treatment, Am. Heart Assoc., 47 (2006) 321-322.
6. Kurtz TW, Chlorthalidone: don't call it "thiazide-like" anymore, Am. Heart Assoc., 56 (2010) 335-337.
7. E.K. Main, D.M. Main, S.G. Gabbe, Chronic oral terbutaline tocolytic therapy as associated with maternal glucose intolerance, Am. J. Obstetrics & Gynecolog., 157 (1987) 644-647.
8. J.E. Gerich, M. Langlois, C. Noacco, V. Schneider, P.H. Forsham, Adrenergic modulation of pancreatic glucagon secretion in man, J. Clinical. Inves., 53 (1974) 1441-1446.
9. L.P. Boulet, A. Becker, D. Bérubé, (CAMJ) Can. Med. Assoc. J., 161 (1999) S1-S62.
10. Z. Jia, T. Ramstad, M. Zhong, Medium-throughput pK a screening of pharmaceuticals by pressure-assisted capillary, Electrophoresis., 22 (2001) 1112-118.
11. C.E. Kibbey, S.K. Poole, B. Robinson, J.D. Jackson, D. Durham, An integrated process for measuring the physicochemical properties of drug candidates in a preclinical discovery environment, J. Pharm. Sci., 90 (2001) 1164-1175.
12. W. Stumm, J.J. Morgan, Aquatic chemistry: chemical equilibria and rates in natural waters, Wiley-Interscience, New York (1996).
13. G. Thomas, Medicinal chemistry, an introduction, John Wiley & Sons: West Sussex (2000).
14. A. Avdeef, J.J. Bucher, Accurate measurements of the concentration of hydrogen ions, Anal. Chem., 50 (1978) 2137-2142.
15. Z. Qiang, C. Adams, Potentiometric determination of acid dissociation constants (pKa) for human and veterinary antibiotics, Water. Res., 38 (2004) 2874-2890.
16. J.L. Beltra´n, N. Sanli, G. Fonrodona, D. Barro´n, G. Ozkanb, J. Barbosa, Spectrophotometric, potentiometric and chromatographic pKa values of polyphenolic acids in water and acetonitrile–water media, Anal. Chim. Acta., 484 (2003) 253-263.
17. H.Y. Ando, T. Heimbach, pKa determinations by using a HPLC equipped with DAD as a flow injection apparatus, J. Pharm & Biomedical. Anal., 16 (1997) 31-39.
18. S.K. Pool, S. Patel, K. Dehring, H. Workman, C.F. Pool, Determination of acid dissociation constants by capillary electrophoresis, J. Chromatography, A., 1037 (2004) 445-454.
19. P. Janoš˘, Determination of equilibrium constants from chromatographic and electrophoretic measurements, J. Chromatography. A., 1037 (2004) 15-28.
20. C.P. Kelly, C.J. Cramer, D.G. Truhlar, Adding explicit solvent molecules to continuum solvent calculations for the calculation of aqueous acid dissociation constants, J. Phys. Chem, A., 110 (2006) 2493-2499.
21. K. Mohle, H.J. Hofmann, Stability order of basic peptide conformations reflected by density functional theory, J. Mol. Model., 4 (1998) 53-60.
22. R.D. Tosso, M.A. Zamora, F.D. Survire, R.D. Enriz, Ab initio and DFT study of the conformational energy hypersurface of cyclic Gly-Gly-Gly, J. Phys. Chem. A., 113 (2009) 10818-10825.
23. P. Hudaky, A. Perczel, Conformation dependence of pKa: Ab initio and DFT investigation of histidine, J. Phys. Chem. A., 108 (2004) 6195-6205.
24. M.D. Liptak, K.C. Gross, P.G. Seybold, S. Feldgus, G.C. Shields, Absolute pKa determinations for substituted phenols, J. Am. Chem. Soc., 124 (2002) 6421-6427.
25. N.S. Sosnowska, Calculation of acidic dissociation constants in water: solvation free energy terms. Their accuracy and impact, Theor. Chem. Account., 118 (2007) 281-289.
26. P. Hohenberg, W. Kohn, Inhomogeneous electron gas, Phys. Rev. B., 136 (1964) 864-871.
27. A.D. Becke, Density-functional exchange-energy approximation with correct asymptotic behavior, Phys. Rev, A., 38 (1988) 3098-4003.
28. C. Lee, W. Yang, R.G. Parr, Development of the Colle-Salvetti correlation-energy formula into a functional of the electron density, Phys. Rev, B., 37 (1988) 785-792.
29. B.G. Johnson, M.J. Frisch, Analytic second derivatives of the gradient-corrected density functional energy. Effect of quadrature weight derivatives, Chem. phys. Lett., 216 (1993) 133-139.
30. W.J. Hehre, L. Radom, P.V.R. Schleyer, A.J. Pople, Ab initio molecular orbital theory, Wiley, New York (1989).
31. Z. Dega-Szafran, A. Katrusiak, M. Szafran, Molecular structure of the complex of N-methylmorpholine betaine with 2,4-dinitrophenol, J. Mol. Struct., 741 (2005) 1-9.
32. Program CS Chem3D 5.0; Program for Molecular Modeling and Analysis; Cambridge Soft Corporation: MA, USA (2000).
33. M.J. Frisch et al. Gaussian 98, revision A.6; Gaussian, Inc.: Pittsburgh, PA (1998).
34. Miertus S, Tomasi EJ, Approximate evaluations of the electrostatic free energy and internal energy changes in solution processes, Chem phys 1982;65: 239-245.
35. H.A. Laitinen, W.E. Harris, Chemical Analysis; McGraw-Hill: New York (1975).
36. R.I. Allen, K.J. Box, J.E.A. Comer, C. Peake, K.Y. Tam, Multiwavelength spectrophotometric determination of acid dissociation constants of ionizable drugs, J.

Pharm & Biomedical. Anal., 17 (1998) 699-712.
37. K. Taka´cs-Nova´k, B. Nosza´l, M. To¨ke´s-Ko¨vesdi, G. Sza´sz, Acid-base properties of terbutaline in terms of protonation macro- and microconstants, J. Pharm & Pharmacology., 47 (1995) 431-438.
38. Z. Szakacs, M. Krasni, B. Noszal, Determination of microscopic acid–base parameters from NMR–pH titrations, Anal & Bioanal. Chem., 378 (2004) 1428-1448.
39. M. Borkovec, M. Brxnda, G.J.M. Koper, B. Spiess, Resolution of microscopic Protonation mechanisms in polyprotic molecules, Int. J. Chem., 56 (2002) 695-700.
40. D.L. Rabenstein, T.L. Sayer, Determination of microscopic acid by nuclear magnetic resonance spectrometry, J. Anal. Chem., 48 (1976) 1141-1146.
41. M. Shalaeva, J. Kenseth, F. Lombardo, A. Bastin, Measurement of dissociation constants (pKa values) of organic compounds by multiplexed capillary electrophoresis using aqueous and cosolvent buffers, J. Pharm. Sci., 97 (2008) 2581-2606.
42. P.W. Atkins, Physical Chemistry, 6th ed., Oxford University Press, England (1998).
43. F. Ruff, I.C. Csizmadia, Organic reactions, equilibria, kinetics and mechanism, Elsevier, London (1994).
44. G.A. Jeffrey, An introduction to hydrogen bonding, Oxford University Press, Oxford (1997).
45. S.E. Blanco, M.C. Almandoz, F.H. Ferretti, Determination of the overlapping pKa values of resorcinol using UV-visible spectroscopy and DFT methods, Spectrochimica. Acta. Part A., 61 (2005) 93-102.
46. Y. Marcus, The properties of organic liquids that are relevant to their use as solvating solvents, Chem. Soc. Rev., 22 (1993) 409-416.
47. F. Kiani, A.A. Rostami, S. Sharifi, A. Bahadori, M.J. Chaichi, Determination of acidic dissociation constants of glycine, valine, phenylalanine, glycylvaline, and glycylphenylalanine in water using ab initio methods, J. Chem & Eng. Data., 55 (2010) 2732-2740.

Reprogramming Human Melanocytes and Melanoma Cells with Yamanaka Factors

İnsan Melanositlerinin ve Melanoma Hücrelerinin Yamanaka Faktörleri ile Yeniden Programlanması

Research Article

Açelya Yılmazer[1,2*] and Hadiseh Taheri[1,3]

[1]Ankara University, Biomedical Engineering Department, Engineering Faculty, Gölbaşı, Ankara, Turkey.

[2]Ankara University, Stem Cell Institute, Balgat, Ankara, Turkey.

[3]Biotechnology Institute, Ankara University, Tandogan, Ankara, Turkey.

ABSTRACT

The generation of induced pluripotent stem (iPS) cells from somatic cells showed that cell fate could be manipulated by simply introducing a few transcription factors. The differentiation potential of iPS cells has uncovered a wide range of potential applications, including disease modeling, drug screening and regenerative therapy. In this study, we aimed to induce reprogramming of human melanocytes and melanoma cell lines via Sendai viral vectors encoding Yamanaka factors. Following transfection, pluripotent stem cell colonies have emerged in the melanocyte cultures, as evident by phase-contrast and fluorescence microscopy images. However, only cell clusters which were not positive for pluripotency markers were obtained in the melanoma cell cultures. This proved that there are differences between healthy and cancer cell reprogramming. Basal gene expression of Yamanaka factors, pluripotency markers and tumor-suppressor genes have been identified in order to understand the different responses for cell reprogramming in melanocytes and cancer cell lines. Future studies that will allow efficient reprogramming of cancer cells can improve our knowledge about cancer biology and therapy

Key Words

iPS cells, melanoma, melanocytes, Yamanaka factors, cell reprogramming.

ÖZ

Somatik hücrelerden uyarılmış pluripotent kök (uPK) hücrelerin üretilmesi, hücre kaderinin sadece birkaç transkripsiyon faktörü kullanılarak değiştirilebileceğini göstermiştir. uPK hücrelerinin farklılaşma potansiyeli sayesinde, rejeneratif terapi dahil olmak üzere hastalık modelleme ve ilaç tarama gibi çok çeşitli potansiyel uygulamaları ortaya çıkmıştır. Bu çalışmada, Yamanaka faktörlerini kodlayan Sendai viral vektörleri kullanılarak insan melanositleri ve melanoma hücre dizilerinin yeniden programlanmasını amaçladık. Viral transfeksiyon sonrasında faz kontrast ve flüoresans mikroskobu görüntülemeleri ile melanosit kültürlerinde pluripotent kök hücre kolonilerinin ortaya çıktığı gözlenmiştir. Buna karşın, melanoma hücre kültürlerinde sadece hücre kümelenmeleri oluşmuş ve bunların pluripotens belirteçleri için pozitif olmadıkları belirlenmiştir. Bu da sağlıklı ve kanserli hücrelerin yeniden programlanması sırasında farklılıklar olduğunu göstermiştir. Yamanaka faktörlerinin, pluripotens belirteçleri ve tümör baskılayıcı genlerin bazal ifade seviyeleri analiz edilerek melanositlerde ve kanser hücre dizilerinde yeniden programlamanın farklı yanıtları anlaşılmaya çalışılmıştır. Kanserli hücrelerin etkin bir şekilde yeniden programlanmasına izin verecek çalışmaların yapılması, kanser biyolojisi ve tedavisi hakkındaki bilgimizi arttıracaktır.

Anahtar Kelimeler

uPK hücreleri, melanoma, melanositler, Yamanaka faktörleri, hücre programlama.

Article History: Received: May 3, 2017; Revised: Oct 12, 2017; Accepted: Oct 12, 2017; Available Online: Feb 20, 2018.

DOI: 10.15671/HJBC.2018.211

Correspondence to: A. Yılmazer; Ankara University, Biomedical Eng. Dept, Engineering Faculty, Gölbaşı, Ankara, Turkey.

Tel: +90 312 6000100 /1850 Fax: +90 312 212 74 64 E-Mail: ayilmazer@ankara.edu.tr

INTRODUCTION

Cellular reprogramming technologies provide many promising options for the treatment of various diseases, as well as improve our understanding of the biology of these diseases. Upon their discovery in 2006, induced pluriptent stem (iPS) cells have been explored extensively with regenerative medicine purposes and accelerated the fate of cellular therapies. The generation of induced pluripotent stem (iPS) cells from somatic cells showed that the cell fate could be manipulated by simply introducing a few key transcription factors [1]. This conceptual revolution has inspired researchers to reprogram and transdifferentiate a variety of cells *in vitro* and *in vivo* for regenerative medicine purposes. The differentiation potential of iPS cells, considered practically equivalent to that of embryonic stem cells, along with the possibility to obtain them from specific human patients has uncovered a wide range of potential applications, including disease modeling, drug screening and regenerative therapy [2-4].

Epigenetic mechanisms, which include DNA methylation, histone modifications and chromatin remodeling, play a major role both in the generation of iPS cells and cancer development [5]. Studies indicate that various epigenetic alterations may happen in pre-malignant cells, leading to their expansion in the early stages of tumor progression and at later stages, more genes might suffer loss of function through epigenetic modification than through genetic defects [5-8]. On the other side, the ability of developmental progression from pluripotent stem cells through progenitors to terminally differentiated cells is accompanied by a gradual deposition of repressive histone marks, followed by chromatin compaction [9-11]. Upon delivery of reprogramming factors to somatic cells, transcription factors bind their recognition elements that are modulated by changes in chromatin structure [12,13]. Cancer cells can also acquire pluripotent character by activating some of their transcription factors and modifying some other chromatin regulators. This means that cancer cells can be reprogrammed to pluripotent stage by the expression of Oct3/4, Klf-4, Sox-2, c-Myc transcription factors. This may lead to the erasure of their epigenetic memory and result in modified tumorigenicity.

In this study, we aimed to investigate the reprogramming efficiency of human melanocytes and two different melanoma cell lines. Sendai viral vectors encoding Yamanaka factors (Oct3/4, Klf-4, Sox-2 and c-Myc) have been used to generate iPSCs. This is a proof-of-concept study investigating the ability to reprogram melanoma cells into a pluripotent stage and comparing the resulting cells to iPS cells obtained from human melanocytes.

MATERIALS and METHODS

Cell Culture

Human melanocytes were obtained from Lonza, and cultured in MGM™-4 Melanocyte Growth Medium-4 (Lonza). Human melanoma cell lines A375 and WM115 were purchased from ATCC (USA). Melanoma cells were maintained in Dulbecco's Modified Eagle Medium (DMEM) supplemented with 10% fetal bovine serum (FBS), 50 U/ml penicillin, 50 μg/ml streptomycin, 1% L-glutamine and 1% non-essential amino acids at 37°C in 5% CO_2.

Reprogramming Protocol

Cells were cultured in 6-well plates in their native culturing medium. Cytotune Reprogramming Kit 2.0 (Life Technologies) was used to generate iPSCs. When the cells reached to 50% confluency, cells were transfected with Sendai viral vectors encoding Oct3/4, Klf-4, Sox-2 and c-Myc (MOI 5,5,3). According to the kit protocol, cells were transferred to inactivated mouse embryonic fibroblast (iMEF, Life Technologies) and cultured in KO DMEM media supplemented with KO serum replacement (20%), non-essential amino acids (1%), 2-mercaptoethanol (0.1%) and b-FGF (4 ng/ml). Cells were observed under an inverted microscope every day in order to observe the formation of pluripotent colonies.

Immunofluorescence Staining

Cells or colonies cultured on 24-well plates were fixed with cold methanol and blocked with 1% BSA in PBS. Following blocking, cells were incubated with anti-human Nanog (Abcam) and anti –human TRA-1-60 antibodies for 2 hour at room temperature. Finally, cells were treated with AF488 and AF546 labelled anti- human secondary antibodies. DAPI was used to counterstain nuclei. Repre-

sentative images were obtained under the EVOS fluorescence microscope (Life Technologies).

RNA Extraction and Quantitative Real Time PCR (qRT-PCR)

Cells ($5x10^5$ cells) were collected and RNA was extracted with the Machery Nagel RNA isolation kit. cDNA synthesis from 1 μg of RNA sample was performed with iScript cDNA synthesis kit (Bio-Rad) according to manufacturer's instructions. 2 μl of each cDNA sample were used to perform real-time RT-qPCR reactions with iO SYBR Green Supermix (Bio-Rad, UK). Samples were run on CFX-96 Real Time System (Bio-Rad) with the following protocol: 95°C for 3 min, 1 cycle; 95°C for 10 sec, 60°C for 30 sec, – repeated for 40 cycles. GAPDH was used as a reference gene and gene expression levels were normalized to untreated control groups.

RESULTS

Human melanocytes and 2 melanoma cell lines (A375 and WM115) were used in the reprogramming protocol. Cultures were observed and images under an inverted microscope (Figure 1). Following Sendai viral transfection, colonies have emerged as early as day 15 in the reprogrammed melanocyte cultures, and they became more distinct and similar in morphology to embryonic stem cells by day 20. For the melanoma cell lines, small cell clusters were observed by day 15 and they did not grow bigger as pluripotent colonies by day 20. Furthermore, in reprogrammed melanoma cultures, cancer cells proliferated too fast and populated the whole culture dish by the end of day 20. These results suggested that Sendai viral transfection was able to generate typical iPS cell colonies in the human melanocytes, whereas only cell clusters were formed in the melanoma cell cultures.

Reprogrammed cell cultures were further analyzed for the expression of pluripotency markers (Nanog and TRA-1-60) via immunofluorescence staining (Figure 2). Reprogrammed melanocytes showed Nanog and TRA-1-60 positive cells within the emerged colonies. On the other hand, there were no signals for the pluripotency markers obtained in the reprogrammed melanoma cultures. Therefore, immunofluorescence staining proved that the colonies obtained in reprogrammed melanocyte cultures were pluripotent. Unlike melanocytes, cell clusters formed after viral transfection in the melanoma cultures were not found to be pluripotent.

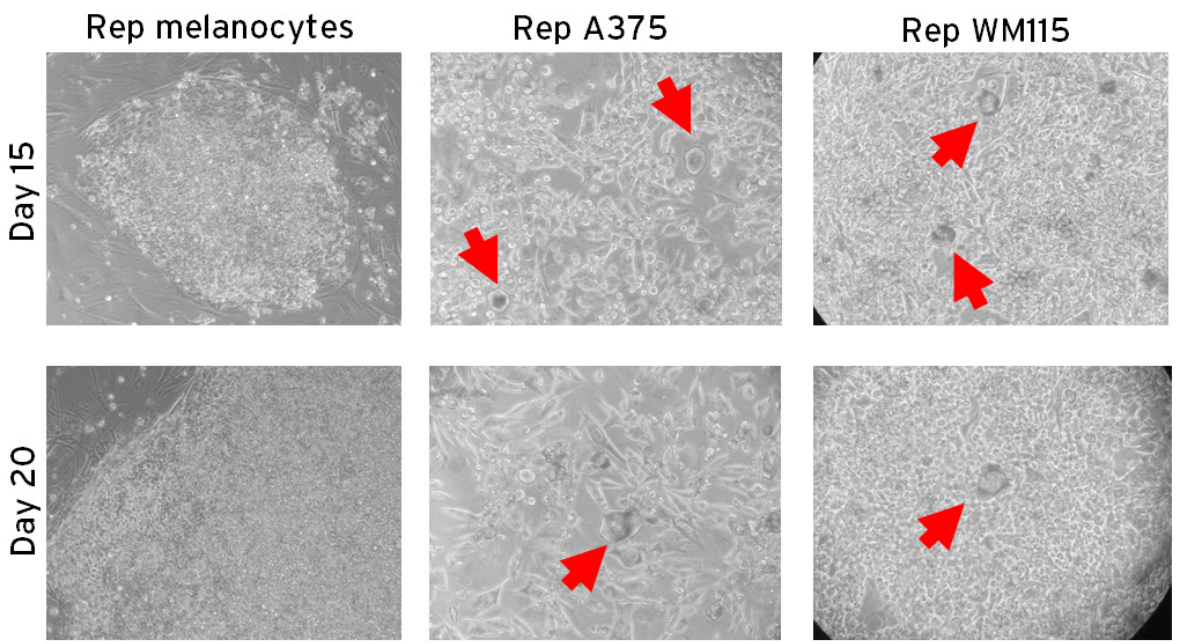

Figure 1. Images of reprogrammed melanocytes and melanoma cells. Human melanocytes and melanoma cell lines (A375 and WM115) were transfected with Sendai viral vectors encoding the Yamanaka Factors. Phase-contrast images (20X) were obtained 15 and 20 days following viral transfection.

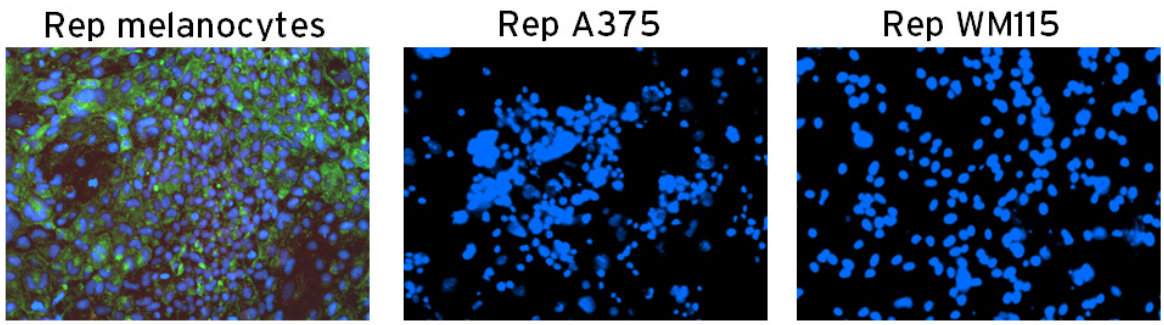

Figure 2. Immunofluorescence staining of reprogrammed melanocytes and melanoma cells. Melanocytes and melanoma cell lines (A375 and WM115) were transfected with Sendai viral vectors encoding the Yamanaka Factors. Cultures were fixed and stained for Nanog (red) and TRA-1-60 (green) expression. Nuclei were counterstained with DAPI (blue). Representative images were obtained using a fluorescence microscope (20X).

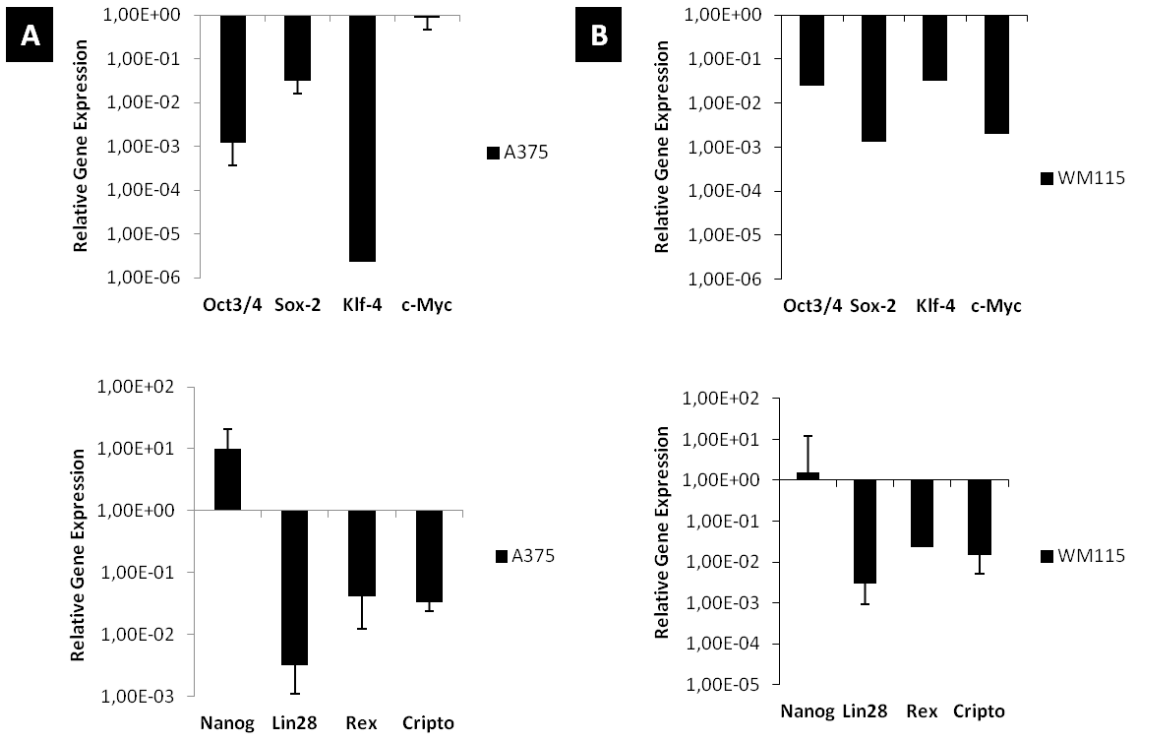

Figure 3. Expression of Yamanaka factors and pluripotency markers in reprogrammed melanocytes and melanoma cells. Melanocytes and melanoma cell lines (A375 and WM115) were transfected with Sendai viral vectors encoding the Yamanaka Factors. RNA was isolated after 21 days and qRT-PCR was performed. Gene expression levels were plotted as relative gene expression (normalized to melanocytes). GAPDH was used as a reference gene.

In order to explore the differences between the reprogrammed melanocytes and melanoma cells, we analyzed the basal expression levels of Yamanaka factors (Oct3/4, Klf-4, Sox-2 and c-Myc) and pluripotency markers (Nanog, Lin28, Rex, Cripto) in naïve cancer cell lines. According to the qRT-PCR data (Figure 3), nearly all Yamanaka factors and pluripotency markers in A375 and WM115 were downregulated compared to human melanocytes. Only Nanog showed up to 10 times upregulation in melanoma cells.

In literature, it has been reported that expression of tumor suppressor genes can inhibit iPSC generation and reduce reprogramming efficiencies. For that reason, P16, P21 and P53 expression were

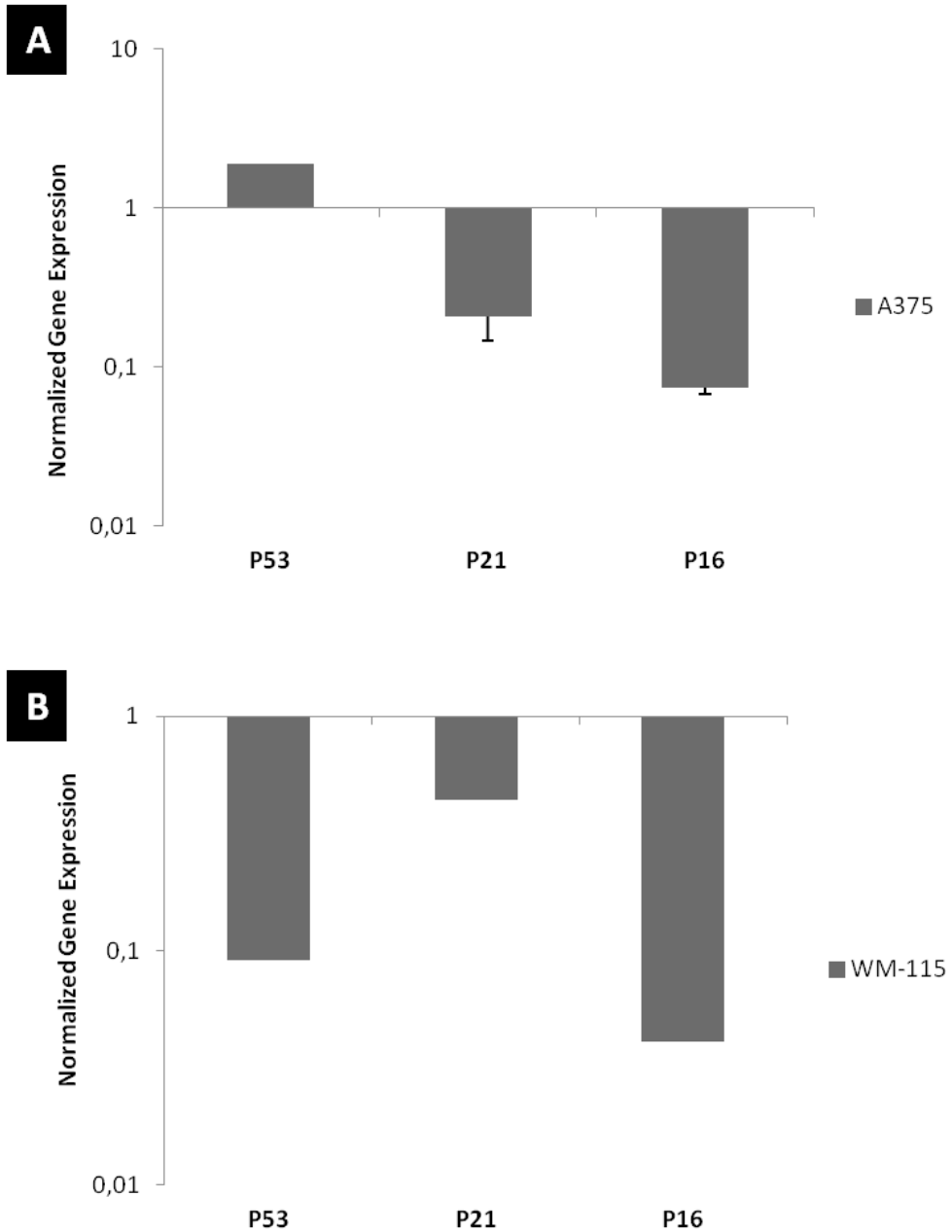

Figure 4. Expression of tumor-suppressor genes in reprogrammed melanocytes and melanoma cells. Melanocytes and melanoma cell lines (A375 and WM115) were transfected with Sendai viral vectors encoding the Yamanaka Factors. RNA was isolated after 21 days and qRT-PCR was performed. Gene expression levels were plotted as relative gene expression (normalized to melanocytes). GAPDH was used as a reference gene.

assessed in naïve melanoma cells. According to the Figure 4, when compared to human melanocytes, A375 cells had 2 times higher expression of P53 gene, whereas P16 and P21 showed up to 10 times lower gene expression. In WM115 cells, all of the tumor-suppressor genes showed downregualtion compared to human melanocytes.

DISCUSSION

In this study, we aimed to induce reprogramming of human melanocytes and melanoma cell lines via Sendai viral vectors encoding Yamanaka factors. Following transfection, pluripotent stem cell colonies have emerged in the melanocyte cultures, as evident by phase-contrast and fluorescence microscopy images. However, only cell clusters which were not positive for pluripotency markers were obtained in the melanoma cell cultures.

This proved that there are differences between healthy and cancer cell reprogramming. In the reprogrammed melanoma cultures, due to higher cell proliferation rates compared to melanocytes, cancer cells grew faster than the cell clusters, and possibly inhibited the formation of pluripotent colonies.

In order to further examine the different responses of melanocytes and melanoma cells to cellular reprogramming, we analyzed the basal gene expression levels of various factors, including Yamanaka factors, pluripotency markers and tumor suppressor genes. Compared to melanocytes, cancer cells showed lower gene expression levels for most of the Yamanaka factors and pluripotency markers, which could account for the inefficient cellular reprogramming in melanoma cells. When the expression of tumor-suppressor genes were analyzed, cancer cells in general expressed lower levels of P16, P21 and P53, suggesting that they were not the main reason of inefficient cancer cell reprogramming. Not only basal expression levels of reprogramming and pluripotency factors, but also epigenetic basis of cancer, long-term culture conditions, heterogeneity of tumors and presence of cancer stem cells have been reported to be important players of cancer cell reprogramming [14]. Therefore, further studies are needed to delineate the other factors determining the fate of cancer cell reprogramming in melanoma cells.

This study suggests that the rate of cell proliferation, endogenous levels of Yamanaka factors, and pluripotency markers play a key role during cellular reprogramming and iPS cell generation. Future studies that will allow efficient reprogramming of cancer cells can open up new windows for cancer biology and therapy. Tumorigenesis and cellular reprogramming share common biological processes, therefore, transcription-factor based cancer cell reprogramming can provide a powerful tool to improve our knowledge about cancer-fate processes, with a potential to develop novel therapeutic approaches.

ACKNOWLEDGEMENT

AY and HT acknowledge support by the Scientific and Technological Research Council of Turkey (TUBITAK, grant number 113S897). Authors confirm that there are no known conflicts of interest associated with this publication.

References

1. K. Takahashi, S. Yamanaka, Induction of pluripotent stem cells from mouse embryonic and adult fibroblast cultures by defined factors, Cell, 126 (2006) 663-76.
2. I.H. Park, N. Arora, H. Huo, N. Maherali, T. Ahfeldt, A. Shimamura, M.W. Lensch, C. Cowan, K. Hochedlinger, G.Q. Daley, Disease-specific induced pluripotent stem cells, Cell, 134 (2008) 877-86.
3. F.T. Merkle, K. Eggan, Modeling human disease with pluripotent stem cells: from genome association to function, Cell. Stem Cell, 12 (2013) 656-68.
4. J. Sng, T. Lufkin, Emerging stem cell therapies: treatment, safety, and biology, Stem Cells Int., 2012 (2012) 521343.
5. M.A. Dawson, T. Kouzarides, Cancer epigenetics: from mechanism to therapy, Cell, 150 (2013) 12-27.
6. S.B. Baylin, J.E. Ohm, Epigenetic gene silencing in cancer - a mechanism for early oncogenic pathway addiction?, Nat. Rev. Cancer, 6 (2006) 107-116.
7. A.P. Feinberg, B. Tycko, The history of cancer epigenetics, Nat. Rev. Cancer, 4 (2004) 143-153.
8. P.A. Jones, S.B. Baylin, The fundamental role of epigenetic events in cancer, Nat. Rev. Genet., 3 (2002) 415-428.
9. C.A. Gifford, Michael J. Ziller, H. Gu, C. Trapnell, J. Donaghey, A. Tsankov, A.K. Shalek, D.R. Kelley, A.A. Shishkin, R. Issner, X. Zhang, M. Coyne, J.L. Fostel, L. Holmes, J. Meldrim, M. Guttman, C. Epstein, H. Park, O. Kohlbacher, J. Rinn, A. Gnirke, E.S. Lander, B.E. Bernstein, A. Meissner, Transcriptional and epigenetic dynamics during specification of human embryonic stem cells, Cell, 153 (2013) 1149-1163.
10. W. Xie, M.D. Schultz, R. Lister, Z. Hou, N. Rajagopal, P. Ray, J. W. Whitaker, S. Tian, R.D. Hawkins, D. Leung, H. Yang, T. Wang, Ah Y. Lee, S.A. Swanson, J. Zhang, Y. Zhu, A. Kim, J.R. Nery, Mark A. Urich, S. Kuan, C.-a. Yen, S. Klugman, P. Yu, K. Suknuntha, N.E. Propson, H. Chen, L.E. Edsall, U. Wagner, Y. Li, Z. Ye, A. Kulkarni, Z. Xuan, W.-Y. Chung, N.C. Chi, J.E. Antosiewicz-Bourget, I. Slukvin, R. Stewart, M.Q. Zhang, W. Wang, J.A. Thomson, J.R. Ecker, B. Ren, Epigenomic analysis of multilineage differentiation of human embryonic stem cells, Cell, 153 (2013) 1134-1148.
11. J. Zhu, M. Adli, J.Y. Zou, G. Verstappen, M. Coyne, X. Zhang, T. Durham, M. Miri, V. Deshpande, P.L. De Jager, D.A. Bennett, J.A. Houmard, D.M. Muoio, T.T. Onder, R. Camahort, C.A. Cowan, A. Meissner, C.B. Epstein, N. Shoresh B.E. Bernstein, Genome-wide chromatin state transitions associated with developmental and environmental Cues, Cell, 152 (2013) 642-654.

12. B. Papp, K. Plath, Epigenetics of reprogramming to induced pluripotency, Cell, 152 (2013) 1324-43.
13. R.P. Koche, Z.D. Smith, M. Adli, H. Gu, M. Ku, A. Gnirke, B.E. Bernstein, A. Meissner, Reprogramming factor expression initiates widespread targeted chromatin remodeling, Cell. Stem. Cell, 8 (2013) 96-105.
14. A. Yilmazer, I. de Lázaro, H. Taheri, Reprogramming cancer cells: a novel approach for cancer therapy or a tool for disease-modeling?, Cancer Letters, 369 (2015) 1-8.

Synthesis and Characterisation of a New Hydrophilic Interaction/Reversed Phase Mixed-Mode Chromatographic Stationary Phase

Yeni bir Hidrofilik Etkileşim/Ters Faz Karışık-Mod Sıvı Kromatografik Sabit Fazın Sentezi ve Karakterizasyonu

Research Article

Hayriye Aral*
University of Batman, Faculty of Science and Art, Department of Chemistry, Batman, Turkey.

ABSTRACT

A novel multifunctional stationary phase based the amide-silica was synthesised starting from L-isoleucine and 2-aminoacetanilide. Hereby, compounds 1, 2, 3 and 4 were synthesised for the first time and 1, 2 and 4 were identified. The stationary phase was synthesised by a reliable and repeatable method and characterized by elemental analysis, solid state 13C NMR, scanning electron microscope (SEM), and Brunauer, Emmett and Teller (BET). This stationary phase possess four amide groups as polar cites, phenyl ring as aromatic non-polar cite and isopropyl as an aliphatic non-polar cite. Therefore, it can act as both hydrophilic interaction (HILIC) and reversed phase (RPLC) chromatographic stationary phase. The stationary phase has also chirality and can be used in enantioseparation of racemic compounds in normal phase chromatography (NPLC).

Key Words
Mixed-mode stationary phase, Hydrophilic interaction liquid chromatography (HILIC), Isoleucine, Chiral stationary phase.

ÖZ

L-izolözin ve 2-aminoasetanilitten yola çıkılarak amid-silika tabanlı çok fonksiyonlu yeni bir dolgu maddesi sentezlendi. Bu vesile ile bileşik 1, 2, 3 ve 4 ilk kez sentezlenmiş olup bileşik 1, 2 ve 4'ün ayrıntılı karakterizasyonları yapılmıştır. Dolgu maddesi güvenilir ve tekrarlanabilir bir yöntemle sentezlenmiş olup yapısı katı faz ^{13}C NMR, taramalı elektron mikroskobisi (SEM), ve Brunauer, Emmett and Teller (BET) ile doğrulandı. Yeni geliştirilen bu dolgu maddesi polar grup olarak dört amid grubu, apolar gruplar olarak da aromatik halka ve alifatik zincir içerir. Bu nedenle, bu dolgu maddesi hem hidrofilik etkileşim (HILIC) hem de ters faz (RPLC) sıvı kromatografisinde kullanılabilir. Dolgu maddesinin L-izolözinden sentezlendiği için aynı zamanda kiraldir ve normal faz kromatografide rasemik bileşiklerin enantiyomerik ayrılmasında kullanılabilir.

Anahtar Kelimeler
karışık-mod dolgu maddesi, hidrofilik etkileşik sıvı kromatografisi (HILIC), izolözin, kiral dolgu maddesi (CSP).

Article History: Received: Oct 21, 2017; Revised: May 18, 2017; Accepted: Feb 02, 2017; Available Online: Feb 20, 2018.

DOI: 10.15671/HJBC.2018.213

Correspondence to: H. Aral, University of Batman, Faculty of Science and Art, Department of Chemistry, Batman, Turkey.
Tel: +90 488 217 3618 Fax: +90 488 217 3618 E-Mail: hayriye.aral@batman.edu.tr

INTRODUCTION

The most important element of the chromatography is the stationary phase. The structure of the stationary phase affects the retention mechanisms, separation selectivity, and column efficiency [1]. Most stationary phases only provided single separation mechanism [2-6] and were applied in single chromatographic mode. A recent trend in HPLC involves the development of new multifunctional stationary phases having polar and nonpolar groups for separations of wide range of analytes classes from polar to nonpolar [7-13]. This type of stationary phase refered as "mixed-mode" [14].

The mixed mode approach has emerged because of the need for better retention control for both polar and non-polar molecules [15-19]. Multiple mechanisms of interactions allow the use of one stationary phase for a much wider range of applications as compared to RP or HILIC approach. At least two interactions between the anlytes and the stationary phase should be present in the mixed-mode mechanism [20]. Thus, simultaneous separation of polar and non-polar, ionisable and neutral and other complex mixtures is possible and the cost of analysing can be reduced using this kind of stationary phase. Several kind of stationary phases with mixed-mode performance have been investigated such as phenylpropanolamine [10], phenylamine [7,21,22], 8-quinolinol [24], poly(1-allylimidazole) [25], imidazole [26,27], pyridine [28,29] and dipyridine [30] functional silicas. In recent years, the mixed-mode chromatography has been shown to be a versatile approach for the simultaneous separation of highly mixed classes of analytes from polar to nonpolar organic compounds [31,32].

Subsequently, polar stationary phases have exhibited novel properties for polar analytes [33]. Recent investigations describing stationary phases containing polar groups have shown the superior performance of these new phases over conventional RPLC stationary phase complex analytes [33,34]. The polar groups, particularly amide, were originally chosen for their ability to interact with both alkaline and acidic analytes [16,19].

RPLC is the mostused HPLC mode for separation of moderately polar and weakly polar analytes, while HILIC is often used to separate strongly polar compounds. Thus, mixed-mode RPLC/HILIC can be used for the separation of both polar and nonpolar analytes, overcoming the deficiencies of RPLC and HILIC [35-50]. There is a continual increase in research in this area to find an ideal stationary phase and to investigate mixed-mode separation mechanisms.

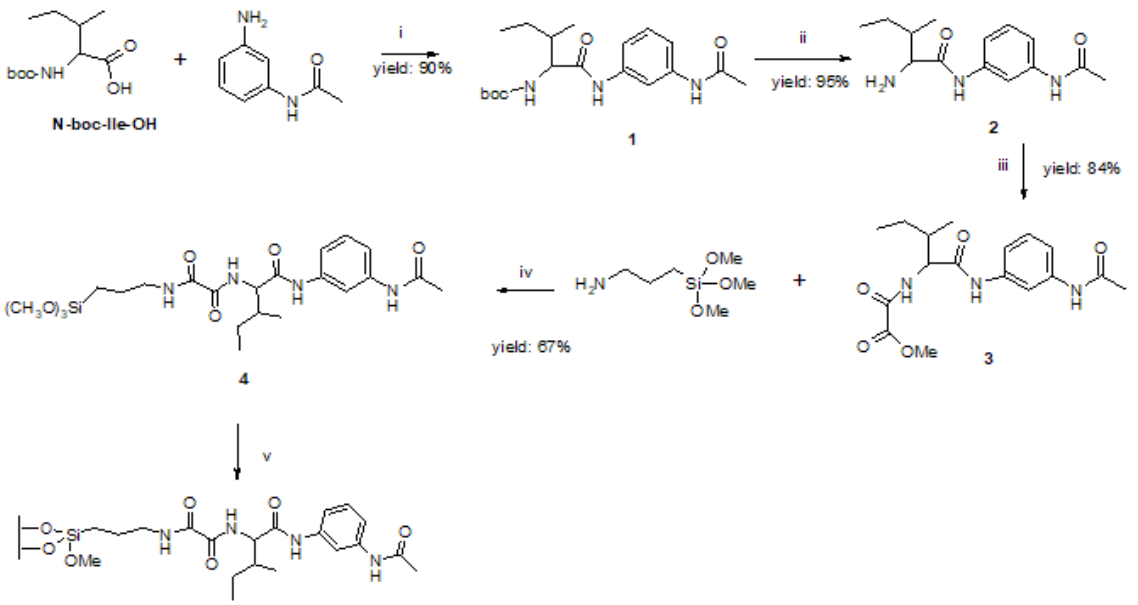

Figure 1. Synthesis of the new amide compounds and ile-AA-mix stationary phase.

In this study, a novel amide-functionalised silica-based multifunctional stationary phase was prepared starting from 3-aminoacetanilide and L-isoleucine as starting materials (Figure 1). The developed stationary phase possesses four amide groups as polar sites, as well as hydrophobic chain and an aromatic ring as nonpolar sites. Hence, this new stationary phase possesses both HILIC and RPLC dual retention mechanisms and should be successfully used for separation of different group of polar and nonpolar compounds.

MATERIALS and METHODS

Reagents and Materials

Spherical silica gel (Lichrospher Si 60, 5 μm, 60 Å, 700 m^2g^{-1}) was purchased from Merck. All of the reagents and solvents were purchased from Sigma-Aldrich or Merck. All of the reagents used in the synthesis were of "reagent grade" unless otherwise specified. The IR spectra were recorded on a Mattson 1000 FTIR spectrometer. Elemental analyses were performed with a Thermo Scientific FLASH 2000 instrument. Deionized water was purified using a Millipore Milli-Q water system. SEM images were obtained using a LEO EVO 40 model instrument (İnönü University, SEM Laboratory). Solid state ^{13}C NMR was recorded using a Bruker Superconducting FT.NMR Spectrometer Avance TM 300 MHz WB instrument (Middle East Technical University, Central laboratory, Solid state NMR laboratory). ^{1}H (400 MHz) and ^{13}C (100 MHz) NMR spectra were recorded on a Bruker DPX-400 High Performance Digital FT-NMR Spectrometer (Dicle University, Faculty of Science, NMR Laboratory). Textural characteristics were determined by nitrogen adsorption at 67 K with an automatic adsorption instrument (Micromeritics, ASAP 2020) and the BET surface area (S_{BET}), total pore volume (V_T) and poresize distribution were determined from nitrogen adsorption-desorption data by using

Table 1. Properties of the Ile-AA-Mix column.

Limit pressure	500 bar
[1]Max. flow rate for 100% EtOH	1.8 ml/min
[1]Max flow rate for EtOH/water: 50/50	1.2 ml/min
[1]Max flow rate for 100% water	2.5 ml/min
[1]Max flow rate for Water/ACN: 50/50	3.1 ml/min
[1]Max flow rate for 100% ACN	5 ml/min (320 bar)
[2]Extent of labelling	13.74% carbon loading
L x I.D.	250 cm x 4.6 mm
Surface coverage	0.50 mmol/gr
Matrix active group	Amide, phenyl, alkyl
[3]Particle size	5 μm
[3]Pore size	60 Å
[4]Surface area	659 m^2 g^{-1}
[4] Total pore volume	0.66 cm^3 g^{-1}
Operation pH range	2.5-9.00

[1]Max. flow rate was determined at the maximum operation pressure (500 bar) and 20°C temperature.
[2]Based on the elemental analysis.
[3]Based on the information given by the company of the blank silica.
[4]Based on the BET analysis.

Quantachrome software (Dicle University, Central Research Laboratory, DÜBTAM).

Packing of Chromatographic Column

An empty stainless steel HPLC column (250x4.6 mm) was packed with an Ile-AA-Mix using the slurry packing technique under 500 bar pressure. Approximately 3.5 g of the stationary phase was used to prepare the column. Ethanol (EtOH) was used as the packing solvent. A total of 4 gr Ile-AA-Mix was dispersed into EtOH and sonicated in the ultrasonic bath for 5 minutes, after which the slurry was packed into the empty column under a constant pressure of 500 bar. Lastly, the prepared columns were rinsed for 5 h with EtOH, 1h with EtOH/water (50:50), 1 h with water, 1 h with water:ACN (50:50) and 1 h with ACN, respectively, as the eluents at 1 mL/min. Several properties of the new Ile-AA-Mix column are given in Table 1.

Synthesis of Compound 1

Dicyclohexylcarbodiimide (DCC, 3.03 g, 14.7 mmol) dissolved in CH_2Cl_2 (10 mL) was added to a stirred solution of N-Boc-isoleucine (3.05 g, 13.4 mmol), 4-phenylbutylamine (2.10 g, 13.4 mmol) and HOBT (2.18 g, 16.1 mmol) in CH_2Cl_2 (200 mL) at 0 °C. After stirring for 24 h at room temperature, the mixture was filtered and extracted with 1 N HCl (100 X2 mL), 5% $NaHCO_3$ (10 mL) and water (10 mL) respectively. The extract was dried over Na_2SO_4, filtered and evaporated under reduced pressure to afford a pure N-boc-ile-AA as a white solid.(TLC: Rf = 0.32 with H:EtOAc = 3:1). Yield: 4.70 g, 99%. Mp: 158-159°C. IR (cm^{-1}); 3335 and 3309 (Amide N-H), 3201 (carbamate N-H), 3063 (Ar-H), 1679 (carbamate C=O), 1665 (amide C=O), 1612 (amide C=O), 1310 (carbamate C-O-C), 1240 (carbamate C-N-C), 1170 (amide C-N-C). ^{1}H NMR ($CDCl_3$): δ (ppm); 0.89 (t, 3H), 0.98 (d, 3H), 1.10-1.30 (m, 1H), 1.44 (s, 9H), 1.50-1.70 (m, 1H), 1.80-2.00 (m, 1H), 2.01 (s, 3H), 4.17 (s, 1H), 5.52 (d, 1H), 7.11-7.19 (m, 2H), 7.34 (m, 1H), 7.53 (m, 1H), 8.07 (s, 1H), 8.91 (s, 1H). ^{13}C NMR ($CDCl_3$): (ppm); 11.12, 15.57, 24.38, 24.89, 28.35, 37.20, 60.12, 80.27, 11.87, 115.88, 116.30, 129.19, 138.03, 138.43, 156.44, 169.06, 171.09.

Removal of the boc-Group to Obtain Compound 2

TFA/AcOH (1:1) (14 mL) was added to a stirred solution of 1 (3.0 g, 8.3 mmol) in CH_2Cl_2 (30 mL) at 0 °C. After stirring 24 h at room temperature, the solvent was evaporated and the pH was adjusted to 9-10 by adding 1 N KOH to the residue. The mixture was extracted with CH_2Cl_2 (30 mLx3), 0.1 N HCl (10 mL) and water (30 mLx2), respectively, and dried over Na_2SO_4, filtered and evaporated under reduced pressure to afford a pure 2 as a viscous oil (monitoring by TLC). R_f = 0 with H:EtOAc = 3:1, R_f = 0.25 with H:EtOAc/TEA = 1:2:0.2. Yield: 2.05 g, 99%.

Synthesis of Compound 3

A solution of dimethyloxalate (18.24 mmol, 2.06 g) in MeOH (15 mL) was added to the Ile-AA (8.5 mmol, 2.13 g) dissolved in MeOH (20 mL). After stirring for 24 h at room temperature under an argon atmosphere, the solvent was evaporated and the residue was purified by column chromatography on silica gel (PE:EtOAc = 2:1) to afford 3 as a white solid. Yield: 2.29 g, 80%. Mp: 168-169. IR ν (cm^{-1}); 3275 (sb, H-N of two amides), 3074 (Ar-H), 3042 (Ar-H), 1754 (C=O, ester), 1656 (NH, amide), 1619 (NH, amide), 1209 (C-O-C, ester), 1175 (C-N-C, amide), 1175 (C-N-C, amide). ^{1}H NMR ($CDCl_3$): δ (ppm);0.83-1.00 (m, 6H), 1.10-1.27 (m, 1H), 1.45-1.68 (m, 1H), 1.90-2.11 (m, 1H), 2.15 (s, 3H), 3.89 (s, 3H), 4.59 (d, 1H), 7.14-7.40 (m, 3H), 7.71 (s, 1H), 8.03 (d, 1H), 8.27 (s, 1H), 9.27 (s, 1H) ^{13}C NMR ($CDCl_3$): δ (ppm); 11.08, 15.38, 24.37, 24.79, 37.81, 53.76, 59.30, 112.19, 116.30, 116.50, 129.31, 137.97, 138.46, 156.61, 160.61, 169.14, 169.46.

Preparation of the Stationary Phase (4 and Ile-AA-Mix)

The mixture of 3 (1 g, 3 mmol) and 3-amino propyltrimethoxysilane (0.50 g, 2.8 mmol) dissolved in MeOH (30 mL) was stirred at room temperature for 24 h. The mixture was cooled to +4°C and the white precipitate was washed with cold MeOH, filtered and evaporated to afford 1.2 g of 5. Yield: 80%. Mp: decomposition, 230-250°C. (IR spectrum was given in Supplementary Materials as Figure S7). Next, 0.4 g of the 5 was dissolved in a mixture of toluene (30 mL) and DMSO (10 mL) at 130°C. Spherical silica gel (2 gr) was added to the mixture. After stirring at 130°C for 48 h, the mixture was filtered and the new silica material was washed with toluene (10 mL), $CHCl_3$ (20 mL), ETOH (20 mL), EtOH:EtOAc (1:1, 20 mL) and acetone (30 mL), respectively. The white powders were dried on a rotary evaporator device at 90°C under reduced pressure for a total of 20 h to afford Ile-PBA-Mix as a new stationary phase.

Elemental analysis: C 13.74, H 2.29, N 2.05 (0.50 mmol of loaded ligand/g SP. The characterizations of the new phase are given in the next sections.

RESULTS and DISCUSSION

Synthesis

The synthesis of the new multifunctional stationary phase based on the amidefunctionalised silica gel is outlined in Figure 1. This stationary phase includes four amide groups as polar sites; and aliphatic and aromatic groups as nonpolar sites. Therefore, it is expected that the Ile-AA-Mix stationary phase can well interact with polar, moderately polar, weakly polar and non-polar compounds to separate complex mixture under HILIC and RPLC condition. In addition, the Ile-AA-Mix stationary phase has two stereogenic centres. Thus, it can act as chiral stationary phase for enantioseparation of several racemic mixtures in NPLC mode.

The new stationary phase was synthesised in five steps. First, compound 1 was obtained in 92% yield by the reaction of N-boc-isoleucine with 3-aminoacetanilid without applying any other purification technique. The deprotection of 1 gave a pure 2 in 99% yields after only with work-up, without any further purification. The reaction of 2 with two equivalents of dimethyl oxalate gave 3 in 80% yields. The 3 was reacted with 3-aminopropyltrimethoxysilane to obtain 4 in 67% yield. This final ligand was attached to the HPLC-quality spherical silica gel to obtain ile-AA-Mix as a novel mixed-mode stationary phase.

Commonly, two main methods have been reported for preparing a chromatographic stationary phase by functionalization of silica particles. The first method is that a silica modified with any of propyltrimethoxysilane (amino- or chloropropyltrimethoxysilanes). Then, the new organic ligands are directly grafted onto the surface of silica. Due to the not required any isolation, purification and identification process in the last two steps, this method is relatively simple [1] but has several serious disadvantages. The most important of these issues is low reproducibility because the controllability of a reaction on a solid phase is quite difficult. Often, all of the amino- or chloro- groups on the propylated silica surface are not replaced with the organically functionalised ligand. This phenomenon leads to low reproducibility of the stationary phase. Hence, the more reactions performed on the solid phase, the lower the reliability.

The second method is that the organically functionalised reagents are first treated with terminally functionalised propyltrimethoxysilane to form trimethoxysilyl-terminated organically functionalised reagents. Then, the new organically functionalised reagents could be directly bonded to the surface of silica [29]. Purification and isolation are needed for all steps and it is difficult to select suitable solvents in the subsequent steps, thus this method is more difficult than first method [1] but is more reliable because there is only a one-step reaction on silica. Thus, controllability and reproducibility are very high. Therefore, we preferred the second, more reliable method. Although the five step synthesis appears to be long and disadvantageous, the high yields of each step, the simplicity of the synthesis procedures and the high reproducibility of the stationary phase make this synthesis process very attractive and reliable.

In a most recent article, a "solvent-free" and green method for controllable and quantitative preparation of chromatographic stationary phase was proposed by Liu and co-authors [46]. In this study, the mixture of 3-chloropropyltrimethoxysilane, silica and excessive N-methylimidazolium were stirred at 120°C for 48 h to obtain the new stationary phase with quantitative yield in one step. Synthesis of a stationary phase in one step and solvent free is very attractive.

Characterization of the Stationary Phase

The stationary phase was synthesized in three separate parts simultaneously to evaluate the reproducibility of the synthesis process, under the same conditions, and using the same amounts of materials. These were named part 1, part 2 and part 3. Elemental compositions were measured for the three parts. As shown in Table 2, the nitrogen contents of each of the three parts of the Ile-AA-Mix were 2.10, 2.04 and 2.01, respectively. There is no significant difference between the three parts. The surface concentration of the Ile-PBA-Mix stationary phase was estimated to be 0.50 mmol g^{-1}, which was calculated from the average

Table 2. Elemental Analysis results of blank silica and three part of Ile-AA-Mix.

Elemental analysis results	C (%)	H (%)	N (%)
Blank Silica	0	0.04.	0
Ile-PBA-Mix Part-1	13.84	2.38	2.10
Ile-PBA-Mix Part-2	13.77	2.22	2.04
Ile-PBA-Mix Part-3	13.65	2.27	2.01
Average	13.74	2.29	2.05

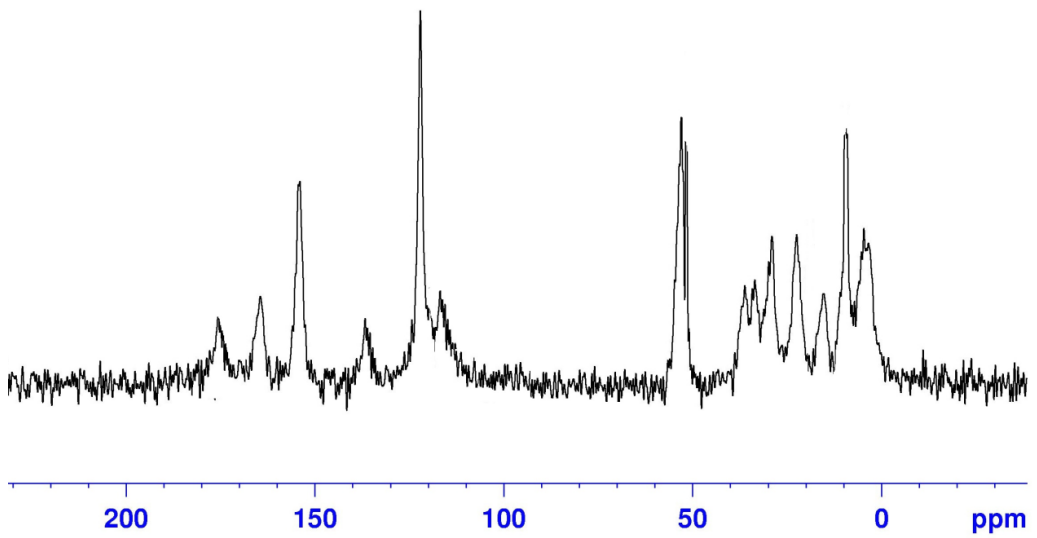

Figure 2. Solid state ^{13}C NMR spectrum of Ile-AA-Mix stationary phase.

nitrogen content. The elemental compositions of the three parts of the Ile-AA-Mix were very close, showing that the reproducibility of the synthesis process is very high.

The Ile-AA-Mix was characterized by solid state ^{13}C NMR (Figure 2). The signal at 150-180 ppm was assigned to the carbon atoms of the carbonyl groups and at 110-140 ppm was assigned to aromatic carbon atoms of the ligand bonded to surface of silica. The resonances between 0-40 ppm were assigned to the aliphatic carbon atoms of methyl (CH_3) and methylene (CH_2). The signals around 50 ppm was assigned to methane (CH) carbons. The IR and NMR results clearly confirmed that the original organic ligand was definitely bonded to the silica surface.

The specific surface area and the total pore volume of the Ile-AA-Mix material measured by the nitrogen adsorption method using BET analysis were calculated to be 659 m^2g^{-1}, 0.66 cm^3g^{-1} respectively, which are greatly reduced compared to those of the blank silica (799 $m^2\,g^{-1}$, 0.79 cm^3g^{-1})

The stationary phase was also identified by SEM to observe if there is a change in particle shape and size of the spherical silica gel after modification. The comparison of the SEM spectra of blank silica gel and that of the Ile-AA-Mix stationary phase showed a narrow particle size distribution and the same geometry with well-defined spherical particles (Figure 3).

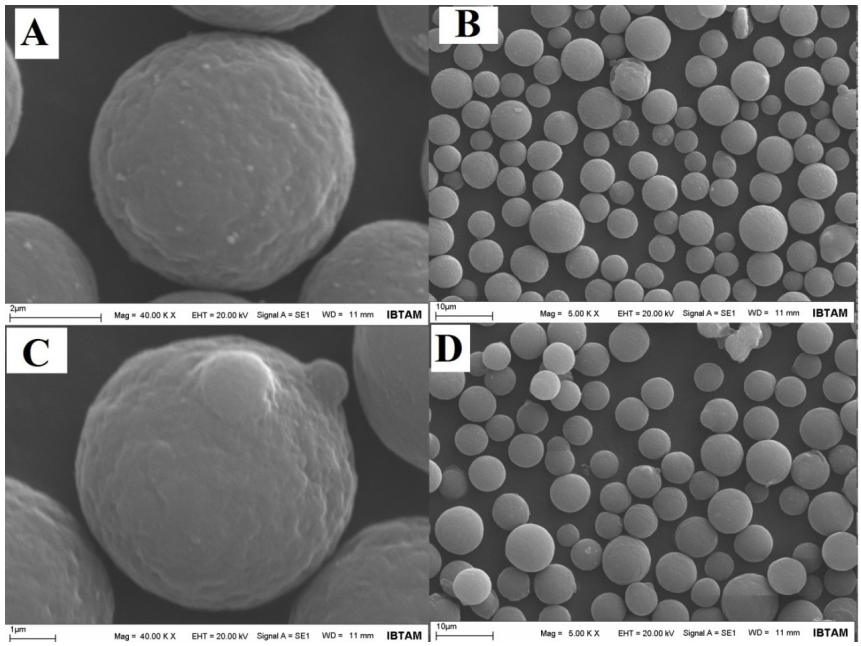

Figure 3. SEM image of blank silica (A) and the Ile-AA-Mix (B).

As a result, four new compounds derived from L-isoleucine were synthesized as a first time and structure of the compound 1 and 3 were identified by IR, ^{1}H NMR and ^{13}C NMR and of compound 4 were identified by IR. The new stationary phase Ile-AA-Mix was characterised by elemental analysis and solid state ^{13}C NMR, BET and SEM measurements and the successful derivatization was confirmed.

Column Stability Tests

The stability tests for the Ile-AA-Mix column were achieved in the pH 2.50-9.00 range using two newly prepared and previously unused 50x4.6 mm columns filled with Ile-AA-Mix stationary phase. The chromatographic conditions for the tests were as follows: mobile phase for low pH values: 100% of 40 mM, pH = 2.50 aqueous ammonium formate and for high pH: 100% of 40 mM, pH = 9.00 aqueous ammonium chloride buffer; flow rate, 1 mL/min; temperature, 60°C; detection, 280 nm; probe, uracil and aniline.

The column was continuously purged with the mobile phase with 2.50 of pH and was periodically tested by recording the retention time of uracil and aniline. After approximately 4000 column volumes of mobile phase with a 3.0 of pH were purged through the column, there was essentially no change in the retention times for uracil and aniline (below 2%). When 2000 volumes of mobile phase with 2.5 of pH passed through the column, there was essentially no change in the retention times for uracil and aniline, while 5-10% change was observed after 4000 column volumes of mobile phase. Therefore, we found that the column is highly stable at 2.50 of pH.

The same experiments were repeated for 9.00 of pH conditions using another unused 50x4.6 mm column filled with Ile-AA-Mix stationary phase. After approximately 2000 column volumes of mobile phase with 9.00 of pH, the changes in the retention for probes are below 2%. However, after 3000 volumes, there was just approximately 3-5% change and after 4000 volumes approximately 10% change in the retention time of adenine and aniline. Hence, although the column is quite stable at 9.00 of pH, it is important to be careful working above pH 9. As a result, this column is very stable between 2.5 and 9 of pH values.

CONCLUSION

A new multifunctional mixed-mode chromatographic stationary phase was prepared by modification of spherical silica gel by five steps. Four new amide compounds and a new

mixed-model chromatographic stationary phase derived from L-isoleucine were synthesised as a first time. The structure of three compounds has been identified and the new stationary phase has been well characterized by many different spectroscopic techniques. The high yields of each step, the simplicity of the synthesis procedures and the high reproducibility of the stationary phase make this synthesis process very attractive and reliable. Future work will be take advantage of this stationary phase to separate very complex analytes composed of very polar or nonpolar compounds.

ACKNOWLEDGEMENT

The authors gratefully acknowledge the financial support provided by the Research Project Council of Batman University (BTÜBAP) (Project No: BTÜBAP-2012-FED-03). In addition, the authors thanks to Dr. Mehmet Çolak for recording the ^{1}H and ^{13}C NMR spectra of all compounds.

References

1. L. Zhang, Q. Dai, X. Qiao, C. Yu, X. Qin, H. Yan, Mixed-mode chromatographic stationary phases: Recent advancement and its aplications for high-performance liquid chromatography, Trends Anal. Chem., 82 (2016) 143-163.
2. P. Janas, S. Bocian, P. Jandera, T. Kowalkowski, B. Buszewski, Separation of flavonoids on different phenyl-bonded stationary phases-the influence of polar groups in stationary phase structure, J. Chromatogr. A, 1429 (2016) 198-206.
3. Y. Liu, Z. Guo, Y. Jin, X. Xue, Q. Xu, F. Zhang, et al., Click oligo(ethylene glycol)": an excellent orthogonal stationary phase to C18 for two-dimensional reversedphase/ reversed-phase liquid chromatography, J. Chromatogr. A, 1206 (2008) 153-159.
4. P. Jandera, Z. Kucˇerova, J. Urban, Retention times and bandwidths in reversedphase gradient liquid chromatography of peptides and proteins, J. Chromatogr. A, 1218 (2011) 8874–8889.
5. X. Guo, X. Zhang, Z. Guo, Y. Liu, A. Shen, G. Jin, et al., Hydrophilic interaction chromatography for selective separation of isomeric saponins, J. Chromatogr. A, 1325 (2014) 121-128.
6. P. Jiang, D.Wu, C.A. Lucy, Determination of void volume in normal phase liquid chromatography, J. Chromatogr. A, 1324 (2014) 63-70.
7. A.J. Alpert, M. Shukla, A.K. Shukla, L.R. Zieske, S.W. Yuen, M.A.J. Ferguson, A. Mehlert, M. Pauly, R. Orlando, Hydrophilic-interaction chromatography of complex carbohydrates, J. Chromatogr. A, 676 (1994) 191-202
8. A.J. Alpert, Advances in Chromatography, 44 (2006) 317-329.
9. M. R. Gama, R. G. C. Silva, C. H. Collins, C. B. G. Bottoli, Hydrophylic interaction chromatography, Trends in Anal. Chem. 37 (2012) 48-60
10. M.A. Strege, S. Stevensen, S. M.Lawrence, Mixed-mode anion—cation exchange/hydrophilic interaction liquid chromatography—electrospray mass spectrometry as an alternative to reversed phase for small molecule drug discovery, Anal. Chem., 72 (2000) 4629-4633
11. M.A. Strege, Hydrophilic interaction chromatography—electrospray mass spectrometry analysis of polar compounds for natural product drug discovery, Anal. Chem., 70 (1998) 2439-2445
12. B.Y. Zhu, C.T. Colin, R.S. Hodges, Hydrophilic-interaction chromatography of peptides on hydrophilic and strong cation-exchange columns, J. Chromatogr., 548 (1991) 13-24.
13. T. Saga, Y. Inoue, K. Yamaguchi, Determination of carbohydrates by hydrophilic interaction chromatography with pulsed amperometric detection using postcolumn pH adjustment, J. Chromatogr. A, 625 (1992) 151-155.
14. Q. W. Yu, B. Lin, Y. Q. Feng, F. P. Zou, Application of humic acid bonded-silica as a hydrophilic-interaction chromatographic stationary Phase in separation of polar compounds, J. Liq. Chromatogr. Related. Technol., 31 (2008) 64-78.
15. X. Liu, C. Pohl, New hydrophilic interaction/ reversed-phase mixed-mode stationary phase and its application for analysis of nonionic ethoxylated surfactants, J. Chromatogr. A, 1191 (2008) 83–89.
16. H. Hinterwirth, M. Lammerhofer, B. Preinerstorfer, A. Gargano, R. Reischl, W. Bicker, et al., Selectivity issues in targeted metabolomics: separation of phosphorylated carbohydrate isomers by mixed-mode hydrophilic interaction/ weak anion exchange chromatography, J. Sep. Sci., 33 (2010) 3273–3282.
17. X. Liu, C.A. Pohl, HILIC behavior of a reversed-phase/ cation-exchange/anionexchange trimode column, J. Sep. Sci., 33 (2010) 779-786.
18. X. Liu, C.A. Pohl, Comparison of reversed-phase/ cation-exchange/anion-exchange trimodal stationary phases and their use in active pharmaceutical ingredient and counterion determinations, J. Chromatogr. A, 1232 (2012) 190-195.
19. X. Liu, C. Pohl, A. Woodruff, J. Chen, Chromatographic evaluation of reversedphase/anion-exchange/cation-exchange trimodal stationary phases prepared by electrostatically driven self-assembly process, J. Chromatogr. A, 1218 (2011) 3407-3412.
20. Y. Zhao, H.C. Law, Z. Zhang, H.C. Lam, Q. Quan, G. Li, et al., Online coupling of hydrophilic interaction/ strong cation exchange/reversed-phase liquid chromatography with porous graphitic carbon liquid chromatography for simultaneous proteomics and N-glycomics analysis, J. Chromatogr. A, 1415 (2015) 57-66.
21. A.S. Feste, I. Khan, Separation of glucooligosaccharides and polysaccharide hydrolysates by gradient elution hydrophilic interaction chromatography with pulsed amperometric detection, J. Chromatogr., 630 (1992) 129-139.

22. S.C. Churms, Recent progress in carbohydrate separation by high-performance liquid chromatography based on hydrophilic interaction, J. Chromatogr. A, 720 (1996) 75-91.
23. S.C. Lin, W.C. Lee, Separation of a fructo-oligosaccharide mixture by hydrophilic interaction chromatography using silica-based micropellicular sorbents, J. Chromatogr. A, 803 (1998) 302-306.
24. A.R. Oyler, B.L. Armstrong, J.Y. Cha, M.X. Zhou, Q. Yang, R.I. Robinson, R. Dunphy, D.J. Burinsky, Hydrophilic interaction chromatography on amino-silica phases complements reversed-phase high performance liquid chromatography and capillary electrophoresis for peptide analysis, J. Chromatogr. A, 724 (1996) 378-383.
25. T. Yoshida, Peptide separation in normal phase liquid chromatography, Anal. Chem., 69 (1997) 3038-3043.
26. C.T. Mant, L.H. Kondejewski, R.S. Hodges, Hydrophilic interaction/cation-exchange chromatography for separation of cyclic peptides, J. Chromatogr. A, 816 (1998) 79-88.
27. T. Yoshida, T. Okada, T. Hobo, R. Chiba, Calculation of amino acid hydrophilicity indices for retention of peptides on amide, diol and silica columns in normal-phase liquid chromatography, Chromatographia, 52 (2000) 418-424.
28. Y. Guo, S. Gaiki, Retention behavior of small polar compounds on polar stationary phases in hydrophilic interaction chromatography, J. Chromatogr. A, 1074 (2005) 71-80
29. Y. Kawachi, T. Ikeami, H. Takubo, Y. Ikeami, M. Miyamoto, N. Tanaka, J. Chromatogr. A, 1218 (2011) 5903-5919.
30. X. Qiao, L. Zhang, N. Zhang, X. Wang, X. Qin, H. Yan, et al., Imidazolium embedded C8 based stationary phase for simultaneous reversed-phase/hydrophilic interaction mixed-mode chromatography, J. Chromatogr. A, 1400 (2015) 107-116.
31. M. Sun, J. Feng, C. Luo, X. Liu, S. Jiang, Benzimidazole modified silica as a novel reversed-phase and anion-exchange mixed-mode stationary phase for HPLC, Talanta, 105 (2013) 135-141.
32. K. HU, W. Zhang, H. Yang, Y. Cui, J. Zhang, W. Zhao, A. Yu, S. Zhang, Calixarene ionic luqiuid modified silica gel: A novel stationary phase for mixed-mode chromatography, Talanta, 152 (2016) 392-400.
33. H. Aral, T. Aral, K.S. Çelik, G. Topal, Preparation of a novel ionic hybdid stationary phase by non-covalent functionalization of single-walled carbon nanotubes with amino-derivatized silica gel for fast HPLC separation of aromatic compounds, Talanta, 149 (2016) 21-29.
34. T. Aral, H. Aral, B. Ziyadanoğulları, R. Ziyadanoğulları, Synthesis of a mixed-model stationary phase derived from glutamine for HPLC separation of structurally different biologically active compounds: HILIC and reversed-phase applications, Talanta, 131 (2015) 64-73.
35. H. Aral, T.Aral, B. Ziyadanoğulları, R. Ziyadanoğulları, Development of a novel amide-silica stationary phase for the reversed-phase HPLC separation of different classes of phytohormones, Talanta, 116 (2013) 155-163.
36. Q. Wang, Y. Long, L. Yao, L. Xu, Z.G. Shi, L. Xu, Preparation, characterization and application of a reversed phase liquid chromatography/hydrophilic interaction chromatography mixed-mode C18-DDT stationary phase, Talanta, 146 (2016) 442-451.
37. D. Kotani, I. D'Acquarica, A. Ciogli, C. Villani, D. Capitani, J. Chromatogr. A, 1232 (2012) 196-211.
38. Y. Li, Y. Feng, T. Chen, H. Zhang, Imidazoline type stationary phase for hydrophilic interaction chromatography and reversed-phase liquid chromatography, J. Chromatogr. A, 1218 (2011) 5987-5994.
39. S. Liu, H. Xu, J. Yu, D. Li, M. Li, X. Qiao, et al., Novel imidazolium-embedded N,N-dimethylaminopropyl-functionalized silica-based stationary phase for hydrophilic interaction/reversed-phase mixed-mode chromatography, Anal. Bioanal. Chem., 407 (2015) 8989-8997.
40. X.D. Cheng, X.T. Peng, Q.W. Yu, B.F. Yuan, Y.Q. Feng, Preparation and chromatographic evaluation of a novel phosphate ester-bonded stationary phase with complexation and hydrophobic interactions retention mechanism, J. Chromatogr. A, 1302 (2013) 81-87.
41. Y. Zhang, Y. Zhang, G. Wang, W. Chen, P. He, Q. Wang, Simultaneous separation of polar and non-polar mixtures by capillary HPLC based on an ostadecylsilane and taurine derivatized silica continuously packed column, Talanta, 161 (2016) 762-768.
42. Q. Wang, M. Ye, L. Xu, Z.G. Shi, A reversed-phase/hydrophilic interaction mixed-mode C18-Diol stationary phase for multiple applications, Anal. Chim. Acta, 888 (2015) 182-190.
43. T. Liang, Q. Fu, A. Shen, H. Wang, Y. Jin, H. Xin, Y. Ke, Z. Guo, X. Liang, Preparation and chromatographic evaluation of newly designed steviol glycoside modified-silica stationary phase in hydrophilic interaction liquid chromatography and reversed phase liquid chromatography, J. Chromatogr. A, 1388 (2015) 110-118.
44. H. Qui, M. Zhang, T. Gu, M. Takafuji, H. Ihara, A Sulphonic-azobenzene–grafted silica amphiphilic material: a versatile stationary phase for mixed-mode chromatography, Chem. Eur. J., 19 (2013) 18004-18010.
45. S. Bocian, A. Nowaczyk, B. Buszewski, New-alkyl-phospate bonded stationary phase for liquid chromatographic separation of biologically active compounds, Anal. Bioanal. Chem., 404 (2012) 731-740.
46. Z. Liu, B.D. Cai, Y.Q. Feng, Rapid determination of endogenous cytokinins in plant samples by combination of magnetic solid phase extraction with hydrophilic interaction chromatography-tandem mass spectrometry, J. Chromatogr. B, 891-892 (2012) 27-35.
47. T. Tang, W.B. Zhang, J.W. Xu, M. Z. Xia, X.D. Gong, F.Y. Wang, T. Li, Synthesis, characterization, and application of a novel multifunctional stationary phase for hydrophilic interaction/reversed phase mixed-mode chromatography, Chinese J. Anal. Chem., 45 (2017) 56-60.

48. L. Qiao, A. Duou, X. Shi, H. Li, Y. Shan, X. Lu, G. Xu, Development and evaluation of new imidazolium-based zwitterionic stationary phases for hydrophilic interaction chromatography, J. Chromatogr. A, 1286 (2013) 137-145.
49. L. Qiao, X. Zhou, Y. Zhang, A. Yu, K. Hu, S. Zhang, 4-Chloro-6-pyrimidinylferrocene modified silica gel: A novel multiple-function stationary phase for mixed-mode chromatography, Talanta, 153 (2016) 8-16.
50. A. Shen, X. Li, X. Dong, J. wei, Z. Guo, X. Liang, Glutathione-based zwitterionic stationary phase for hydrophilic interaction/cation-exchange mixed-mode chromatography, J. Chromatogr. A, 1314 (2013) 63-69.

Radiation Synthesis of Molecularly Imprinted Hydroxyethylmethacrylate-based Matrices for Glucose Recognition

Glikoz Tanıması için Hidroksietilmetakrilat Esaslı Moleküler Baskılı Matrislerin Radyasyon ile Sentezi

Research Article

Meshude Akbulut Söylemez* and Olgun Güven
Hacettepe University, Department of Chemistry, Beytepe, Ankara, Turkey.

ABSTRACT

In this study, 2-hydroxyethyl methacrylate (HEMA) was used as functional monomer and diethylene glycol diacrylate (DEGDA) and polyethylene glycol (200) diacrylate (PEG(200)DA) were used as crosslinking agents to imprint D(+)glucose. D(+)glucose imprinted polymers were prepared in the presence of dimethyl sulfoxide (DMSO) /isopropyl alcohol (IPA) (3/1, v/v) at room temperature, in the air by radiation-induced polymerization/crosslinking. The control polymers were synthesized by the same procedure in the absence of D(+)glucose. In order to evaluate the recognition and separation properties of the imprinted system high performance liquid chromatography (HPLC) experiments were carried out where β (-) lactose, D(+)glucose and glycerol were used as analytes. To increase the affinity of the template to the stationary phase polarity of the mobile phase was decreased by the addition of acetonitrile into water. Optimum composition of acetonitrile/water (1/5 v/v) was determined according to the swelling experiments. The sizes of the cavities in the polymeric networks were determined by positron annihilation lifetime spectroscopy (PALS). The average radii of cavities were found as 0.254 and 0.279 nm for freeze-dried imprinted polymers prepared by using PEG(200)DA after swollen in water and acetonitrile/water mixture (1/5 by volume), respectively.

Key Words
Molecularly imprinted polymers, poly(2-hydroxyethyl methacrylate), glucose recognition, gamma irradiation.

ÖZ

Bu çalışmada D (+) Glikoz baskılamak amacıyla fonksiyonel monomer olarak 2-hidroksietil metakrilat (HEMA), çapraz bağlayıcı olarak dietilenglikol diakrilat (DEGDA) ve polietilenglikol (200) diakrilat (PEG(200)DA) kullanılmıştır. D (+) Glikoz baskılı polimerler dimetil sülfoksit (DMSO)/izopropil alkol (İPA) (hacimce, 3/1) varlığında oda sıcaklığında, havada radyasyonla başlatılan polimerizasyon/çapraz bağlanma ile hazırlanmıştır. Kontrol polimerleri D (+) glikoz yokluğunda aynı reçete ile sentezlenmiştir. Baskılı sistemin tanıma ve ayırma özelliklerini değerlendirmek amacıyla β (-) laktoz, D (+) glikoz and gliserolün analit olarak kullanıldığı yüksek performanslı sıvı kromatografisi (HPLC) deneyleri yapılmıştır. Hedef molekülün durgun faza olan ilgisini arttırmak amacıyla suya asetonitril eklenerek hareketli fazın polaritesi azaltılmıştır. Asetonitril/su (1/5, v/v) için optimum bileşim şişme deneylerine göre belirlenmiştir. Polimerik ağ yapı içindeki boşlukların boyutları positron yok olma ömrü spektroskopisi (PALS) ile hesaplanmıştır. PEG(200)DA kullanılarak hazırlanan suda ve asetonitril/su (hacimce, 1/5) karışımında şişirildikten sonra dondurularak kurutulmuş baskılı polimerlerin ortalama yarıçapları sırasıyla 0.254 ve 0.279 nm olarak hesaplanmıştır.

Anahtar Kelimeler
Moleküler baskılı polimerler, poli(2-hidroksietil metakrilat), glikoz tanıma, gama ışınlaması.

Article History: Received: May 16, 2017; Revised: Jul 12, 2017; Accepted: Feb 08, 2017; Available Online: Feb 20, 2018.

DOI: 10.15671/HJBC.2018.214

Correspondence to: M. Akbulut Söylemez, Hacettepe University, Department of Chemistry, Beytepe, Ankara, Turkey.
Tel: + 90 312 297 6394 Fax: +90 312 297 79 73 E-Mail: meshude@gmail.com

INTRODUCTION

Molecular imprinting is a powerful tool to prepare synthetic receptors for recognition of various molecules such as drugs [1,2], herbicides [3], carbohydrates [4], amino acids [5], proteins [6], ions [7,8]. Imprinting method comprises the formation of a pre-polymerization complex between a template and functional monomer/monomers via covalent, non-covalent bonds or metal coordination interactions followed by polymerization/crosslinking reaction in the presence of a crosslinking agent to provide stability to the binding sites in the network. After removal of the template, specific binding sites that show chemical and physical complementarity towards the template molecule remain in the network. Combination of chemical affinity with size exclusion/inclusion towards a certain target molecule provides a big potential for use as intelligent drug delivery, catalytic and sensor systems.

Molecular imprinting can be categorized due to interactions between template and functional monomer/monomers as covalent and non-covalent imprinting. In covalent imprinting, the main forces between the template and the functional monomer/monomers are reversible covalent bonds such as boronic acid esters, acetals, ketals, Schiff bases, disulfide bonds, and coordination bonds [9]. This method provides more homogenous binding sites than non-covalent imprinting, however, there are some limitations for template and functional monomers selection based on the lack of functional moieties which result in formation of reversible covalent bonds. On the other hand, non-covalent imprinting is a simpler method and it facilitates to imprint a wide range of template molecules. The binding sites however, show more heterogeneity because of the uncertainty in the stoichiometry of pre-polymerization complex [10,11].

Since the beginning of the imprinting studies, sugars were most frequently used as template materials. The Wullf group was the first to prepare an imprinting system by using 4-vinylphenylboronic acid as functional monomer forming reversible covalent bonds with sugars [12].

There are several studies on imprinting of glucose [13]. A different method has been proposed which uses the hydrogels synthesized by crosslinking of poly(allylamine hydrochloride) with (±)-epichlorohydrin instead of methacrylate- or acrylate- based reagents. In this system template was D-glucose-6-phosphate monobarium salt instead of unmodified glucose. These hydrogels show preferential binding of D-glucose relative to D-fructose in deionized water [14]. Another approach to imprint glucose was by using coordination of metals to monomers [15]. These types of materials have the ability of binding of their templates in water, as well. However, these systems are not feasible for biological systems.

In our laboratory, several studies have been conducted on imprinting of glucose. Firstly, Bodugöz et al. [16] achieved to create three dimensional binding sites for glucose using 2-hydroxyethyl methacrylate and methacrylic acid as functional monomers and poly(ethylene glycol) (PEG) as the crosslinking agent. Then, Ates and Güven [17] showed how to control the size of the binding sites (cavities) for glucose to separate it from its structural analogues, galactose and fructose by using MIPs as support material in HPLC system.

The purpose of this study was to synthesize polymeric matrices with the capability of recognizing D(+)glucose by using radiation induced polymerization/crosslinking in a solvent mixture. For this purpose, 2-hydroxyethyl methacrylate (HEMA) was used as a functional monomer, diethylene glycol diacrylate (DEGDA) [17] and polyethylene glycol (200) diacrylate (PEG(200)DA) were used as crosslinking agents to imprint D(+)glucose. In this imprinting system, a solvent mixture composed of dimethyl sulfoxide (DMSO) and isopropyl alcohol (IPA) was used. In order to evaluate the separation performance of MIPs, β (-) lactose and glycerol were used as analogues of D(+)glucose. In order to evaluate the size of the binding sites of the MIPs, positron annihilation lifetime spectroscopy (PALS) experiments were conducted.

MATERIALS and METHODS

Experimental

Dimethyl sulfoxide (DMSO) was purchased from Merck (Darmstadt, Germany). All the other chemicals, including template molecule, D(+) glucose and crosslinking agents, diethylene glycol diacrylate (DEGDA), polyethylene glycol(200) diacrylate (PEG(200)DA) and isopropyl alcohol were obtained from Sigma-Aldrich (Milwaukee, USA). Functional monomer, 2-hydroxyethyl methacrylate (HEMA) was purchased from Fluka (Buchs, Switzerland). All chemicals were used as received.

Synthesis of D(+)Glucose Imprinted Polymers

D(+)Glucose imprinted polymers were synthesized in the presence of dimethyl sulfoxide (DMSO) /isopropyl alcohol (IPA) (3/1, v/v) mixture as solvent in order to provide solubility and miscibility to glucose-monomer mixture (DMSO) and crosslinking agent (IPA) at room temperature, in air by free radical polymerization where γ-rays were used as initiator. Irradiation dose was selected as 15 kGy because no difference was observed in the crosslinking density at higher doses in HEMA-based MIPs [17], the mole ratio of functional monomer to target molecule was kept as 3/1 as determined before by Djourelov et al. [18] considering the hydrogen bonding interaction between the template molecule glucose and HEMA, and the amount of crosslinking agents used was 20 and 30%, by mole. In a typical synthesis, firstly glucose was dissolved in DMSO, and then HEMA was added to provide formation of the pre-polymerization complex between the template and functional monomer. The crosslinking agent was dissolved in IPA and then added to the mixture of HEMA and D(+)glucose. The solution was purged with nitrogen for 5 min. Free radical polymerization was carried out in glass vials in the air at room temperature in a Gammacell 220, ^{60}Co-γ irradiator (Nordion, Canada). The dose rate 0.101 kGy/h was measured by Fricke dosimetry. Upon completion of the polymerization, polymer monoliths were crushed, ground to particle sizes between 100-150 μm. In addition to the monoliths, to obtain matrixes in disc form for PALS experiments, some of the imprinted polymers were synthesized between the clamped glass slides (60 mm - 60 mm - 2 mm) separated from each other with natural rubber O-ring. Both type of imprinted polymers were washed by water to remove template molecule and unpolymerized material if any. The swelling solution was changed at every 12 h, and eluents were checked by UV-visible spectrophotometry (Varian, Cary100) and HPLC (Waters). After washing was completed the discs were dried at 40°C in an oven. The non-imprinted polymers (NIPs), without D(+)glucose, were synthesized following the same procedure.

Swelling Experiments

Swelling experiments were done by using water and water/acetonitrile mixtures with different compositions which were used as mobile phases in HPLC systems wherein synthesized MIPs was used as the stationary phase. Acetonitrile was used to increase the affinity of the template to the stationary phase by reducing the polarity of the mobile phase. Swelling curves were constructed by measuring the water/solvent uptake of gel particles gravimetrically with time.

High Pressure Liquid Chromatography (HPLC)

In order to evaluate recognition performance of MIPs as a function of some variables such as the composition of mobile phase, type and amount of crosslinker, HPLC experiments were carried out. In these experiments, β(-)lactose and glycerol were used as analytes together with D(+)glucose. All analyses were performed by Water HPLC system with a binary pump system and a refractive index detector. The ground MIP or NIP particles were filled into two commercial stainless steel HPLC columns (4.0 mm inner diameter, and 150 mm length) (TOSOH, Japan) and tested separately. Substrate solutions were prepared of each at a concentration of 500 mg/L and 200 μL of solution was injected for analysis. Each injection was repeated three times. All chromatographic analyses were carried out at 30°C.

Positron Annihilation Lifetime Spectroscopy (PALS)

The positron source, a droplet of ^{22}NaCl from a carrier-free neutral solution (activity: 35 μCi), was dried between two DuPont Kapton® foils (thickness 1.08 mg/cm^{-3}), which were afterward glued together. The source was inserted between two identical discs of MIPs or NIPs in a typical

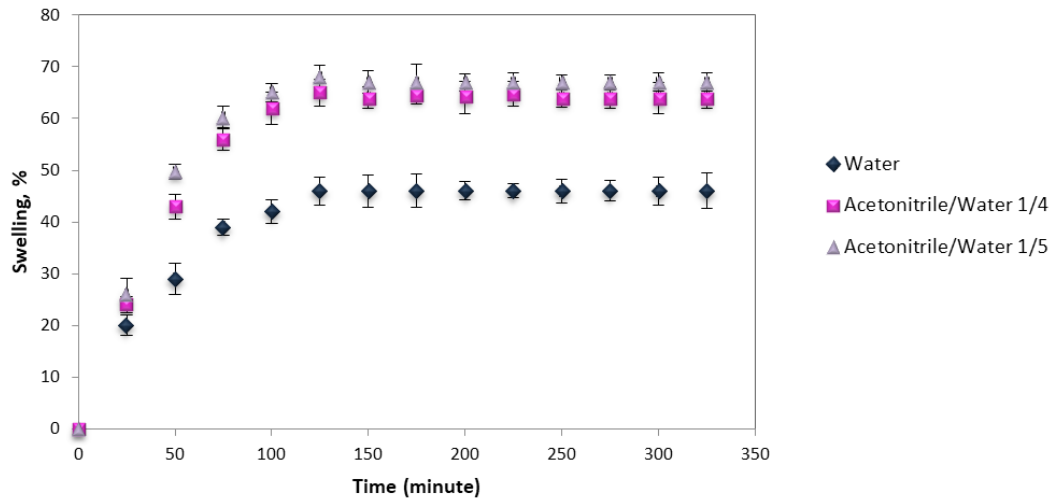

Figure 1. Swelling curves of MIPs prepared with HEMA/Glucose 3/1, and 20% PEG(200)DA as crosslinker in water (◆), acetonitrile/water 1/5 (v/v) (■) and acetonitrile/water 1/4 (v/v) (▲).

'sandwich' configuration. The discs of MIPs and NIPs were obtained by lyophilisation at -40°C and $1x10^{-3}$ mbar pressure after swelling in water and water/acetonitrile mixtures.

PALS experiments were carried out using a conventional fast - fast coincidence system having a time resolution (full width at half-maximum, FWHM) of about 312 ps. The measurements were carried out in the air at room temperature. The spectra were recorded at every 3 hours with total counts in each spectrum being $1.8x10^6$ Then, for each type of sample, five spectra were summed together resulting in statistics of $9x10^6$ counts. The spectra were evaluated by LT9 programme.

RESULTS AND DISCUSSION

Effect of Solvent Composition on Swelling Behaviour of MIPS

The swelling experiments were carried out for MIPs prepared by using PEG(200)DA and DEGDA as crosslinking agents. Maximum swelling in water was obtained as 26% and 49% for MIPs synthesized using DEGDA and PEG(200)DA as the crosslinking agent, respectively. The maximum swelling ratios in acetonitrile/water mixture (1/5 by volume) showed the same tendency and found as 58% and 65% for MIPs prepared with DEGDA and PEG(200)DA, respectively.

Higher swelling maximum values were obtained for PEG(200)DA that has a longer chain length with five ethylene oxide groups than the DEGDA in both water (49%) and acetonitrile/water mixtures with different composition (65% and 67% for acetonitrile/water 1/5 (v/v) and 1/4 (v/v), respectively) (Figure 1).

The maximum swelling of MIPs synthesized with DEGDA was not big enough to provide a selective binding [19], consequently, all the other evaluations were made for MIPs prepared with PEG(200)DA.

Acetonitrile was used to increase the affinity of the glucose to the stationary phase by decreasing polarity of the aqueous medium. Increasing the amount of acetonitrile in the solvent mixture caused an increase in swelling of MIPs, Table 1. Higher swelling of MIPs reduces the specific size selectivity for template [19,20]. Thus acetonitrile/water mixtures with 1/4 and 1/5 ratios by volume were tested as mobile phases for investigating swelling and chromatographic behaviour of this imprinting system.

Chromatographic Evaluation of MIPs

MIPs prepared with different type and amount of crosslinking agents were used as a stationary phase to evaluate their recognition properties. In addition to the template glucose, glycerol and lactose were used as the other competitive compounds due to their size differences. Also, it is possible for these three reagents to exist together in a biological sample, as glycerol 3-phosphate is a product of carbohydrate metabolism and

lactose is a disaccharide of glucose and galactose. Different mobile phases were used to see their effects on the performance of the imprinting systems in separation of these compounds.

Effect of the Type of Crosslinking Agent on Separation

In a previous MIP work from this laboratory, it was found that cavities of radiation crosslinked HEMA matrix were smaller than the cavities of the matrix prepared by using crosslinking agents [18]. Presence of a crosslinking agent prevents the formation of the denser crosslinked structure of pure HEMA by limiting the mesh size. Based on this result, MIPs were prepared using two different crosslinking agents with different ethylene glycol unit number on the chain in the present work.

There was no separation of the three analytes when DEGDA was used as crosslinking agent as seen in Figure 2a. By using columns filled with MIPs prepared with PEG(200)DA, a more effective separation was observed, Figure 2b. Because the size of the cavities inside the network that was prepared by using DEGDA were not big enough for an effective separation [18]. This result was supported by swelling experiments, as well.

Effect of the Amount of Crosslinking Agent on Separation

MIPs prepared by using two different amounts of PEG(200)DA (20 and 30%, by mole) were used as packing material in HPLC system. Ground MIP particles were filled into the columns. When these columns were employed in HPLC system the retention times of glucose were 9.64 and 9.37 min, for MIPs prepared using 20 and 30% crosslinking agent, respectively. This shows that increasing by 10 percent of the amount of PEG(200)DA did not affect the separation property of MIPs, because this increase in the amount of the crosslinking agent did not cause a change in the radius of the cavities which was found to be 0.254±0.001 nm, for both MIP systems, as determined by PALS.

Effect of the Mobile Phase on Separation

As seen in Figure 3a, a certain extent of separation was obtained in HPLC system wherein MIP particles used as stationary phase were prepared with 20% PEG(200)DA as crosslinking agent and ratio of HEMA/glucose 3/1, with a flow rate 0.30 mL/min for glycerol, glucose, and lactose whose hydrated diameters are 0.275, 0.425 and 0.525 nm, respectively [26]. The chromatograms show that separation by size of these three analytes was achieved. Considering the swelling experiments acetonitrile/water mixture with a ratio of 1/5 by volume was selected as the mobile phase for these imprinting systems. It can be seen from the result of swelling tests (Figure 1), the maximum swelling increases with increasing amount of acetonitrile which causes a change in polarity as well as in values of the solubility parameter of solvent mixtures (Table 1). This affects the separation property, due to the expansion of the cavity size according to the amount of acetonitrile. In this respect, in the HPLC system where acetonitrile/water was used as mobile phase, a better separation was obtained as seen in Figure 3b.

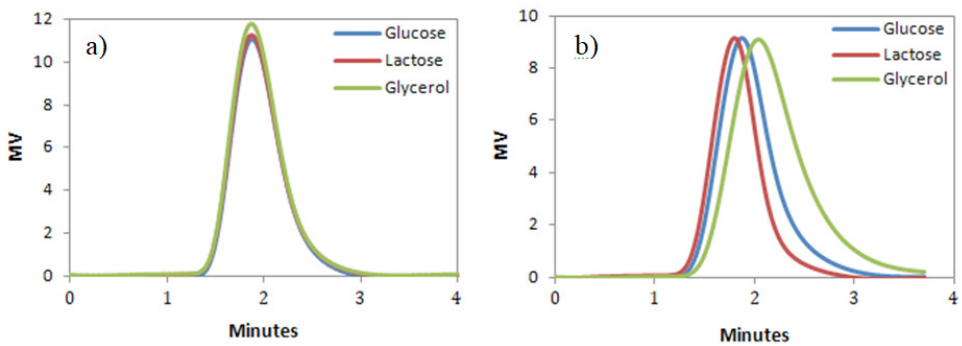

Figure 2. Chromatograms of D(+)Glucose, β(-)Lactose and Glycerol using MIPs synthesized with (a) 20% DEGDA and (b) 20% PEG(200)DA (mobile phase; water, flow rate 1.00 mL/min).

Table 1. The change in the maximum swelling values of MIPs prepared with 20% PEG(200)DA as a function of the solubility parameters; solubility parameter of acetonitrile is 11.9 $(cal/cm^3)^{1/2}$ [21].

Solvent/Solvent Mixture	Solubility Parameter $(cal/cm^3)^{1/2}$	Maximum Swelling %
Water	23.4	49
Acetonitrile/Water 1/5, v/v	21.5	65
Acetonitrile/Water 1/4, v/v	21.1	67

The solubility parameters of solvent mixtures were calculated by using Molar Volume Method [22].

Also, in order to optimize separation efficiency, it is necessary to maximize the number of theoretical plates (N), which requires reducing the plate height. Addition of acetonitrile into the mobile phase provides a certain increase in N value for each molecule (Table 2). The number of theoretical plates (N) was calculated using Equation 1, where t_R is the retention time and W is the peak width of the analyte tested. The numbers given in Table 2 show that by adding acetonitrile into the water the separation performance of the columns was improved for all three analytes as compared to using only water as the effluent.

$$N = 16\left(\frac{t_R}{W}\right)^2 \quad (1)$$

PALS Experiments

The sizes of the cavities in MIP and NIP networks were determined by using Equation (2) which is developed by Nakanishi and Jean according to the quantum-mechanical model of Tao [23] later developed by Eldrup et al [24].

$$\tau_{o-Ps} = 0.5\left[1 - \frac{R}{R+\Delta R} + \frac{1}{2\pi}\sin\left(\frac{2\pi R}{R+\Delta R}\right)\right]^{-1} \quad (2)$$

In this equation $\tau_{o\text{-}Ps}$ is the lifetime of the ***o***-Ps in ns, R is the radius of free volume holes in nm, and ΔR is a constant whose value is 0.1656 nm. The lifetime of ***o***-Ps, $\tau_{o\text{-}Ps}$ is determined by plotting of lifetime spectrum as typically shown in Figure 4 from the slope of the corresponding line. The results for MIPs prepared with different amounts of PEG(200) DA (20% and 30%) as the crosslinking agent are found to be nearly the same, 0.254 nm. This result is supported by swelling experiments, as well. The maximum swelling amounts of these MIPs in water are 49% and 50%, respectively.

The hole radius values of imprinted polymers synthesized with 20% PEG(200)DA as the crosslinking agent are 0.254 and 0.279 nm which

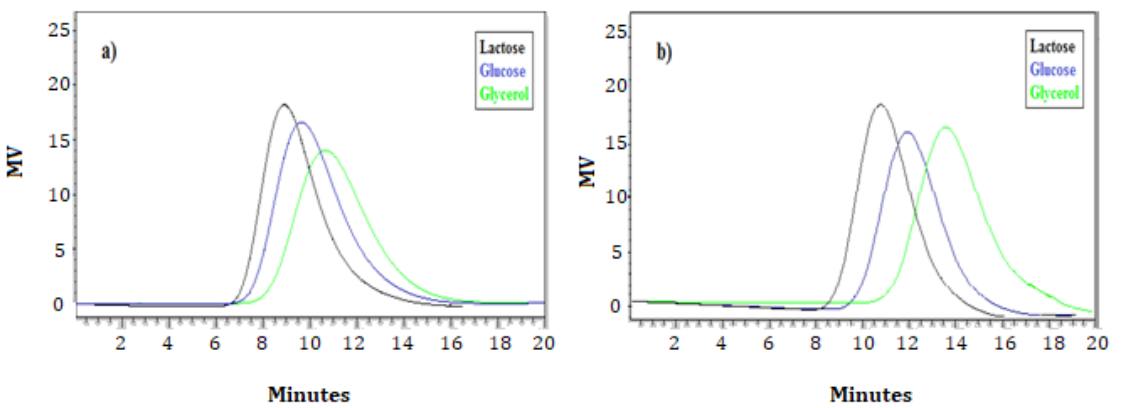

Figure 3. Chromatograms for D(+)Glucose, β(-)Lactose and Glycerol by using water (a) and acetonitrile-water (v/v, 1/5) as mobile phase (MIP particles used as stationary phase were prepared with 20% PEG(200)DA as crosslinking agent and ratio of HEMA/glucose 3/1, flow rate 0.30 mL/min).

Table 2. The number of theoretical plates (N) for glucose, lactose, and glycerol determined from the respective chromatograms of analytes.

	Water	Acetonitrile/Water (1/5)
Glucose, N_{Glu}	10.46	25.35
Lactose, N_{Lac}	11.27	28.44
Glycerol, N_{Gly}	9.29	33.52

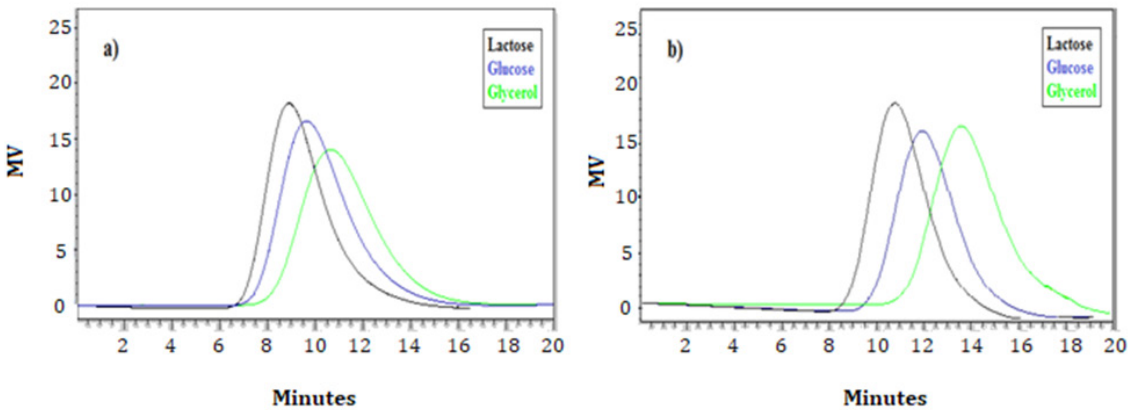

Figure 4. A typical lifetime spectrum of positron and positronium in a polymer with three lifetime components is indicated as (τ_1) the shortest lifetime p-Ps, (τ_2) lifetime of free positrons, and (τ_3 or $\tau_{o\text{-}Ps}$) the longest lifetime o-Ps [25].

were freeze-dried after swollen in water and water/acetonitrile (1/5 v/v) mixture, respectively.

This difference is also reflected in swelling results, Figure 1. The molecular diameter of hydrated glucose is known to be 0.425 nm [26] which shows a very good match with the cavity sizes obtained in this work 0.508nm.

CONCLUSION

In this study, molecularly imprinted polymers were prepared for glucose by using two different crosslinking agents in different amounts via radiation induced polymerization/crosslinking method. The advantages of this method are the following; no need for initiators since radiation chemical processes provide a continuous supply of free radicals in the system; conduction of the polymerization process at room or any desired temperature. It was tried to optimize the type and amount of the crosslinking agent and composition of the mobile phase by changing its polarity in the HPLC system in which MIPs prepared by using PEG(200)DA as crosslinking agent were used as stationary phase. The size of the free volume cavities was determined by using PALS. It was shown by this study that controlling of cavity size in the molecularly imprinted network by using proper crosslinking agent improves the size selectivity of the MIPs.

References

1. B. Sellergren, Direct drug determination by selective sample enrichment on an imprinted polymer, Anal. Chem., 66 (1994) 1578-1582.
2. L. Fischer, R. Müller, B. Ekberg, K. Mosbach, Direct enantioseparation of beta-adrenergic blockers using a chiral stationary phase prepared by molecular imprinting, J. Am. Chem. Soc., 113 (1991) 9358-9360.
3. S.A. Piletsky, E.V. Piletskaya, A.V. Elgersma, K. Yano, I. Karube, Y.P. Parhometz, A.V. El'skaya, Atrazine sensing by molecularly imprinted membranes, Biosens. Bioelectron., 10 (1995) 959-964.
4. D. Kriz, K. Mosbach, Competitive amperometric morphine sensor based on an agarose immobilised molecularly imprinted polymer, Anal. Chim. Acta, 300 (1995) 71-75.
5. M. Kempe, K. Mosbach, Chiral recognition of Na-protected amino acids and derivatives in molecularly imprinted polymers, Int. J. Peptide Protein Res., 44 (1994) 603-606.
6. K. Haupt, Imprinted polymers: tailor-made mimics of antibodies and receptors, Chem. Commun., (2003) 171-178.

7. Y. Ren, X. Wei, M. Zhang, Adsorption character for removal Cu(II) by magnetic Cu(II) Ion imprinted composite adsorbent, J. Hazard. Mater., 158 (2008) 14-22.
8. G. Sener, L. Uzun, A. Denizli, Lysine-promoted colorimetric response of gold nanoparticles: a simple assay for ultrasensitive mercury(II) detection, Anal. Chem., 86 (2014) 514-520.
9. A. Martín-Esteban, Molecularly imprinted polymers: new molecular recognition materials for selective solid-phase extraction of organic compounds, Fresenius J. Anal. Chem., 370 (2001) 795-802.
10. R.J. Umpleby, M. Bode, K.D. Shimizu, Measurement of the continuous distribution of binding sites in molecularly imprinted polymers, Analyst, 125 (2000) 1261–1265.
11. R.J. Umpleby, S.C. Baxter, Y. Chen, R.N. Shah, K.D. Shimizu, Characterization of molecularly imprinted polymers with the Langmuir-Freundlich isotherm, Anal. Chem., 3 (2001) 4584-4591.
12. G. Wulff, R. Grobe-Einsler, A. Sarhan, Enzyme-analogue built polymers, on the specificity distribution of chiral cavities prepared in synthetic polymers, Macromol. Chem., 178 (1977) 2817-2825.
13. A. Ersöz, A. Denizli, A. Ozcan, R. Say, Molecularly imprinted ligand-exchange recognition assay of glucose by quartz crystal microbalance, Biosens. Bioelectron., 20 (2005) 2197-2202.
14. P. Parmpi, P. Kofinas, biomimetic glucose recognition using molecularly imprinted polymer hydrogels, Biomaterials, 25 (2004) 1969-1973.
15. C. Chen, G. Chen, Z. Guan, D. Lee, F.H. Arnold, Polymeric sensor materials for glucose, Polym. Prepr., 37 (1996) 216-217.
16. H. Bodugoz, O. Güven, N.A. Peppas, Glucose recognition capabilities of hydroxyethyl methacrylate-based hydrogels containing poly(ethylene glycol) chains, J. Appl. Polym. Sci., 103 (2007) 432-441.
17. Z. Ateş, O. Güven, Radiation induced molecular imprinting of D-glucose onto poly(2-hydroxyethyl methacrylate) matrices using various crosslinking agents, Rad. Phys. Chem., 79 (2010) 219-222.
18. N. Djourelov, Z. Ateş, O. Güven, M. Misheva, T. Suzuki, Positron annihilation lifetime spectroscopy of molecularly imprinted hydroxyethyl methacrylate based polymers, Polymer, 48 (2007) 2692-2699.
19. C. Yu, K. Mosbach, Molecular imprinting utilizing an amide functional group for hydrogen bonding leading to highly efficient polymers, J. Org. Chem., 62 (1997) 4057-4064.
20. B. Sellergren, K.J. Shea, Influence of polymer morphology on the ability of imprinted network polymers to resolve enantiomers, J. Chromatogr., 635 (1993) 31-49.
21. J. Brandrup, E.H. Immergut, 1989. Polymer Handbook, third ed. John Wiley & Sons Inc., USA.
22. P.B. Rathi, Determination and evaluation of solubility parameter of satranidazole using dioxane-water system, Indian J. Pharm. Sci., 72 (2010) 671-674.
23. S.J. Tao, Positronium annihilation in molecular substances, J. Chem. Phys., 56 (1972) 5499-5510.
24. M. Eldrup, D. Lightbody, J.N. Sherwood, The temperature dependence of positron lifetimes in solid pivalic acid, Chem. Phys., 63 (1981) 51-58.
25. C. Ranganathaiah, 2010. Characterization of polymer nanocomposites by free-volume measurements, S., Thomas, G.E., Zaikov, S.V., Valsaraj, A.P. Meera, (Eds.), Recent advances in polymer nanocomposites: synthesis and characterisation, Taylor & Francis Group, New York, pp. 305-335.
26. G. Knowles, The reduced glucose permeability of the isolated malpighian tubules of the blowfly *calliphora vomitoria*, J. Exp. Biol., 62 (1975) 327-340.

Modification of Functional Polyesters Bearing Norbornene Moieties via Olefin Metathesis Reactions

Olefin Metatez Tepkimeleri ile Norbornen İçeren Fonksiyonel Poliesterlerin Modifikasyonu

Research Article

Bengi Özgün Öztürk*
Department of Chemistry, Faculty of Science, Hacettepe University, Ankara, Turkey.

ABSTRACT

In this study, unsaturated functional polyester derivatives were synthesized via polycondensation reactions of 5-norbornene-2,3-dicarboxylic anhydride and 1,6-hexanediol. Functional unsaturated polyesters were modified using methyl acrylate as ring opening/cross-metathesis reaction partner. The solubility and hydrophobic/hydrophilic character of polyester was tuned by integrating allyl end capped poly(ethyleneglycol) by ring opening/cross-metathesis reactions. Norbornene moiety of unsaturated polyesters allowed us to use ring opening metathesis polymerization reactions to form side-chain poly(norbornene) on main polyester chain using Grubbs 1st, 3rd and Hoveyda-Grubbs 2nd generation catalysts as initiators, resulting in gel-like materials.

Key Words
Ring opening/cross-metathesis, polyesters, ruthenium, polycondensation.

ÖZ

Bu çalışmada doymamış fonksiyonel poliester türevleri 5-norbornen-2,3-dikarboksilik anhidrit ve 1,6-hekzandiol bileşiklerinin polikondenzasyon tepkimeleri ile elde edilmiştir. Fonksiyonel doymamış poliesterler metil akrilat kullanılarak halka açılma/çapraz metatez tepkimeleri ile modifiye edilmiştir. Poliesterlerin çözünürlük ve hidrofobik/hidrofilik karakterleri halka açılma/çapraz metatez tepkimeleri ile alil son grubuna sahip poli(etilenglikol) bileşikleri entegre edilerek değiştirilmiştir. Doymamış poliesterlerdeki norbornen grubu sayesinde jel benzeri malzemeler, Grubbs birinci, üçüncü ve Hoveyda-Grubbs ikinci nesil katalizörleri varlığında halka açılım metatez polimerizasyon tepkimeleri ile ana poliester zinciri üzerinde yan poli(norbornen) zincirlerinin oluşumu ile elde edilmiştir.

Anahtar Kelimeler
Halka açılım/çapraz metatez, poliester, rutenyum, polikondenzasyon.

Article History: Received: Jun 02, 2017; Revised: Aug 12, 2017; Accepted: Oct 18, 2017; Available Online: Feb 20, 2018.

DOI: 10.15671/HJBC.2018.215

Correspondence to: B.Ö. Öztürk, Department of Chemistry, Faculty of Science, Hacettepe University, Ankara, Turkey.
Tel: +90 312 297 62 99 Fax: +90 312 299 21 63 E-Mail: bengi04@hacettepe.edu.tr

INTRODUCTION

The functionalization of synthetic polymers is in great importance owing to their application fields such as smart materials design, drug-delivery, biomaterials and gene-therapy [1-4]. In order to adapt polyester derivatives to above mentioned applications polymers should have amorphous, water-soluble and must have reactive groups to functionalize polymer chain [5]. The traditional polymers such as poly(L-lactic acid) (PLLA) poly(glyclolic acid) (PGA), poly(caprolactone) (PCL) are synthesized by ring-opening polymerization (ROP), mostly yielding hydrophobic and semi-crystalline polymers [6]. For the past decade, several studies are focused on the synthesis of amorphous aliphatic polyesters that can be used in several fields [7]. The integration of functional polar group on polymer chain is used as an efficient strategy. Amsden and research group have reported acrylate terminated star shaped polymers bearing amorphous poly(DL-lactic acid) (PDLLA) [8]. The cross-linking ability of the material was investigated by varying the length of the arms of the stars and photo-curing conditions. Sebacic acid and glycerol was used by Langer et. al for the synthesis of a though biodegradable elastomer, exhibiting total amorphous property at 37°C [9]. In 2007 Sheares et. al. have used linear diols and dicarboxylic monomers to obtain unsaturated aliphatic polyesters via step growth polycondensation [10]. In addition to anhydride-diol combination, epoxy based materials were also polymerized with anhydride based monomers [11]. Unsaturated polyesters are in great importance in polymer chemistry since they can be used to synthesize functional materials by modification through double bonds [12]. Cross-metathesis is a valuable partner for modification of unsaturated polymers [13-14] β-heptenolactone (βHL) based polyesters were modified via olefin cross-metathesis reactions altering the thermal, chemical and physical properties of polymers [15]. In addition to repeating unit modification reactions, cross-metathesis reactions are also used for end-capping of polymers [16]. Recently, greener approaches have been developed for polyester synthesis utilizing furfural [17] and epoxides [18].

Here in, we report an efficient method for post-modification of unsaturated polyester derivatives via ring opening/cross-metathesis and ring opening metathesis polymerization. The effect of cross-metathesis modification on T_g and solubility of the polymer was investigated in details. Thermoplastics with relatively higher thermal stabilities were obtained by ROMP of norbornene moiety of unsaturated polyesters in the presence of Grubbs 1st, 3rd and Hoveyda-Grubbs 2nd generation catalysts.

MATERIALS and METHODS

Chemicals and Instruments

Otherwise noted all chemicals were purchased from Sigma-Aldrich and used as received. Umicore@M1 was purchased from Strem Chemical Inc. ^{1}H and ^{13}C nuclear magnetic resonance (NMR) spectra were recorded at 25°C with a Bruker GmbH 400 MHz high-performance digital FT-NMR spectrometer using $CDCl_3$ as the solvent. Molecular weights were determined with a GPC System LC-20A from Shimadzu equipped with SIL-20A autosampler, RID-10A, and a refractive index detector. The analysis was performed on the following column system operating on THF (flow rate 1 mL min^{-1}) at 40°C: main-column PSS SDV analytical (5 μm, 300 mm × 8.0 mm, 10 000 Å) and a PSS SDV analytical precolumn (5 μm, 50 mm × 8.0 mm). The calibration was created using narrow linear poly(methyl methacrylate) standards (Polymer Standards Service PPS, Germany) ranging from 1100 to 981 000 Da.

Synthesis of P1

A Schlenk reactor was charged with 5-norbornene-2,3-dicarboxylic anhydride (1.0 g, 6.10 mmol) and 1,6-hexanediol (7.30 mmol, 0.865 g). The reaction mixture was taken to a pre-heated oil bath (120°C) and stirred for 10 min prior to addition of catalyst; $Sn(Oct)_2$ (0.061 mmol). After addition of catalyst to the reactor, Schlenk reactor was connected to a vacuum pump (vacuum value; 30-40 torr) and reaction mixture was stirred for 12 h under these conditions. After 12 h, reaction mixture was cooled down and poured into cold-methanol and stirred for additional 30 min. P1 was isolated by simple filtration, followed by washing with cold methanol/acetone mixture. P1 was characterized by ^{1}H, ^{13}C NMR and GPC.

^{1}H NMR (400 MHz, $CDCl_3$) δ 6.17 (m, 2H), 4.31 – 3.79 (m, 24H), 3.43 (d, J = 18.2 Hz, 2H), 3.33 – 2.95 (m, 2H), 1.55-1.29 (m, 10H).

^{13}C NMR (101 MHz, $CDCl_3$) δ 175.23 – 170.19 (m), 137.78 (d, J= 30.8 Hz), 134.92 (d, J= 16.4 Hz), 66.15 – 61.50 (m), 49.86 (d, J= 140.0 Hz), 51.81 – 43.47 (m), 32.13 – 27.77 (m), 26.49 – 22.44 (m).

Cross-Metathesis Reactions of P1

A Schlenk reactor was charged with P1 (0.10 g, M_n: 4000 Da) in toluene (5 ml). The reactor was taken to a pre-heated oil bath at 85°C and stirred for 10 min prior to addition of Hoveyda-Grubbs 2nd generation catalyst (commercial code C711, 0.01 g, 0.014 mmol). After addition of the catalyst, reaction mixture was stirred for 12 h at 85°C. The reaction was terminated by addition of excess ethyl vinyl ether (2 ml). Resulting polymer (P2) was precipitated in cold methanol and filtrated. Same reactions were also applied for PEG modification of P1, resulting in P3.

Ring Opening Metathesis Polymerization of P1

A Schlenk reactor was charged with P1 (0.10 g, M_n: 4000 Da) in CH_2Cl_2 (1 ml). Grubbs 3rd generation catalyst (0.01 g, 0.011 mmol) dissolved in CH_2Cl_2 (1 ml) was added to the reaction mixture. Gelation occurred within 1-2 hours. Reaction mixture was kept under same conditions for 24 h to make sure for the termination of gelation reaction.

RESULTS and DISCUSSION

Optimum reaction conditions were investigated for the polymerization of 5-norbornene-2,3-dicarboxylate, 5-norbornene-2,3-dicarboxylate, 5-norbornene-2,3-dicarboxylic acid with 1,6-hexanediol in the presence of tin(II) ethylhexanoate, titanium (IV) isopropoxide and 1,5,7-triazabicyclodecene (TBD) (Scheme 1).

The optimal polymerization reaction found to proceed at 120°C with a catalytic loading of 1% $Sn(Oct)_2$ at reduced pressure (40 Torr) for 24h. The results were listed in Table 1. Polyesters with varying M_n values between 2000-11000 Da. All polymers are at viscously oil form at room temperature. ^{1}H NMR spectrum of P1 can be seen in Figure 1. Olefinic proton signals of norbornene ring appeared at 6.17 ppm. -CH_2COO- group of aliphatic fragment was observed at 3.86-4.00 ppm as multiplets. Other norbornene protons were observed between 3.40-3.09 and 1.29-.1.54 ppm. Aliphatic fragment of polymer showed signals at 1.29-1.54 ppm. ^{13}C NMR spectrum of P1 showed a singlet peak at 172.50 ppm indicating the presence of -C=O group. Olefinic carbon signals appeared at 134.90 ppm (Figure 2). A second olefinic peak appeared at 137.78 ppm, which belongs to the norbornene unit of polymer chain end-group. -OCH_2 signal was appeared at 64.29 ppm, Differential Scanning Calorimetry (DSC) analysis of P1 showed a glass-transition temperature (T_g) at -19.70°C. The olefinic moiety of polyester chains allows one to modify polymer via olefin metathesis reactions. The integration of several functional groups to polymer chains extend the applications of these polyester based materials. P1 was modified using cross-metathesis reactions. Olefinic norbornene moiety of P1 was reacted with methylacrylate and allyl poly(ethyleneglycol); allyl-PEG. Grubbs 1st generation (G1), Grubbs 2nd generation (G2), Grubbs 3rd generation (G3) and Hoveyda-Grubbs 2nd generation (HG2) catalysts were used in olefin metathesis reactions of P1. In order to optimize the reaction conditions; several reaction parameters such as; temperature, catalytic loading %, olefin/polyester ratio and solvent effect were investigated in details.

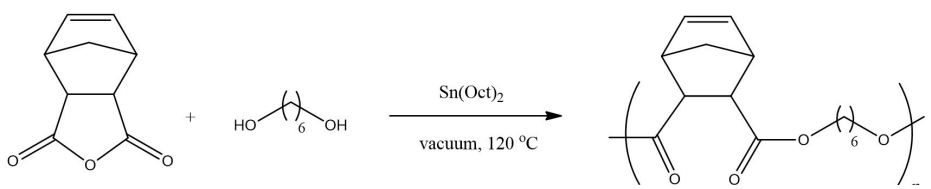

Scheme 1. Polycondensation reactions.

Table 1. Polycondensation reactions (P1).

Entry	Catalyst	Catalyst (%)	M_n (GPC)(Da)[a]	PDI[a]	Yield (%)
1	TBD	0.5	11200	2.4	80
2	TBD	1	6000	2.1	90
3	TBD	2	4000	2.0	95
4	$Sn(Oct)_2$	0.5	8700	2.2	85
5	$Sn(O_ct)2$	1	5500	2.1	90
6	$Sn(Oct)_2$	2	4100	1.9	94
7	$Ti(O\text{-}i\text{-}Pr)_4$	0.5	8200	2.2	75
8	$Ti(O\text{-}i\text{-}Pr)_4$	1	6100	2.1	85
9	$Ti(O\text{-}i\text{-}Pr)_4$	2	3700	1.7	88

a: Determined by GPC analysis in THF (1.0 ml/min) against lineer poly(methylmethylacrylate) standarts.

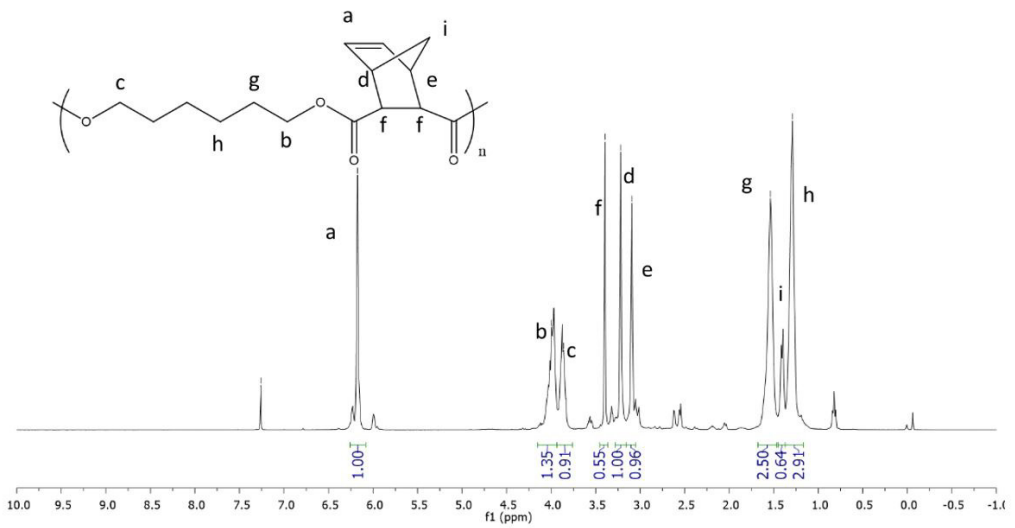

Figure 1. ^1H NMR spectrum of P1.

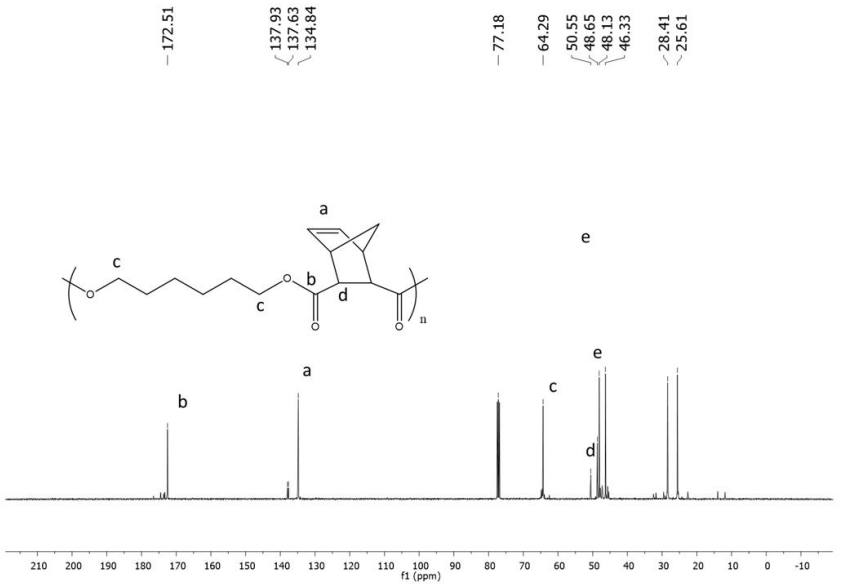

Figure 2. ^{13}C NMR spectrum of P2.

The olefinic moiety of polyester chains allows one to modify polymer via olefin metathesis reactions. The integration of several functional groups to polymer chains extend the applications of these polyester based materials. P1 was modified using cross-metathesis reactions. Olefinic norbornene moiety of P1 was reacted with methylacrylate and allyl poly(ethyleneglycol); allyl-PEG. Grubbs 1st generation (G1), Grubbs 2nd generation (G2), Grubbs 3rd generation (G3) and Hoveyda-Grubbs 2nd generation (HG2) catalysts were used in olefin metathesis reactions of P1. A set of terminal olefins, methyl acrylate, methyl end capped poly(ethylene glycol) Mn: 500 Da), allyl bromide and acrylic acid was chosen for ring-opening cross metathesis (ROM-CM) reactions. Well-known ruthenium metathesis initiators; Grubbs 1st (G1), 2nd (G2) and 3rd (G3) and Hoveyda-Grubbs 2nd generation (HG2) complexes were employed in order to find the best performing catalyst. First model reaction was carried out using methyl acrylate as cross-metathesis partner and P1 in toluene at 80°C in the presence of 1 % G1, G2, G3 or HG2 (Scheme 2).

The catalysts were compared in means of thermal stability, robustness and activity. Among the tested catalysts HG2 was chosen as best catalyst in means of conversion, selectivity and stability. After 24h of intense stirring at 80°C, reaction was terminated by addition of excess ethyl vinyl ether to reaction media and stirred for an additional 30 min. Polymer was precipitated in cold-methanol. Isolated polymer was labelled as P2. The conversion was determined by ^{1}H NMR by evaluating olefinic proton signals of norbornene and the side-groups of resulting cyclopentane ring. As it can be concluded from ^{1}H NMR spectrum, ROM-CM reaction of P1 with methyl acrylate proceeded with di-substitution of cyclopentane ring (Figure 3) with full conversion.

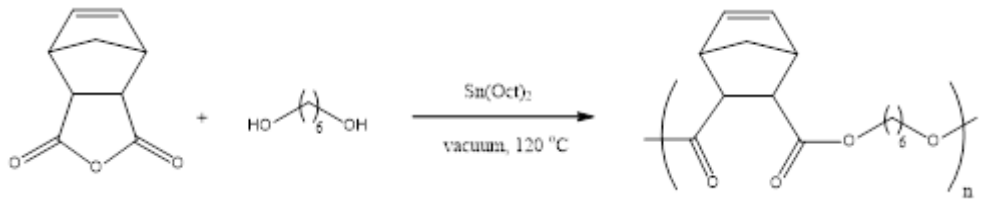

Scheme 2. Synthesis of P2.

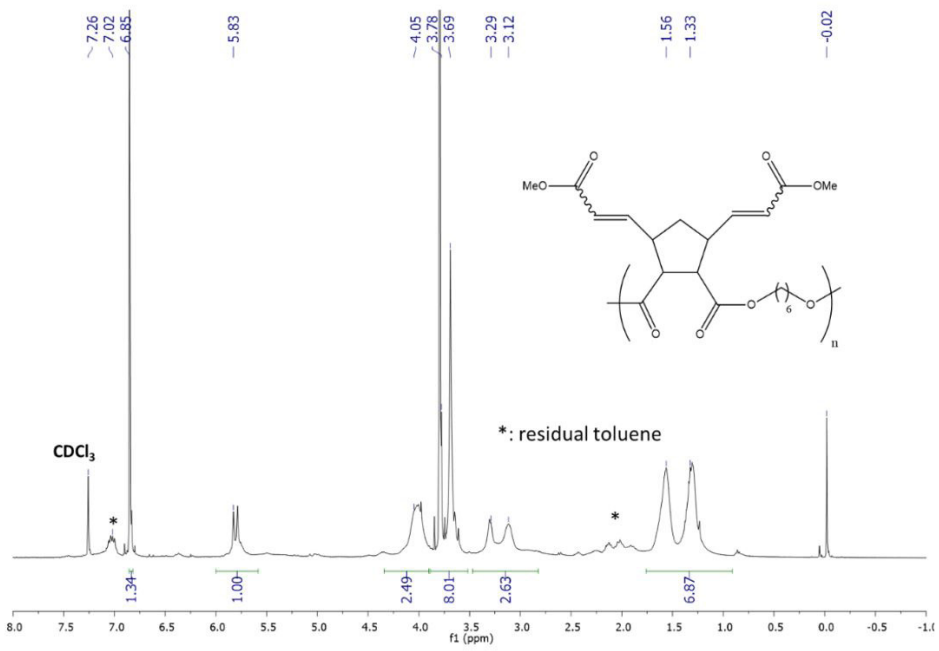

Figure 3. ^{1}H NMR spectrum of P2.

Olefinic proton signals were observed at 6.85 (2H, d, J=) and 5.83 (2H, d, J=) ppm, indicating predominant trans-configuration. $-OCH_2-$ group appeared at 4.05 ppm (4H, as multiplet) and 3.78 ppm. $-OCH_3$ group was observed at 3.69 ppm. Although promising results were obtained with methyl acrylate, modification of P1 with other olefins; allyl bromide and acrylic acid were failed due to catalyst decomposition. All catalysts; G1, G2, G3 and HG2 were poisoned in the presence of these olefinic materials. In the search for water soluble polyester derivatives, we used methyl end capped allyl-PEG (500 Da) for modification of P1 via ROM-CM (Scheme 3). The reaction was carried out at predetermined optimum reaction conditions that for P2. Once the reaction is completed, P3 was isolated by pouring the reaction mixture to diethyl ether and stored at -24°C overnight for precipitation.

^{1}H NMR results showed that norbornene moiety underwent ROM-CM reactions to form vinyl substituted cyclopentane ring (Figure 4). Vinylic double bond proton peaks appeared at 5.01-5.12 ppm as multiplets, hydrogen atoms bonded to PEG substituted vinyl group appeared at 6.05-5.71 ppm. Hydrogens, the vinyl neighbouring ones, were appeared at 3.85 ppm. The repeating group of PEG ($-OCH_2CH_2-$) were appeared at 3.47 ppm as a very intense peak. $-OCH_2$ group of polyester chain was observed at 3.20 ppm.

The solubility of P1, P2 and P3 was compared in Table 2. As it can be seen in Table 2, P1 and

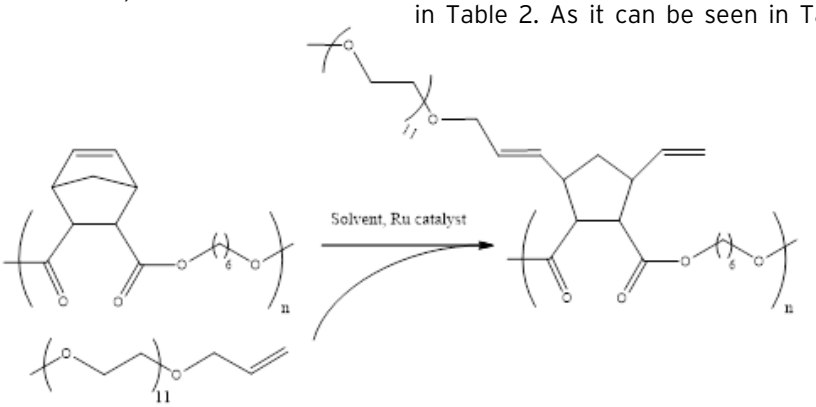

Scheme 3. Synthesis of P3.

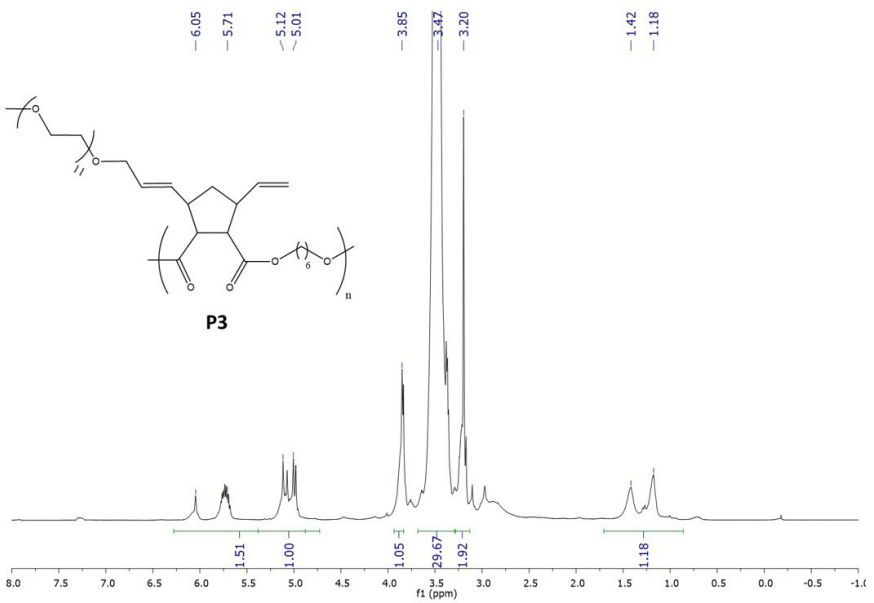

Figure 4. ^{1}H NMR of P3.

P2 is readily soluble in common organic solvents such as toluene, tetrahydrofuran, dichloromethane, chloroform and slightly soluble in acetone and insoluble in hexane and water. P3 is soluble in water and common organic solvent; dichloromethane, chloroform, toluene, THF and insoluble in n-hexane.

Following the modification P1 with allyl PEG group (P3), the glass transition temperature (T_g) was reduced from -13.20°C to -19.70°C due to the contribution of PEG group on overall conformational flexibility of polymer structure.

Table 2. Solubility of polyesters (P1, P2 and P3).

Entry[a]	CH_3OH	$CHCl_3$	CH_2Cl_2	Acetone	Toluene	H_2O	THF	Hexane
P1	-	+	+	=	+	-	+	-
P2	-	+	+	=	+	-	+	-
P3	+	+	+	=	+	+	+	-

a: -: non-soluble, =: partially soluble, +: soluble.

Table 3. Thermal stability of P1 after cross-linking.

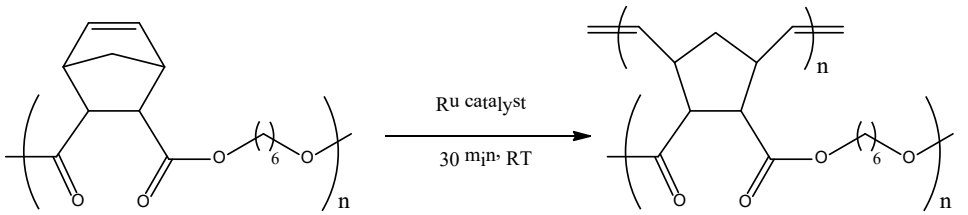

Entry	Catalyst	Weight loss (°C)[a]		
		5 (%)	10 (%)	40 (%)
1	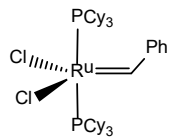	230	275	400
2	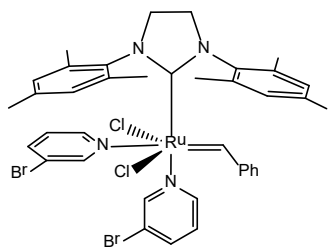	300	350	430
3	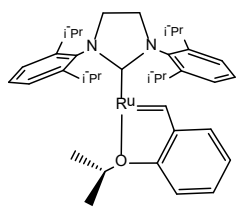	240	290	410
4	-	195	240	360

a: Determined by TGA.

On the next trial, ring-opening metathesis reactions of P1 was carried out using Grubbs 1st,3rd, Hoveyda-Grubbss 2nd generation catalysts to investigate the gelation behaviour of P1. It is well known in literature that highly strained norbornene ring can undergo ring opening metathesis reactions in the presence of Grubbs type ruthenium catalysts, forming oligomeric/polymeric vinly substituted cyclopentane rings. In the case of P1, which is a polyester derivative with repeating norbornene rings, norbornene group can undergo ring opening-cross metathesis via inter-molecular or intra molecular pathways, resulting in a cross-linked polymeric material. The effect of cross-link on thermal stability of the polymers was investigated using TGA analysis. As it can be seen in Table 3, the 5, 10 and 40% weight loss values shifted to higher temperature values, indicating the effect of cross-linking on overall structure of P1.

CONCLUSION

Unsaturated polyesters derived from polycondensation of 1,6-hexanediol and 5-norbornene-2,3-dicarboxylic anhydride were successfully modified via ring opening/cross metathesis reactions. It has shown that polymer properties (T_g, solubility, polarity) can be tuned by integrating functional groups via cross metathesis. In addition, thermoplastic like materials were synthesized from unsaturated polyesters using Grubbs type ruthenium metathesis catalysts. The effect of cross-link, which was exerted by ring-opening metathesis polymerization of norbornene moiety was demonstrated by TGA analysis.

References

1. K.E. Uhrich, S.M. Cannizzaro, R.S. Langer, K.M. Shakesheff, Polymeric systems for controlled drug release, Chem. Rev., 99 (1999) 3181-3198.
2. G. Chen, T. Ushida, T. Tateishi, Scaffold design for tissue engineering Macromol. Biosci., 2 (2002) 67-77.
3. C.M. Agrawal, K.F. Haas, D.A. Leopold, H.G. Clark, Evaluation of poly(L-lactic acid) as a material for intravascular polymeric stents, Biomaterials, 13 (1992) 176-182.
4. A. Lendlein, R. Langer, Biodegradable, elastic shape-memory polymers for potential biomedical applications, Science, 296 (2002) 1673-1676.
5. F.B. Bujans, R. Martinez, M.Y.Y. Pedram, P. Ortiz, H. Frey, Water-soluble polyesters from long chain alkylesters of citric acid and poly(ethylene glycol), Eur. Polym. J., 43 (2007) 1288-1301.
6. J.F. Lutz, Sequence-controlled polymerizations: the next Holy Grail in polymer science, Polym. Chem., 1 (2010) 55-62.
7. Y. Tachibana, T. Masuda, M. Funabashi, M. Kunioka, Chemical synthesis of fully biomass-based poly(butylene succinate) from inedible-biomass-based furfural and evaluation of its biomass carbon ratio, Biomacromolecules, 11 (2010) 2760-2765.
8. B.G. Amsden, G. Misra, F. Gu, H.M. Younes, Synthesis and characterization of a photo-cross-linked biodegradable elastomer, Biomacromolecules, 5 (2004) 2479-2486.
9. Y. Wang, G.A. Ameer, B.J. Sheppard, R.A. Langer, Tough biodegradable elastomer, Nat. Biotechnol., 20 (2002) 602-606.
10. A.H. Brown, V.V. Sheares, Amorphous unsaturated aliphatic polyesters derived from dicarboxylic monomers synthesized by Diels–Alder chemistry, Macromolecules, 40 (2007) 4848-4853.
11. R. Baumgartner, Z. Song, Y. Zhang, J. Cheng, Functional polyesters derived from alternating copolymerization of norbornene anhydride and epoxides, Polymer Chemistry, 6 (2015) 3586-3590.
12. A.B. Cherian, B.T. Abraham, E.T. Thachil, Modification of unsaturated polyester resin by polyurethane prepolymers, J. App. Polym. Sci., 100 (2006) 449-456.
13. C. Ai, G. Gong, X. Zhao, P. Liu, Determination of carboxyl content in carboxylated nitrile butadiene rubber (XNBR) after degradation via olefin cross metathesis, Polym. Test., 60 (2017) 250-252.
14. L. Fournier, C. Robert, S. Pourchet, A. Gonzales, L. Williams, J. Prunet, C.M. Thomas, Facile and efficient chemical functionalization of aliphatic polyesters by cross metathesis, Polym. Chem., 7 (2016) 3700-3704.
15. F. Sinclair, L. Chen, B.W. Greenland, M.P. Shaver, Installing multiple functional groups on biodegradable polyesters via post-polymerization olefin cross-metathesis, Macromolecules, 49 (2016) 6826-6834.
16. X. Michel, S. Fouquay, G. Michaud, F. Simon, J.M. Brusson, J.F. Carpentier, S.M. Guillaume, α,ω-Bis(trialkoxysilyl) difunctionalized polycyclooctenes from ruthenium-catalyzed chain-transfer ring-opening metathesis polymerization, Polym. Chem., 7 (2016) 4810-4823.
17. Y. Tachibana, M. Yamahata, K. Kasuya, Synthesis and characterization of a renewable polyester containing oxabicyclic dicarboxylate derived from furfural, Green Chem., 15 (2013) 1318-1325.
18. R.F. Fischer, Polyesters from epoxides and anhydrides, J. Polym. Sci. Part A: Polym. Chem., 44 (1960) 155-172.

Controlled Release of Vitamin C from Chitosan Nanoparticles

C Vitaminin Kitosan Nanoparçacıklardan Kontrollü Salımı

Research Article

Aylin Altınışık Tagaç[1]*, Önder Sarp[2], Kadir Yurdakoç[1]
[1]Science Faculty, Chemistry Department, Dokuz Eylul University, Buca, Izmir, Turkey.
[2]Health Sciences Institute, Department of Pharmaceutical Nanotechnology, Trakya University, Edirne, Turkey,

ABSTRACT

This work is consisted of two parts. The first was the synthesis and characterization of nanoparticles (ChNPs) from Chitosan, a natural biopolymer. In the second part, preparation of Vitamin C loaded ChNPs and release of vitamin C from the loaded nanoparticles were investigated. ChNPs were synthesized according to the ionic gelation method and sodium tripolyphosphate (TPP) was used as the crosslinking agent. The particle size distribution of the synthesized ChNPs was determined by using Zeta Sizer. Surface morphologies and crystal structures of the nanoparticles were investigated by Scanning Electron Microscopy (SEM) and X- ray diffraction (XRD) analysis, respectively. Structural analysis and thermal properties of ChNPs were also investigated by Fournier Transform Infrared Spectroscopy (FTIR) and thermogravimetric analysis (TGA), respectively. Release porofile of the Vitamin C loaded nanoparticles at same time were determined. As a result, average particle size of the ChNPs was measured as 10 nm and loading efficiency of the ChNPs was calculated as 86% with very high vitamin C concentration. Finally, the release mechanism of vitamin C from nanoparticles was determined to be controlled by diffusion and swelling.

Key Words
Chitosan nanoparticles, ionic gelletion,release kinetic, vitamin C.

ÖZ

Bu çalışma iki aşamadan oluşmaktadır. Birinci aşama kitosanın nanoparçacıkların (ChNPs) sentezi ve karakterizasyonudur. İkincisi aşama, C vitamin yüklü ChNPS eldesi ve C vitamininin salım kinetiğinin incelenmesidir. ChNPs iyonik jelleşme yöntemine göre sentezlenmiştir. Sodyum tripolifosfat (TPP) çapraz bağlayıcı olarak kullanılmıştır. Sentezlenen ChNPs örneklerinin tanecik boyutu dağılımları, yüzey morfolojileri ve kristal yapıları sırasıyla Nanosizer, Taramalı Electron Mikroskobu (SEM) ve X-ışını difraktometresi (XRD) ile incelenmiştir. Hazırlanan ChNPs örneklerinin yapısal analizleri ve termal özellikleri sırasıyla, Fourier Transform Infrared (FTIR) spektrofotometresi ve termal gravimetrik analiz ile incelenmiştir. Aynı zamanda C vitamin yüklü ChNPs örneklerinin salım profilleri belirlenmiştir. Çalışmaların sonucunda, ChNPs örneklerinin ortalama parçacık boyutları 10 nm olarak ölçülmüştür. C vitamini yükleme verimi %86 C vitamini derişimi olarak hesaplanmıştır. Son olarak, C vitaminin ChNPs örneklerinden salım mekanizmasının difüzyon ve şişme kontrollü olduğu belirlenmiştir.

Anahtar Kelimeler
Kitosan nanoparçacık, iyonik jelleşme, salımı kinetiği, C vitamin.

Article History: Received: Jun 08, 2017; Revised: Oct 18, 2017; Accepted: Dec 18, 2017; Available Online: Feb 20, 2018.

DOI: 10.15671/HJBC.2018.221

Correspondence to: A. Altinisik Tagac, Science Faculty, Chemistry Department, Dokuz Eylul University, Buca, Izmir, Turkey.
Tel: +90 232 3017908 Fax: +90 232 453 41 88 E-Mail: aylin.altinisik@deu.edu.tr

INTRODUCTION

Chitosan, produced from Chitin, among the entire natural, is one of the most promising biopolymers. Chitosan is a linear copolymer which is consisted of both 2-acetamido-2-deoxy-β-d-glucan and 2-amino-2-deoxy-β-d-glucan units. These two groups with interesting physicochemical and biological properties provide the important features for biomedical applications. For example, Chitosan has been used as drug systems in many different forms such as film [1], microcapsule [2], nanoparticles [3] etc. Within these forms, many studies have been carried out to obtain chitosan nanoparticles [4-8]. Many syntheses including electrostatic complexes have been developed [9-13]. Electrostatic complexation method appears to be very charming since it allowed to detail nanoparticles nanoparticles i) with sizes in the nanometer range, and narrow size distributions, ii) in a mild environment (such as an aqueous medium). In this process, toxic cross-linking agent such as glutaraldehyde is not used to stabilize the nanoparticles. Chitosan nanoparticles formation by electrostatic complexation is depended on the cationic sites ($-NH_3^+$) available the polymer chains. If the anionic species such as citrate, sulphate or (poly)phosphate uses for the complexation of chitosan chains are molecules, the method is more specifically mentioned as "ionic gelation method" [7]. Up until now, to prepare the chitosan nanoparticles, lots of studies have been carried out with ionic gelation method, particularly by using sodium tripolyphosphate (TPP) as ionic agent [11-13].

On the other hand, Vitamin C is an imperative nutrient required to maintain the physiological process of people and some animals [14,15]. Even, Vitamin C is one of the most significant antioxidants that may decrease the risk of cancer by using various mechanisms [14,16-18]. In the same time, vitamin C is one of the most significant antioxidants that may decrease the risk of cancer by using various mechanisms [19]. This is an important anti-oxidant that may reduce the risk of cancer by neutralizing reactive oxygen species or other free radicals that can damage DNA [2,16]. Besides, vitamin C is also used in food or food additives and it has been shown to decrease LDL cholesterol in some patients [20-22]. Therefore, nano-loading systems and the release of vitamin C should continue to be developed in many applications, from food to biomedical applications.

This study was aimed to prepare and characterize ChNPs. At same time, another aim of this study was in order to load with vitamin-C to ChNPs and to investigate release of vitamin C from ChNPs.

MATERIALS and METHODS

Materials

Chitosan (viscosity, 200-400 mPa.s, 1% in acetic acid), Vitamin C, acetic acid (CH_3COOH, glacial) as used solvent and Sodium tripolyphosphate as used crosslinker were all purchased from Sigma Aldrich. All the chemicals were used without any further purification.

Preparation of the ChNPs

The ChNPs were synthesized based upon ionic gelation method by using chitosan and TPP. Briefly, chitosan (1 mg/ml) was dissolved in 1% (v/v) acetic acid solution and NaTPP (1.75 mg/ml) were dissolved in deionized water to obtain solutions. The ChNPs were synthesized with the addition of prepared TPP solution into chitosan solution via mechanical stirring (750 rpm) at room temperature. The vitamin-C loaded- ChNPs were similarly prepared by using a chitosan solution containing the drug. 25 mg Vitamin C dissolve in chitosan solution (1 mg/ml) and prepared TPP solution (1.75 mg/ml) was added into this chitosan solution in which vitamin C was dissolved. Formed nanoparticles were reserved from solution by centrifuge at 1000 rpm for 10 min.

Determination of Loading Efficiency

Vitamin C (25 mg) loaded ChNPs were dissolved in 100 ml 0.1 N HCl. The sample was centrifuged at 10000 rpm within 10 min and then vitamin C content was analyzed by measuring the absorbance at 244 nm (λ_{max} of vitamin C in 0.1 N HCl) after suitable dilution using an UV spectrophotometer (PG instrument T80/80+).

$$\text{Loading efficiency (\%)} = ([\text{vitamin C}]_c / [\text{vitamin C}]_t) \times 100 \quad (1)$$

Characterization of the ChNPs

The morphology of the samples was monitored by scanning electron microscopy (SEM). The images were obtained using 10 kV accelerating voltage. SEM images were taken at different magnifications (in the range of 1.000× and 10.000×) using Toledo University/Toledo-Ohio/US in JEOL JSM-7500F SEM instrument.

The particle sizes were determined using Zetasizer (MALVERN Zetasizer Nano Series Nano-S).

The Chitosan and ChNPs were characterized structurally by Fourier transform infrared (FTIR) spectroscopy. FTIR was used to investigate the interaction of Chitosan, TPP, and NPs. FTIR spectra were recorded by a Perkin- Elmer FTIR spectrophotometer Spectrum BX-II in the range 4,000–400 cm^{-1} with the sum of 20 scans at a resolution of 4 cm^{-1}.

The thermal properties of the prepared samples were also analyzed with a Perkin-Elmer Diamond TG/ DTA instrument. TG/DTG profiles were performed from 30 to 600°C at a heating rate of 10°C/min under N_2 flow of 10 mL/min.

In vitro release studies

Vitamin C concentration was determined using UV-Vis spectrophometrically the absorbance at 265 nm ($\lambda_{\mu ax}$ of vitamin C in PBS buffer 7.4) after suitable dilution from a calibration curve. In the experiment of determination of vitamin C concentrations, UV spectrophotometer (PG instrument T80/80+) was used. Chitosan nanoparticles equivalent to 25mg of vitamin C were taken into a cellulose dialysis bag (previously soaked in dissolution medium) containing 30ml of dissolution medium to suspend the ChNPs in the dissolution medium. The in vitro release studies of vitamin C were carried out at rinsing bath of 100 rpm in 500 mLof phosphate buffer (pH 7.4 and 25°C). 1 ml of release medium was taken at pre-determined time intervals for determining content of vitamin C. An equivalent volume of fresh dissolution medium was added in release medium after every measurement.

RESULTS and DISCUSSIONS

Characterization of the ChNPs

The ionic gelation using TPP as ionic agent is nowadays an appropriate method to prepare, monodisperse, and nanosize chitosan particles [11-13]. The known ionic gelation method has been composed of the ionic interaction between the protonated amino group (-NH_3) of CS solution and the phosphate groups (-PO_4^{3-}) of the anionic TPP [11-13]. Synthesized by ionic gelation method the smallest particles up to now have been obtained in this study. The avarage size of ChNPs was in rage of 20-30 nm with a broad size distruption as shown in zeta sizer output in Figure 1.

On the other hand, SEM images (Figure 2) are used to characterize the morphology and size of ChNPs. According to the SEM images of six different parts (area) of ChNPs, it has observed that all parts of ChNPs morphology has been continuous, spherical, uniform and individual particles with the approximately diameter of 10 nm with a magnification value of 300,000X. Due to the sample preparation procedure at zeta sizer, ChNPs might have aggregated together and size of nanoparticles may higher than SEM results. Another characterization method is X-Ray powder

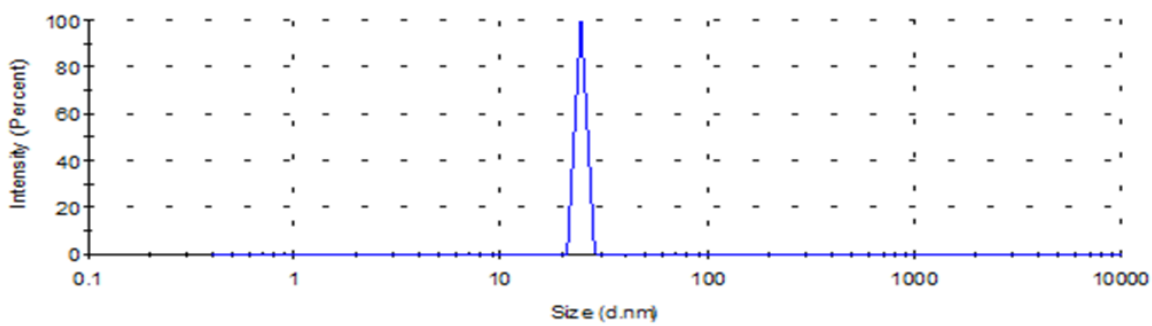

Figure 1. Zeta sizer diagram of ChNPs.

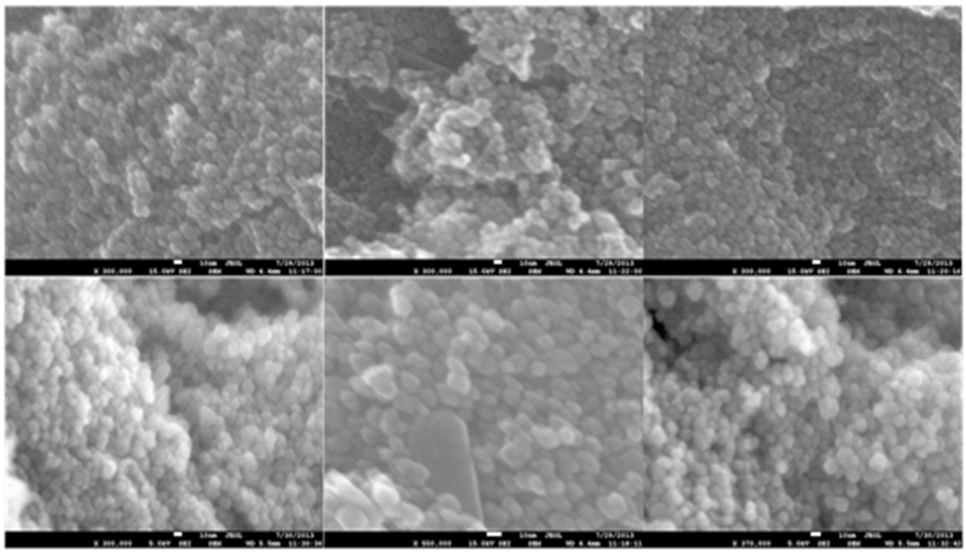

Figure 2. SEM analysis of ChNPs.

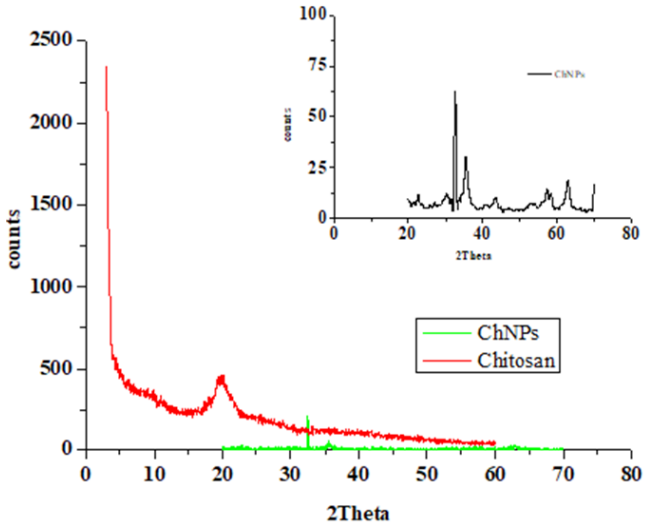

Figure 3. XRD pattern of Chitosan and ChNPs.

diffraction whose patterns of Chitosan and ChNPs are shown in Figure 3.

There is only one strong peak in the diffractogram of Chitosan at 2θ = 20°, indicating the high degree of crystallinity of Chitosan, its crystal lattice constant ***CrI*** corresponding to 45% [1]. Two intense narrow peaks at 2θ = 33.28° and 19.32° for TPP [23] were also observed. These peaks are related with TPP and exhibiting a high degree of crystallinity. However, in this study, two broad peaks were observed at 2θ = 32.62° and 35.56 in Figure 3, for ChNPs indicating, the crystalline nature of CS was lost due to its cross linking with TPP. Ionic interactions exist in this reaction namely an intense electrostatic interaction between the positively charged amine groups of CS and negatively charged TPP.

In accordance with Debye–Scherrer Equation, the ChNPs had an average diameter of 6.45 nm which was appropriate to SEM result for ChNPs.

In the physicochemical characterization methods, the result of FTIR spectra of chitosan and ChNPs are shown in Figure 4. The absorption bands in the spectrum of Chitosan around 1640 and 1560 cm^{-1} are referred to asymmetric C=O stretching (Amide I) and N–H bending (Amide II) of acetamido groups, respectively [1]. ChNPs

are showed the presence of the P=O and P-O groups at the frequency of 1203 cm^{-1} and 1239 cm^{-1},respectively [23,24]. In the case of ChNPs after addition of TPP (Figure 4), the bant of amide-I was shifted to from 1653 cm^{-1} to 1664 cm^{-1} and N-H band in amines was shifted from 1561 cm^{-1} (Amide-II) to 1549 cm^{-1} representing the electrostatic interactions between the $-NH_3$ groups in CS with the phosphoric groups in TPP. Furthermore, there would also be shifting at the broad band above 3465 cm^{-1} and 3186 cm^{-1} corresponding to N-H and O-H bonds, respectively [23,24].

The thermal properties of Chitosan and ChNPs were determined by TG analysis as shown in Figure 5 and the thermal analysis results were presented in Table 1. There were two degradation steps on the thermograms. In Table

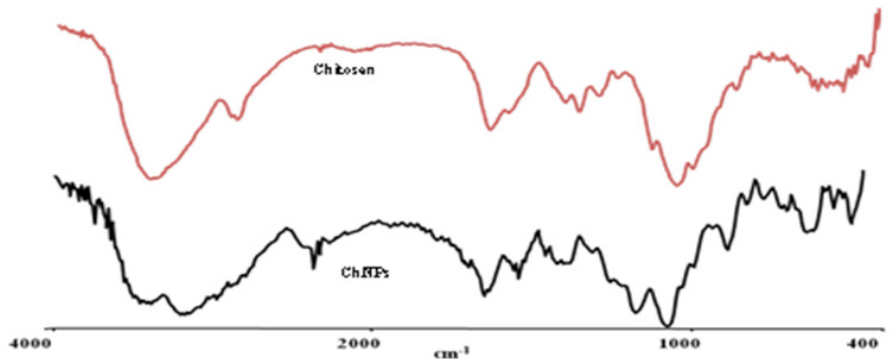

Figure 4. FTIR spectra of chitosan and ChNPs.

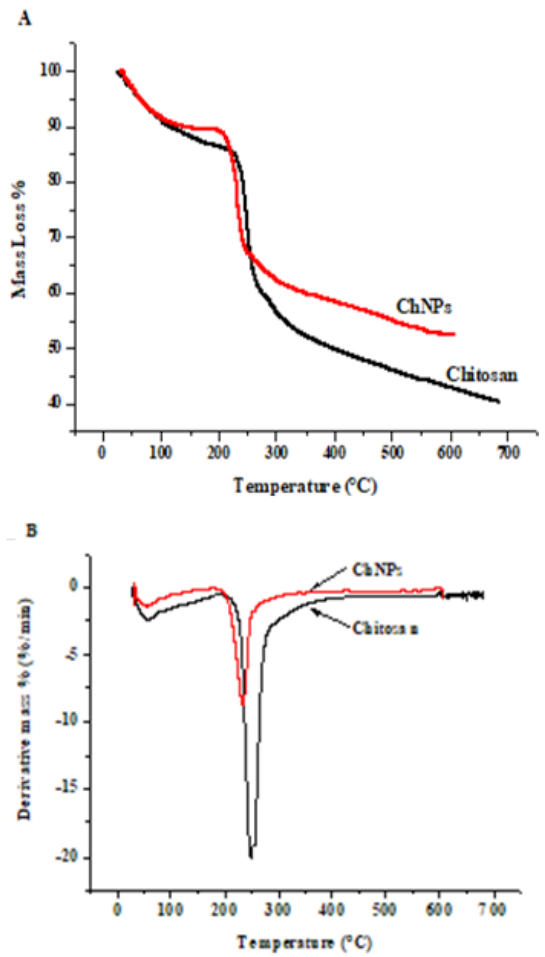

Figure 5. Thermogram of chitosan and ChNPs, TG curve (A), DTG curve (B).

Table 1. Thermal analysis results of Chitosan and CsNPs.

	TG/DTG							
	1st step		2nd step		DSC			
	Mass loss (%)	T (°C)	Mass loss (%)	T (°C)	Tg (°C)	Tm (°C)	Td (°C)	ΔH (J/g)
Chitosan	13	56.6	46.1	250	25	-	251	-48.5
ChNPs	10	55.5	36.8	234	-	61	238.9	-36.4

Table 2. Particle size and loading efficiency relationship.

Nanoparticles size (nm)	Loading Efficiency (%)	Ref
198	69.02	[25]
153	≤50	[26]
40	n.d	[27]
100	60-65	[28]
20	20	[29]
260	10 (theoretical)	[30]
140	Nd.	[31]
250	80	[32]
10	86	In this study

*nd: not determined

1, the first step of mass loss was due to moisture at same temperature. On the other hand, the thermograms of ChNPs, second step mass loss was observed at 234°C in Figure 5. This degradation (36.8%) refers to the degradation of ChNPs. Besides, degradation temperature of chitosan was determined as 250°C and the mass loss was 46.1% at that temperature. It is obvious that both the degradation temperature and the amount of mass loss were decreased.

Kinetic Study

Vitamin C (25 mg) loaded ChNPs was used to evaluate the loading efficiency. According to the Equation 1, the loading efficiency has determined as 86%. This high efficiency is due to the low particles size. The particle size was almost 100 nm in studies carried out up to now and it has observed that the loading efficiency is lower as well. For the comparison, same experimental data obtained from cited references given in Table 2.

The five different release kinetic models have used to determine the suitable Vitamin-C release kinetic model. The results of kinetic study have given in Table 3. According to the Table 3, it can be seen clearly that first order kinetic model and Korsemeyer-Peppas model has been suitable for vitamin C release from ChNPs. The graphical peresentaion of the kinetic madels were shown in Figure 6.

First order model describes absorption and/or elimination of some drugs. This model can be used to describe the drug dissolution in pharmaceutical dosage forms such as those containing water-soluble drugs in porous matrices. On the other hand, Korsmeyer et al. [33,34] derived a simple relationship which described drug release from a polymeric system. The first 60% drug release data were applied in Korsmeyern Peppas model to find out the mechanism of drug release. The n value in Korsmeyer Equation is used to determine different release characterize for polymeric matrices. In this model, the n value identifies the release mechanism as described in Table 4. In this study, the n value has calculated as 0.7885 in the Table 4. According to the calculated n value, it is obviously seen that the release of vitamin C depends on swelling and diffusion control mechanism.

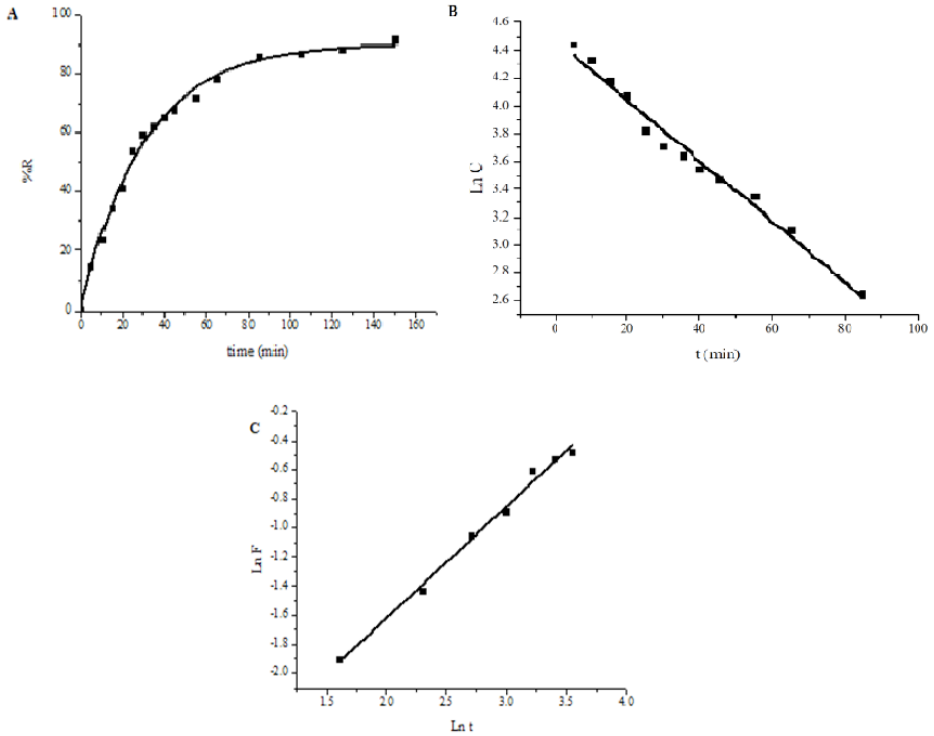

Figure 6. Results of release kinetic study; Release time (A), First order model (B) and Korsemeyer-Peppas model (C).

Table 3. Results of release kinetic study [33].

Kinetic Model	Q_o(mg)	K (mg/min)	R^2
Zero order			
$Q_t = Q_o + K_0 t$	4.14	0.2160	0.8595
First order			
$InC = InC_o - Kt$	19.64	0.0219	0.9827
Hixon-Crowell			
$Q_t^{1/3} = Q_o^{1/3} - Kt$	1.28	0.0155	0.9545
Higuchi			
$Q = K.t^{1/2}$	-	2.1811	0.9571
	n	K (mg/min)	R^2
Korsemeyer-Peppas			
$F = M_t/M = K.t^n$	0.7885	24.66	0.9943

Table 4. Interpretation of diffusional release mechanisms.

Release Exponent (n)	Drug transport mechanism	Rate as function of time
0.5	Fickian diffusion	$t^{-0.5}$
0.45 < n=0.89	Non- Fickian transport	t^{n-1}
0.89	Case II transport	Zero order release
Higher than 0.89	Super case II transport	t^{n-1}

CONCLUSION

In this study, Chitosan nanoparticles were successfully synthesized by ionic gelation method and confirmed with FTIR spectra. The improvement of crystal structure of ChNPs was estimated from XRD patterns of ChNPs. The particle size was also calculated to be 6.45 nm from XRD results. This result also has been supported by SEM images which the particles size determined as around 10 nm. The loading efficiency of vitamin C in synthesized nanoparticles has been determined as 85%. This value is stated as high efficiency for drug loading system. Release of vitamin C from CsNPs has determined as diffusion and swelling control release mechanisms by using different kinetic models.

References

1. A. Altinisik, K. Yurdakoc, Chitosan/poly(vinyl alcohol) hydrogels for amoxicillin release, Polym. Bull., 71 (2014) 759-774.
2. K.G.H. Desai, H. J. Park, Encapsulation of vitamin C in tripolyphosphate cross-linked chitosan microspheres by spray drying, J. Microencapsul., 22 (2005) 179-192.
3. M. Dogan, N. Ugurlu, F. Yulek, Ketorolac tromethamine loaded chitosan nanoparticles as a nanotherapeutic system for ocular diseases, J. Biol. Chem., 41 (2013) 81-86.
4. L. Bugnicourt, L. Catherine, Interests of chitosan nanoparticles ionically cross-linked with tripolyphosphate for biomedical applications, Prog. Polym. Sci., 60 (2016) 1-17.
5. K.A. Janes, P. Calvo, M.J. Alonso, Polysaccharide colloidal particles as delivery systems for macromolecules, Adv. Drug. Deliv. Rev., 47 (2001) 83-97.
6. M. Garcia-Fuentes, M.J. Alonso, Chitosan-based drug nanocarriers: where do we stand?, J. Control. Release., 161 (2012) 496-504.
7. A. Grenha, Chitosan nanoparticles: a survey of preparation methods, J. Drug Target., 20 (2012) 291-300.
8. M. de la Fuente, et al, Chitosan-based nanostructures: a delivery platform for ocular therapeutics, Adv. Drug Deliv. Rev., 62 (2010) 100-117.
9. B. Sarmento, et al, Development and comparison of different nanoparticulate polyelectrolyte complexes as insulin carriers, Int. J. Pept. Res. Ther., 12 (2006) 131-138.
10. P. Calvo, et al, Novel hydrophilic chitosan-polyethylene oxide nanoparticles as protein carriers, J. Appl. Polym. Sci., 63 (1997) 125-132.
11. L. Bugnicourt, P. Alcouffe, C. Ladavière, Elaboration of chitosan nanoparticles: favorable impact of a mild thermal treatment to obtain finely divided, spherical, and colloidally stable objects, Coll. Surf. A., 457 (2014) 476-486.
12. W. Fan, W. Yan, Z. Xu, H. Ni, Formation mechanism of monodisperse, low molecular weight chitosan nanoparticles by ionic gelation technique, Coll. Surf. B., 90 (2012) 21-27.
13. M. Hamidi, A. Azadi, H. Ashrafi, P. Rafiei, S. Mohamadi-samani, Taguchi orthogonal array design for the optimization of hydrogel nanoparticles for the intravenous delivery of small-molecule drugs, J. Appl. Polym. Sci., 126 (2012) 1714-1724.
14. E. Esposito, F. Cervellati, E. Menegatti, C. Nastruzzi, R. Cortesi, Spray dried Eudragit microparticles as encapsulation devices for vitamin C, Int. J. Pharm., 242 (2002) 329-334.
15. S.Y. Shiau, T.S. Hsu, Quantification of vitamin C requirement for juvenile hybrid tilapia, Oreochromisniloticus=*Oreochromis aureus*, with L-ascorbyl-2 monophosphate-Na and L-ascorbyl-2-monophosphate-Mg, Aquaculture, 175 (1999) 317-326.
16. E.J. Jacobs, C.J. Connell, A.V. Patel, A. Chao, C. Rodriguez, J. Seymour, et al., Vitamin C and vitamin E supplement use and colorectal cancer mortality in a large American cancer society cohort, Cancer Epidemiol. Biomar. Prev,, 10 (2001) 17-23.
17. G. Shklar, J.L. Schwartz, Ascorbic acid and cancer, Subcell. Biochem., 25 (1996) 233-247.
18. H.M. Zhang, N. Wakisaka, Vitamin C inhibits the growth of a bacterial risk factor for gastric carcinoma: *Helicobacter pylori*, Cancer, 80 (1997) 1897-1903.
19. A. Alishahi, et al., Shelf life and delivery enhancement of vitamin C using chitosan nanoparticles, Food Chem., 126 (2011) 935-940.
20. M. Mietus-Snyder, M. J. Malloy, Endothelial dysfunction occurs in children with two genetic hyperlipidemias: improvement with antioxidant vitamin therapy, J. Pediatr., 133 (1998) 35-40.
21. M. Jeserich, T. Schindler, M. Olschewski, M. Unmüssig, H. Just, U. Solzbach, Vitamin C improves endothelial function of epicardial coronary arteries in patients with hypercholesterolaemia or essential hypertension—assessed by cold pressor testing, Eur. Heart J., 20 (1999) 1676-1680.
22. B. Mosinger, Higher cholesterol in human LDL is associated with the increase of oxidation susceptibility and the decrease of antioxidant defence: experimental and simulation data, BBA Mol. Bas., 1453 (1999) 180-184.
23. H. Ravi, V. Baskaran, Biodegradable chitosan-glycolipid hybrid nanogels: A novel approach to encapsulate fucoxanthin for improved stability and bioavailability, Food Hydrocoll., 43 (2015) 717-725.
24. S. Vimal, et al., Synthesis and characterization of CS/TPP nanoparticles for oral delivery of gene in fish, Aquaculture., 358 (2012) 14-22.
25. J. Gu, K. Al-Bayati, E.A. Ho, Development of antibody-modified chitosan nanoparticles for the targeted delivery of siRNA across the blood-brain barrier as a strategy for inhibiting HIV replication in astrocytes, Drug. Deliv. Transl. Res., (2017) 1-10.
26. K. Santhi, et al., In-vitro Characterization of chitosan nanoparticles of fluconazole as a carrier for Sustained ocular delivery, J. Nanosci. Nanotechnol., 7 (2017) 41-50.
27. Q. Lifeng, et al. Preparation and antibacterial activity of chitosan nanoparticles, Carbohydr. Res., 339 (2004) 2693-2700.

28. S. Mitra, et al. Tumour targeted delivery of encapsulated dextran–doxorubicin conjugate using chitosan nanoparticles as carrier, J. Control. Release., 74 (2001) 317-323.
29. Y. Xu, Y. Du., Effect of molecular structure of chitosan on protein delivery properties of chitosan nanoparticles, Int. J. Pharm., 250 (2003) 215-226.
30. K.A. Janes, et al., Chitosan nanoparticles as delivery systems for doxorubicin, J. Control. Release., 73 (2001): 255-267.
31. Q. Gan, et al., Modulation of surface charge, particle size and morphological properties of chitosan–TPP nanoparticles intended for gene delivery, Colloid. Surf. B Biointer., 44 (2005) 65-73.
32. Y. Pan, et al., Bioadhesive polysaccharide in protein delivery system: chitosan nanoparticles improve the intestinal absorption of insulin in vivo, Int. J. Pharm., 249 (2002) 139-147.
33. S. Dash, et al., Kinetic modeling on drug release from controlled drug delivery systems, Acta Pol Pharm, 67 (2010) 217-23.
34. R.W. Korsemeyer, R. Gurny, E.M. Doelker, P. Buri, N.A. Peppas, Mechanism of solute release from porous hydrophilic polymers, Int. J. Pharm., 15 (1983) 25-35.

DFT Studies of Carbon Structures Supported Vanadia Catalysts for Oxidative Dehydrogenation of Propane: Kinetic and Thermodynamic

Yoğunluk Fonksiyon Teorisi (DFT) ile Propanın Oksidatif Dehidrojenasyonu için Karbon Yapı Destekli Vanadyum Katalizörlerinin Çalışılması: Kinetik ve Termodinamik

Research Article

Abdollah Fallah Shojaei[1]*, Ali-Morad Rashidi[2], Mina Ghiasi[3], Robabe Mosavi[1]

[1]Department of Chemistry, Faculty of Sciences, University of Guilan, Rasht, Iran.

[2]Research Institute of Petroleum Industry (RIPI), Nanotechnology Research Center, Tehran, Iran.

[3]Department of Chemistry, Faculty of Physics & Chemistry, Alzahra University,Tehran, Iran.

ABSTRACT

The detailed mechanism for oxidative dehydrogenation of propane on the $^1VO_4(CH_3)_3$ surface has been studied in depth with density functional theory (DFT) calculations at the B3LYP level and standard split-valance basis set, 6-31+G*. Monomeric vanadia specie was considered and modeled as catalysis. In addition, the mechanisms of the two complete catalytic cycle, involving the regeneration of the reduced catalyst using O_2 gaseous have been reported. The reaction proceeds in two subsequent steps which at the first, one hydrogen abstracting by the vanadium of V= O1 group with about 48.35 cal/mol activation energy is the rate determining step. Subsequently, second intermediate has been formed through a bond formed between the propyl radical and O_2 atom (V-O2). In continue, the O1 atom abstracts one hydrogen atom from the methyl group with a 131.63 kcal/mol barrier to form propene by passing to second transition state. The results of our calculations have found that all the reactions involve vanadyl oxygen (V=O1), with the bridging oxygen (V-O-C) serving to stabilize the isopropyl radical intermediate.

Key Words

Vanadia, propane, oxidative dehydrogenation, DFT calculation.

ÖZ

Bu çalışmada propanın $^1VO_4(CH_3)_3$ yüzeyindeki oksidatif dehidrojenasyonu, bölünmüş valans temel kümesi 6-31+G* ve B3LYP seviyesinde Yoğunluk Fonksiyon Teorisi hesaplamaları ile incelenmiştir. Monomerik vanadyum türleri kataliz için gözönüne alınmış ve modellenmiştir. Bunlara ek olarak O_2 gazı kullanılarak yenilenen indirgenmiş katalizör içeren iki tamamlanmış katalitik döngü sunulmuştur. Tepkime iki alt basamakta ilerlemektedir; birinci basamakta bir hidrojen 48,35 cal/mol aktivasyon enerjisiyle V= O1 vanadyum grubu tarafından alıkonulur ve hız belirleyici basamaktır. Sonrasında propil radikali ve O_2 atomu arasında (V-O2) oluşan bağ dolayısıyla ikinci ara ürün oluşur. Devamında O1 atomu propen oluşumu ve ikinci geçiş haline ulaşmak için metil grubundan 131.63 kcal/mol enerjiyle bir hidrojen koparır. Sonuçların, bütün tepkimelerde izopropil ara radikali kararlı kale getirmek için vanadil oksijen (V= O1) ve köprüleme oksijeni (V-O-C) kullanıldığını göstermiştir.

Anahtar Kelimeler

Vanadyum, propan, oksidatif dehidrasyon, yoğunluk fonksiyonel teorisi.

Article History: Received: Jun 21, 2017; Revised: Oct 28, 2017; Accepted: Feb 08, 2017; Available Online: Feb 20, 2018.

DOI: 10.15671/HJBC.2018.216

Correspondence to: A.F. Shojaei, Department of Chemistry, Faculty of Sciences, University of Guilan, Rasht, Iran.

Tel: +98 911 232 3638 Fax: +98 337 40152 E-Mail: a.f.shojaie@guilan.ac.ir

INTRODUCTION

The oxidative dehydrogenation (ODH) of propane is a particular alternative to the direct catalytic dehydrogenation, which is the main process step in the highly efficient and technically mass production of many intermediates and petrochemicals such as acrylonitrile, propylene oxides and propylene. The catalytic activation of C-H bonds is of fundamental interest because it is the crucial step in important technological processes and in many enzymatic reactions [1]. In general, for producing the chemicals for polymer and fine organic synthesis, short-chain hydrocarbons, mainly ethane [2], propane [3] and butane [4,5] have been considered as substrates in oxidative dehydrogenation reactions. In propylene preparation, propane oxidation often serves as a model for carbon-catalyzed oxidation reactions. The following reaction is thermal cracking of propane with and without oxygen [6, 7]:

$$C_3H_8 \rightarrow C_3H_6 + H_2 \qquad \Delta H = +30 \text{ kcal/mol} \quad (1)$$

$$2C_3H_8 + 1/2\ O_2 \rightarrow C_3H_6 + H_2O \qquad \Delta H = -28 \text{ kcal/mol} \quad (2)$$

It should be noted that dehydrogenation of propane in propylene preparation is a conventional method which suffers from high-energy consumption, thermodynamic restrictions and pyrolysis side reactions such coke deposition. Applying dehydrogenation process in the presence of oxygen overcomes the mentioned above difficulties [8,9]. Propane is dehydrated to propylene under following oxidation dehydrogenation (ODH) conditions:

$$2C_3H_8 + O_2 \rightarrow 2C_3H_6 + 2H_2O \quad (3)$$

$$C_3H_8 + 5O_2 \rightarrow 3CO_2 + 4H_2O \quad (4)$$

$$2C_3H_6 + 9O_2 \rightarrow 6CO_2 + 6H_2O \quad (5)$$

$$4C_3H_8 + 2\,O_2 \rightarrow C_2H_4 + CO_2 + 2H_2O \quad (6)$$

$$2C_3H_6 + 3O_2 \rightarrow 2C_2H_4 + 2CO_2 + 2H_2O \quad (7)$$

Different supports have been used in oxidative dehydrogenation of propane including alumina, titania, vanadia, silica and so on [1,10-13]. Among various supports used as heterogeneous catalysts, carbon materials are in high interest due to their large surface area and chemical stability, which results in high active sites loading. Besides, this property assists their resistance in both acidic and basic media. Carbon nanotubes, graphene and porous graphene are the examples of carbon materials which are produced and exploited at industrial scales for various applications [14,15]. In this study, transition metal oxides, that is to say, supported vanadia, are studied as catalysts [16]. Supported vanadia is the most selective and active material because of its elevated activity and selectivity in ODH of light alkanes to alkenes. The reason for This outstanding property is vanadium can provide lattice oxygen in removing hydrogen from propane [9,17,18]. It is worth indicating that carbon materials and metal oxides present the same characteristics regarding their catalytic properties and surface structures, which make them great candidates to be used in ODH reactions [19]. So far, the effect of support and methods on preparation of vanadia supported materials has been investigated in some studies which convincing results have been released [20]. For example, V_2O_5 supported on TiO_2 is a promising catalyst for ODHP process [21]. Other supported for vanadium oxide such as Al_2O_3, TiO_2 are studied, as well [22-24]. Although substantial progress has been made in using carbon materials as catalyst support such as carbon nanotubes and graphene-supported catalysts [25] in ODH reactions. In order to have a better perspective about experimental laboratory researches and the mechanism of ODH, we have decided to take advantage of computational methods to check the possibility of the reaction and possible pathways, theoretically. In some studies the application of computational chemistry has been used to understand the catalytic reactions in details, thus, computational experiments have been applied on transition metal oxides for their surface structure and designing catalysts [26,27].

Among different computational methods, DFT is a common method in determining catalyst structure, explanation of spectroscopic information, investigation of reaction networks and mechanisms [1,4,28]. This information can provide useful information about the characteristics of catalysts such as the nature of active center and its catalytic activity. DFT method also declares the interaction between oxygen and carbon surfaces, edge sites and reaction

Figure 1. Presentation of monomeric and dimeric structures of tetrahedral VOx model system (S is CH_3 as support).

mechanism of oxidative dehydrogenation. The possible mechanism for ODH with SiO_2 supported vanadium oxide is reported by Rozanska et al [1,29] using silsesquioxane $H_8Si_8O_{12}$ cluster model by B3LYP method. In recent experimental results, it has been confirmed that three types of vanadium species comprising monovanadate, one- and two-dimensional vanadate chains (polyvanadate), and crystallites of V_2O_5 are present on supports in V_2O_5/TiO_2, and V_2O_5/Al_2O_3 that depends on V_2O_5 loading on support [30]. Oyama et al found that a single vanadium center for ethylene ODH is necessary on the basis of relationship between vanadium oxide concentration on an SiO_2 support and the ethylene turnover rate [31-33]. Monovanadates have higher activity and better selectivity to ODH of propane on V_2O_5/ZrO_2 catalysts than bulk V_2O_5 and polyvanadates [34].

Other studies show that the polyvanadate structures are significantly more active than monovanadate structure. This conclusion can be taken that one of the monovanadates or polyvanadates is better but know that these sites are more important than crystalline V_2O_5. In spite of large studies in this field, there are some uncertainties in the details of mechanism of ODH reactions. The common structure of supported vanadium oxide is coordinated vanadia in tetrahedral geometry with terminal vanadyl oxygen (V=O) and three bridge oxygen atoms which are connected to cautions through V-O-S (S is support) or neighbor V_2O_5 units (V-O-V) as monomeric and dimeric structures (Figure 1). In the present study, our attention focuses on several mechanistic aspects to achieve a complete understanding on the molecular scale; (1) the details of mechanism of ODH reactions, (2) study of different transition states and intermediates through the reaction path. To achieve these goals, we have investigated the mechanism of activating the C-H bond of propane with subsequent formation of propene. The results of this model can be used in mechanisms of supported vanadia catalysts.

Computational Methods

All calculations were performed using the Gaussian 98 [20] software. The geometries and energies of model system of reactants, transition states, intermediates and products were calculated by employing a hybrid Hartree-Fock- density functional scheme, the adiabatic connection method –Becke three-parameter with Lee-Yang-Parr (B3LYP) functional [35] of density functional theory (DFT) [36] with the standard 6-31+G* basis set. Any symmetry constrains were applied to full optimization. The B3LYP functional has been demonstrated to provide accurate description for compounds including transition metals and involving hydrogen bond interactions [34-36]. The QST3 procedure has been used to search for transition states. Intrinsic reaction coordinate (IRC) calculations [37] were employed to ensure the identity of the reactants and products corresponding to each transition structure. Vibrational analyses were performed on all optimized structures with the same functional and basis set as the corresponding geometry optimizations. In addition, the thermodynamic properties of all compounds were obtained from frequency calculations at 298.15 K and 1.0 atmosphere pressure. All reported enthalpies were zero-point (ZPE) corrected with unscaled frequencies.

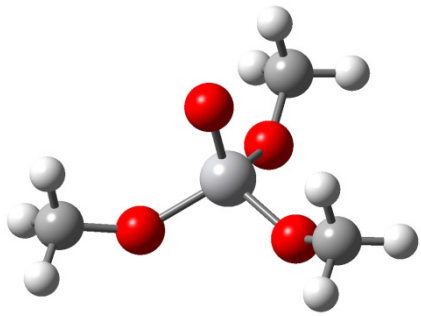

Figure 2. Optimized structure of vanadium oxide supported on carbon atom at the B3LYP/6-31+G* method with some structural details.

RESULTS and DISCUSSION

Optimization of $VO_4(CH_3)_3$ as a Model System

The $VO_4(CH_3)_3$ in Figure 1 (left) was considered as a topological model to investigate top surface layer of vanadia surface mapped on to carbon structures. With the aim of reducing computational expenses, instead of using carbons of carbon materials, CH_3 was placed. The model contains the vanadyl (V=O) and the V-O-C sites. Vanadium atom in $VO_4(CH_3)_3$ model have a formal oxidation state of +5, one of oxygen atoms is connected to vanadium via double bond and other three oxygen atoms are connected to carbons through single bond. The optimize geometry as well as some structural details of the $VO_4(CH_3)_3$ model system is presented in Figure 2. The bond distances for V=O and V-O are equal 1.59Å and 1.80 Å respectively that is in good agreement with the experimental values of V=O= 1.58 Å and V-O 1.78 Å obtained for the bulk V_2O_5 [37]. Also periodic DFT calculations on the V_2O_5(001) surface lead to V=O = 1.59 Å and V-O= 1.80 Å [38]. The result of natural bond orbital analysis (NBO) shows QV= 1.41, QO1= -0.31 and QO2= -0.73 electrons. This result is in good agreement with the values of shows QV= 1.46, QO1= -0.39 and QO2= -0.71 electrons that derived from electrostatic field analyzing. Therefore, each V-O bond could have a charge transfer of 0.37 electrons from V to O atom. While the net transfer in the V=O bond is 0.31 electrons despite two polar covalent bonds. It is noticeable that the small charge transfer from V to O atom is due to the high oxidation number. Calculation of vibrational frequencies has confirmed stationary point with no negative eigenvalue observed in the force constant matrix. Results of frequency calculations show four vibrational frequencies in the range of 1015-1042 cm^{-1} for the V=O bond stretching; comparison with experimental values of 1040 cm^{-1} for bulk V_2O_5 1010 cm^{-1} for V_2O_5/ZrO_2 [16] and 1042 cm^{-1} for V_2O_5/SiO_2 shows good agreement [34,39]. On the basis of the geometrical and energetic similarities of the $VO_4(CH_3)_3$ model to V_2O_5 (001), we conclude that the $VO_4(CH_3)_3$ model is a suitable model for studding alkane ODH reaction and gaining insight in to the whole mechanism.

Oxidative Dehydrogenation of Propane on $VO_4(CH_3)_3$

Abstraction of the First Hydrogen from Propane

Two types of addition reactions that involve heterolytic C-H bond cleavage from first type and second type of carbon that leads to $\cdot CH_2CH_2CH_3$ and $CH_3 \cdot CHCH_3$ radicals and two kinds of hydrogen abstraction reactions that involve hemolytic C-H bond cleavage. The optimized geometries as well as relative calculated energies of four reaction paths are depicted in Figure 3. Path (1) and path (2) involve an addition reaction utilizing V=O1 group, where the hydrogen atom of propane group binds to O1. In path (1), the hydrogen atom binds to first type of carbon (H1) connected to O1 atom. The V= O1 bond distance in transition state geometry (TS11) in path (1) is 1.55 Å; the V-O2 bond distance elongates from 1.74 to 1.86 Å. The C-H bond distance elongates from 1.09 to 1.50 Å and the C-O2 bond distances elongate 1.40 to 1.43 Å. The activation barrier for path (1) is about 48.35 kcal/mol. Path 2 is also V= O1 addition reaction, but hydrogen of second type of carbon (H2) attacks to O1 atom. In the transition state (TS12) the V= O1 bond is 1.86 Å; the V-O2 bond elongates from 1.55 Å to 1.86 Å; the C-H bond distance elongates from 1.09 to 1.60 Å and the CH_3-O (2) bond distances

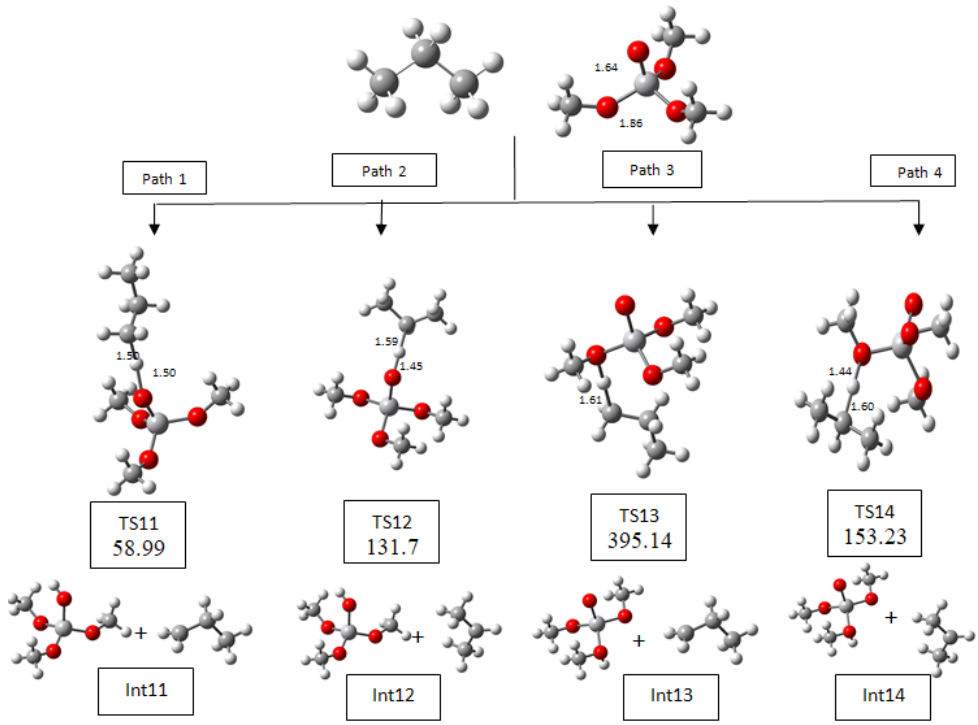

Figure 3. Reaction pathways and (ΔE, kcal/mol) for initial C-H bond activation of propane (The bond distances are according to angstrom (Å)).

elongates from 1.39 to 1.43 Å. The energy barrier for TS12 is equal 151.39 kcal/mol. Vanadium hydride, propyl and isopropyl radicals are formed in the first intermediate in both reactions path (1) and (2) (Int11 and Int12). In vanadium hydride optimized geometry, the H-O1, and V-O1 bond distances are 0.95 and 1.79 Å, respectively. Path (3) and (4) include hydrogen abstraction reaction. In both path (3) and (4) the bridging oxygen O2 abstracts the hydrogen atom from the first and second type of carbon of propane respectively. The O2-H and H-C bond distances in TS13 are 1.43 Å and 1.61 Å respectively, 1.44 Å, and 1.60 Å in TS14. The activation barrier for path (3) and (4) are about 123.86 and 143.38 kcal/mol respectively. The corresponding intermediate, Int13 and Int14 for path (3) and path (4) respectively have bond distances of V=O1 equal 1.86 Å, V-O2= 1.86 Å and C-O= 1.43 Å. Comparison between different reaction paths indicate that path (1) with activation energy about 48.35 kcal/mol, is the most energetically desirable and possible pathway among the four reaction pathways. In addition, hydrogen abstraction pathways are more favorable than the addition pathways. As the π bond of V=O1 has a singly occupied orbital available to bond to the H atom and pointing toward it, the obtained result seems reasonable, whereas for O2 atom the orbital overlapping the H is a filled lone pair orbital.

In conclusion, the hydrogen abstraction reactions have the σ-orbital of C-H bond aligned with the lone pair electrons orbital of O1 or O2 atoms. However, the addition reaction needs σ-orbital of C-H bond in propane to break almost completely before it can overlap with the filled lone pair orbital on oxygen atom and the empty d-orbital on vanadium, cause to a high barrier. In the case of the C-H bond activation of propane on the $VO_4(CH_3)_3$ model, this conclusion is taken that hydrogen abstraction by O1 atom is the first common step for alkane ODH reaction, hence it can be considered as the initial step for the propane ODH mechanism.

Abstraction of the Second Hydrogen from Propylene

The optimized structure of the intermediate1 from path (1), Int11, is considered as the initial point for the final part of the mechanism, dissociation of product and catalyst reoxidation, Figure 4. There are three possible reaction paths to propene

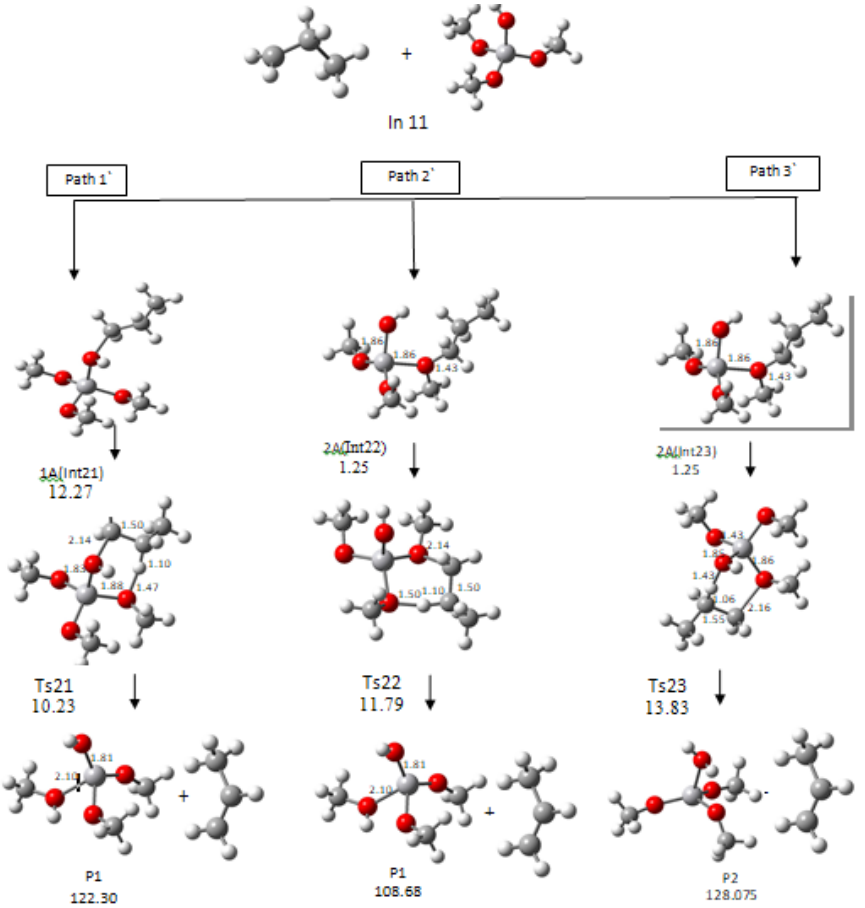

Figure 4. Presentation of three different reaction pathways for binding of propyl radical to the $VO_4H(CH_3)_3$ followed by the second hydrogen abstraction to release the propene product, the first row of the energetic parameters is ΔE, kcal/mol (the bond distances are according to angstrom (Å)).

formation, O2, O1-H are used with the aim of abstracting the second hydrogen from a methyl group to form propene and $VO_4H_2(CH_3)_3$ catalyst. In Path (1′), the propyl radical binds to the O1-H group to form second intermediate, Int21 (1A), which is 106.17 kcal/mol more stable than Int11. In the final step in Path 1′, O2 abstracts the second hydrogen from the methyl group, leading to propene and P1 by passing to second transition state, Ts21, with an activation barrier of -96.18 kcal/mol. Paths 2′ and 3′ start with the formation of the same intermediate, Int22 and Int23, (2A), via a bond which is formed between the propyl radical and O2 atom. In Path 2′, O1 abstracts one hydrogen from the methyl group with a -82.76 kcal/mol barrier to form propene and P1 via TS22. Path (3) (Hydroxyl-H 2nd-abs step), starting from the same intermediate, 2A (Int23), uses the O1-H group to abstract a hydrogen atom from the methyl group, leading to the formation of propene and P2, with about -170.35 kcal/mol barrier (Ts23).

In the Ts23 structure, the bond distance of V-O1 decreases from 1.86 Å in Int23 (2A) to 1.84 Å, while the V-O2 bond distance decreases from 1.86 Å to 1.84 Å. Path 2` has the lowest reaction barrier among the three possible reaction pathways studied in this work, -82.76 kcal/mol but path 3′ is more favorable than other paths because H_2O easily released from P2 than P1. The representative potential energy profile of the total reaction was obtained and is shown in Figure 5.

Vanadium Reoxidation

The most favorable step, path (3)′ lead to P2 product that we consider as the starting point for the final section of the mechanism, dissociation of the product and catalyst reoxidation. It is expected that water would easily dissociate from P2 to create a vacant VIII site. However, the dissociation energy calculated 60.5 kcal/mol, which is higher than the activation barriers for

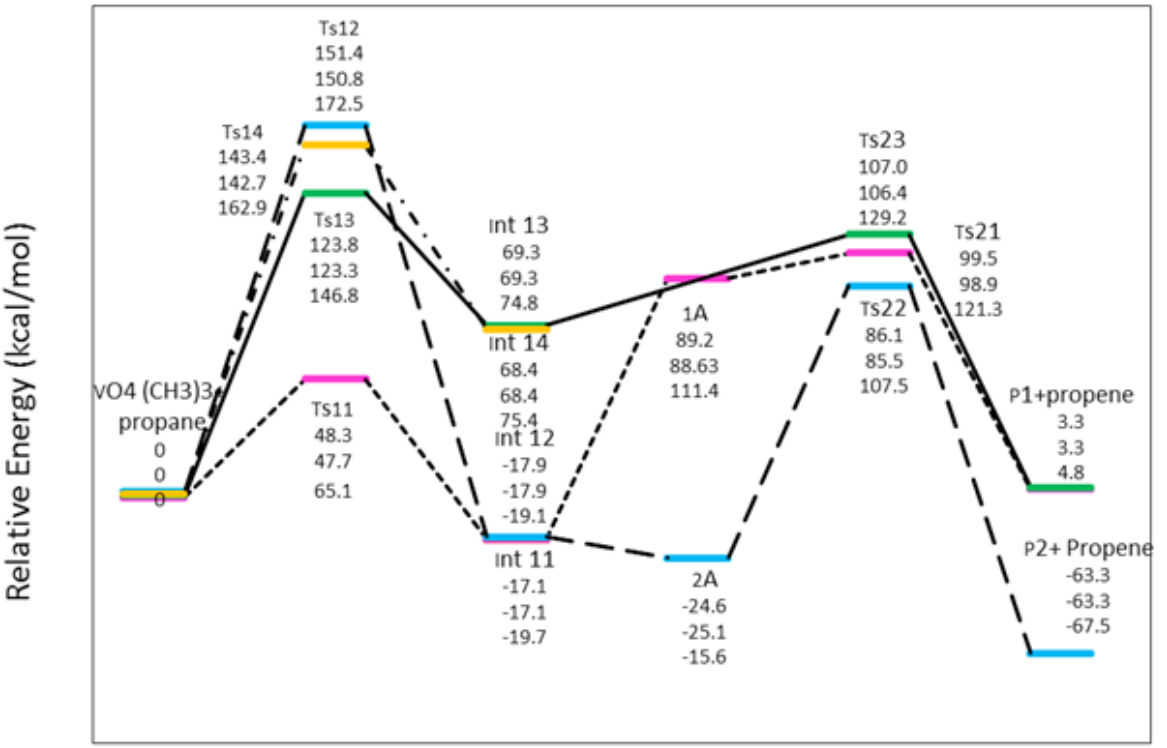

Figure 5. Calculated energy profiles for propane ODH on $VO_4(CH_3)_3$, the first row of the energetic parameters is ΔE_{298}, the second row is ΔH_{298} and the third row is ΔG_{298} respectively.

the conversion of propane to propene. Instead, we used another associative mechanism where water dissociation is assisted by the oxidant, O_2. In this mechanism, at first, O_2 binds to P2 with 2.0 kcal/mol for bonding of dioxygen to P2 eventually resulting in the $VO_3(CH_3)_3O_2H_2$ (complex1-Figure 6), which can be considered as a complex of $VO_3(CH_3)_3O_2$ (complex 2-Figure 6) and water. In complex 1 the VOO forms cyclic peroxide.

To take the VOO plane as xz, this involves rehybridizing the dz2 and dxz orbitals on the V atom to obtain orbitals which can spin pair directly with the pz orbitals on each oxygen atom to form VO bonds. The H_2O lone pair keeps coordinating to the empty dyz orbital of the V, and the V-OH_2 bond distance in complex 1 is 4.2 Å, that is 2.06 Å longer than in P2, indicating a dramatically weakened bond. In the second step, H_2O has been desorbed from complex 1 to form complex 2. Binding O_2 to P2 has the effect of destabilizing the bonding of H_2O. Thus, the energy to desorb H_2O from complex 1 is only 8.56 kcal/mol (rather than the 37.42 kcal/mol from P2).

In the third step, complex 2 converts to reform the initial catalyst, $VO_4(CH_3)_3$. In order to accomplish the catalytic cycle, the proxy specie 2 must be converted back to the initial $VO_4(CH_3)_3$ complex. As we expected, complex 2 would be more reactive than the initial model catalyst, $VO_4(CH_3)_3$. However, bonding an hydrogen atom to complex 2 to form a bound V-OOH gains 12.81 kcal/mol, as compared to 60.79 kcal/mol for bonding H to the V=O1 of $VO_4(CH_3)_3$, indicating more reactivity. We have hypothesized that complex 2 might activate a second propane instead. We use an easy hydrogen abstraction mechanism by using peroxo moiety with a calculated barrier of 23.66 kcal/mol, lower than the barrier for the initial hydrogen abstraction step (Ts12) using the $VO_4(CH_3)_3$ catalyst (with 49.35 kcal/mol barrier energy). In the subsequent step, the propyl radical fragment in complex 3 bonds with the other oxygen atom of the peroxo group to form complex 4 with 23.8 Kcal/mol barrier. The second molecule of propene and water are formed by passing through a six-membered ring transition state, Ts 4-1 (Figure 6). For this step, the activation energy is 23.1 kcal/

mol. The initial $VO_4(CH_3)_3$ catalyst is regenerated, completing the catalytic cycle. Catalyst cycle is summarized in Figure 7, schematically.

The potential energy surface for this cycle is shown in Figure 8. The overall reaction is:

$$VO_4(CH_3)_3 + 2C_3H_8 + O_2 \rightarrow VO_4(CH_3)_3 + 2C_3H_6 + 2H_2O$$
$$\Delta E = -28.0 \text{ kcal/mol} \quad (8)$$

In the above mentioned catalytic cycle, the V=O1 is the active site for all steps however O_2 only playing the role of stabilizing the propyl radical by forming the stable intermediate.

CONCLUSION

The ODHP reaction over a vanadium–carbon catalyst by using DFT method was investigated in order to study the oxidative reaction and possible pathways in detail. We have applied $VO_4(CH_3)_3$ model for studding the catalysis on V supported C (as carbon structure). The initial step is hydrogen abstraction from propane by cooperation of both terminal and interface oxygen sites for the first and second C–H activation, respectively. The second step initiates with propoxide intermediate on the O1 site of $VO_4(CH_3)_3$. There are three competitive reaction pathways leading to the formation of the propene as product. The complete catalytic cycle for conversion of propane to propene on $VO_4(CH_3)_3$ including reoxidation of the active site is reported here. Consequently, we have proposed that the rate determining step corresponds to the first hydrogen abstraction. In our catalytic cycle, gaseous O_2 promotes water desorption and re-oxidizing the reduced vanadium oxide catalyst. Our calculated results predicted that complex 2 (Figure 6) activate the methylene C-H bond in propane with a reaction barrier 14.7. As the C-H bond of propene product is weaker than the H-iPr bond in propane, the V=O (1) sites could react more rapidly with the product than reactant, leads to some products such as CO_2. With the purpose of avoiding such disadvantages in selectivity process, the product should be protected from V=O sites. This might be the reason of high selectivity property of supported catalysts. In catalytic cycle, the V=O1 sites play an essential role in all reaction steps, while bridging oxygens (V-O-C) play the stabilizing role in the propyl intermediate. This study reveals that the activity

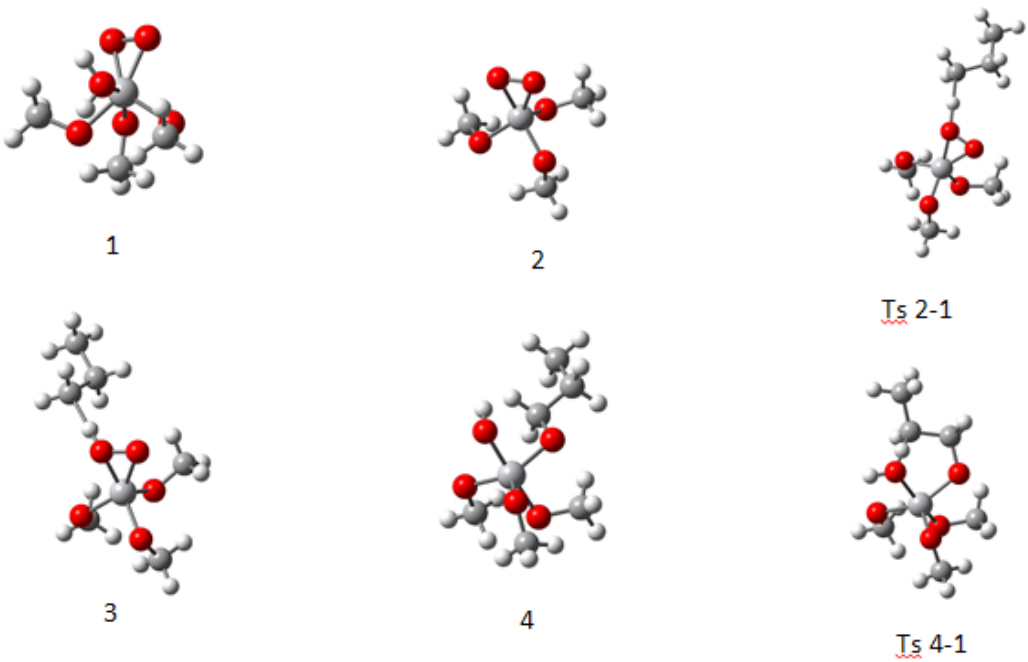

Figure 6. Presentation of optimized structures for the intermediate and transition states of the vanadium reoxidation step.

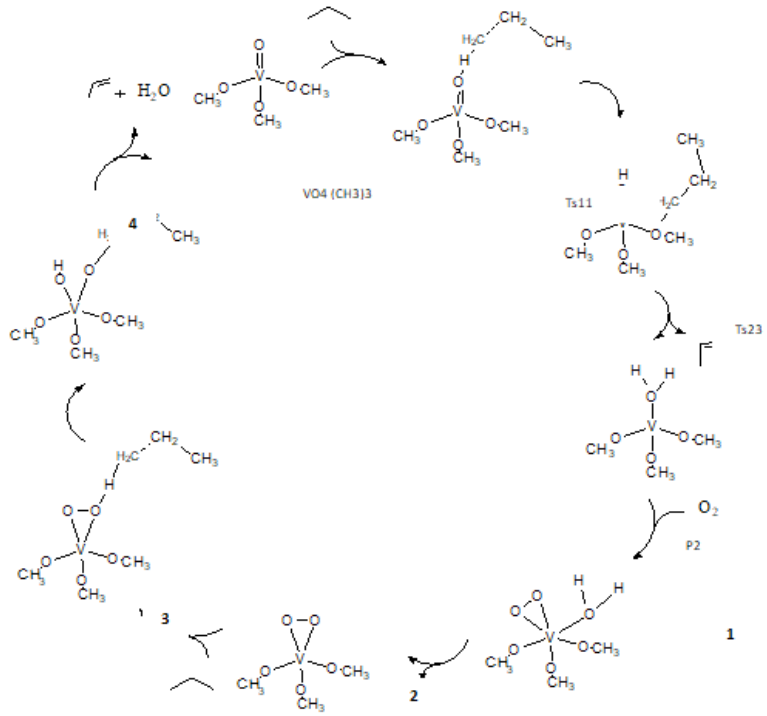

Figure 7. The proposed catalylic cycle for propane ODH on $VO_4(CH_3)_3$ derived from the Quantum mechanical calculations.

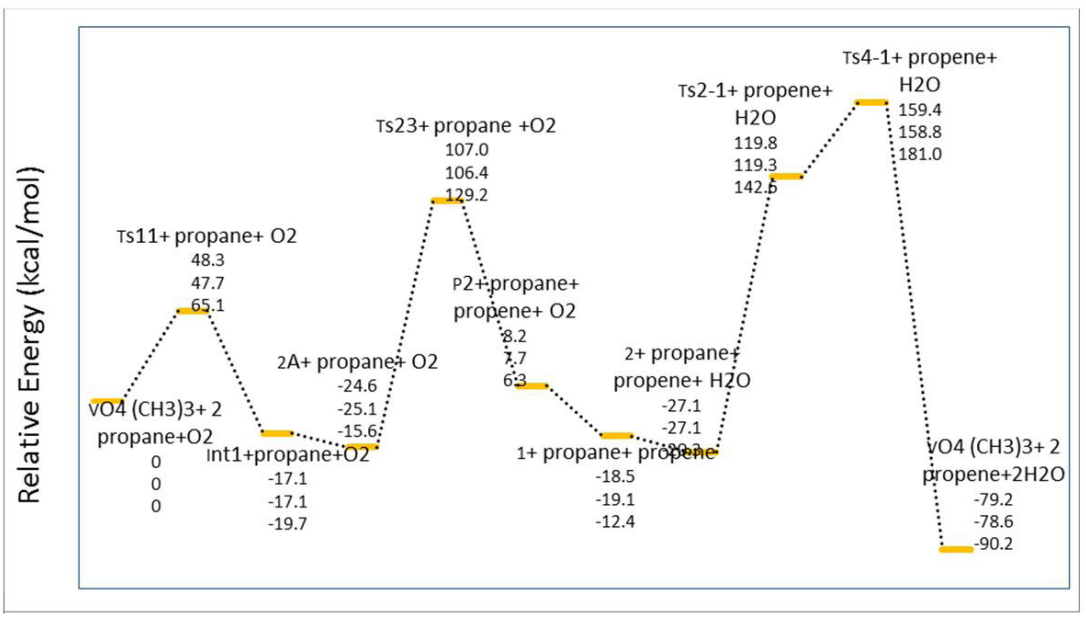

Figure 8. Energy profiles of the single-site vanadyl activation and reoxidation catalytic cycle for propane ODH on $VO_4(CH_3)_3$, The first row of the energetic parameters is ΔE_{298}, the second row is ΔH_{298} and the third row is ΔG_{298} respectively.

and selectivity of ODH reaction is correlated to the structure and surface chemistry of carbon materials based on the proposed reaction mechanism. Our results may inspire application of 13 this process for carbon materials and in experimental reactions, as well. More DFT studies in future are highly recommended, which could make better rational design of the catalysts to achieve better selectivity, hence better results.

ACKNOWLEDGEMENTS

The authors gratefully acknowledge research council of Al-zahra and Guilan Universities.

References

1. X. Rozanska, R. Fortrie, J. Sauer, Oxidative dehydrogenation of propane by monomeric vanadium oxide sites on silica support, J. Phys. Chem. C., 111 (2007) 6041-6050.
2. B. Frank, M. Morassutto, R. Schomäcker, R. Schlögl, D.S. Su, Oxidative dehydrogenation of ethane over multiwalled carbon nanotubes, ChemCatChem., 2 (2010) 644-648.
3. B. Frank, J. Zhang, R. Blume, R. Schlögl, D.S. Su, Heteroatoms increase the selectivity in oxidative dehydrogenation reactions on nanocarbons, Angew. Chem. Int. Ed., 48 (2009) 6913-6917.
4. J. Zhang, X. Liu, R. Blume, A. Zhang, R. Schlögl, D.S. Su, Surface-modified carbon nanotubes catalyze oxidative dehydrogenation of n-butane, Science, 322 (2008) 73-77.
5. C. Liang, H. Xie, V. Schwartz, J. Howe, S. Dai, S.H. Overbury, Open-Cage fullerene-like graphitic carbons as catalysts for oxidative dehydrogenation of isobutane, J. Am. Chem. Soc., 131 (2009) 7735-7741.
6. T. García, J. López, J.L. Nieto, R. Sanchis, A. Dejoz, M. Vázquez, B. Solsona, Insights into the catalytic production of hydrogen from propane in the presence of oxygen: Cooperative presence of vanadium and gold catalysts, Fuel Process. Technol., 134 (2015) 290-296.
7. M. Sheintuch, D.S. Simakov, Alkanes dehydrogenation, membrane reactors for hydrogen production processes, Springer, (2011) 183-200.
8. B. Barghi, M. Fattahi, F. Khorasheh, Kinetic modeling of propane dehydrogenation over an industrial catalyst in the presence of oxygenated compounds, reaction kinetics, React. Kinet. Mech. Cat., 107 (2012) 141-155.
9. S.A. Al-Ghamdi, H.I. de Lasa, Propylene production via propane oxidative dehydrogenation over VOx/γ-Al_2O_3 catalyst, Fuel, 128 (2014) 120-140.
10. H. Kim, G.A. Ferguson, L. Cheng, S.A. Zygmunt, P.C. Stair, L.A. Curtiss, Structure-specific reactivity of alumina-supported monomeric vanadium oxide species, J. Phys. Chem. C, 116 (2012) 2927-2932.
11. C. Popa, M.V. Ganduglia-Pirovano, J. Sauer, Periodic density functional theory study of von species supported on the CeO_2 surface, J. Phys. Chem. C, 115 (2011) 7399-7410.
12. M.J. Cheng, K. Chenoweth, J. Oxgaard, A. van Duin, W.A. Goddard, Single-site vanadyl activation, functionalization, and reoxidation reaction mechanism for propane oxidative dehydrogenation on the cubic v4o10 cluster, J. Phys. Chem. C, 111 (2007) 5115-5127.
13. M.V. Ganduglia-Pirovano, C. Popa, J. Sauer, H. Abbott, A. Uhl, M. Baron, D. Stacchiola, O. Bondarchuk, S. Shaikhutdinov, H.J. Freund, Role of ceria in oxidative dehydrogenation on supported vanadia catalysts, J. Am. Chem. Soc., 132 (2010) 2345-2349.
14. X. Fan, G. Zhang, F. Zhang, Multiple roles of graphene in heterogeneous catalysis, Chem. Soc. Rev., 44 (2015) 3023-3035.
15. O.V. Khavryuchenko, B. Frank, A. Trunschke, K. Hermann, R. Schlögl, Quantum-chemical investigation of hydrocarbon oxidative dehydrogenation over spin-active carbon catalyst clusters, J. Phys. Chem. C, 117 (2013) 6225-6234.
16. B. Frank, R. Blume, A. Rinaldi, A. Trunschke, Oxygen insertion catalysis by sp^2 carbon, R. Schlögl, Angew. Chem. Int. Ed., 50 (2011) 10226-10230.
17. F. Cavani, F. Trifiro, The oxidative dehydrogenation of ethane and propane as an alternative way for the production of light olefins, Catal. Today, 24 (1995) 307-313.
18. M.D. Argyle, K. Chen, A.T. Bell, E. Iglesia, Effect of catalyst structure on oxidative dehydrogenation of ethane and propane on alumina-supported vanadia, J. Catal., 208 (2002) 139-149.
19. D. Whitehurst, Abstracts of papers of the American Chemical Society, Am. Chem. Soc., 1155 16TH ST, NW, Washington, DC 20036, 1997, pp. 77-FUEL.
20. E. Mamedov, V.C. Corberán, Oxidative dehydrogenation of lower alkanes on vanadium oxide-based catalysts. The present state of the art and outlooks, Appl. Catal. A-Gen., 127 (1995) 1-40.
21. A.S. Kootenaei, J. Towfighi, A. Khodadadi, Y. Mortazavi, Stability and catalytic performance of vanadia supported on nanostructured titania catalyst in oxidative dehydrogenation of propane, Appl. Surf. Sci., 298 (2014) 26-35.
22. M. Calatayud, B. Mguig, C. Minot, A periodic model for the V_2O_5–TiO_2 (anatase) catalyst. stability of dimeric species, Surf. Sci., 526 (2003) 297-308.
23. M. Calatayud, B. Mguig, C. Minot, A DFT study on the hydrated V_2O_5-TiO_2-anatase catalyst: stability of monomeric species, Theor. Chem. Acc., 114 (2005) 29-37.
24. M. Calatayud, C. Minot, Reactivity of the V_2O_5-TiO_2-anatase catalyst: role of the oxygen sites, Top. Catal., 41 (2006) 17-26.
25. C.A. Carrero, R. Schlögl, I.E. Wachs, R. Schomaecker, Critical literature review of the kinetics for the oxidative dehydrogenation of propane over well-defined supported vanadium oxide catalysts, ACS Catal., 4 (2014) 3357-3380.
26. B. Hammer, J.K. Nørskov, Theoretical surface science and catalysis—calculations and concepts, Adv. Catal., 45 (2000) 71-129.
27. J.K. Nørskov, T. Bligaard, J. Rossmeisl, C.H. Christensen, Towards the computational design of solid catalysts, Nature Chem., 1 (2009) 37-46.
28. B. Frank, S. Wrabetz, O.V. Khavryuchenko, R. Blume, A. Trunschke, R. Schlögl, Calorimetric study of propane and propylene adsorption on the active surface of multiwalled carbon nanotube catalysts, Chem. Phys. Chem., 12 (2011) 2709-2713.
29. W. Daniell, A. Ponchel, S. Kuba, F. Anderle, T. Weingand, D. Gregory, H. Knözinger, Characterization and catalytic behavior of VO_x-CeO_2 catalysts for the oxidative dehydrogenation of propane, Top. Catal., 20 (2002) 65-74.
30. A. Khodakov, B. Olthof, A.T. Bell, E. Iglesia, Structure and catalytic properties of supported vanadium oxides: support effects on oxidative dehydrogenation reactions, J. Catal., 181 (1999) 205-216.

31. S.T. Oyama, Adsorbate bonding and the selection of partial and total oxidation pathways, J. Catal., 128 (1991) 210-217.
32. J. Le Bars, J. Vedrine, A. Auroux, B. Pommier, G. Pajonk, Calorimetric study of vanadium pentoxide catalysts used in the reaction of ethane oxidative dehydrogenation, J. Phys. Chem., 96 (1992) 2217-2221.
33. H.H. Kung, Oxidative dehydrogenation of light (C2 to C4) Alkanes, Adv. catal. 40 (1994) 1-38.
34. C. Pieck, M. Banares, J. Fierro, Propane oxidative dehydrogenation on VO_x/ZrO_2 catalysts, J. Catal., 224 (2004) 1-7.
35. A.D. Becke, Density functional thermochemistry, III the role of exact exchange, J. Chem. Phys., 98 (1993) 5648-5652.
36. R.G. Parr, W. Yang, Density-Functional Theory of atoms and molecules, Oxford University Press, 1989.
37. R. Enjalbert, J. Galy, A refinement of the structure of V_2O_5, Acta. Cryst. Sect. C: Cryst. Struct. Commun., 42 (1986) 1467-1469.
38. M. Ganduglia-Pirovano, J. Sauer, Stability of reduced V_2O_5 (001) Surfaces, Phys. Rev. B, 70 (2004) 045422-1-045422-13.
39. S.T. Oyama, G.T. Went, K.B. Lewis, A.T. Bell, G.A. Somorjai, Oxygen chemisorption and laser Raman spectroscopy of unsupported and silica-supported vanadium oxide catalysts, J. Phys. Chem., 93 (1989) 6786-6790.

Production of Thermostable α-Amylase Through Solid State Fermentation (SSF) by Using Thermophilic *Anoxybacillus* sp.

Termofilik *Anoxybacillus* sp. Kullanarak Katı Faz Fermantasyonu (SSF) ile Isılkararlı α-Amilaz Üretimi

Research Article

M. Serkan Yalçın[1]* and Sadin Özdemir[2]

[1]Dep. of Chemical and Chemical Processing Technologies, Technical Science Vocational School, Mersin University, Mersin, Turkey.
[2]Food Processing Programme, Technical Science Vocational School, Mersin University, Yenisehir, Mersin, Turkey.

ABSTRACT

The production of extracellular α-amylase (1,4-α-D-glucan glucanohydrolase, EC 3.2.1.1) by a newly isolated thermophilic bacterium *Anoxybacillus* sp. was studied in solid state fermentation (SSF). Bacterial strain was isolated from a thermal spring of Ömer, Afyonkarahisar in Turkey. Agricultural wastes such as banana husk, wheat bran, rice husk, apple bark, orange bark, maize oil cake, lentil bran and pistachio shell were used for α-amylase production as solid substrates. Growth on rice husk gave the highest α-amylase activity. The maximum enzyme activity obtained was 3.628 U/mg of under optimum conditions of an fermentation time of 48 h, an incubation temperature of 60°C, a pH of 6.0, a substrat particle size 1.500 μm, an initial moisture level of 60% and an inoculum level of 40% (v/w).

Key Words
Agricultural waste, α-amylase, solid-state fermentation (SSF), thermophilic bacterium.

ÖZ

Ekstrasellüler α-amilaz (1,4-α-D-glukan glukanohidrolaz, EC 3.2.1.1) üretimi yeni izole edilmiş bir termofilik bakteri olan *Anoxybacillus* sp. kullanılarak katı faz fermantasyon (SSF) yöntemiyle gerçekleştirilmiştir. Bakteri ırkı, Türkiye'de Afyonkarahisar, Ömer, termal kaplıcasından izole edilmiştir. α-Amilaz üretimi için, muz kabuğu, buğday kepeği, pirinç kabuğu, elma kabuğu, portakal kabuğu, mısır yağı pastası, mercimek kepeği ve antep fıstığı kabuğu gibi tarımsal atıklar katı substrat olarak kullanılmıştır. En yüksek α-amilaz aktivitesi, pirinç kabuğu üzerindeki mikroorganizma üremesinde elde edilmiştir. Maksimum enzim aktivitesi, 3.628 U/mg, 48 saatlik fermantasyon süresi, 60°C'lik bir inkübasyon sıcaklığı, pH 6.0, substrat parçacık boyutu 1.500 μm, başlangıç nem seviyesi %60 ve aşılama seviyesi %40 (v/w) optimum koşulları altında elde edilmiştir

Anahtar Kelimeler
Tarımsal atık, α-amilaz, katı hal fermantasyon (SSF), termofilik bakteri.

Article History: Received: Sep 08, 2017; Revised: Oct 26, 2017; Accepted: Jun 26, 2018; Available Online: Feb 20, 2018.

DOI: 10.15671/HJBC.2018.217

Correspondence to: M.S. Yalçın; Dep. Chem. Chemic. Process. Technol., Techn. Sci. Voc. Sch., Mersin University, Mersin, Turkey.
Tel: +90 324 3610001/16852 Fax: +90 324 3610041 E-Mail: serkanyalcin@mersin.edu.tr

INTRODUCTION

-Amylase (1,4-α-D-glucan glucanohydrolase, αEC 3.2.1.1) is a common secretory enzyme that catalyze the hydrolysis of internal α-D-(1,4) glycosidic bonds of starch at random points [1]. α -amylase is an important enzyme for industrial operations such as starch processing, pulp industries, textile, yeasting, baking, distillation industries and pharmaceutics [2,3]. This enzyme represents an industrial enzyme category which has a 25% share (approximately) in the enzyme sector [4,5]. α-amylase can be produced from various sources such as plants, animals and microorganisms. Enzymes originating from microbial sources generally meet industrial demand [4].

Solid state fermentation (SSF) is a process where microorganisms grow without any free water or in an environment containing a very small amount of free water. Due to its historical importance, it is being used for the production of basic foodstuff such as bread and cheese in the West and koji in the East for thousands of years [6]. Considering the last century and the past couple of decades, it is still being used for the production of biomolecules and products that are important for many industries, including food, pharmaceuticals, textile, biochemicals, bioenergy, and others [7,8]. As compared to conventional submerged fermentation (SmF), SSF offers important advantages such as low energy requirements, high productivity and less inhibitor effect for enzymatic production [9]. Its application at industrial scale, however, seems to be limited because of technological issues such as reactor design, heat transfer problems or cost of sterilization [10].

Thermophilic bacteria usually grow at temperatures as high as 50–80ºC [11]. Because thermophilic character is not associated with Gram identity (Gram + or -), spore formation state (spore forming or not) and respiratory type (aerobic or anaerobic) of the bacteria, thermophilic members can be found in each bacteria group. Thermophilic bacteria can produce DNA polymerases, lipases, amylases, proteases, xylanases and also exo-polysaccharides resistant to high temperature, salt and extreme pH conditions [12]. For these reasons, thermophilic bacteria have been great attention in biotechnology in recent years by many researchers.

The aim of this investigation was the optimization of α-amylase production by using thermophilic bacterium *Anoxybacillus* sp. under SSF. For this reason, the various process parameters were checked out such as various agriculture wastes, fermentation time, temperature and pH, particle size, initial moisture level, inoculum volume and influence of different metal ions.

MATERIALS and METHODS

Isolation and Identification of Thermophilic Bacterial Strain

In this study, bacterial strain was isolated from a thermal spring of Ömer, Afyonkarahisar in Turkey. Based on the quantities of α-amylase secreted by solid state media and the features of the enzyme, one strain was selected for following studies and identified as *Anoxybacillus* sp. on the basis of different biochemical and morphological tests and 16S rRNA gene sequence analysis. The phylogenetic tree was arranged with the neighbor joining process utilizing the Molecular Evolutionary Genetics Analysis (MEGA) [13].

Preparation of Inoculum

The thermophilic isolate was cultured in 50 mL of Nutrient Broth in a 250 mL glass bottle and inoculated with a loopfull of cells from one night old slant and kept at 55ºC in a shaker (120 rpm). After 12 h of incubation, 1000 μL of this medium was utilized for inoculation. By serial dilution and plating, the quantities of viable colonies in the inoculation medium was determined to be 7.4×10^7 CFU/mL.

Solid-State Fermentation (SSF)

Banana husk (BH), wheat bran (WB), rice husk (RH), apple bark (AB), orange bark (OB), lentil bran (LB), maize oil cake (MOC) and pistachio shell (PS) were provided from a regional market in Mersin, Turkey. One half of a gram of solid substrates which passed through sieve of 1.000 μm were put into 50 mL glass bottle. To adjust moisture contents (% by mass per volume), Tris HCl (0.1 M and pH 7.0) was added and then autoclaved at 121ºC for 15 min. The glass bottles were waited for cooling after autoclaving and then were inoculated with 1 mL spore suspension. After inoculation, the SSF mediums were incubated at 55ºC at 120 rpm.

Optimization of Process Parameters

Investigation of the influence of different physico-chemical factors and cultural conditions was necessary for the optimization of enzyme production of *Anoxybacillus* sp. used in SSF. The strategy was to optimize every factor independently and we studied the optimal conditions after in each experiments. Fermentation time (24–144 h), temperature (40-75°C), pH (citrate buffer 0.1 M, pH 3.0, 4.0, 5.0, and 6.0, Tris-HCl buffer 0.1 M, pH 7.0, 8.0, and 9.0, carbonate/bicarbonate buffer 0.1 M, pH 10), particle size (500–2.000 μm), inoculum size (10–60% by mass per volume), initial moisture level of the SSF substrate (40–70% by mass per volume) and different metal ions (Co^{2+},Ca^{2+}, Mn^{2+},Cu^{2+}, Pb^{2+}, Cd^{2+}) were optimized.

Enzyme Extraction and Assay

The fermented SSF substrates were mixed properly with water and then shaked by shaker at 120 rpm for 60 min. The fermented extracts were compressed using muslin cloth. The extracts were centrifuged at 10.000 g for 8 min. The upper solution used as the crude enzyme after centrifugation. α-Amylase assay was determined by Bernfeld method [14].

RESULTS and DISCUSSION

Morphological, Physiological, Biochemical Tests and 16S rRNA Gene Sequence Analysis

It was observed that isolated bacteria (SO-6) were in the form of bacilli, gram positive, creates spores, mobile and thermophilic (Table 1). It was determined that this isolate was close to *Anoxybacillus* sp. according to the results of morphological, physiological and biochemical tests and 16 rRNA analysis (Accession no. KJ434783). Figure 1 demonstrates the phylogenetic tree analysis. 16rRNA sequence is as follows:

GCTTTTGGATCGTTAGCGGCGGACGGGTGAG-
TAACACGTGGGCAACCTGCCCTGTAGACGGGG
ATAACACCGAGAAATCGGT-GCTAATACCGGAT
AACACGAAAGGCCGCATGGTCTTTCGTTGAA-
AGGCGGCGCAAGCTGTCGCTACAGGATGGGCCCG-
CGGC-GCATTAGCTAGTTGGTGAGGTAACGGC-
TCACCAAGGCGACGATGCGTAGCCGACCTGAG
AGGGTGATCGGCCACACTGGGACTGAGACACG
GCCCAGACTCCTACGGGAGGCAGCAGTAGGGA-
ATCTTCCGCAATGGACGAAAGTCTGACGGAGCAAC
GCCGCGTGAGCGAAGAAGGCCTTCGGGTCGTAAA
GCTCTGTTGTTAGGGAAGAACAAGTACCGCAGT-
CACTGGCGGTACCTTGACG-GTACCTAACGAGGA-
AGCCACGGCTAACTACGTGCCAGCAGCCGCGGTA-
ATACGTAGGTGGCAAGCGTTGTCCGGAATTATTG-
GGCGTAAAGCGCGCGCAGGCGGTTCCTTAAGT
CTGATGTGAAAGCCCACGGCTCAACCGTGGAGG
GTCATTGGAAACTGGG-GGACTTGAGTGCAGA-
AGAGGAGAGCGGAATTCCACGTGTAGCGGTGA-
AATGCGTAGAGATGTGGAGGAACACCAGTG-
GCGAAGGCGGCTCTCTGGTCTGTAACTGACG
CTGAGGCGCGAAAGCGTGGGGAGCAAACAG
GATTAGATACCCTGGTAGTCCACGCCGTAAAC-
GATGAGTGCTAAGTGTTAGAGGGTATCCACCC-
TTTAGTGCTGTAGCTAACGCATTAAGCACTCCGC
CTGGGGAGTACGCTCGCAAGAGTGAAACTCAA-
AGGAATTGACGGGGGCCCGCACAAGCGGTGGA-
ACCTTGTGGTTTAATTCGAAGCAACGCGAAGA-
ACCTTACCAGGTCTTGACATCCCCTGACAACCCGA-
GAAATCGGGCGTCCCCCTTCG...

Effect of Different Agriculture Wastes on α-amylase Production

Selection of a suitable solid substrate for fermentation process in SSF method is an important factor [15]. Various agroindustrial materials, particularly BH, WB, RH, AB, OB, MOC, LB and PS were tested for the selection of the most convenient substrate material to optimize bacterial growth and enzyme production. As can be seen in Figure 2, maximum amylase production (2.532 U/mg) was obtained in a medium containing RH alone as the substrate. The order of production of α -amylase from maximum to minimum was found to be RH>WB>MOC>BH>OB>AB>LB>PS. Therefore, RH was used as a substrate in all subsequent studies.

Effect of Fermentation Time on α -amylase Production

Incubation period required to reach maximum enzyme level depends on culture characteristics and it is based on growth speed and enzyme production [16]. To determine the best fermentation period, tests were conducted from 24 h to 144 h. A gradual increase was seen in enzyme production from 24 to 48 h and maximum enzyme activity was determined to be 2.820 U/mg in 48 h, after

Table 1. Morphological, physiological and biochemical tests.

Properties	Isolate SO-6
Gram Staining	+
Spore	+
Cell Shape	Bacilli
Pigmentation	Yellow
Aerobic respiration	+
Growth Temperature	25-80°C
Growth Ph	3.0-11.0
Mobility	+
Casein Hydrolysis	+
Starch Hydrolysis	+
Gelatin hydrolysis	-
Lipase Activity	+
Catalase Activity	+
Urease Activity	-

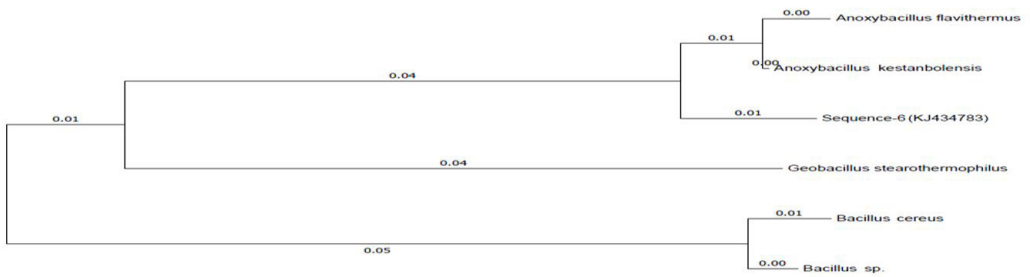

Figure 1. Evolutionary relationships of taxa.

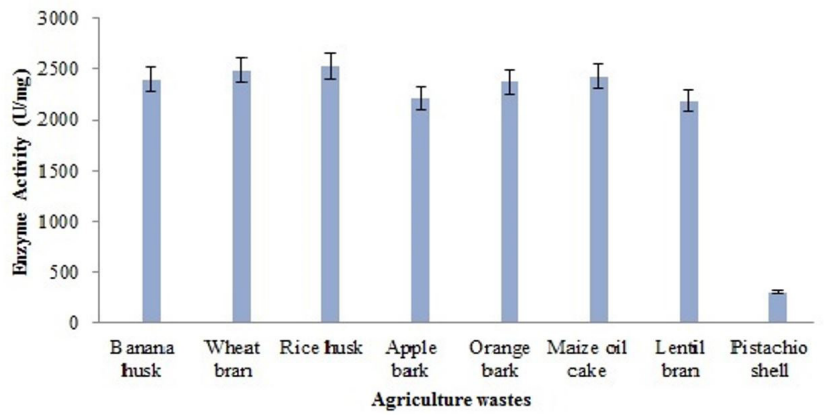

Figure 2. Effect of different substrates on α-amylase production by *Anoxybacillus* sp. using SSF. Process conditions: initial moisture content 50% (% by volume per mass), inoculum size 30% (% by volume per mass), particle size 1.000 μm, fermentation time 24 h, pH 7.0 and temperature 55°C.

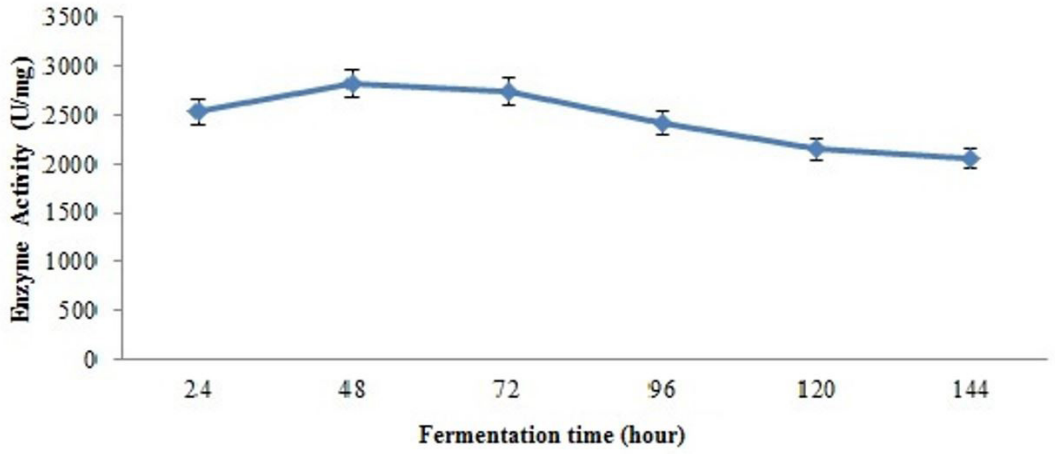

Figure 3. Effect of fermentation time on α-amylase production by *Anoxybacillus* sp. under SSF using RH as substrate. Process conditions: initial moisture content 50% (% by volume per mass), inoculum size 30% (% by volume per mass), particle size 1.000 μm, temperature 55°C and pH 7.0.

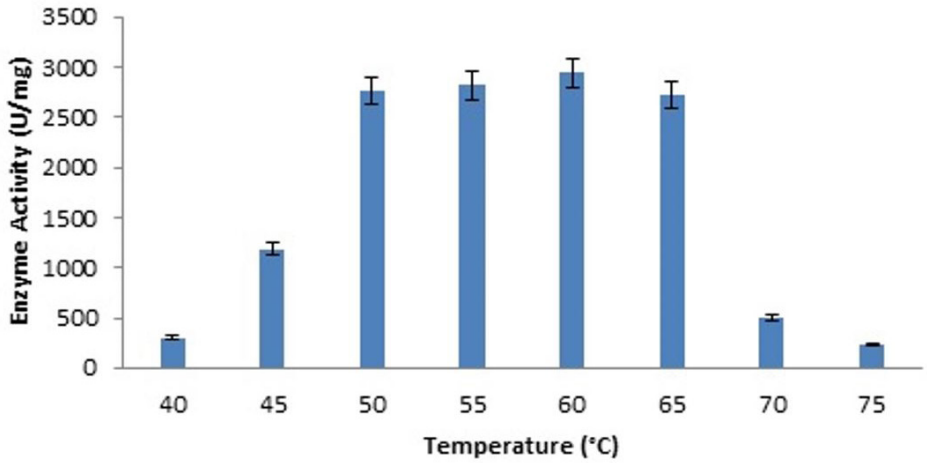

Figure 4. Effect of temperature on α-amylase production by *Anoxybacillus* sp. under SSF using RH as substrate. Process conditions: initial moisture content 50% (% by volume per mass), inoculum size 30% (% by volume per mass), particle size 1.000 μm, fermentation time 48 h and pH 7.0.

which a gradual decrease was observed (Figure 3). Decrease in enzyme efficiency after that hour may depend on the depletion of media or the denaturation of enzyme resulting from its interaction with other components in the medium or a variation in pH of the medium [17]. Fermentation time was applied as 48 h in all subsequent experimental works.

Effect of Temperature on Bacterial Growth and α -amylase Production

Temperature control in substrate bed has crucial importance to SSF because bacterial growth and the production of enzymes or metabolites is generally sensitive to temperature [15,18,19]. As shown in Figure 4, the enzyme activity increased 9.7 times with an increasing in the temperature from 40 to 60°C and the optimum enzyme production temperature of *Anoxybacillus* sp. was determined as 60°C (2.942 U/mg). The production of thermophiles at high temperatures is technically and economically important that it minimizes the risk of contamination, facilitates mixture by reducing adhesiveness, and causes a high level of substrate solubility [20]. The enzyme activity decreased 13 times when the temperature increased from 60 to 75°C. This reduction can be attributed to the decreased of bacterial growth

above the optimum fermentation temperature (data not shown). Thus, temperature in the substrate bed of 60°C was used for further studies.

Effect of pH on α -amylase Production

pH is one of the important factors for each fermentation process and depends on the type of moistening agent used in media. Each microorganism has an optimum pH range so that it can grow and become active. A substrate formation taking account of the buffering capacity of different components used or a buffer formulation containing components which do not have a harmful effect on biological effectiveness should be used for overcoming pH variation problem during SSF process [21]. As inferred from Figure 5, optimum pH value was determined to be 6.0 (3.060 U/mg) by using different buffers for various pH values for the production of α-amylase. Subsequent works were carried out by using this value as a basis.

Effect of Substrate Particle Size on α-amylase Production

The size of substrate particle is the most critical factor for microbial growth and enzyme activity [22]. The enzyme activity rised up 8.2 times with an increasing in the particle size from 500 to 1.500 μm. The highest enzyme production (3.060 U/mg) was found in the medium with a particle size of 1500 μm (Figure 6). It is preferred for microbial growth as surface are might grow due to smaller particle size, but growth may be inhibited as substrate may be agglomerated in smaller sizes. At 2.000 μm, activity of enzyme dropped down up to 57.3% as compared to the optimum enzyme activity at 1.500 μm. In larger sizes, it is not preferred as an insufficient surftace area will be formed for microbial attack [23]. Substrate with 1.500 μm particle size was preferred for subsequent works.

Effect of Initial Moisture Content of Substrate on α-amylase Production

The critical importance of humidity level in a SSF setting and its effects on the biosynthesis and oscillation of enzymes may be attributed to the effect of humidity on the physical characteristics of solid particles in the medium [16]. A low humidity content will cause a decrease in the solubility of substrate nutrients and a lower inflation level [24]. However, it is believed that an increase in humidity level reduces the porosity of wheat bran and thus, limits oxygen transfer [18]. As shown in Figure 7, maximum enzyme efficiency i.e. 3.175 U/mg was obtained in 60% substrate humidity content in trials conducted for determining the optimum humidity content because of its importance. Subsequent works were carried out based on this humidity content.

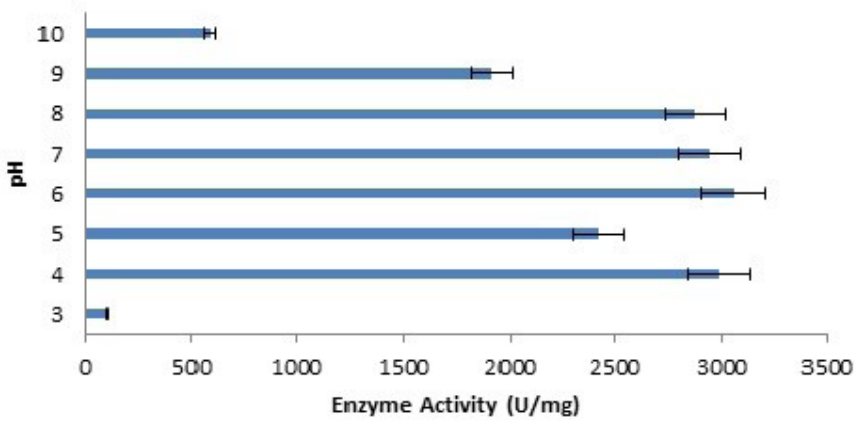

Figure 5. Effect of pH on α–amylase production by *Anoxybacillus* sp. under SSF using RH as substrate. Process conditions: initial moisture content 50% (% by volume per mass), inoculum size 30% (% by volume per mass), particle size 1.000 μm, fermentation time 48 h and temperature 60°C.

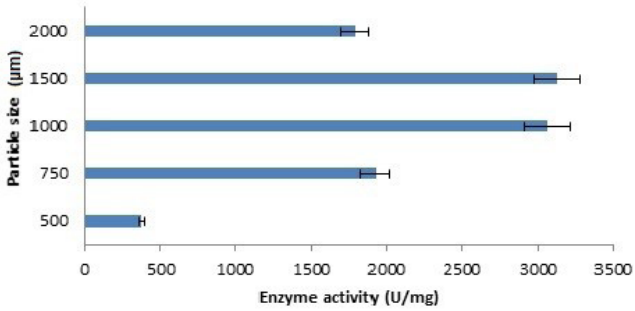

Figure 6. Effect of substrate particle size (µm) on α-amylase production by *Anoxybacillus* sp. under SSF using RH as substrate. Process conditions: initial moisture content 50% (% by volume per mass), inoculum size 30% (% by volume per mass), fermentation time 48 h, pH 6.0 and temperature 60°C.

Effect of inoculum Size on α-amylase Production

Inoculum level is one of the other important parameters for the production of α-amylase [25]. As presented in Figure 8, the lowest enzyme yield was obtained at the lowest value of 10% inoculum size, whereas the maximum enzyme yield (3.274 U/mg) was obtained at 40% inoculum size. At 60% inoculum size activity of enzyme dropped down up to 55.5% as compared to the optimum enzyme activity at 40% inoculum size. This results agreed with that of Ozdemir et al., [25]. Thus, 40% was used for further studies.

Effect of Metal Ions on α-amylase Production

Different metals exhibit different behavior in terms of their ability to act as an effector [26]. Metallic co-factors are important for enzymatic reaction because the existence or absence of metal regulates enzyme activity. The presence of a specific metallic ion in addition to the source of basic nutrient may inhibit or reinforce enzyme production. Co^{2+}, Ca^{2+}, Mn^{2+} ,Cu^{2+}, Pb^{2+} and Cd^{2+} metal ions in a 5 mg/L concentration and a control group without any metal ion were tested under the optimum fermentation conditions. As shown in Figure 9, α-amylase production increased in presence of Ca^{2+}, Co^{2+} and Mn^{2+} ions, but slightly decreased in presence of Cu^{2+}. Michelin et al., (2010) reported that amylase was activated by calcium (34%), cobalt (41%), and manganese chlorates (47%). Saboury (2002) also determined Co^{2+} as activator of α-amylase from *Bacillus amyloliquefaciens*.

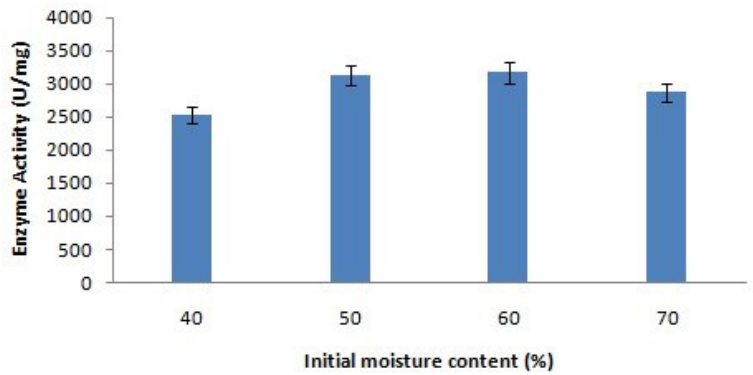

Figure 7. Effect of initial moisture content on α-amylase production by *Anoxybacillus* sp. under SSF using RH as substrate. Process conditions: inoculum size 30% (% by volume per mass), particle size 1.500 µm, fermentation time 48 h, pH 6.0 and temperature 60°C.

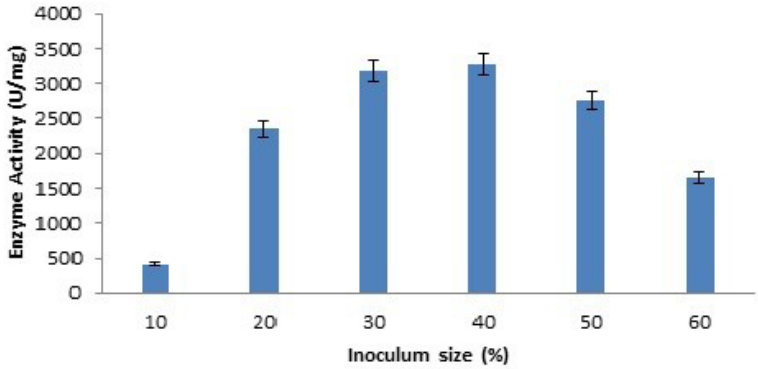

Figure 8. Effect of inoculum size (% by volume per mass) on α-amylase production by *Anoxybacillus* sp. under SSF using RH as substrate. Process conditions: initial moisture content 60% (% by volume per mass), particle size 1.500 μm, fermentation time 48 h, pH 6.0 and temperature 60°C.

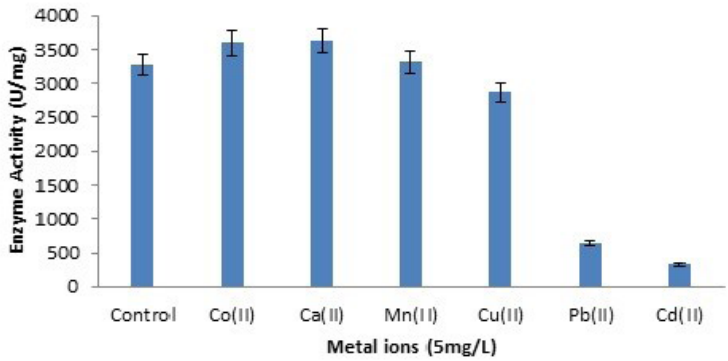

Figure 9. Effect of metal ions on α-amylase production by *Anoxybacillus* sp. under SSF using RH as substrate. Process conditions: initial moisture content 60% (% by volume per mass), inoculum size 40% (% by volume per mass), particle size 1.500 μm, fermentation time 48 h, pH 6.0 and temperature 60°C.

Our results showed good similarity with their findings. Enzyme production sharply decreased in presence of Pb^{2+} and Cd^{2+} ions. It is well known that Pb^{2+} and Cd^{2+} ions are not essential for living organisms. This reduction can be attributed to the inhibition of bacterial growth because of toxic effect of Pb^{2+} and Cd^{2+} ions (data not shown).

CONCLUSIONS

This study determined optimum conditions for the production of thermostable α -amylase through SSF technique by using thermophilic *Anoxybacillus* sp. The effects on enzyme production of different agricultural wastes, fermentation period, temperature, pH, particle size, humidity, inoculum level, and metal ions were explored and enzyme production was optimized. The highest enzyme activity was obtained as 3.628 U/mg at 48th hour, 60°C, pH: 6.0, 1500 μm particle size, 60% initial humidity and 40% inoculation volume and in presence of Ca^{2+} ion by using RH as substrate.

References

1. R. Gupta, P. Gigras, H. Mohapatra, V.K. Goswami, B. Chauhan, Microbial α-amylases: A biotechnological perspective, Process Biochem., 38 (2003) 1599-1616.
2. R.K. Saxena, K. Dutt, L. Agarwal, P. Nayyar, A highly thermostable and alkaline amylase from a *Bacillus* sp. PN5, Bioresour. Technol., 98 (2007) 260-265.
3. A. Pandey, C.R. Soccol, P. Nigam, V.T. Soccol, Biotechnological potential of agro-industrial residues: I. Sugarcane bagasse, Bioresour. Technol., 74 (2000) 69-80.
4. B. Arikan, Highly thermostable, thermophilic, alkaline, SDS and chelato rresistant amylase from a thermophilic *Bacillus sp*. Isolate A3-15, Bioresour. Technol., 99 (2008) 3071-3076.
5. M. Asgher, M.J. Asad, S.U. Rahman, R.L. Legge, A thermostable α-amylase from a moderately thermophilic *Bacillus subtilis* strain for starch processing, J. Food. Eng.,79 (2007) 950-955.
6. C.R. Soccol, E.S. Ferreira da Costa, L.A.J. Letti, S.G. Karp, A.L. Woiciechowski, L.P.S. Vandenberghe, Recent developments and innovations in solid state fermentation, Biotechnology Research&Innovation., 1 (2017) 52-71.
7. A. Pandey, Solid-state fermentation, Biochem. Eng. J.,13 (2003) 81-84.
8. C.R. Soccol, L.P.S. Vandenberghe, Overview of solid state fermentation in Brazil, Biochem. Eng. J., 13 (2003) 205-218.
9. R.Kuhad, D. Deswal, S. Sharma, A. Bhattacharya, K. Jain, A. Kaur, Revisiting cellulase production and redefining current strategies based on major challenges, Renew. Sust. Energ. Rev., 55 (2016) 249-272.
10. D. Pessoa, A. Finkler, A. Machado, L. Luz, D. Mitchell, Fluid dynamics simulation of a pilot-scale solid-state fermentation bioreactor, Chem. Eng. Trans., 49 (2016) 49-54.
11. D.H. Bergey, Thermophilic bacteria, J. Bacteriol., 4 (1919) 301-306.
12. T. Aanniz, M. Ouadghiri, M. Melloul, J. Swings, E. Elfahime, J. Ibijbijen, M. Ismaili, M. Amar, Thermophilic bacteria in Moroccan hot springs, salt marshes and desert soils, Braz. J. Microbiol., 46 (2015) 443-453.
13. K. Tamura, J. Dudley, M. Nei, S. Kumar, MEGA4: molecular evolutionary genetics analysis (MEGA), Mol. Biol. Evol., 24 (2007) 1596-1599.
14. P. Bernfeld, Amylases, α and β. In: Methods in Enzymology I. Academic, New York (1955).
15. K.S. Harmeet, S. Kanupriya, K.G. Jugal, K.S. Sanjeev, Production of a thermostable α-amylase from *Bacillus* sp. PS-7 by solid state fermentation and its synergistic use in the hydrolysis of malt starch for alcohol production, Process Biochem., 40 (2005) 525-534.
16. A. Kunamneni, K. Permaul, S. Singh, Amylase production in solid-state fermentation by the thermophilic fungus *Thermomyces lanuginosus*, J. Biosci. Bioeng., 100 (2005) 168-171.
17. N. Mahanta, A. Gupta, SK. Khare, Production of protease and lipase by solvent tolerant *Pseudomonas aeruginosa* PseA in solid-state fermentation using Jatropha curcas seed cake as substrate, Bioresour. Technol., 99 (2008) 1729-1735.
18. K.R. Babu, T. Satyanarayana, α-Amylase production by thermophilic *Bacillus coagulans* in solid state fermentation, Process, Biochem., 30 (1995) 305-309.
19. S.M. Kotwal, M.M. Gote, S.R. Sainkar, M.I. Khan, J.M. Khire, Production of α-galactosidase by thermophilic fungus *Humicola* sp. in solid state fermentation and its application in soya milk hydrolysis, Process Biochem., 33 (1998) 337-43.
20. P. Turner, G. Mamoand E.N. Karlsson, Potential and utilization of thermophiles and thermostable enzymes in biorefining, Microbial. Cell Factories., 6:9 (2007) 1-23.
21. A. Pandey, C.R. Soccol, J.A. Rodriguez Leon, P. Nigam, Factors that influence on solid state fermentation. In: Pandey A, ed. Solid State Fermentation in Biotechnology: Fundamentals and Applications. New Delhi: Asiatech Publishers Inc., (2001) pp. 21-9.
22. B.L. Luiand, Y.M. Tzeng, Water content and water activity for the production of cyclodepsipeptide in solid state fermentation, Biotechnol. Lett., 21 (1999) 657-661.
23. M. Elibol, A.R. Moreira, Optimization some factors affecting alkaline protease production by a marine bacterium *Teredinobacter turnirae* under solid-state substrate fermentation, Process. Biochem., 40 (2005) 1951-1956.
24. R.V. Feniksova, A.S. Tikhomirova, E.E. Rakhleeva, Conditions for forming amylase and proteinase in surface cultures of *Bacillus subtilis*, Microbiologia., 29 (1960) 745-748.
25. S. Özdemir, F. Matpan, V. Okumus, A. Dündar, M.S. Ulutas, M. Kumru, Isolation of a thermophilic *Anoxybacillus flavithermus* sp. nov. and production of thermostable α-amylase under solid-state fermentation (SSF), Ann. Microbiol., 62 (2012) 1367-1375.
26. W.F. Li, X.X. Zhou, P. Lu, Structural features of thermozymes, Biotechnol. Adv., 23 (2008) 271-281.
27. M. Michelin, T. M. Silva, V. M. Benassi, S. C. Peixoto-Nogueira, L. A. Moraes, J. M. Leão, J. A. Jorge, H. F. Terenzi, M. L. Polizeli, Purification and characterization of a thermostable a-amylase produced by the fungus *Paecilomyces variotii*, Carbohydrate Res. 345 (2010) 2348-2353.
28. A.A. Saboury, Stability, activity and binding properties study of α-amylase upon interaction with Ca^{2+} and Co^{2+}, Biologia, 57 (2002) 221-228.

Trichoderma citrinoviride: A Potent Biopriming Agent for the Alleviation of Salt Stress in Maize

Trichoderma citrinoviride: Mısırda Tuz Stresinin Azaltılmasında Kullanılabilecek Potansiyel Bir Ön Muamele Ajanı

Research Article

Abdullah M. Yesilyurt*, Necla Pehlivan*, Nuran Durmus, Sengul A. Karaoglu
Department of Biology, Faculty of Arts and Sciences, Recep Tayyip Erdogan University, Rize, Turkey.

ABSTRACT

The rapid increase in global population and industrial pollution pose severe environmental threats to agriculture that are exacerbated by salt stress. Molecular characterization of new fungal isolates and assessment of their impact on agriculture might be an eco-friendly approach to modulating salt tolerance. Herein, fungal seed biopriming was conducted on salt (NaCl) stressed maize in a dose-dependent manner. Genetic lineages of fungi were identified using well-known fungal ITS (internal transcribed spacer) barcodes that revealed similarity to the *Trichoderma citrinoviride* (T11C) species. Fv/Fm, ETR and qP were recorded as close to optimum in bioprimed maize plants after application of salt stress. NPQ (nonphotochemical quenching) decreased slightly in respective groups. Higher photosynthetic pigment contents were also detected. T11C seed biopriming decreased the lipid oxidation remarkably under salt stress. SOD, GPX, GR and CAT activities were not found to be significantly induced in the roots or leaves of T11C after biopriming. However, higher RWC (relative water content), soluble protein and proline were measured in bioprimed test groups treated with high salt stress, demonstrating increased osmoregulatory capacity. Our ongoing research is directed toward developing powdered fungal biopreperations to assay multiple stress tolerances in agriculture for agro-economically important cereals such as maize.

Key Words
Trichoderma citrinoviride, seed biopriming, maize, chloropyhll fluorescence.

ÖZ

Küresel nüfus artışı ve endüstriyel kirlilik, tuz stresi ile birleştiğinde, tarımsal şartları ağırlaştıran çevresel tehditlere dönüşmektedir. Yeni fungal izolatların moleküler karakterizasyonu ve bunların tarım üzerindeki etkilerinin araştırılması, tuz stresi toleransının kontrolünde çevre dostu bir yaklaşım olabilir. Bu bağlamda mevcut çalışmada, doza bağımlı tuz (NaCl) stresi uygulanan mısır tohumlarına fungal ön muamele gerçekleştirilmiştir. Fungusun genetik bağlantıları iyi bilinen ITS barkodları kullanılarak tanımlanmış ve *Trichoderma citrinoviride* (T11C) türüne benzerlik gösterdiği ortaya çıkarılmıştır. Fungal uygulamanın yapıldığı stres altındaki mısır bitkilerinde, maksimum kuantum verimi (Fv/Fm), elektron transfer oranı (ETO), ve fotokimyasal kullanılmanın (qP) optimuma yakın olduğu, bununla birlikte NPQ (fotokimyasal olmayan floresans sönmesi) değerlerinin ise; ilgili gruplarda azaldığı belirlenmiştir. Ayrıca, fotosentetik pigment içeriklerinin yüksek olduğu kaydedilmiştir. T11C fungal muamelesinin, tuz stresi altındaki bitkilerde lipid oksidasyonunu düşürdüğü tespit edilmekle birlikte, mısır kök ve yapraklarında SOD, GPX, GR ve CAT aktivitelerini belirgin şekilde arttırmadığı gözlenmiştir. Yüksek tuz stresi uygulanan test gruplarında, yüksek RWC (göreceli su içeriği), çözünebilir protein ve prolinin tespiti, fungal ön muamelenin, bitkilerde artan bir osmoregülasyon kapasitesini tetiklediğini kanıtlamıştır. Devam eden çalışmalar, mısır gibi ekonomik açıdan önemli tahıllarda çoklu stres toleranslarını test etmek adına, tarımsal uygulamalarda kullanılabilecek toz halindeki mantar biyopreparatlarının geliştirilmesine yöneliktir.

Anahtar Kelimeler
Trichoderma citrinoviride, tohum ön muamelesi, mısır, klorofil floresans.

Article History: Received: Sep 10, 2017; Revised: Nov 22, 2017; Accepted: Dec 06, 2017; Available Online: Feb 20, 2018.

DOI: 10.15671/HJBC.2018.218

Correspondence to: A.M. Yeşilyurt and N. Pehlivan, Department of Biology, Recep Tayyip Erdogan University, Rize, Turkey.
Tel: +90 464 223 6126-1839 Fax: +90 464 223 40 19 E-Mail: necla.pehlivan@erdogan.edu.tr

INTRODUCTION

Salt stress is one of the most important agricultural threats expected to impact crop yields in the near future due to intensive irrigation, chemical contamination from inorganic fertilizers and destruction of natural vegetation lands on earth [1]. These effects are expected to become increasingly catastrophic in agriculture considering the compounding threat of severe climate fluctuations and increased air pollution across the globe. Consequently, crop yields may decline and jeopardize our food security. Hence it is necessary to take precautions that can reduce plant stresses and stave off damages to the environment.

Maize is a crucial cereal for the agricultural provisions required by mankind. Maize is employed in a wide range of applications including clothing, food and alternative fuels [2]. Aside from a few exception genetic variants [3], maize is a salt-sensitive plant with significant reduction in crop yield following salt stress. Thus, genetic modifications that bolster salt tolerance may improve yields in maize.

Though maize does recruit various mechanisms to combat salt stress, even moderately elevated soil salt content can debilitate growth. Accordingly, crop yield may improve with incorporation of externally derived stress relief agents during key growth phases [4]. Chemical priming is one approach to increasing stress tolerance that entails exposing the plant to periodically increasing chemical stressors over a prolonged time frame to safely activate endogenous defense mechanisms. However, the chemicals used for plant priming are mostly synthetic chemicals (reactive oxygen, nitrogen, sulfur species (RONSS) [5] or fungicides (pyrabactin) [6] and have potential to be toxic to the environment and consumers throughout the food web. Natural agents/metabolites may be used as an eco-friendly approach. Fungal genus *Trichoderma* may serve as a viable candidate and is the focus of this study. *Trichoderma* are endophytic plant symbionts that are commonly used for the biological control of various plant pathogens via chemotropic and mycoparasitic interactions [7]. Some *Trichoderma* strains can interact with roots for disease resistance and abiotic stress tolerance consequently improving plant growth and development under unfavorable environmental conditions [8]. However, since different genetic backgrounds of this genus might exert variable potency to eliminate stress-related injuries in the plant cell, molecular identification of new fungal isolates can be important for agricultural preparate purposes as organic stress-relieving fertilizers. Additionally, since the photosynthetic efficiency of salt-stressed maize after *Trichoderma* biopriming is unknown in the literature, our approach is to modulate the salt stress response using our own isolate, T11C, to mitigate salt stress in before maize seeds reach germination.

MATERIALS and METHODS

Isolation and Molecular Identification of Target Fungal Strain

Microfungus used in this study were isolated from the soil of tea gardens in Rize-İyidere of Turkey (41°0.731'N, 40°21.649'E) [9] and stored in the Culture Collection Unit of the Microbiology subdivision at Recep Tayyip Erdogan University, Turkey. Annual precipitation in this area exceeds 2400 mm annually and is classified as a humid, subtropical climate. After phenotypic identification, the isolate was further verified by molecular characterization via a 700 base pair polymerase chain reaction using fragment amplification of the 5.8 S rDNA gene (using oligonucleotides 5'-ATG AGT ATT CAA CAT TTC CG -3' and 5'-CCA ATG CTT AAT CAG TGA GG-3') of ITS-1 and ITS-2 regions.

Revival of the Culture and Preparation of Fungus Inoculum

The target microfungus was derived from the cultures grown on petri dishes containing Potato Dextrose Agar (Merck, Germany) incubated at 25°C for 14 days. Hyphae and spores acquired from pure culture were then transferred into flasks filled with broth media (Malt Extract) and were positioned in a rotary shaker (GFL, Germany) at 27°C for 12 days. Filtration was performed to obtain mycelia which were washed with sterile H_2O and placed in liquid nitrogen. Conidial densities in the spore suspension were

recorded by a Neubauer slide under a basic light microscope (Olympus BX41, USA). The method of Goettel and Inglis [10] was used to set the density of inoculum up to 1×10^7 conidia/mL.

Preparation of Fungus Suspension

T11C fungal inoculum was mixed with 2% carboxymethyl cellulose and 1% Tween 20 to achieve adhesion and homogeneity, respectively. Then, Zea mays L. cv. Samada 07 seeds were subjected to a volume of 1×10^7 conidia/mL suspension. Control seeds were soaked in equal volume of sterile distilled water. Incubation was performed for one hour after 30 min seed sterilization with 1% bleach solution (NaClO) and rinsed thoroughly in distilled water.

Salt Stress Applications

The applications were organized into a randomized block design. Six seeds for each treatment were placed into plastic pots (12 by 12 by 5 cm) and incubated at 25±1°C with 16 h of light with 70% relative humidity and 350 μmol m^{-2} s^{-1} light intensity period in a growth chamber. Soil used for planting was autoclaved in polyethylene bags two times before used. Six different groups were used to conduct salt stress experiments: non-bioprimed control seeds watered with pure H_2O (control); 50 mM NaCl; or 100 mM NaCl; and seeds bioprimed with the isolated T11C strain and no salt treated (T11C), bioprimed with T11C at first, thereafter subjected to the 50 mM NaCl (50 mM + T11C) and 100 mM NaCl (100 mM + T11C). The efficacy of T11C inoculum on the growth of maize seedlings was evaluated after 2 weeks following seed planting. 50 mM and 100 mM NaCl were exposed to the seedlings every two days for 10 days. Controls were watered with pure H_2O. In case of nutrient deficiency, Hoagland solution was applied every 5 days from sowing to harvested day. Maize seedlings from each treatment were gently separated from the pots and phenotypic and biochemical analyses were conducted.

Growth Measurements

Planting mix of the maize seedlings of each treatment were gently removed from the root system. Roots and shoots were dried at 70°C for 72 hours to record dry weight (DW) values. Root fresh weight (FW) and DW of maize seedlings besides respective lengths were recorded. Turgid weights of 0.5 g leaf samples were noted after soaking in distilled H_2O in the dark at 4°C for 16 h to measure the RWC [11].

Analysis of Biochemical Compounds

Following plant salt stress, response parameters were determined in the second fully developed apical leaves of each test plant based on the cited references: concentration of photosynthetic pigments (total chlorophyll (Chl) and carotenoid (Car)) [12,13], and malondialdehyde (MDA) expressed as nmol MDA per g FW) which is the end-product of lipid oxidation [14] and proline accumulation was given as mg proline per g FW in the presented figures [15].

Antioxidant Enzyme activities

Antioxidant enzymes, such as superoxide dismutase (SOD, EC 1.15.1.1), guaiacol peroxidase (GPX, EC 1.11.1.7), catalase (CAT, EC 1.11.1.6) and glutathione reductase (GR, EC 1.6.4.2) were determined spectrophotometrically by using the methods of Dhindsa and Matowe [16], Urbanek et al. [17], Aebi [18] and Foyer and Halliwell [19], respectively. Enzyme extractions for the activity assays were conducted in potassium phosphate (K_2HPO_4) buffer (50 mM, pH 7.0) prepared with 1 mM EDTA and 1% polyvinylpolypyrrolidone. Bovine serum albumin was used for soluble protein measurements [20].

Chlorophyll Fluorescence Measurements

The measurements were conducted after day 10 of salt stress exposure. The chlorophyll fluorescence parameters which were recorded by OS5P modulated fluorometer (Opti-Sciences, Hudson, NH, USA) measured in second fully developed apical leaf. The maximum quantum efficiency of PSII readings (Fv/Fm (maximal efficiency of PSII photochemistry); Fv= Fm–F0 of dark adapted leaves were collected with dark leaf clip after a short 20 min dark-acclimation period. Fm (maximum) and F0 (minimum) yields of the fluorescence of an illuminated leaf obtained based on the method of saturation pulse. The quantum yield of PSII photochemistry (ΦPSII) data was acquired by a steady state light adapted yield protocol that yields the ratio between the light amount absorbed in the photochemistry of PSII and the light absorbed by chlorophyll pigments of PSII. Nonphotochemical (NPQ) and photochemical

quenching (Pq) besides the electron transport rate (ETR) were documented using the Quenching protocol with a PAR clip apparatus. All mentioned parameters were calculated by Fluorometer software itself.

Statistical Analysis

All tests were performed in triplicate with at least three technical and three biological replicates per treatment. Analysis of variance (ANOVA) with post-hoc Tukey's range test was used to compare averages between different groups. Statistical significance was set to a level of 5% ($P < 0.05$) [21]. Statistical analyses were performed using the SigmaPlot 12 software (Systat Software Inc., Chicago, USA).

RESULTS

Identification of *Trichoderma citrinoviride* Strain 11C

Amplified DNA sequences of fungus were subjected to the ClustalW multiple sequence alignment in BioEdit. Dendrogram created by neighbor-joining analysis showed that the fungal strain is phylogenetically linked to the *Trichoderma citrinoviride* T200 with 99% sequence similarity (NCBI GenBank: HQ596983.1) from now on, we have labeled the inoculant as T11C for further physiological tests (unpublished data).

T11C Seed Biopriming Improves Phenotypic Growth Traits Under Dose Dependent NaCl Stress

We have analyzed if T11C biopriming have potential to provide increased tolerance in dose dependent NaCl stressed maize plants. The tolerance capacity/performance of the plants from each treatment (control (C), the 50 mM NaCl, 100 mM NaCl, T11C only treated and 50 mM and 100 mM NaCl stressed plus T11C treated (50 mM + T11C and 100mM + T11C respectively) were evaluated (Figure 1). At 50 mM and 100 mM NaCl concentrations, both root and shoot lengths displayed reductions in comparison to the well-watered control plants (Figure 1A). T11C seed biopriming improved both root and shoot growth of 50 mM and 100 mM NaCl stressed plants (50 mM + T11C and 100mM + T11C) in comparison with

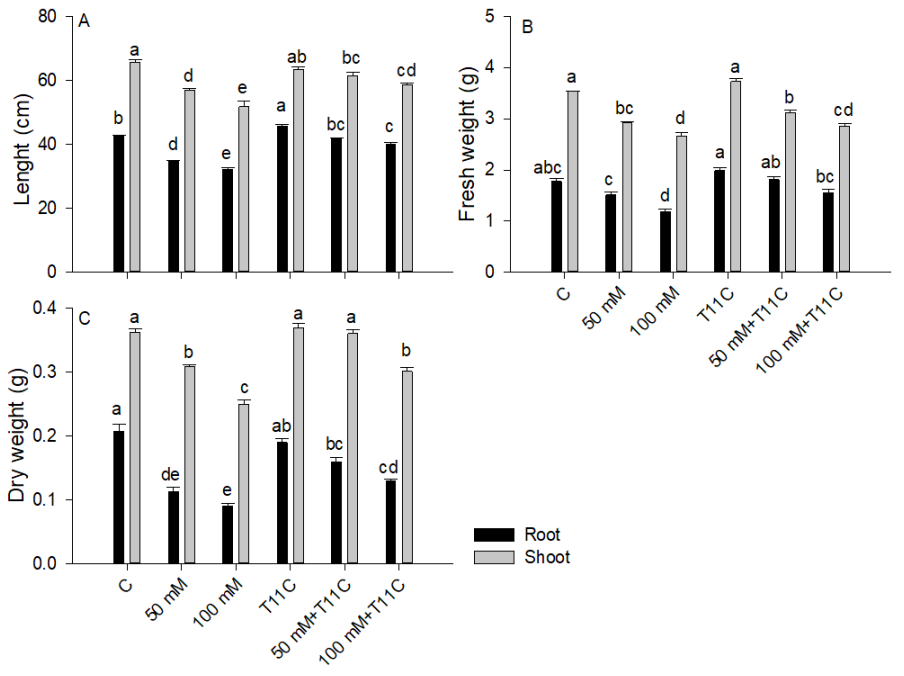

Figure 1. The impact of seed biopriming of *Trichoderma citrinoviride* strain 11C on (A) growth and (B,C) biomass yield of maize plants under different salt concentrations for ten days. The plants were organized into 6 treatments: well-watered only (C), exposed to 50 and 100 mM NaCl only (50 mM, 100 mM), seed bioprimed with T11C and well-watered (T11C), seed bioprimed with T11C and 50 mM NaCl stressed (50mM + T11C), seed bioprimed with T11C and 100 mM NaCl stressed (100 mM + T11C). Error bars indicate standard deviation and different letters (a, b, c, d, e, f) represent significant difference (ANOVA, $p < 0.05$) among the different treatments (n= 3).

the non-bioprimed 50 mM and 100 mM NaCl plant groups by 20.67% and 24.06% and 7.89% and 13.52% respectively (Figure 1A).

Conversely, remarkable differences were detected in fresh and dry weights of roots and shoots upon either salt treatment or priming. The reductions in root fresh and dry weights were found to be at least 14% and 45%, respectively, under salt stress compared to with weights of well-watered control plants. When salt concentration was increased to 100 mM, 100mM + T11C bioprimed plants showed improved root fresh and dry weight at a increase of 31.69% and 43.33%, respectively, when compared to the 100 mM salt stressed only group of plants (Figures 1B and 1C).

Additionally, when shoot data was analyzed in terms of fresh and dry weights, seed biopriming displayed similar protective effects, yet with lesser increases by 6.5% and 19.48% (for the 50 mM + T11C group), respectively, besides 7.28% and 20.48% (for the 100mM + T11C group) respectively, compared to the salt stressed only plants (50 mM and 100 mM NaCl only group (Figures 1B and 1C).

T11C Bioprimed Maize Seeds Outperform the Control Plants with Regard to the Water Utilization

To analyze how seed biopriming of T11C would affect maize plants in terms of water status and pigment concentrations (Chl and Car) under salinity, different levels of NaCl concentrations were applied separately. At the end of the experimental period (10 days) the reduction observed in the RWC of the control roots and leaves was significant under salt stress, whereas T11C seed biopriming applied shortly before germination leading to an induction of robust water status of roots and leaves of 50 mM and 100 mM NaCl stressed plants for each dose of stress by keeping the water rate by 92.36% and 91.78% for the roots and 93.29% and 91.54% for the leaves for respective treatments (Figure 2A).

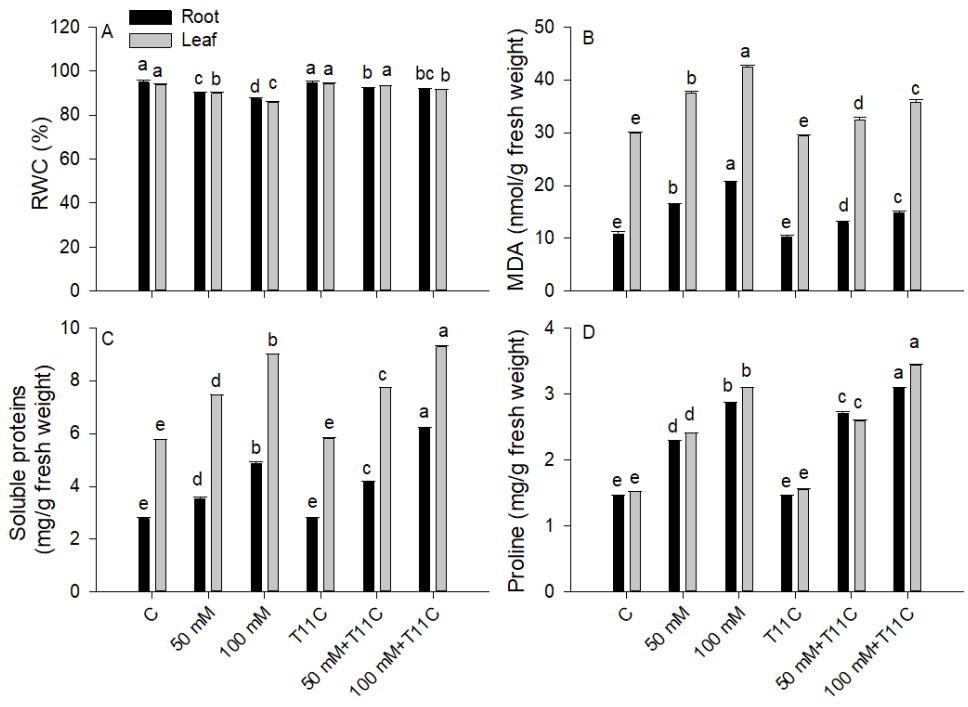

Figure 2. The potency of seed biopriming of *Trichoderma citrinoviride* strain 11C on relative water (RWC) (A), malondialdehyde (MDA) (B), soluble proteins (C) and proline (D) contents of maize plants under different salt concentrations for ten days. The plants were organized into 6 treatments: well-watered only (C), exposed to 50 and 100 mM NaCl only (50 mM, 100 mM), seed bioprimed with T11C and well-watered (T11C), seed bioprimed with T11C and 50 mM NaCl stressed (50mM + T11C), seed bioprimed with T11C and 100 mM NaCl stressed (100 mM + T11C). Error bars indicate standard deviation and different letters (a, b, c, d, e, f) represent significant difference (ANOVA, $p < 0.05$) among the different treatments (n= 3).

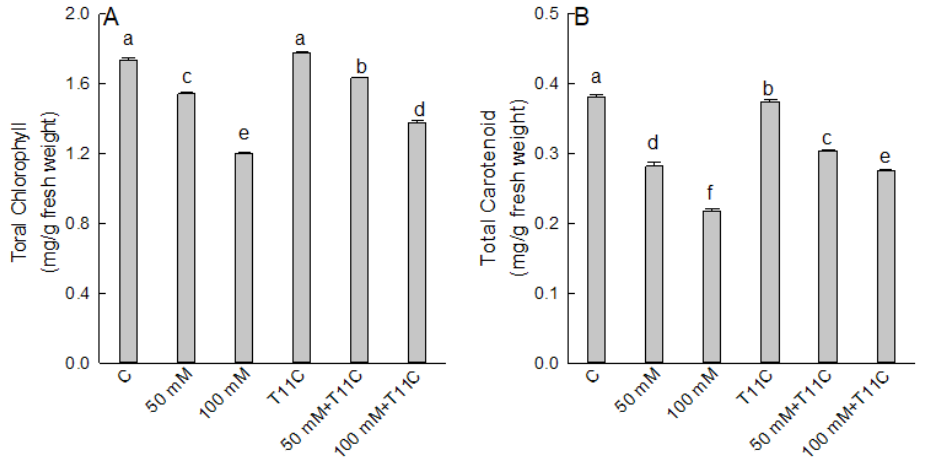

Figure 3. The potency of seed biopriming of *Trichoderma citrinoviride* strain 11C on total chlorophyll (A) and carotenoid (B) contents of maize plants under different salt concentrations for 10 days. The plants were organized into 6 treatments: well-watered only (C), exposed to 50 and 100 mM NaCl only (50 mM, 100 mM), seed bioprimed with T11C and well-watered (T11C), seed bioprimed with T11C and 50 mM NaCl stressed (50mM + T11C), seed bioprimed with T11C and 100 mM NaCl stressed (100 mM + T11C). Error bars indicate standard deviation and different letters (a, b, c, d, e, f) represent significant difference (ANOVA, $p < 0.05$) among the different treatments (n= 3).

T11C Bioprimed Maize Seeds Confer Healthier Biochemical Characteristics and Photosynthetic Pigment Content Under either Dose of NaCl Stress

To document the effect of T11C seed biopriming in maize under different doses of NaCl, relevant biochemical parameters were assayed (Figures 2, 3 and 4). Without NaCl in the soil mix, no significant difference was observed between well-watered control and T11C treated only control groups. However, high dose of salt led to significant proline accumulation with at least 7% and 8% increase in the roots and leaves, respectively, compared to the non-bioprimed but NaCl only treated group. T11C seed biopriming also remarkably reversed the lipid oxidation percentage in each dose of NaCl stressed maize roots by decreasing the production of MDA at a rate of 20.47% and 28.12% with respect to the 50 mM and 100 mM NaCl only irrigated plants, respectively. A similar healing effect (at least by 13% increase) was detected in turn in the leaves of maize with T11C presence (Figure 2B). Soluble protein content, on the other hand, was assayed in the roots and leaves of maize plants and almost 30% increase was detected in the roots of 100 mM + T11C treated plants with regard to the 100 mM NaCl treated only ones (Figure 2C). We have also detected that proline as an osmoprotectant significantly accumulated in the roots and leaves of the plants irrigated with two different NaCl concentrations as anticipated (Figure 2D).

On the other hand, total Chl of the maize plants grouped into 50 mM + T11C and 100mM + T11C were found to be represented the identical tendency by 5.99% and 14.61% increase rates when compared with 50 mM and 100 mM NaCl irrigated only plants (Figure 3A). For the concentrations of Car, increase was recorded by 7.79% and 26.49% for the respective treatments (Figure 3B).

All antioxidant enzymes were induced gradually both in the roots and leaves of the maize plants under either concentrations of NaCl stress with regard to the well-watered control (Figure 4). Interestingly the SOD activity markedly decreased by at least 9% and 21.36% in the roots and the leaves, respectively, of the T11C bioprimed plants that were irrigated with 100 mM NaCl (Figure 4A).

However, GPX activity was increased by 14.74% and 5.78% in the roots and 5.45% and 2.36% in the leaves of 50 mM + T11C and 100mM + T11C treated groups, respectively, when compared to the 50 mM and 100 mM NaCl only treatments

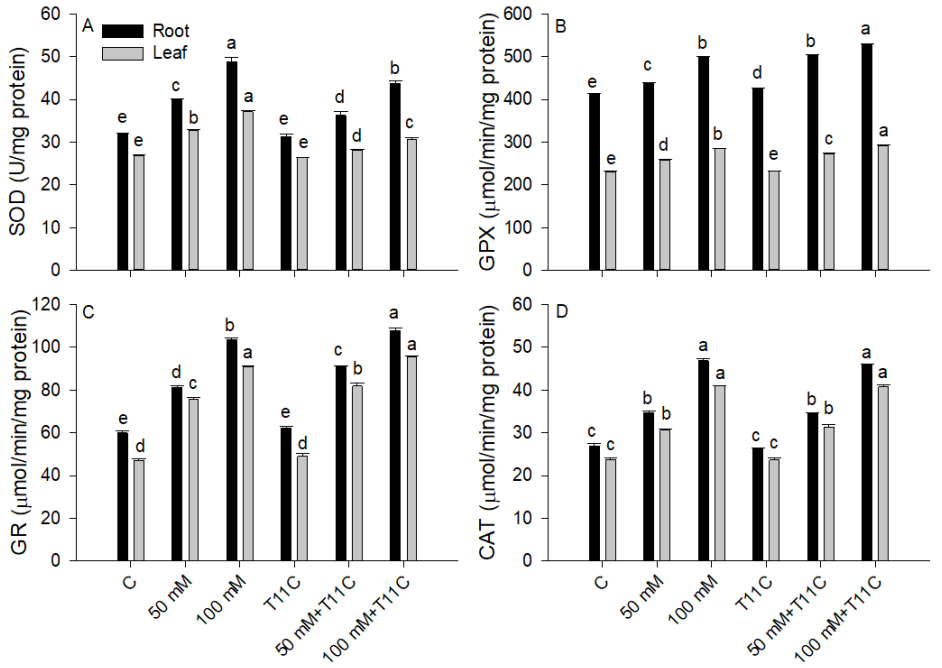

Figure 4. The potency of seed biopriming of *Trichoderma citrinoviride* strain 11C on SOD (A), GPX (B), GR (C) and CAT (D) activities in maize plants under different salt concentrations for ten days. The plants were organized into 6 treatments: well-watered only (C), exposed to 50 and 100 mM NaCl only (50 mM, 100 mM), seed bioprimed with T11C and well-watered (T11C), seed bioprimed with T11C and 50 mM NaCl stressed (50 mM + T11C), seed bioprimed with T11C and 100 mM NaCl stressed (100 mM + T11C). Error bars indicate standard deviation and different letters (a, b, c, d, e, f) represent significant difference (ANOVA, $p < 0.05$) among the different treatments (n= 3).

(Figure 4B). Accordingly, when we analyzed the GR data, the increase was 12% and 4.28% for the roots and 7.96% and 5% for the leaves of the 50 mM + T11C and 100mM + T11C group of plants in comparison with the above mentioned respective groups of treatments (Figure 4C). However, no significant difference was detected in the CAT activity either in the roots or leaves of the plants inoculated with 50 mM + T11C and 100mM + T11C treatments compared with respective NaCl only groups (Figure 4D).

T11C Bioprimed Maize Seeds Display Improved Chlorophyll Fluorescence

The efficiency measured as Fv/Fm was decreased relative to the control plants after 10 days of salt stress under each concentration of salt (50 mM and 100 mM NaCl) (Figure 5). Reductions were observed in Fv/Fm, ETR, qP and ΦPSII by each dose of salt concentration whereas, NPQ values were slightly increased depending on NaCl dosage (Figure 5A, B, C, D and E). Subsequently, T11C biopriming apparently elevated the efficacy of the photosynthetic apparatus in maize plants. Data reported improvements by 4.41% in Fv/Fm, 3.01% in ΦPSII, 10.61% in ETR and 4.73% in qP. In addition, a decline by 16.38% in NPQ was detected in 100 mM + T11C treatments with regard to the 100 mM NaCl treatment only (Figure 5).

DISCUSSION

Salts are essential criteria for robust soil characteristics. However, excessive amounts of salt in the soil, especially NaCl (table salt), induce changes in the genetic expressions of plants that limit their productivity, causing yield penalties and death [22]. The degree of growth impairment might vary based on salt dose and the plant's genetic composition. However, glycophytes are particularly susceptible to stress under high concentrations of salt [3].

One of the most important crops for food security is maize but most strains are glycophytes, excluding the few salt tolerant varieties resulting from polymorphisms during evolution or natural cross-pollination [3]. Maize has a wide range of applications, from our clothing to our food. It

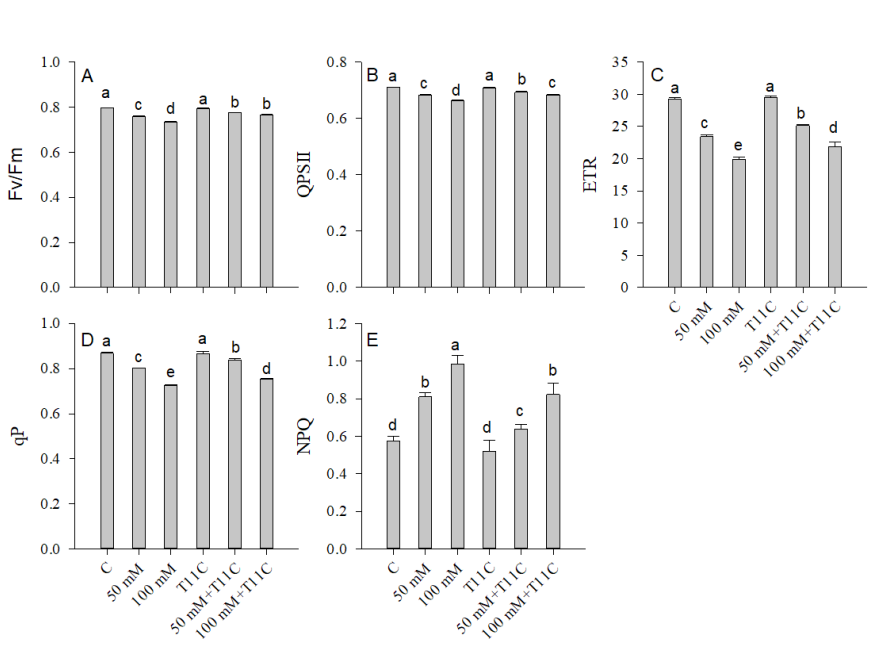

Figure 5. The impact of seed biopriming of *Trichoderma citrinoviride* strain 11C on chlorophyll fluorescence parameters (A, B, C, D and E) of maize plants under different salt concentrations for ten days. The plants were organized into 6 treatments: well-watered only (C), exposed to 50 and 100 mM NaCl only (50 mM, 100 mM), seed bioprimed with T11C and well-watered (T11C), seed bioprimed with T11C and 50 mM NaCl stressed (50mM + T11C), seed bioprimed with T11C and 100 mM NaCl stressed (100 mM + T11C). Error bars indicate standard deviation and different letters (a, b, c, d, e, f) represent significant difference (ANOVA, $p < 0.05$) among the different treatments (n= 3).

is also an important source of alternative fuels and raw dextrin derived from processed starch. Using maize in thousands of processed products demonstrates its agro-economic importance [2]. Given that most strains of maize are glycophytic, even moderate concentrations of salt are sufficient to impair yields. Additionally, global climate change is worsening secondary stresses that decrease salt tolerance. Therefore, food security is becoming increasingly compromised. Securing agricultural productivity in a safe manner is ultimately a must. The problem demands eco-friendly approaches that do not exert additional stress on the environment. The current chemical solutions are problematic for human health and accrue large costs, in addition to harming the beneficial microbial flora in the soil [23]. In this context, *Trichoderma* genus poses heightened suitability. Instead of using chemical solutions, molecular identification of new families of microorganisms that possess the capacity for stress relief might provide safe, organic and affordable stress control.

The *Trichoderma* genus, in addition to *Bacillus*, *Azotobacter* and *Rhizobium*, are important as biotic stress-fighting agents and microbial fertilizers [24,25]. Harman and Kubicek [24] also show that the yield quality in the field can be increased by 300% after the addition of *Trichoderma hamatum* or *Trichoderma koningii*. *Trichoderma* is therefore not only a good biocontrol agent, but also triggers fertility. Furthermore, some species have been shown to produce effective antibiotics, but should be used for biocontrol purposes carefully [26]. Although they are used in biopesticide and organic bio-fertilizer production in agriculture due to their beneficial properties, we have not come across any other data showing the improvement of photosynthetic efficiency for NaCl tolerance (when *Trichoderma* is exposed in advance as a seed biopriming agent). The main goal of the present study was to investigate the biopriming capability of T11C characterized from the soil of tea plants around Rize located in the southeastern Black Sea region in Turkey. Since a well-known factor that has a negative impact on plants under salinity conditions is the accumulation of reactive oxygen species (ROS),

we have tested whether T11C has the ability to reduce damages resulting from accumulation of ROS by inducing antioxidant defense in maize seedlings during dose dependent (50 mM and 100 mM) NaCl stress.

Trichoderma biocontrol strains have mechanisms to enhance plant root development [27]. The rhizosphere being changed by the genus provides a set of benefits to the plant by supporting ventilation in the plant root system [24]. Our results supported this notion and we have found outperforming root and shoot lengths as well as root and shoot fresh/dry biomasses in T11C bioprimed plants under salt stress as compared with the plants treated with NaCl only. Even under well-watered conditions T11C biopriming led to better performance than that of the well-watered only group of plants. Interestingly, when low dose salt (50 mM) exists in the soil, T11C biopriming provided better root fresh weight than that of the well-watered control.

Reduced accumulation of MDA in seed bioprimed group of maize plants was compatible with the above mentioned phenomenon and showed a significant decrease compared to salt only groups after ten days of stress under each dose of NaCl. These findings demonstrate that the oxidation of lipids (reflecting membrane injury) was ameliorated to some extent both in roots and leaves of maize plants bioprimed with T11C, after subjected to varying salt concentrations. Detected pattern in terms of MDA amount was similar between the roots and leaves (Figure 2B). This data is consistent with the hypothesis that T11C exerts a healing effect following NaCl-induced oxidative injury.

Based on our data corroborating that T11C affects the germination of plants by utilizing the positive effect on growth and promoting fertility, greenness, photosynthesis activity, and CO_2 uptake, T11C seed biopriming might be attributable to the improvement in the rate of photosynthesis by controlling the three parameters discussed previously. Apart from that, because of its very effective enzyme systems, Trichodermas are also widely used in other applications such as textiles, food and paper [28]. These enzyme activities help plants increase water-use efficiency particularly due to its capability in the growth of roots and water-extracting and/or holding capacity of plant cells [25,27]. Another hypothesized impact of Trichoderma spp. on plants is the solubilisation of some insoluble or semi-soluble minerals by acidifying the soil environment. This subsequently leads to more efficient nutrient availability and/or uptake besides an increase in the chelation capability of some metals (iron particularly) for the plants by siderophores [29]. In accordance with that, we have found that T11C bioprimed maize plants perform better in terms of RWC under both concentrations of salt in either roots or leaves (Figure 2A).

We first have found a considerable decline in Chl and Car content under higher doses of NaCl stress (100 mM) as anticipated. However, an hour of T11C seed biopriming in advance of the germination phase was found to improve plant photosynthetic efficiency under both saline conditions (50 mM and 100 mM). Indeed, there is proof that the target fungus bolsters plant tolerance to abiotic stresses in different developmental stages [25,27]. Yet the efficiency grade was found to be higher with lower dose (50 mM) of NaCl stressed maize plants than with higher dose (100 mM) (Figure 3A and 3B). It is a well-known characteristic of salt stress that salt reduces the Car or Chl pigments in the photosynthetic apparatus [30]. In this aspect, Figure 3A and 3B show that T11C seed biopriming reversed the hazardous impact of both NaCl doses (commonly achieved in nature), consequently allowing protection from reduced photosynthetic efficiency and decrease in the free radical damage potential. Intactness of the Car pigments is reportedly responsible for the suppression of the photo-inhibition of chlorophyll pigments and benefits from increased antioxidant capacity [30]. Some phytohormones triggered by T11C (mainly auxin and its derivatives) might be one of the reasons for this protection in terms of suppressing pigment degradation.

Many studies report that salt stress causes disorganization of ROS scavenging [31-36]. Given the importance of antioxidant enzymes, induction is a protective pathway against the injurious

effects of ROS, there is a non-enzymatic pathway to modify ROS into less injurious forms within the plant cell [31]. Our enzyme activity data showed no significant increases in SOD, GPX, GR and CAT activities in T11C bioprimed maize plants in the presence of salinity stress both in roots and shoots (Figure 4A, 4B, 4C and 4D). This data is consistent with our previous report, in which we have not determined significant changes in enzyme activity under salt stress by using a different species of this genus [34]. Proline and soluble protein accumulation on the other hand, (osmoregulation by osmoprotectant accumulation in other words) might be the key factor responsible for salt tolerance of the 100 mM NaCl stressed group that leads to vigorous physiological characteristics observed in T11C bioprimed maize plants shortly before germination.

We have also measured Fv/Fm, NPQ, qPSII, ETR and qP values, all of which are vital parameters for tracking the effectiveness of photosynthetic capacity. By considering the knowledge that Fv/Fm is also a favorable parameter which allows detection of damage and possible photo-inhibition of PSII [35], we have deduced that PSII photochemistry (which shows the ratio between Fv and Fm) was much closer to optimum in bioprimed maize plants under NaCl stress (Figure 5) although no significant difference between lower and higher dose of salt treated groups in terms of Fv/Fm ratio was detected. ETR and qP was also improved greatly under salt stress in T11C-inoculated plants compared to the salt stress only group. On the other hand, since the light harvesting process of pigments occurs depending on each other, any favorable output in a parameter might cause depletion in the output of the other parameters [36], thus the decline detected in the NPQ values might be a result of the increase in the photochemistry of photosynthesis in the T11C inoculated maize plants.

CONCLUSIONS

In conclusion, seed biopriming with T11C has shown plant growth triggering capacity that improves the root and shoot quality of maize in addition to enhancing resistance to moderate and high salt stress conditions. The use of T11C at the commercial scale may therefore improve crop yields in agricultural applications. With the help of ongoing formulation experiments, we seek to develop cost-effective salt stress relief powder formulas to replace the expensive nitrogen, phosphorus and/or potassium-containing commercial fertilizers which are frequently used in agriculture today.

ACKNOWLEDGEMENTS

Present work was supported via research funds (project numbers: 2012.102.03.3 and 2015.53001.102.03.07) provided by the Recep Tayyip Erdogan University.

References

1. M. Pessarakli, I. Szabolcs, Handbook of Plant Crop Stress, NY (1999) USA: CRC Press.
2. Food and Agriculture Organization of the United Nations Save and Grow in practice maize rice wheat. A guide to sustainable cereal production, (2016) Rome.
3. P.M. Hasegawa, R.A. Bressan, J.K. Zhu, H.J. Bohnert, Plant cellular and molecular responses to high salinity. Ann. Rev. Plant Physiol. Plant Mol. Biol., 51 (2000) 463-499.
4. J.K. Zhu, Genetic analysis of plant salt tolerance using arabidopsis, Plant Physiol., 124 (2000) 941-948.
5. V. Fotopoulos, A. Christou, C. Antoniou, G. Manganaris, Hydrogen sulphide: a versatile tool for the regulation of growth and defence responses in horticultural crops, J. Hortic. Sci. Biotechnol., 90 (2015) 227-234.
6. P. Filippou, C. Antoniou, T. Obata, K. Van Der Kelen, V. Harokopos, L. Kanetis, V. Aidinis, F. Van Breusegem, AR. Fernie, V. Fotopoulos, Kresoxim-methyl primes Medicago truncatula plants against abiotic stress factors via altered reactive oxygen and nitrogen species signalling leading to downstream transcriptional and metabolic readjustment, J. Exp. Bot., 67 (2016) 1259-1274.
7. A. Sofo, G. Tataranni, A. Scopa, B. Dichio, C. Xiloyannis, Direct effects of *Trichoderma harzianum* strain T-22 on micropropagated GiSeLa6 (R) (Prunus spp.) rootstocks, Environ. Exp. Bot. 76 (2012) 33-38.
8. R. Hermosa, A. Viterbo, I. Chet, E. Monte, Plant-beneficial effects of *Trichoderma* and of its genes, Microbiology 158 (2012) 17-25.
9. S.A. Karaoglu, S. Ulker, Isolation, identification and seasonal distribution of soilborne fungi in tea growing areas of Iyidere-Ikizdere vicinity (Rize-Turkey), J. Basic Microbiol., 46 (2006) 208-218.
10. M.S. Goettel, D.G. Inglis Fungi: Hyphomycetes. In: Lacey LA, editor. Manual of techniques in insectpathology, London, UK: Academic Press, (1997) 213-249.
11. F.J. Castillo, Antioxidative protection in the inducible CAM plant *Sedum album* L. following the imposition of severe water stress and recovery, Oecologia, 107 (1996) 469-477.

12. D.I. Arnon, Copper Enzymes in Chloroplasts, Polyphenoloxidase in *Beta vulgaris*, Plant Physiol., 24 (1949) 1-15.
13. E.M.J. Jaspars, Pigmentation of tobacco crown-gall tissues cultured in vitro in dependence of the composition of the medium, Physiol. Plant, 18 (1965) 933-940.
14. R.L. Heath, L. Packer, Photoperoxidation in isolated chloroplast, I. Kinetics and stochiometry of fatty acid peroxidation, Arc. Biochem Biophys., 125 (1968) 189-198.
15. L.S. Bates, R.P. Waldren, L.D. Teare, Rapid determination of free proline for water-stress studies, Plant Soil, 39 (1973) 205-207.
16. R.S, Dhindsa, W. Matowe, Drought tolerance in two mosses: correlated with enzymatic defence against lipid peroxidation, J. Exp. Bot., 32 (1981) 79-91.
17. H. Urbanek, E. Kuzniak-Gebarowska, K. Herka, Elicitation of defense responses in bean leaves by *Botrytis cinerea* polygalacturanase, Acta. Physiol. Plant, 13 (1991) 43-50.
18. H. Aebi, Catalase. In: Bergmeyer H, editor. Methods of Enzymatic Analysis. 3rd ed. Weinheim, Germany: Verlag Chemie, (1983) 273-286.
19. C.H. Foyer, B. Halliwell, Presence of glutathione and glutathione reductase in chloroplast: a proposed role in ascorbic acid metabolism, Planta, 133 (1976) 21-25.
20. M.M. Bradford, A rapid and sensitive method for the quantitation of microgram quantities protein utilizing the principle of protein-dye binding, Ann. Biochem., 72 (1976) 248-254.
21. J.N. Miller, J.C. Miller, Statistics and Chemometrics for Analytical Chemistry, Atlanta, Pearson/Prentice USA, 2005.
22. B. Gupta, H. Bingru, Mechanism of salinity tolerance in plants: physiological, biochemical, and molecular characterization, Int. J. Genom., (2014) http://dx.doi.org/10.1155/2014/701596.
23. J. Dluzneiwska, Reaction of fungi of *Trichoderma* genus to selected abiotic factors, E. J. Polish Agric. Uni. Agro., 6 (2003) 239-242.
24. G.E. Harman, P.K, Kubicek *Trichoderma* and *Gliocladium*: Enzymes, biological control and commercial applications, London, UK (1998) Taylor and Francis.
25. H. Bae, R.C. Sicher, M.S. Kim, S.H. Kim, M.D. Strem, RL. Melnick, BA. Bailey, The beneficial endophyte *Trichoderma hamatum* isolate DIS 219b promotes growth and delays the onset of the drought response in *Theobroma cacao*, J. Exp. Bot., 60 (2009) 3279-295.
26. T. Benitez, A.M. Rincon, M.C. Limon, A.C. Codon, Biocontrol mechanisms of *Trichoderma* strains, Int. Microbiol., 7 (2004) 249-260.
27. G.E. Harman, Myths and dogmas of biocontrol-changes in perceptions derived from research on *Trichoderma harzianum* T-22, Plant Disease, 84 (2000) 377-393.
28. R. Hermosa, L. Botella, M. Montero-Barrientos, A. Alonso-Ramirez, V. Arbona, A. Gomez-Cadenas, C. Nicolas, Biotechnological applications of the gene transfer from the beneficial fungus T*richoderma harzianum* to plants, Plant Signal. Behav., 6 (2011) 1235-1236.
29. M. Eisendle, H. Oberegger, R. Buttinger, P. Illmer, H. Haas Biosynthesis and uptake of siderophores is controlled by the PacC-mediated ambient-pH Regulatory system in *Aspergillus nidulans*, Eukaryot. Cell, 3 (2004) 561-563.
30. R.K. Behera, PC. Mishra, N.K. Choudhary, High irradiance and water stress induced alterations in pigment composition and chloroplast activities of primary wheat leaves, J. Plant Physiol., 159 (2002) 967-973.
31. R. Mittler, Oxidative stress, antioxidants and stress tolerance, Trends in Plant Sci., 7 (2002) 405-410.
32. N. Pehlivan, A.M. Yesilyurt, N. Durmus, S.A. Karaoglu, *Trichoderma lixii* ID11D seed biopriming mitigates dose dependent salt toxicity in maize, Acta Physiol. Plant., (2017) 10.1007/s1738-017-2375-z.
33. S.E. Ahmed, M.H. Nawata, Y. Domae, T. Sakuratani, Alterations in photosynthesis and some antioxidant enzymatic activities of mungbean subjected to waterlogging, Plant Sci., 163 (2002) 117-123.
34. K. Maxwell, GN. Johnson, Chlorophyll fluorescence-a practical guide, J. Exp. Bot, 51 (2000) 659-668.
35. A.F. Lodeyro, M. Giró, H.O. Poli, G. Bettucci, A. Cortadi, A.M Ferri, N. Carrillo, Suppression of reactive oxygen species accumulation in chloroplasts prevents leaf damage but not growth arrest in salt-stressedtobacco plants. PLoS One, 11 (2016). http://doi.org/10.1371/journal.pone.0159588
36. F. Moradi, A.M. Ismail, Responses of photosynthesis, chlorophyll fluorescence and ROS-scavenging systems to salt stress during seedling and reproductive stages in rice, Ann Bot., 99 (2007) 1161-1173.

Functional Polysaccharides Blended Collagen Cryogels

Fonksiyonel Polisakkaritler İçeren Kollajen Kriyojeller

Research Article

Sedat Odabas
Department of Chemistry, Faculty of Sciences, Ankara University, Ankara, Turkey.

ABSTRACT

Researches investigate new types of scaffolds for tissue engineering and regenerative medicine applications to support cell proliferation and growth as well as tissue repair and regeneration. Although, there are several types of polymeric materials and various kinds of preparation techniques are already used today; there is still no consensus on the answer of the question "what is the best scaffold for tissue repair and regeneration?". Cryogels, which is a kind of hydrogels and, cryogelation, which is the technique for cryogel preparation, are rather new for tissue engineering applications. Here in this study, dextran and carboxymethyl cellulose functional polysaccharides blended collagen cryogels were prepared and characterized by chemical, structural and biological evaluations. Results show that, these collagen cryogels with their polysaccharides functional components have proper chemical and thermal characteristics and show good bio and hemo-compatibility. Therefore, these cryogels can be used as a candidate scaffold for tissue engineering and regenerative medicine applications.

Key Words
Collagen, polysaccharides, cryogels, tissue engineering .

ÖZ

Araştırmacılar doku mühendisliği ve rejeneratif tıp uygulamalarında, hücre çoğalması ve büyümesi, doku hasarının onarılmasını ve yenilenmesini desteklemek için yeni doku iskeleleri araştırmaları yapmaktadırlar. Günümüzde çok sayıda farklı polimerik malzeme ve değişik hazırlama teknikleri kullanılsa da, henüz hangi doku iskelesinin doku tamiri ve yenilenmesi için en iyidir? sorusunun cevabı için bir uzlaşı yoktur. Hidrojellerin bir türü olan kriyojeller ve kriyojel hazırlama tekniği olan kriyojelasyon, doku mühendisliği uygulamaları açısından kısmen yeni sayılırlar. Bu çalışmada, karboksimetil selüloz ve dekstran içeren fonksiyonel polisakkarit içeren kollajen kriyojeller hazırlanmış ve kimyasal, yapısal ve biyolojik değerlendirmeler ile karakterize edilmiştir. Sonuçlar, hazırlanan fonksiyonel polisakkarit birimleri içeren kollajen kriyojellerin kimyasal ve termal olarak uygun özelliklerinin yanında biyo ve kan uyumluluklarının iyi olduğunu ortaya koyulmuştur. Sonuç olarak, bu kriyojeller doku mühendisliği ve rejeneratif tıp uygulamaları için uygun bir aday doku iskelesi olarak kullanılabilirler.

Anahtar Kelimeler
Kollajen, polisakkaritler, kriyojeller, doku mühendisliği.

Article History: Received: Nov 5, 2017; Revised: Jan 22, 2017; Accepted: Feb 02, 2017; Available Online: Feb 20, 2018.

DOI: 10.15671/HJBC.2018.219

Correspondence to: S. Odabas, Department of Chemistry, Faculty of Sciences, Ankara University, Ankara, Turkey.
Tel: +90 312 212 67 20 /1170 Fax: +90 312 223 23 95 E-Mail: odabas@ankara.edu.tr

INTRODUCTION

Tissue engineering is a scientific perspective that combines cells, biologically active molecules and proper scaffolds, to repair or regenerate the damaged tissues [1]. Scaffolds can act as matrix material to support cell adhesion, growth and proliferation as well as cell differentiation and new tissue formation. There are several kinds of scaffolds that can be used in tissue engineering applications [2]. Some scaffolds can be derived from biological origin such as collagen, hyaluronic acid, silk fibroin. On the other hand, some scaffolds can be produced from synthetic polymers such as polylactic acid (PLA) and poly-ε-caprolactone (PCL) or polydimethylsiloxane (PDMS) [2,3]. There is still not a consensus on which biomaterial or source origin is the best for tissue engineering applications [3,4]. But there is a consensus about what a scaffold should have the properties, such as has no or limited toxicity, excellent biocompatibility, non-immunogenicity and non-carcinogenicity, easy fabrication and having enough stability and mechanical strength [2-5].

Cryogels are kind of hydrogels that have macropores in their structure. Cryogels can be formed via cryogelation technique at below 0°C, which is based on the principle of forming pores or lamellar structures while expelling water from the surrounding [6]. Today cryogels have found great interest in various fields of applications such as bioseparation, purification, wastewater treatment and some other biotechnological processes [7-10]. In recent years, remarkable studies also showed that cryogels have a potential at tissue engineering and regenerative medicine applications [11-15].

Collagen is one of the abundant natural polymer in entire body and it is the main structural protein in extracellular matrices. Therefore many reports have been published to present that collagen based biomaterials can be candidate scaffolds for tissue engineering applications alone or in blended forms. With its unique fibrillar protein formation and its cell inductive property, collagen can easily support cell proliferation, differentiation and new tissue formation [16-19].

Scaffolds that are used in tissue engineering are mostly cross-linked in their last form. There are various types of cross-linking agent reported in literature [20,21]. Among all chemical cross-linkers, glutaraldehyde and formaldehyde are very well-known but highly toxic ones. Moreover, 1-Ethyl-3-(3-dimethylaminopropyl)-carbodiimide (EDC) is also a chemical cross-linker that couple carboxyl or phosphate groups to primary amines and provide zero-length cross-linking. However scaffolds after EDC crosslinking often shows weak stability and mechanical properties. For about a decade, researchers use a technique based on periodate oxidation of carbohydrate sugar groups. Dextran is one of the most biocompatible one among other carbohydrates. Dextran is a hydrophilic branched polysaccharides with α-1,6 D-glucopyranose residues and α-1,2 , α-1,3 and α-1,4 side chains in the structure. It can be used for artificial plasma, anti-thrombolytic agent and binder in biomedical applications. Its oxide form - oxide dextran, has been used as biocompatible chemical cross-linker agent to cross-linked the polymer while integrating of the polymer main structure [22].

Cellulose is also a well-known biopolymer. Although, the sole form of cellulose has found limited application in biomaterial field due to its insoluble characteristics in water, its modified forms such as carboxymethyl cellulose (CMC), cellulose acetate, cellulose nitrate have been used in several application such as binding, dialysis system, chromatography, controlled release system as well as some sort of other biomedical applications for decades [23,24].

Here in this study, collagen cryogels having functional polysaccharides components are prepared in blend form and characterized by chemical, structural and biological evaluations. Collagen was used as a main biopolymeric compound as it has superior biological induction property. Moreover, CMC was chosen to improve cryogel swelling property. Lastly, dextran was chosen to cross-linked and strengthen the cryogel as well as to improve the biocompatibility in its last form.

MATERIALS AND METHODS

Preparing Cryogels

All chemicals were purchased from Sigma-Aldrich (Germany) and used as instructed unless otherwise stated. Cryogels were prepared as reported elsewhere with slight modifications [14]. Briefly, collagen (from rat-tail) is the basic component of the cryogels so collagen was swollen in acetic acid (0.1%; v/v) under gentle mixing for about 24h. CMC solution (5%; w/v) was prepared from its sodium salt in distilled water. Dextran (MW: 20.000 Da) was oxidized with periodate by catalysis free aqueous reaction which also reported elsewhere [14]. Here, collagen and CMC were mixed with appropriate amount of oxide-dextran (2:2:1; w/w/w) and stirred for 5 min in room temperature and the solution was then poured into wells and quickly placed into cryostat for 24h. Samples were then lyophilized and kept +4°C till use.

Characterization of Cryogels

Biodegradation Properties

The degradation profiles of the fabricated cryogels were evaluated in an enzyme-free media containing 1% sodium azide (w/v) at 37°C in a shaking incubator. Evaluation was performed triplicate and samples were weighted prior to evaluation. Analyses were performed gradually with lyophilized samples in defined time points.

Swelling Properties

In order to evaluate the swelling properties of the cryogels, samples (N=3) were soaked into 0.01 M phosphate buffer (pH 7.4) at room temperature. All samples were weighted before and after the swelling up to 15 min. The ratios of swelling (SD (%)) were determined via given equation (Equation 1) where W_1 and W_2 represent the dry and wet weight of the cryogels respectively.

$$SD\ (\%) = (W_2 - W_1)/(W_1) \times 100 \quad (1)$$

Chemical and Structural Characterization

Cryogels were evaluated in terms of their chemical composition, structural, thermal and morphological properties. Thermogravimetric analysis (TGA; (Pyris; Perkin Elmer, USA) was carried out by up to 900°C at a heating rate of 10°C/min. Crystallography pattern of the cryogels were evaluated by X-Ray Diffractometer (Rigaku D/Max 2200 ULTIMAN, Japan) under nitrogen atmosphere. Samples were scanned in 2 Theta with a scan rate of 5°/min. Chemical characterization was performed by Fourier Transform Infra Red Spectroscopy (FTIR-ATR; Perkin Elmer, USA) with a frequency range of 600-4000 cm^{-1}. Morphological and structural analysis of the cryogels was evaluated with Scanning Electron Microscopy (FEI Nova, USA) with accelerating voltage of 10kV. Samples were coated with a thin layer of gold prior to analysis. All evaluations were performed in triplicate.

Biological Evaluations of the Cryogels

Cytotoxicity Assessment

Possible cytotoxic effects of the cryogels were determined by means of cell viability were determined by well-known indirect MTT assay. Briefly, 1 cm^2 samples (N= 3) were soaked in DMEM/F12 culture media supplemented with 10% Fetal Bovine Serum and 1% (v/v) antibiotic/antimycotic solution for about 24 h at 37°C (extraction media). Meanwhile $1x10^4$ MG3T3 mouse osteoblastic cells were seeded on 96 well plates. Cells were cultured with 200 µl of fresh culture medium and incubated at 37°C; 5% CO_2 for 24h. Later on, medium was discarded and 100 µl of extraction media were added to each well except control group. Cells were incubated at 37°C; 5% CO_2 for another 24h. After 24h, MTT assay was performed. The absorbance values were measured at 570 nm with a micro plate reader (Biotek Instruments, USA) and cell viabilities were calculated with respect to control.

Hemocompatibility of the Cryogels

To assess the hemocompatibility of the cryogels, basic blood compatibility parameters such as prothrombin time (PT), fibrinogen adsorption and hemolytic activity of the cryogels were evaluated. For anticoagulant activity, 1cm^2 cryogel samples (N= 3) were incubated with healthy citrated blood for 1hr. at 37°C under gentle agitation. After the incubation, blood plasma and reagents were added in a transparent plastic tube immediately and coagulation times were measured. To

evaluate the hemolysis, 1 cm^2 cryogel samples were incubated with 2 ml citrated blood (1/10 diluted) per tube. Distilled water was used as positive control and PBS was used as negative control. Diluted blood and samples were incubated under gentle agitation for 1h at 37°C. Later on, samples were removed and tubes were centrifuged at 1500 rpm for 10 min. Absorbance of the supernatant was measured at 545 nm and the percent of hemolysis from each sample was calculated according to following equation (Equation 2).

Hemolysis(%) = (Absorbance of the scaffold)-(Absorbance of negative control)/(Absorbance of positive control)x100. (2)

RESULTS AND DISCUSSION

Characterization of Cryogels

Cryogels are relatively emergent type of biomaterials, which may potentials in tissue engineering and regenerative medicine applications. Here, collagen-oxide dextran-CMC cryogels were prepared. Oxide-dextran act as a biocompatible cross-linker, took apart of the body of the cryogels and cross-linked the entire polymeric blend in its last form.

In a typical tissue engineering application, biodegradable scaffolds can be used according to the need of the application. Here, the swelling and in vitro degradation profile of the cryogels was analyzed and results were given in Figure 1. According to these results, cryogels shows great swelling property over time (nearly 1150% with respect to its initial dry form by the end of 15 min.) and could degrade entirely at the end of a month. Of course, the degradation time can be adjusted by changing the ratio of oxide-dextran in the structure. As oxide dextran act as cross-linker, changing the ratio of oxide dextran may affect the swelling behavior of the cryogels.

Thermal behavior and thermal stability of the cryogels were assess by thermogravimetric analysis (TGA) and result was given in Figure 2a. According to TGA thermogram, nearly 10% weight loss by 100°C can be corresponded to moisture loss and chemical water in the cryogel. The main weight losses occurred between 100°C-250°C and 250°C-550°C. These findings are similar with the literature [25,26]. The final residue after mass decomposition can be associated with ashes and undecomposed material.

According to X-Ray Crystallography spectrum of cryogels that was given in Figure 2b, collagen and CMC shows broad widen peak at around 10°-30° that is very compatible with the literature. Moreover, typical broad peaks from dextran are also appeared around same degrees like from collagen and CMC [25-27].

For chemical characterization of collagen/oxide dextran/CMC cryogels, attenuated total reflection FTIR-ATR spectrum was used by means of different functional groups and bond linkage. FTIR spectrum was depicted in Figure 3. Spectrum of collagen, cellulose and dextran consisting main blend cryogel revealed peaks around 3300 cm^{-1} that can be associated with N-H stretching, amide A and –OH stretching. Peaks around 2900 cm^{-1} can be associated with CH_2 stretching and peaks around 1700 to 1640 cm^{-1} can be associated C=O stretching of amide I and –OH bending. There is also peak around 1580 cm^{-1} that is associated

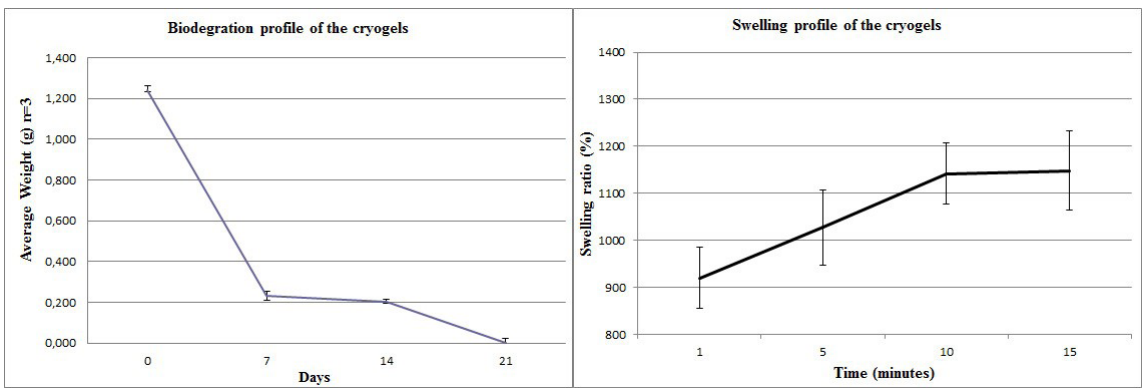

Figure 1. Biodegradation and swelling profiles of the cryogels.

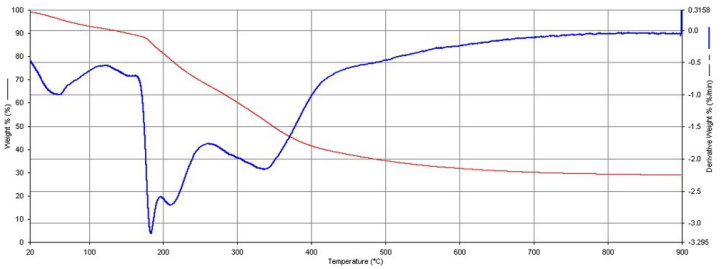

(a)

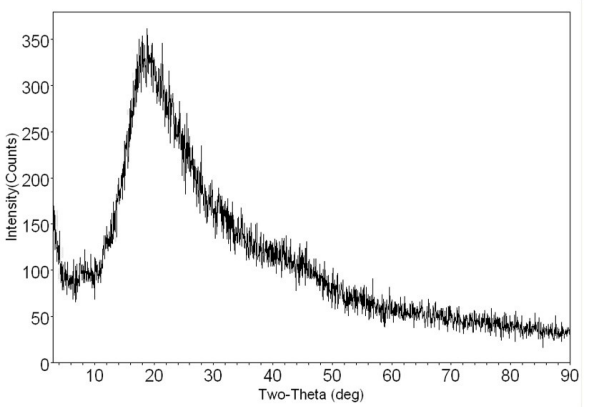

(b)

Figure 2. TGA (a) and X-RD (b) analysis of the cryogels.

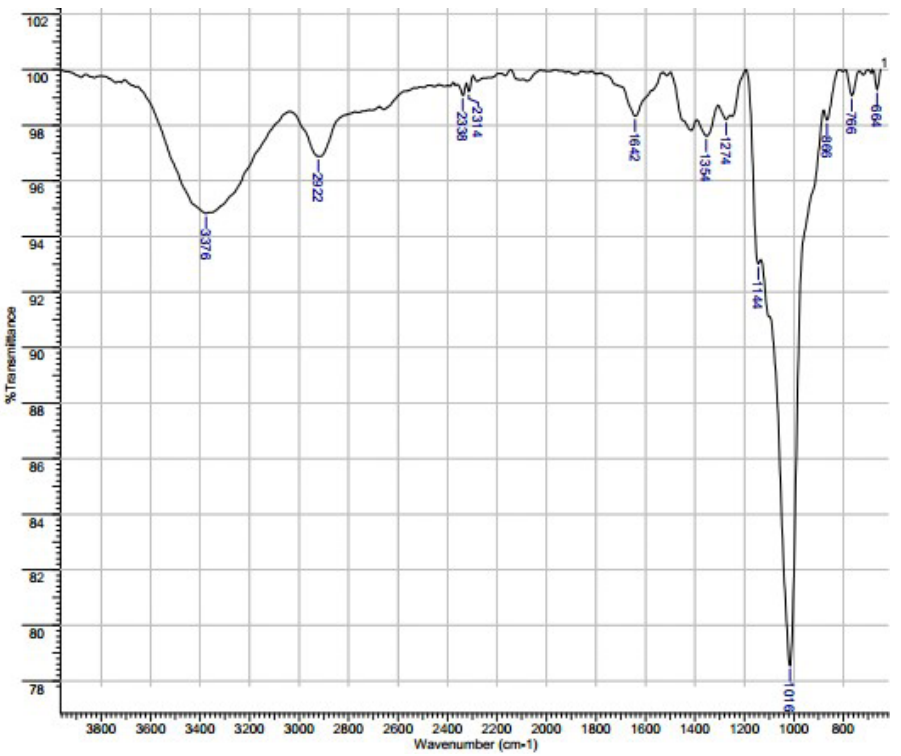

Figure 3. FTIR spectrum of the cryogels.

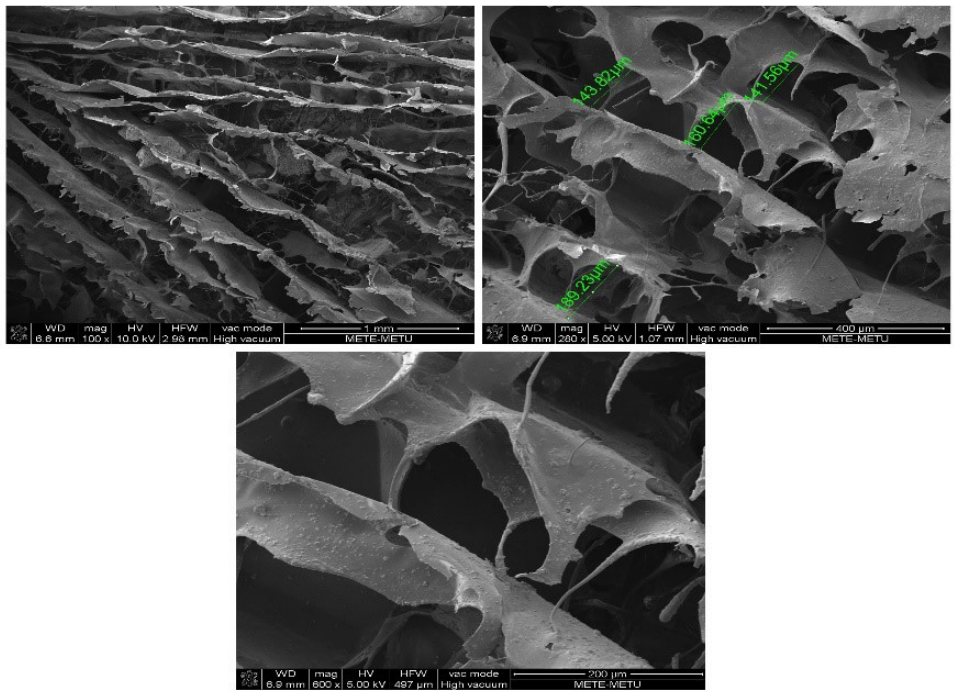

Figure 4. Scanning Electron Micrographs of the cryogels.

with N-H bending for amide II. The peaks from 1400 cm^{-1} to 1000 cm^{-1} can be associated with deformation of CH_2, CH_3, -OH and C-O. The all spectrum results shows typical similarities with previously published reports about biopolymer based scaffold [25,27].

Figure 4 shows the SEM images of collagen/oxide dextran/CMC cryogels. According to these images, cryogels shows anisotropic pore structure and irregular morphology as well as having almost lamellar formation. The pore structure and the morphology is crucial for tissue formation and regeneration. A candidate scaffold should have both macro and micro pores. Micropores are crucial for gas exchange and nutrient diffusion. Macropores on the other hand are crucial for cell attachment and growth. The macropore sizes of a candidate scaffold for tissue engineering applications especially for hard tissue repair should be in the range of 150-300 micron in diameter. The cryogels depicted here have interconnected pores and sheets that have well enough diameters to enable cell attachment and ingrowth as well as possible new tissue formation.

Biological Evaluations of the Cryogels

Biological evaluations of the cryogels were performed via indirect MTT assay and basic hemocompatibility examination. The components of the cryogels used for this study are already known as biocompatible and have no cytotoxic effect. Therefore, here in this study indirect MTT assay was chosen to determine the possible toxic extracts of forefront residues that can come from the cryogels in its last form. According to the results in Table1, cryogels have shown quite cytocompatible (over 96% cell viability) with respect to the control after 24 h. This result also means that the degradation extracts of the cryogels show no toxic effects to the cells.

Blood compatibility is also a key determination for tissue engineering and regenerative medicine applications. In addition to the MTT results, cryogels shows also quite blood compatible considering the hemocompatibility results that have also presented in Table 1. Hemocompatibility test parameters such as prothrombin time (PT), fibrinogen adsorption and hemolysis (%) are coherent with the reference and the control. Hemolysis ratio (3.38±0.88%) is under the

Table 1. Cyto and Hemo-compatibility of the collagen-oxide dextran-CMC cryogels.

Collagen-Oxide dextran-CMC cryogels (%)	Cell Viability *(%)	Protrombin Time (sec)	Fibrinogen (mg/ml)	Hemolysis
	96.86±8.37	11.4±0.2	2.77±0.12	3.38±0.88

* Cell viability was calculated with respect to the control at the end of 24 h.
** Reference values: Prothrombin time (9.4–12.5 s); fibrinogen (2.00–3.93 mg/mL).

permissible limit of 5% [28]. Results show that there is no undesirable condition related with the cryogels and cryogels have no significant effect on coagulation pathways.

CONCLUSION

In this study, collagen was blended with carboxymethylcellulose and dextran functional polysaccharides and scaffolds were prepared by cryogelation technique. Dextran is also act as a biocompatible cross-linker in its oxide form. Results presented here indicated that these biocompatible cryogels can be a good candidate for tissue engineering and regenerative medicine applications.

ACKNOWLEDGEMENTS

Author thank to Dr. Serhat Odabas, Dr. Batur Ercan, Dr. Handan Sevim, Mr. Atakan Tevlek for their support in analysis.

References

1. R.M. Nerem, A. Sambanis, Tissue engineering: from biology to biological substitutes, Tissue Eng., 1 (1995) 3-13.
2. S. Yang, K.F. Leong, Z. Du, C.K. Chua, The design of scaffolds for use in tissue engineering. Part I. Traditional factors, Tissue Eng., 7 (2001) 679-689.
3. L.E. Freed, G. Vunjak-Novakovic, R.J. Biron, D.B. Eagles, D.C. Lesnoy, S.K. Barlow, R. Langer, Biodegradable polymer scaffolds for tissue engineering, Biotechnol., 12 (1994) 689-693.
4. B.P. Chan, K.W. Leong, Scaffolding in tissue engineering: general approaches and tissue-specific considerations, European spine journal: official publication of the European Spine Society, the European Spinal Deformity Society, and the European Section of the Cervical Spine Research Society 17 Suppl. 4 (2008) 467-479.
5. S.J. Hollister, R.D. Maddox, J.M. Taboas, Optimal design and fabrication of scaffolds to mimic tissue properties and satisfy biological constraints, Biomaterials, 23 (2002) 4095-4103.
6. V.I. Lozinsky, I.Y. Galaev, F.M. Plieva, I.N. Savina, H. Jungvid, B. Mattiasson, Polymeric cryogels as promising materials of biotechnological interest, Trends Biotechnol., 21 (2003) 445-451.
7. M. Andac, I.Y. Galaev, H. Yavuz, A. Denizli, Molecularly imprinted cryogels for human serum albumin depletion in: Affinity Chromatography: Methods and Protocols, S. Reichtelt, ed., Methods in Molecular Biology Series, volume 1286, pp 233-237, Humana Press, 2015.
8. D. Cimen, F. Yilmaz, I. Percin, D. Turkmen, A. Denizli, Dye affinity cryogels for plasmid DNA purification, Mater. Sci. Eng. Mater. Biol. Appl., 56 (2015) 318-324.
9. A. Kumar, A. Bhardwaj, Methods in cell separation for biomedical application: cryogels as a new tool, Biomed. Mater., 3 (2008) 1-12.
10. M. Uygun, A.A. Karagozler, A. Denizli, Molecularly imprinted cryogels for carbonic anhydrase purification from bovine erythrocyte, Artif. Cells Nanomed. Biotechnol., 42 (2014) 128-137.
11. N. Bolgen, I. Vargel, P. Korkusuz, E. Guzel, F. Plieva, I. Galaev, B. Matiasson, E. Piskin, Tissue responses to novel tissue engineering biodegradable cryogel scaffolds: an animal model, J. Biomed. Mater. Res. A, 91 (2009) 60-68.
12. C.H. Chen, C.Y. Kuo, Y.J. Wang, J.P. Chen, Dual function of glucosamine in gelatin/hyaluronic acid cryogel to modulate scaffold mechanical properties and to maintain chondrogenic phenotype for cartilage tissue engineering, Int. J. Mol. Sci., 17 (2016) 1-22.
13. M.V. Konovalova, P.A. Markov, E.A. Durnev, D.V. Kurek, S.V. Popov, V.P. Varlamov, Preparation and biocompatibility evaluation of pectin and chitosan cryogels for biomedical application, J. Biomed. Mater. Res. A, 105 (2017) 547-556.
14. S. Odabas, G.A. Feichtinger, P. Korkusuz, I. Inci, E. Bilgic, A.S. Yar, T. Cavusoglu, S. Menevse, I. Vargel, E. Piskin, Auricular cartilage repair using cryogel scaffolds loaded with BMP-7-expressing primary chondrocytes, J. Tissue Eng. Regen. Med., 7 (2013) 831-840.
15. A. Sharma, S. Bhat, T. Vishnoi, V. Nayak, A. Kumar, Three-dimensional supermacroporous carrageenan-gelatin cryogel matrix for tissue engineering applications, Bio. Med. Res. Int., X (2013) 1-15.
16. L. Cen, W. Liu, L. Cui, W. Zhang, Y. Cao, Collagen tissue engineering: development of novel biomaterials and applications, Pediatric Res., 63 (2008) 492-496.
17. P. Fratzl, K. Misof, I. Zizak, G. Rapp, H. Amenitsch, S. Bernstorff, Fibrillar structure and mechanical properties of collagen, J. Struc. Biol., 122 (1998) 119-122.
18. L. Ma, C. Gao, Z. Mao, J. Zhou, J. Shen, X. Hu, C. Han, Collagen/chitosan porous scaffolds with improved biostability for skin tissue engineering, Biomaterials, 24 (2003) 4833-4841.

19. M. Rafat, F. Li, P. Fagerholm, N.S. Lagali, M.A. Watsky, R. Munger, T. Matsuura, M. Griffith, PEG-stabilized carbodiimide crosslinked collagen-chitosan hydrogels for corneal tissue engineering, Biomaterials, 29 (2008) 3960-3972.
20. S. Mavila, O. Eivgi, I. Berkovich, N.G. Lemcoff, Intramolecular cross-linking methodologies for the synthesis of polymer nanoparticles, Chem. Rev., 116 (2016) 878-961.
21. R. Kluger, A. Alagic, Chemical cross-linking and protein-protein interactions-a review with illustrative protocols, Bioorganic Chem., 32 (2004) 451-472.
22. R.A.C. João Maia, Jorge F.J. Coelho, Pedro N.Simões, M. Helena Gil, Insight on the periodate oxidation of dextran and its structural vicissitudes, Polymer, 52 (2011) 258-265.
23. Y.D. Czaja WK, Kawecki M, Brown RM Jr., The future prospects of microbial cellulose in biomedical applications, Biomacromol., 8 (2007) 1-12.
24. N.A. Hoenich, Cellulose for medical applications: past, present, and future, BioResources, 1 (2006) 1-11.
25. B. León-Mancilla, M. Araiza-Téllez, J. Flores-Flores, M. Piña-Barba, Physico-chemical characterization of collagen scaffolds for tissue engineering, J. Appl. Res. Tech., 14 (2016) 77-85.
26. P.R.F.D.S. Moraes, S. Saska, H. Barud, L.R.D. Lima, V.D.C.A. Martins, A.M.D.G. Plepis, S.J.L. Ribeiro, A.M.M. Gaspar, Bacterial cellulose/collagen hydrogel for wound healing, Mater. Res., 19 (2016) 106-116.
27. T. Nagai, N. Suzuki, Y. Tanoue, N. Kai, Collagen from tendon of Yezo Sika deer (*Cervus nippon yesoensis*) as By-Product, Food Nutr. Sci., 3 (2012) 72-79.
28. J. Autian, Biological model systems for the testing of the toxicity of biomaterials, Polymers in Medicine and Surgery, Springer, Boston, MA, 1975.

Assessment of the Cytotoxicity of *Melia azedarach L.* Extracts on Human Adipose-derived Mesenchymal Stem Cells

Melia azedarach L. Özütlerinin İnsan Adipoz Kaynaklı Mezenkimal Kök Hücreleri Üzerindeki Sitotoksisitesinin Değerlendirilmesi

Research Article

Burcu Efe, Yusuf Furkan Galata,Yavuz Emre Arslan*
Regenerative Biomaterials Lab., Dept. of Bioengineering, Eng. Faculty, Çanakkale Onsekiz Mart University, Canakkale, Turkey.

ABSTRACT

In this study, aqueous extracts of *Melia azedarach* L. green fruit and leaves were obtained using two different extraction methods. The extraction yields of the green fruit and leaves were found as 24.11% and 37.98% for the infusion method; 17.76% and 27.00% for the rotating method, respectively. The total phenolic content, related to the infusion method, was ascertained for green fruit extract 173.67±10.84 mg Gallic Acid Equivalent (GAE)/g dry weight and leaf extract 312.33±9.81 mg GAE/g dry weight. In other respects, antioxidant activity related to the infusion method was determined for green fruit extract 172.51±13.23 mg Trolox/L and leaf extract 569.16±10.41 mg Trolox/L. Gas chromatography-mass spectrometry (GC-MS) analysis was performed to identify the chemical composition of the extracts. The cytotoxicity levels of the extracts were assessed on human adipose-derived mesenchymal stem cells (hAMSCs) using commercially available XTT assay. Consequently, it has been found that the green fruit extract has more cytotoxic activity than the leaf extract on hAMSCs.

Key Words
Melia azedarach L., total phenolic compounds, cytotoxicity, human adipose-derived mesenchymal stem cells.

ÖZ

Bu çalışmada, *Melia azedarach* L. yeşil meyve ve yapraklarının sulu özleri iki farklı özütleme yöntemi kullanılarak elde edildi. Yeşil meyve ve yaprakların özütleme verimleri sırasıyla, demleme yöntemi için %24.11 ve %37.98; çalkalama yöntemi için ise %17.76 ve %27.00 olarak bulundu. Demleme yöntemi ile ilgili toplam fenolik içerik, yeşil meyve özü için 173.67±10.84 mg galik asit eşdeğeri (GAE)/g kuru ağırlık ve yaprak özü için 312.33±9.81 mg GAE/g kuru ağırlık cinsinden tespit edildi. Diğer yandan demleme yönteminde, yeşil meyve özü için 172.51±13.23 mg Trolox/L ve yaprak özü için ise 569.16±10.41 mg Trolox/L cinsinden antioksidan aktivite belirlendi. Özütlerin kimyasal bileşimini tanımlamak için gaz kromatografisi-kütle spektrometresi (GC-MS) analizi yapıldı. Özütlerin insan adipoz kaynaklı mezenkimal kök hücreleri (iAMKH'leri) üzerindeki sitotoksisite seviyeleri ticari olarak mevcut olan XTT testi ile değerlendirildi. Sonuç olarak, yeşil meyve özütünün iAMKH'leri üzerine yaprak özütünden daha fazla sitotoksik aktiviteye sahip olduğu bulunmuştur

Anahtar Kelimeler
Melia azedarach L., toplam fenolik bileşikler, sitotoksisite, insan adipoz kaynaklı mezenkimal kök hücreler.

Article History: Received: Dec 06, 2017; Revised: Jan 02, 2017; Accepted: Feb 08, 2017; Available Online: Feb 20, 2018.

DOI: 10.15671/HJBC.2018.220

Correspondence to: Y.E. Arslan, Department of Bioengineering, Eng. Faculty, Çanakkale Onsekiz Mart Univ., Canakkale, Turkey.
Tel: +90 286 218 0018 Fax: +90 286 218 0541 E-Mail: yavuzea@gmail.com

INTRODUCTION

Plants have been used from ancient times until today due to their bioactive substances for the treatment of diseases and/or other medical purposes in traditional medicine. Nowadays, plants are still a prominent option in modern medicine, pharmaceutical chemistry and chemical entities for generating synthetic drugs. Researches on significant biomolecule extraction from medicinal plants have become more notable with an increase in novel methods or technologies such as maceration and Soxhlet extraction presenting opportunities to obtain desired compounds [1,2]. *Melia azedarach* is an evergreen tree and the species of deciduous tree in the mahogany family found mostly in Indian sub-continent [3]. These plants constitute approximately 45 genera and 750 species [4]. The origin of *M. azedarach* is Northern India and China, but today, it can be grown in a few more continents. These trees were previously used for timber and ornamental purposes, until the presence of several cytotoxic and bioactive components was discovered [5].

In recent years, research has revealed this plant to contain excessive amounts of biological active agents such as antioxidants and phenolic components [3]. Because of its extraordinary cytotoxic and antimicrobial activity, *M. azedarach* has been investigated for its use as an anti-tumor agent, pesticide, for skin disease, viral infections, arthritis, inflammation and analgesic [6,7]. The effective results have been obtained when this plant was used as an anti-ulcer, anti-malarial, anti-protozoal, anthelmintic and wound healing agent. In addition to these, Asokan et al. (2015) reported its effect in reducing blood sugar levels [8], and Sultana et al. (2014) exhibited its reducing effect on the urinary calcium, oxalate and phosphate levels [9].

Human mesenchymal stem cells (hMSCs) have been considered as a potential source for cell therapeutics in incurable diseases. hMSCs revitalize regeneration and manage inflammation due to their self-renewal and multi-lineage differentiation features, making them an attractive source in tissue engineering and regenerative medicine. hMSCs can be isolated from a variety of sources such as bone marrow, dental pulp, adipose tissues, placenta, amniotic fluid, tendons, the umbilical cord, etc. Due to their therapeutic nature, these cells are capable of healing various clinically significant diseases [10–14]. In the current study, we prepared aqueous extracts of *M. azedarach* L. leaves and green fruit. Chemical composition of extracts was characterized by GC-MS, whereas the total phenolic compound and anti-oxidant activities were determined via spectrophotometric techniques. Cytotoxicity levels of the extracts were examined with the XTT assay. Human adipose-derived MSCs (hAMSCs) were then treated with these aqueous extracts. The aim of this study was to investigate and determine the effects of the cytotoxicity levels of the extracts on hAMSCs. We believe that this pioneering study will open a pathway for promising new studies in tissue engineering and regenerative medicine applications.

MATERIALS and METHODS

Plant Collection

M. azedarach L. leaves and green fruit were collected in April from Canakkale, Turkey. Fresh leaves and green fruits were rinsed with distilled water. Then, they were evenly spread and dried in an incubator (Memmert, UN55, Germany) for 24h. The outer layer of the dried fruit was removed before the extraction process. The dried material was separately homogenized (IKA, T-18 Basic Ultra TURRAX, Germany) in order to obtain their powder form.

Extraction of *M. azedarach* L.

The extraction process was performed with two different groups. The dried samples were first dissolved in Milli-Q water (Merck-Millipore, Direct-Q3 UV, Germany) at a ratio of 2% (w/v). Group-I samples were extracted at 80°C for 2h with a Soxhlet apparatus (Buchi, Rotavapor R210, Switzerland) (also named the infusion method). The extract was then centrifuged at 6000 rpm for 10 minutes (Hettich, Mikro 120, Germany) and filtered (Macherey-Nagel, MN-615, Germany) under reduced pressure (Buchi, Vacuum pump V-700, Switzerland).

Group-II samples in suspension form were subjected to continuous stirring (also named the ro-

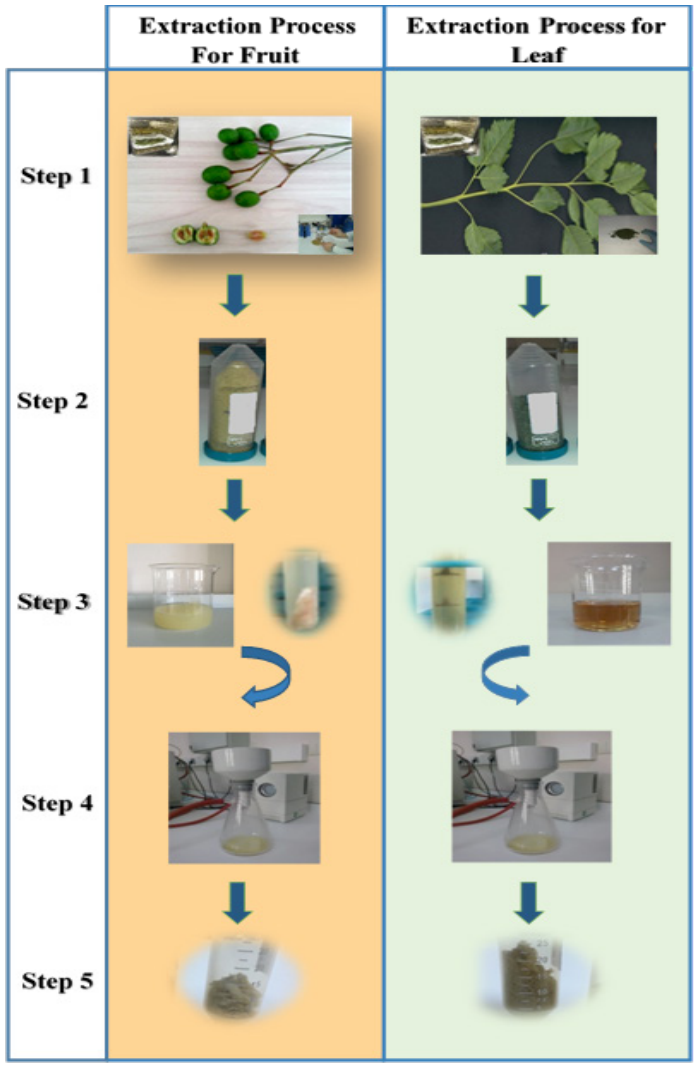

Figure 1. An overview of the extraction processes of *M. azedarach* L. green fruit and leaf. Step 1: Green fruit and leaf were harvested and dried in incubator. Step 2: Green fruit and leaf were homogenized. Step 3: Green fruit and leaf extracts were obtained according to infusion method (Group I) and centrifuged to eliminate the insoluble substances. Step 4: Green fruit and leaf extracts were filtered by vacuum under reduced pressure. Step 5: Fruit and leaf extracts were lyophilized to obtain their water-soluble powder form.

tating method) at room temperature for 72 h. The solutions were then centrifuged at 6000 rpm for 10 minutes and the resulting suspension filtered using filter paper under reduced pressure. The extracts were evaporated under reduced pressure at 80°C to concentrate the solution and stored at -26°C for overnight before the lyophilization process. Lyophilization procedure was conducted for overnight (Telstar, LyoQuest, Spain) and the lyophilized extracts were stored at -26°C for further use. All processes were summarized in Figure 1.

Determination of Total Phenolic Content

The total phenolic content (TPCs) was spectrophotometrically determined using the Folin Ciocalteu reagent [15]. Dried specimens of the leaf and green fruit extracts were dissolved in Milli-Q water at a ratio of 1% (w/v). Briefly, 10 mg of the sample was suspended in 1 of mL Milli-Q water at room temperature. Then, 900 µL of Milli-Q water, 5 mL of the Folin reagent (0.2 N) and 4 mL of sodium carbonate solution (7.5%, w/v) were added into each 100 µL sample. The solutions were rested for 2 h at room temperature in the dark. The absorbance was measured at 765 nm against a blank solution (Shimadzu UV-mini 1240, Japan). The phenolic content was calculated in terms of Gallic acid (GA) and the results were given as the GA equivalent (GAE) in terms of mg/g dry sample. All chemicals were purchased from Sigma-Aldrich (Germany) unless otherwise specified.

Determination of the CUPRAC Antioxidant Capacities of the Extracts

To analyze the antioxidant values of the extracts, the CUPRAC test was applied. Briefly, 20 μL of each sample was suspended in 1 mL of $CuCl_2.2H_2O$ (0.01M, prepared in Milli-Q water), 1 mL of Neocuproine ($7.5x10^{-3}$ M, prepared in Ethanol), 1 mL of ammonium acetate solution (pH= 7.0, in Tris-buffer) and 1.08 mL of Milli-Q water. After the solutions were incubated in the dark for 30 minutes at room temperature, the absorbance was measured at 450 nm against a blank solution.

Gas chromatography/Mass Spectrometry Analysis

M. azedarach L. leaf and fruit powders were dissolved in Milli-Q water and filtered through a 0.45 μm sterile filter. GC-MS analysis was performed using a Thermo MS Finnigan Trace DSQ instrument, with a DB-WAX (30mx0.25mm i.d.; film thickness 0.25μm) column. The GC oven temperature was programmed in the following manner; 50°C for 1 minute, followed by an increase rate of 3°C/minute up to 220°C. Helium was used as the carrier gas at a flow rate of 1ml/minute. All data were processed using the Xcalibur software.

Cell Culture Experiment

Human adipose mesenchymal stem cells (hAMSCs) (Merck-Millipore, human adipose mesenchymal stem cell kit, cat. no. SCC038 and lot no. QVP1303200, USA) were expanded, and their multipotency capacities validated according to a previously reported method [16,17]. Passages between 2 and 5 were utilized for all experiments. hAMSCs were seeded on 96-well plates with a density of $1x10^4$ cells/well, and incubated at 37°C, under 5% CO_2 and 95% relative humidity conditions (Panasonic, Japan) for 24 h. Aqueous extracts of *M. azedarach* L. at various concentrations to the hAMSCs. Briefly, the extracts were added into mesenchymal stem cell medium at different ratios depending on its nature; 150, 600, 900, 1500 and 2100 μg/well for that of the fruit, and 100, 200, 400 and 600 μg/well for that of the leaf.

Measuring Cell Viability

Cytotoxicity of the extracts were assessed using commercially available the XTT assay kit (Biological Industry, USA). In brief, hAMSCs were seeded in 96-well plates and incubated for 24 h ensuring they reached 85-90% confluence. The stem cells were then treated with green fruit and leaf extracts 24 h under conventional culture conditions. Subsequently, the XTT activation reagent was added into each well and incubated for a further 4 h. The absorbances were then measured at wavelength range of 450-500 nm against the control group (n= 3) with a microplate reader (Thermo-Scientific, Multiskan™ GO).

RESULTS and DISCUSSIONS

Determination of the Success of Extraction Process

The yield percentage of the green fruit and leaf extracts were calculated using the equation given below. The infusion technique produced extraction yields of 24.11% and 37.98% for the green fruit and leaf respectively, whereas 17.76% and 27.00% were obtained through the rotation process.

$$SampleYield = \left[\frac{(Initial(dry))Weight - LyophilizedWeight}{Initial(dry)Weight}\right] x100 \quad (1)$$

The infusion extraction yields were significantly higher than those of rotation extract yields. Similar results have been obtained in literature [18].

Assessment of the Total Phenolic Contents of Extracts

TPCs of the green fruit and leaf extracts were found to be 173.67 and 312.33 mg GAE/g dry weight, respectively. The data clearly outlines that leaf extracts contain a richer phenolic content (Figure 2A) with respect to that of the fruit extract resulting in high free radical-sweeping and antioxidant activities [19]. Phenolic compounds are one of the major secondary metabolite classes of plants which possess a wide range of biological effects including antioxidant activity, antimutagenicity, anti-carcinogenicity, etc. [20]. In a similar study, *M. azedarach* L. was extracted using various organic solvents in order to investigate the potential antifeedant activities of its biological contents [5].

In a study, aqueous extracts of *M. azedarach* L. green and ripe fruit were prepared, where the phenolic content was found to be 10.54 mg

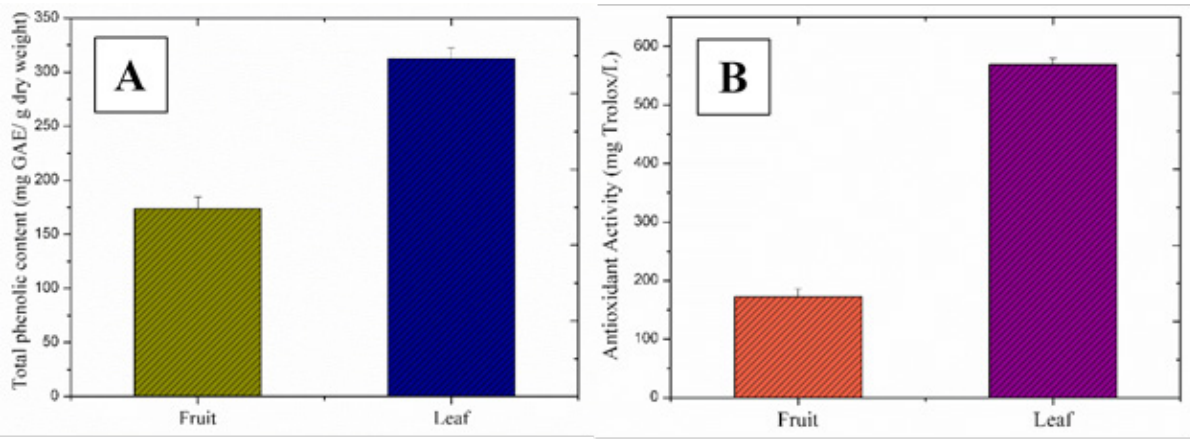

Figure 2. Total phenolic contents (A) and antioxidant activities (B) of green fruit and leaf extracts.

GAEs/g dry weight [4]. In our study, TPC of green fruit was found as 173.67±10.84 mg GAEs/g dry weight according to the infusion method which reveals the importance of the temperature during the extraction process. It should not be forgotten that a number of factors (collection time, geographical origin, climatic conditions, etc.) also have influence on the phenolic compound content in a plant extract [4].

CUPRAC Antioxidant Capacity

The CUPRAC method is based on the Cu(II)–Cu (I) reduction by antioxidants in the presence of neocuproine. It is important that CUPRAC reagent should be freshly prepared [21,22] it is desirable to establish a method that can measure the total antioxidant activity level directly from vegetable extracts. The current literature clearly states that there is no \"total antioxidant\" as a nutritional index available for food labeling because of the lack of standard quantitation methods. Thus, this work reports the development of a simple, widely applicable antioxidant capacity index for dietary polyphenols and vitamins C and E, utilizing the copper(II. In our study, the antioxidant content of the leaf and green fruit extracts were determined by the CUPRAC method, which showed leaf extracts to have the maximum antioxidant activity according to Trolox calculations.

As shown in Figure 2B, the leaf and green fruit extracts exhibit strong antioxidant activity. Cupric reducing capacity of the aqueous green fruit and leaf extracts were found to be 172.51±13.23 and 569.16±10.41 mg Trolox/L, respectively. Aoudia et al. (2013), found the cupric reducing capacity of aqueous leaf extracts to be 78.71 mg Trolox/L which underlines the success of infusion process seed and almonds of *Melia azedarach* grown in Algeria were defatted and extracted with three solvents, aqueous 70%, v/v [23].

GC-MS Results

In order to identify the chemical composition of the leaf and green fruit extracts, GC-MS, a very widespread analytical technique, was performed. According to the results, stearic acid, polyunsaturated fatty acid, furfural, 2-furancarboxyaldehyde-5-(methyl), acetic acid, 5-hydroxymethyl-2-furaldehyde, hexanoic acid, monoterpenes, phytosterol, flavonoids, 2,3-Dihydro-3,5-Dihyroxy-6-Methyl-4H-Pyran-4-One and ethyl nonadecanoate were determined in the green fruit extract (Figure 3A). The leaf extract on the other hand revealed the presence of flavonoids, furfural, 2-furancarboxyaldehyde-5-(methyl), acetic acid, 5-Hydroxymethyl-2-furaldehyde, hexanoic acid, phytosterol, monoterpenes, Vitamin E and 2,3-Dihydro-3,5-Dihyroxy-6-Methyl-4H-Pyran-4-One (Figure 3B). GC-MS screening showed that the most abundant substance (%) was acetic acid according to the peak area.

Organic acids and furfural derivatives have been used against plant parasitic nematodes, for years. On the other hand, flavonoid derivatives are potential chemical substances used as anti-inflammatory and anti-cancer agents. Additionally, vitamin E is an antioxidant and it protects tissues from deleterious free radicals. Apart from these,

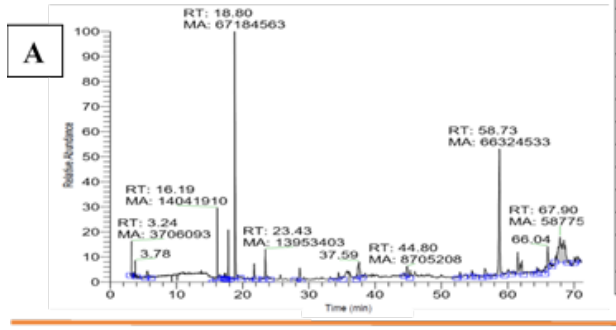

RT	M.Wt	M.F.	Compound Name
13,21	284	$C_{18}H_{36}O_2$	Stearic acid
13,21	294	$C_{18}H_{30}O_2$	Polyunsaturated fatty acid
16,38	96	$C_5H_4O_2$	Fufural
19,53	110	$C_6H_6O_2$	2-furancarboxyaldehyde-5-(methyl)
21,15	60	$C_2H_4O_2$	Acedic Acid
39,94	126	$C_6H_6O_3$	5-Hydroxymethyl-2-furaldehyde
37,88	116	$C_6H_{12}O_2$	Hexanoic acid
37,57	152	$C_{10}H_{16}O$	Monoterpenes
39,17	414	$C_{29}H_{50}O$	Phytosterol
45,31	222	$C_{13}H_{14}N_2O_3$	Flavonoids
58,77	144	$C_6H_8O_4$	2,3-Dihydro-3,5-Dihyroxy-6-Methyl-4H-Pyran-4-One
60,54	326	$C_{21}H_{42}O_2$	Ethyl nonadecanoate

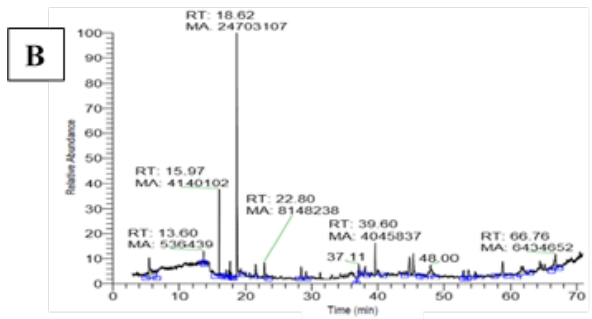

RT	M.Wt	M.F.	Compound Name
11,49	222	$C_{13}H_{14}N_2O_3$	Flavonoids
16,38	96	$C_5H_4O_2$	Fufural
19,53	110	$C_6H_6O_2$	2-furancarboxyaldehyde-5-(methyl)
21,15	60	$C_2H_4O_2$	Acedic Acid
39,94	126	$C_6H_6O_3$	5-Hydroxymethyl-2-furaldehyde
37,88	116	$C_6H_{12}O_2$	Hexanoic acid
40,25	414	$C_{29}H_{50}O$	Phytosterol
42,61	412	$C_{29}H_{48}O$	Phytosterol
45,61	152	$C_{10}H_{16}O$	Monoterpenes
56,35	536	$C_{40}H_{56}$	Vitamin E
58,77	144	$C_6H_8O_4$	2,3-Dihydro-3,5-Dihyroxy-6-Methyl-4H-Pyran-4-One

Figure 3. GC-MS chromatograms of green fruit (A) and leaf (B) extracts.

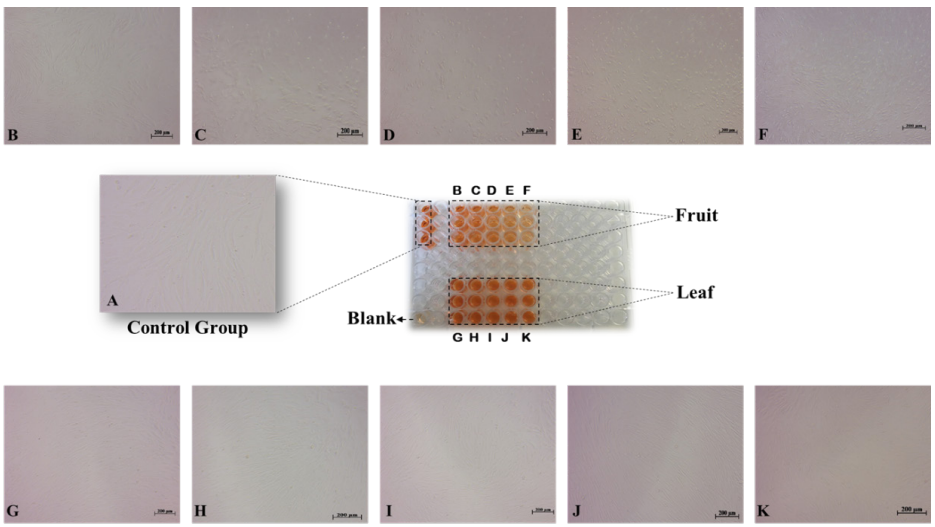

Figure 4. Experimental setup for XTT assay and inverted phase-contrast microscopy images of hAMSCs that were treated with various concentrations of the extracts. Un-treated hAMSCs as control (A), microscopic images of green fruit extract (B, C, D, E and F) and leaf extract (G, H, I, J and K) as dose-depended concentrations (Black scale bar: 200 μm).

monoterpenes can inhibit microbial proliferation and prevent dehydration, etc. [24,25]. Finally, the active substance/s that cause cell apoptosis were not specified because of the huge chemical composition of the green fruit extract.

Cytotoxicity

Human adipose-derived MSCs were treated with aqueous leaf and green fruit extracts, and the cell viability was determined via the XTT assay often used in the identification of cytotoxicity levels (Figure 4). The colorimetric assay depends on the reduction of tetrazolium salts (XTT) to orange colored formazan products by living cells (metabolically active). Cell viability measurements obtained from the XTT assay are represented in Figure 5.

M. azedarach L. green fruit extracts showed dose dependent cytotoxic effect on hAMSCs. The IC_{50} value for green fruit extract was found to be 728.05 μg/well, whereas no value could be determined for the leaf extract because it did not show any cytotoxic effect against the

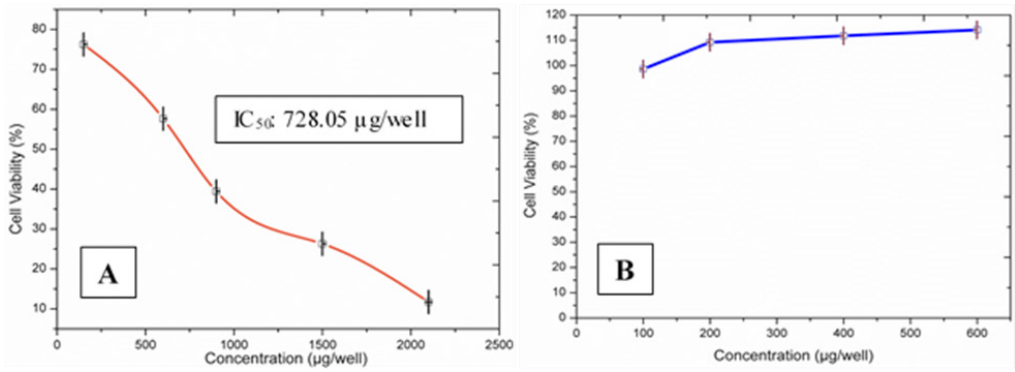

Figure 5. Cell viability assessment of green fruit (A) and leaf (B) extract.

hAMSCs. Green fruit extracts inhibited the cell proliferation as shown in Figure 5A. Although the TPC and antioxidant capacities of leaf extracts were higher than that of the green fruit extract (Figure 2), surprisingly, the green fruit extract showed a remarkable cytotoxic effect on hAMSCs in contrast to leaf extract (Figure 5B). The absence of similar studies in the literature limits our interpretation about these results. It is noteworthy in mentioning that the underlying reason of cytotoxicity is not related to the TPC or antioxidant capacity, but probably, to the presence of a chemical compound.

CONCLUSION

Plants have been used as alternative medicine for therapeutic purposes since the beginning of mankind. Therefore, the identification of extraordinary chemical contents is crucial for their use in the healthcare industry. Nowadays, hMSCs, hAMSCs in particular, are utilized in the treatment of many types of diseases. Exploring novel agents or substances from medicinal plants for proliferation, differentiation or maintenance of hMSCs may present and lead to new opportunities in tissue engineering and regenerative medicine applications. *M. azedarach* L. leaf and green fruit extracts were prepared and applied to hAMSCs with the aim of evaluating their cytotoxicity levels, which in turn is the preliminary phase in understanding the potential effect of these extracts on hAMSCs.

The green fruit extract was found to be highly cytotoxic in contrast to leaf extract. We believe further studies on *M. azedarach* L. extracts should be designed in order to gain a better understanding of the main underlying causes of the cytotoxicity or proliferation of hAMSCs.

Conflict of interest

The authors declare that they have no conflict of interest.

Acknowledgements

The authors acknowledge the financial support of the Çanakkale Onsekiz Mart University, Scientific Research Projects Coordination Unit (Project ID. FBA-2015-549). We would also like to thank the Çanakkale Onsekiz Mart University, Science and Technology Application & Research Center for their support regarding the GC-MS analyses. Finally, we would like to thank Prof. Kaan C. Emregul for his comments and language proofreading.

References

1. S.S. Handa, S.P.S. Khanuja, G. Longo, D.D. Rakesh, Extraction technologies for medicinal and aromatic plants, J. Nat. Prod., 5 (2008) 440.
2. B. Biswas, K. Rogers, F. Mclaughlin, D. Daniels, A. Yadav, Antimicrobial activities of leaf extracts of guava (*Psidium guajava* l.) on two gram-negative and gram-positive bacteria, Int. J. Microbiol., (2013) 1-6.
3. M. Azam, A. Mamun-Or-Rashid, N. Towfique, M. Sen, S. Nasrin, Pharmacological potentials of *Melia azedarach* L., A review, Am. J. Biosci., 1 (2013) 44-49.
4. I. Khan, M. Yasinzai, Z. Mehmood, I. Ilahi, Comparative study of green fruit extract of *Melia azedarach* linn. with its ripe fruit extract for antileishmanial, larvicidal, antioxidant and cytotoxic activity, Asian J. Nat. Appl. Sci., 2 (2014) 442-454.
5. C. Carpinella, C. Ferrayoli, G. Valladares, M. Defago, S. Palacios, Potent limonoid insect antifeedant from *Melia azedarach*, Biosci. Biotechnol. Biochem., 66 (2002) 1731-1736.
6. T. Akihisa, X. Pan, Y. Nakamura, T. Kikuchi, N. Takahashi, M. Matsumoto, E. Ogihara, M. Fukatsu, K. Koike, H. Tokuda, Limonoids from the fruits of *Melia azedarach* and their cytotoxic activities, Phytochemistry, 89 (2013) 59-70.

7. K. Sangeetha, S. Rajarajan, In vitro antiviral activity of indian medicinal plants to asian and east central south african lineage of Chikungunya virus, Int. J. Pharm. Sci. Res., 6 (2015) 692-697.
8. B. Asokan, B. Rajkumar, S. Balamuruganvelu, S. Jaikumar, In vivo antidiabetic activity of ethanolic flower extract *Melia azedarach* L., Acta Biomed. Sci., 2 (2015) 215-217.
9. S. Sultana, H.M. Asif, N. Akhtar, M. Waqas, S.U. Rehman, Comprehensive review on ethanobotanical uses, phytochemistry and pharmacological properties of *Melia azedarach* linn., Asian J. Pharm. Res Heal. Care, 6 (2014) 26-32.
10. J. Yu, Y. Wang, Z. Deng, L. Tang, Y. Li, J. Shi, Y. Jin, Odontogenic capability: bone marrow stromal stem cells versus dental pulp stem cells, Biol. Cell, 99 (2007) 465-474.
11. H. Jin, Y. Bae, M. Kim, S.-J. Kwon, H. Jeon, S. Choi, S. Kim, Y. Yang, W. Oh, J. Chang, Comparative analysis of human mesenchymal stem cells from bone marrow, adipose tissue, and umbilical cord blood as sources of cell therapy, Int. J. Mol. Sci., 14 (2013) 17986-18001.
12. Y.E. Arslan, M.M. Hız, T. Sezgin Arslan, The use of decellularized animal tissues in regenerative therapies, Kafkas Univ. Vet. Fak. Derg., 21 (2015) 139-145.
13. I. Jun, Y. Bin Lee, Y.S. Choi, A.J. Engler, H. Park, H. Shin, Transfer stamping of human mesenchymal stem cell patches using thermally expandable hydrogels with tunable cell-adhesive properties, Biomaterials, 54 (2015) 44-54.
14. M.T. Sutton, D. Fletcher, S.K. Ghosh, A. Weinberg, R. van Heeckeren, S. Kaur, Z. Sadeghi, A. Hijaz, J. Reese, H.M. Jane, D.P. Lennon, A.I. Caplan, T.L. Bonfield, Antimicrobial properties of mesenchymal stem cells: therapeutic potential for cystic fibrosis infection, and treatment., Stem Cells Int., 2016 (2016) 1-12.
15. V.L. Singleton, J.A. Rossi, J. Jr, Colorimetry of total phenolics with acid reagents, Am. J. Enol. Vitic., 16 (1965) 144-158.
16. E. Erten, T. Arslan Sezgin, B. Derkus, Y.E. Arslan, Detergent-free decellularization of bovine costal cartilage for chondrogenic differentiation of human adipose mesenchymal stem cells in vitro, RSC Adv., 6 (2016) 94236-94246.
17. Y.E. Arslan, T. Sezgin Arslan, B. Derkus, E. Emregul, K.C. Emregul, Fabrication of human hair keratin/jellyfish collagen/eggshell-derived hydroxyapatite osteoinductive biocomposite scaffolds for bone tissue engineering: From waste to regenerative medicine products, Coll. Surf. B Biointerf., 154 (2017) 160-170.
18. A.V. Khân, A.A. Khan, I. Shukla, In vitro antibacterial potential of *Melia azedarach* crude leaf extracts against some human pathogenic bacterial strains, Ethnobot. Leafl., 12 (2008) 439-445.
19. J. Kubola, S. Siriamornpun, Phenolic contents and antioxidant activities of bitter gourd (*Momordica charantia* L.) leaf, stem and fruit fraction extracts in vitro, Food Chem., 110 (2008) 881-890.
20. G. Zengin, C. Sarikurkcu, P. Uyar, A. Aktumsek, S. Uysal, M.S. Kocak, R. Ceylan, *Crepis foetida* L. subsp. rhoeadifolia (Bieb.) Celak. as a source of multifunctional agents: Cytotoxic and phytochemical evaluation, J. Funct. Foods, 17 (2015) 698-708.
21. R. Apak, K. Güçlü, M. Özyürek, S.E. Karademir, Novel total antioxidant capacity index for dietary polyphenols and vitamins C and E, using their cupric ion reducing capability in the presence of neocuproine: CUPRAC Method, J. Agric. Food Chem., 52 (2004) 7970-7981.
22. S.D. Çekiç, K.S. Başkan, E. Tütem, R. Apak, Modified cupric reducing antioxidant capacity (CUPRAC) assay for measuring the antioxidant capacities of thiol-containing proteins in admixture with polyphenols, Talanta, 79 (2009) 344-351.
23. H. Aoudia, B.D. Oomah, F. Zaidi, R. Zaidi-Yahiaoui, J.C.G. Drover, J.E. Harrison, Phenolics, antioxidant and anti-inflammatory activities of *Melia azedarach* extracts, Int. J. Appl. Res. Nat. Prod., 6 (2013) 19-29.
24. N.G. Ntalli, S. Vargiu, U. Menkissoglu-Spiroudi, P. Caboni, Nematicidal carboxylic acids and aldehydes from *Melia azedarach* fruits, J. Agric. Food Chem., 58 (2010) 11390-11394.
25. A. Sen, A. Batra, Chemical composition of methanol extract of the leaves of *Melia azedarach* L., Asian J. Pharm. Clin. Res., 5 (2012) 42–45.

Assessment of the Cytotoxicity of *Melia azedarach L.* Extracts on Human Adipose-derived Mesenchymal Stem Cells

Melia azedarach L. Özütlerinin İnsan Adipoz Kaynaklı Mezenkimal Kök Hücreleri Üzerindeki Sitotoksisitesinin Değerlendirilmesi

Research Article

Burcu Efe, Yusuf Furkan Galata,Yavuz Emre Arslan*
Regenerative Biomaterials Lab., Dept. of Bioengineering, Eng. Faculty, Çanakkale Onsekiz Mart University, Canakkale, Turkey.

ABSTRACT

In this study, aqueous extracts of *Melia azedarach* L. green fruit and leaves were obtained using two different extraction methods. The extraction yields of the green fruit and leaves were found as 24.11% and 37.98% for the infusion method; 17.76% and 27.00% for the rotating method, respectively. The total phenolic content, related to the infusion method, was ascertained for green fruit extract 173.67±10.84 mg Gallic Acid Equivalent (GAE)/g dry weight and leaf extract 312.33±9.81 mg GAE/g dry weight. In other respects, antioxidant activity related to the infusion method was determined for green fruit extract 172.51±13.23 mg Trolox/L and leaf extract 569.16±10.41 mg Trolox/L. Gas chromatography-mass spectrometry (GC-MS) analysis was performed to identify the chemical composition of the extracts. The cytotoxicity levels of the extracts were assessed on human adipose-derived mesenchymal stem cells (hAMSCs) using commercially available XTT assay. Consequently, it has been found that the green fruit extract has more cytotoxic activity than the leaf extract on hAMSCs.

Key Words
Melia azedarach L., total phenolic compounds, cytotoxicity, human adipose-derived mesenchymal stem cells.

ÖZ

Bu çalışmada, *Melia azedarach* L. yeşil meyve ve yapraklarının sulu özleri iki farklı özütleme yöntemi kullanılarak elde edildi. Yeşil meyve ve yaprakların özütleme verimleri sırasıyla, demleme yöntemi için %24.11 ve %37.98; çalkalama yöntemi için ise %17.76 ve %27.00 olarak bulundu. Demleme yöntemi ile ilgili toplam fenolik içerik, yeşil meyve özü için 173.67±10.84 mg galik asit eşdeğeri (GAE)/g kuru ağırlık ve yaprak özü için 312.33±9.81 mg GAE/g kuru ağırlık cinsinden tespit edildi. Diğer yandan demleme yönteminde, yeşil meyve özü için 172.51±13.23 mg Trolox/L ve yaprak özü için ise 569.16±10.41 mg Trolox/L cinsinden antioksidan aktivite belirlendi. Özütlerin kimyasal bileşimini tanımlamak için gaz kromatografisi-kütle spektrometresi (GC-MS) analizi yapıldı. Özütlerin insan adipoz kaynaklı mezenkimal kök hücreleri (iAMKH'leri) üzerindeki sitotoksisite seviyeleri ticari olarak mevcut olan XTT testi ile değerlendirildi. Sonuç olarak, yeşil meyve özütünün iAMKH'leri üzerine yaprak özütünden daha fazla sitotoksik aktiviteye sahip olduğu bulunmuştur

Anahtar Kelimeler
Melia azedarach L., toplam fenolik bileşikler, sitotoksisite, insan adipoz kaynaklı mezenkimal kök hücreler.

Article History: Received: Dec 06, 2017; Revised: Jan 02, 2017; Accepted: Feb 08, 2017; Available Online: Feb 20, 2018.

DOI: 10.15671/HJBC.2018.220

Correspondence to: Y.E. Arslan, Department of Bioengineering, Eng. Faculty, Çanakkale Onsekiz Mart Univ., Canakkale, Turkey.
Tel: +90 286 218 0018 Fax: +90 286 218 0541 E-Mail: yavuzea@gmail.com

INTRODUCTION

Plants have been used from ancient times until today due to their bioactive substances for the treatment of diseases and/or other medical purposes in traditional medicine. Nowadays, plants are still a prominent option in modern medicine, pharmaceutical chemistry and chemical entities for generating synthetic drugs. Researches on significant biomolecule extraction from medicinal plants have become more notable with an increase in novel methods or technologies such as maceration and Soxhlet extraction presenting opportunities to obtain desired compounds [1,2]. *Melia azedarach* is an evergreen tree and the species of deciduous tree in the mahogany family found mostly in Indian sub-continent [3]. These plants constitute approximately 45 genera and 750 species [4]. The origin of *M. azedarach* is Northern India and China, but today, it can be grown in a few more continents. These trees were previously used for timber and ornamental purposes, until the presence of several cytotoxic and bioactive components was discovered [5].

In recent years, research has revealed this plant to contain excessive amounts of biological active agents such as antioxidants and phenolic components [3]. Because of its extraordinary cytotoxic and antimicrobial activity, *M. azedarach* has been investigated for its use as an anti-tumor agent, pesticide, for skin disease, viral infections, arthritis, inflammation and analgesic [6,7]. The effective results have been obtained when this plant was used as an anti-ulcer, anti-malarial, anti-protozoal, anthelmintic and wound healing agent. In addition to these, Asokan et al. (2015) reported its effect in reducing blood sugar levels [8], and Sultana et al. (2014) exhibited its reducing effect on the urinary calcium, oxalate and phosphate levels [9].

Human mesenchymal stem cells (hMSCs) have been considered as a potential source for cell therapeutics in incurable diseases. hMSCs revitalize regeneration and manage inflammation due to their self-renewal and multi-lineage differentiation features, making them an attractive source in tissue engineering and regenerative medicine. hMSCs can be isolated from a variety of sources such as bone marrow, dental pulp, adipose tissues, placenta, amniotic fluid, tendons, the umbilical cord, etc. Due to their therapeutic nature, these cells are capable of healing various clinically significant diseases [10–14]. In the current study, we prepared aqueous extracts of *M. azedarach* L. leaves and green fruit. Chemical composition of extracts was characterized by GC-MS, whereas the total phenolic compound and anti-oxidant activities were determined via spectrophotometric techniques. Cytotoxicity levels of the extracts were examined with the XTT assay. Human adipose-derived MSCs (hAMSCs) were then treated with these aqueous extracts. The aim of this study was to investigate and determine the effects of the cytotoxicity levels of the extracts on hAMSCs. We believe that this pioneering study will open a pathway for promising new studies in tissue engineering and regenerative medicine applications.

MATERIALS and METHODS

Plant Collection

M. azedarach L. leaves and green fruit were collected in April from Canakkale, Turkey. Fresh leaves and green fruits were rinsed with distilled water. Then, they were evenly spread and dried in an incubator (Memmert, UN55, Germany) for 24h. The outer layer of the dried fruit was removed before the extraction process. The dried material was separately homogenized (IKA, T-18 Basic Ultra TURRAX, Germany) in order to obtain their powder form.

Extraction of *M. azedarach* L.

The extraction process was performed with two different groups. The dried samples were first dissolved in Milli-Q water (Merck-Millipore, Direct-Q3 UV, Germany) at a ratio of 2% (w/v). Group-I samples were extracted at 80°C for 2h with a Soxhlet apparatus (Buchi, Rotavapor R210, Switzerland) (also named the infusion method). The extract was then centrifuged at 6000 rpm for 10 minutes (Hettich, Mikro 120, Germany) and filtered (Macherey-Nagel, MN-615, Germany) under reduced pressure (Buchi, Vacuum pump V-700, Switzerland).

Group-II samples in suspension form were subjected to continuous stirring (also named the ro-

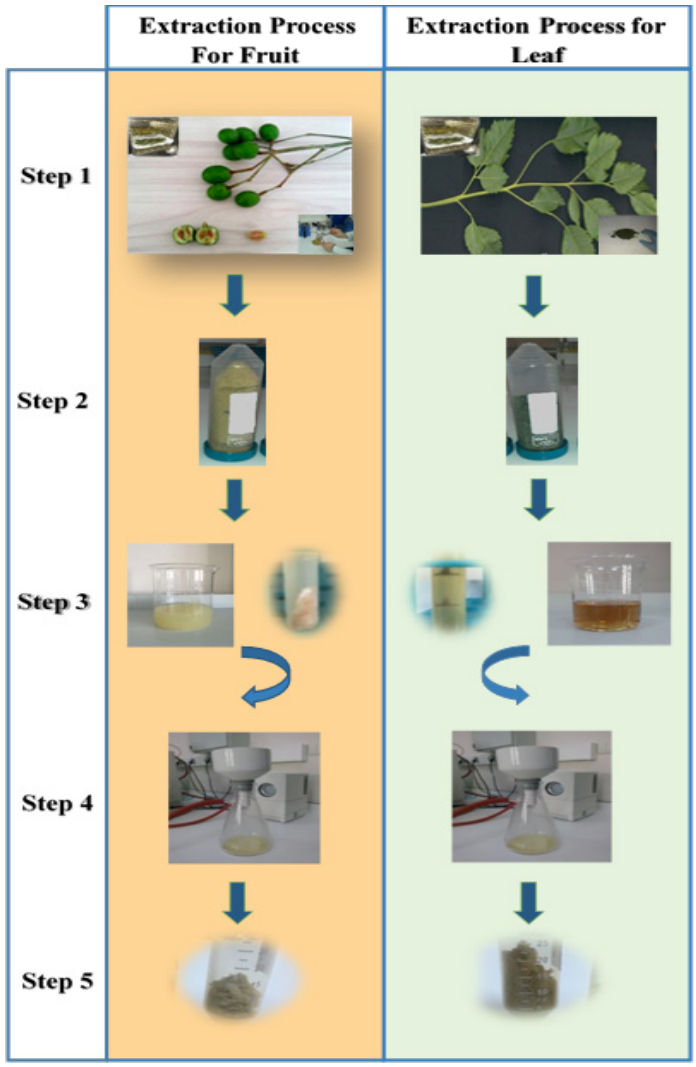

Figure 1. An overview of the extraction processes of *M. azedarach* L. green fruit and leaf. Step 1: Green fruit and leaf were harvested and dried in incubator. Step 2: Green fruit and leaf were homogenized. Step 3: Green fruit and leaf extracts were obtained according to infusion method (Group I) and centrifuged to eliminate the insoluble substances. Step 4: Green fruit and leaf extracts were filtered by vacuum under reduced pressure. Step 5: Fruit and leaf extracts were lyophilized to obtain their water-soluble powder form.

tating method) at room temperature for 72 h. The solutions were then centrifuged at 6000 rpm for 10 minutes and the resulting suspension filtered using filter paper under reduced pressure. The extracts were evaporated under reduced pressure at 80°C to concentrate the solution and stored at -26°C for overnight before the lyophilization process. Lyophilization procedure was conducted for overnight (Telstar, LyoQuest, Spain) and the lyophilized extracts were stored at -26°C for further use. All processes were summarized in Figure 1.

Determination of Total Phenolic Content

The total phenolic content (TPCs) was spectrophotometrically determined using the Folin Ciocalteu reagent [15]. Dried specimens of the leaf and green fruit extracts were dissolved in Milli-Q water at a ratio of 1% (w/v). Briefly, 10 mg of the sample was suspended in 1 of mL Milli-Q water at room temperature. Then, 900 µL of Milli-Q water, 5 mL of the Folin reagent (0.2 N) and 4 mL of sodium carbonate solution (7.5%, w/v) were added into each 100 µL sample. The solutions were rested for 2 h at room temperature in the dark. The absorbance was measured at 765 nm against a blank solution (Shimadzu UV-mini 1240, Japan). The phenolic content was calculated in terms of Gallic acid (GA) and the results were given as the GA equivalent (GAE) in terms of mg/g dry sample. All chemicals were purchased from Sigma-Aldrich (Germany) unless otherwise specified.

Determination of the CUPRAC Antioxidant Capacities of the Extracts

To analyze the antioxidant values of the extracts, the CUPRAC test was applied. Briefly, 20 μL of each sample was suspended in 1 mL of $CuCl_2.2H_2O$ (0.01M, prepared in Milli-Q water), 1 mL of Neocuproine ($7.5x10^{-3}$ M, prepared in Ethanol), 1 mL of ammonium acetate solution (pH= 7.0, in Tris-buffer) and 1.08 mL of Milli-Q water. After the solutions were incubated in the dark for 30 minutes at room temperature, the absorbance was measured at 450 nm against a blank solution.

Gas chromatography/Mass Spectrometry Analysis

M. azedarach L. leaf and fruit powders were dissolved in Milli-Q water and filtered through a 0.45 μm sterile filter. GC-MS analysis was performed using a Thermo MS Finnigan Trace DSQ instrument, with a DB-WAX (30mx0.25mm i.d.; film thickness 0.25μm) column. The GC oven temperature was programmed in the following manner; 50°C for 1 minute, followed by an increase rate of 3°C/minute up to 220°C. Helium was used as the carrier gas at a flow rate of 1ml/minute. All data were processed using the Xcalibur software.

Cell Culture Experiment

Human adipose mesenchymal stem cells (hAMSCs) (Merck-Millipore, human adipose mesenchymal stem cell kit, cat. no. SCC038 and lot no. QVP1303200, USA) were expanded, and their multipotency capacities validated according to a previously reported method [16,17]. Passages between 2 and 5 were utilized for all experiments. hAMSCs were seeded on 96-well plates with a density of $1x10^4$ cells/well, and incubated at 37°C, under 5% CO_2 and 95% relative humidity conditions (Panasonic, Japan) for 24 h. Aqueous extracts of *M. azedarach* L. at various concentrations to the hAMSCs. Briefly, the extracts were added into mesenchymal stem cell medium at different ratios depending on its nature; 150, 600, 900, 1500 and 2100 μg/well for that of the fruit, and 100, 200, 400 and 600 μg/well for that of the leaf.

Measuring Cell Viability

Cytotoxicity of the extracts were assessed using commercially available the XTT assay kit (Biological Industry, USA). In brief, hAMSCs were seeded in 96-well plates and incubated for 24 h ensuring they reached 85-90% confluence. The stem cells were then treated with green fruit and leaf extracts 24 h under conventional culture conditions. Subsequently, the XTT activation reagent was added into each well and incubated for a further 4 h. The absorbances were then measured at wavelength range of 450-500 nm against the control group (n= 3) with a microplate reader (Thermo-Scientific, Multiskan™ GO).

RESULTS and DISCUSSIONS

Determination of the Success of Extraction Process

The yield percentage of the green fruit and leaf extracts were calculated using the equation given below. The infusion technique produced extraction yields of 24.11% and 37.98% for the green fruit and leaf respectively, whereas 17.76% and 27.00% were obtained through the rotation process.

$$SampleYield = \left[\frac{(Initial(dry))Weight - LyophilizedWeight}{Initial(dry)Weight}\right] x100 \quad (1)$$

The infusion extraction yields were significantly higher than those of rotation extract yields. Similar results have been obtained in literature [18].

Assessment of the Total Phenolic Contents of Extracts

TPCs of the green fruit and leaf extracts were found to be 173.67 and 312.33 mg GAE/g dry weight, respectively. The data clearly outlines that leaf extracts contain a richer phenolic content (Figure 2A) with respect to that of the fruit extract resulting in high free radical-sweeping and antioxidant activities [19]. Phenolic compounds are one of the major secondary metabolite classes of plants which possess a wide range of biological effects including antioxidant activity, antimutagenicity, anti-carcinogenicity, etc. [20]. In a similar study, *M. azedarach* L. was extracted using various organic solvents in order to investigate the potential antifeedant activities of its biological contents [5].

In a study, aqueous extracts of *M. azedarach* L. green and ripe fruit were prepared, where the phenolic content was found to be 10.54 mg

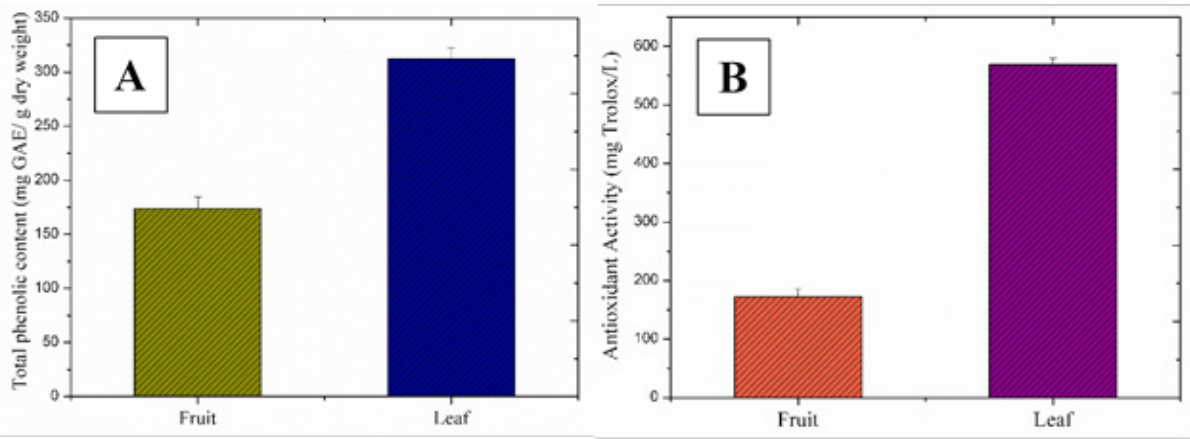

Figure 2. Total phenolic contents (A) and antioxidant activities (B) of green fruit and leaf extracts.

GAEs/g dry weight [4]. In our study, TPC of green fruit was found as 173.67±10.84 mg GAEs/g dry weight according to the infusion method which reveals the importance of the temperature during the extraction process. It should not be forgotten that a number of factors (collection time, geographical origin, climatic conditions, etc.) also have influence on the phenolic compound content in a plant extract [4].

CUPRAC Antioxidant Capacity

The CUPRAC method is based on the Cu(II)–Cu (I) reduction by antioxidants in the presence of neocuproine. It is important that CUPRAC reagent should be freshly prepared [21,22] it is desirable to establish a method that can measure the total antioxidant activity level directly from vegetable extracts. The current literature clearly states that there is no \"total antioxidant\" as a nutritional index available for food labeling because of the lack of standard quantitation methods. Thus, this work reports the development of a simple, widely applicable antioxidant capacity index for dietary polyphenols and vitamins C and E, utilizing the copper(II. In our study, the antioxidant content of the leaf and green fruit extracts were determined by the CUPRAC method, which showed leaf extracts to have the maximum antioxidant activity according to Trolox calculations.

As shown in Figure 2B, the leaf and green fruit extracts exhibit strong antioxidant activity. Cupric reducing capacity of the aqueous green fruit and leaf extracts were found to be 172.51±13.23 and 569.16±10.41 mg Trolox/L, respectively. Aoudia et al. (2013), found the cupric reducing capacity of aqueous leaf extracts to be 78.71 mg Trolox/L which underlines the success of infusion process seed and almonds of *Melia azedarach* grown in Algeria were defatted and extracted with three solvents, aqueous 70%, v/v [23].

GC-MS Results

In order to identify the chemical composition of the leaf and green fruit extracts, GC-MS, a very widespread analytical technique, was performed. According to the results, stearic acid, polyunsaturated fatty acid, furfural, 2-furancarboxyaldehyde-5-(methyl), acetic acid, 5-hydroxymethyl-2-furaldehyde, hexanoic acid, monoterpenes, phytosterol, flavonoids, 2,3-Dihydro-3,5-Dihyroxy-6-Methyl-4H-Pyran-4-One and ethyl nonadecanoate were determined in the green fruit extract (Figure 3A). The leaf extract on the other hand revealed the presence of flavonoids, furfural, 2-furancarboxyaldehyde-5-(methyl), acetic acid, 5-Hydroxymethyl-2-furaldehyde, hexanoic acid, phytosterol, monoterpenes, Vitamin E and 2,3-Dihydro-3,5-Dihyroxy-6-Methyl-4H-Pyran-4-One (Figure 3B). GC-MS screening showed that the most abundant substance (%) was acetic acid according to the peak area.

Organic acids and furfural derivatives have been used against plant parasitic nematodes, for years. On the other hand, flavonoid derivatives are potential chemical substances used as anti-inflammatory and anti-cancer agents. Additionally, vitamin E is an antioxidant and it protects tissues from deleterious free radicals. Apart from these,

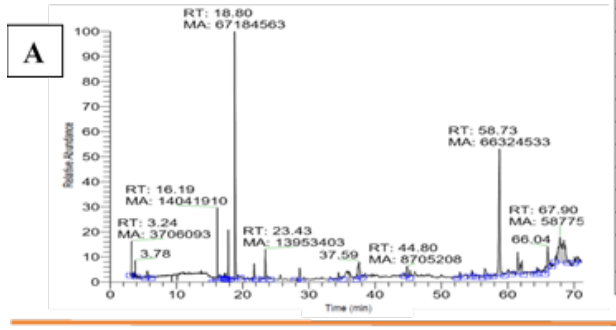

RT	M.Wt	M.F.	Compound Name
13,21	284	$C_{18}H_{36}O_2$	Stearic acid
13,21	294	$C_{18}H_{30}O_2$	Polyunsaturated fatty acid
16,38	96	$C_5H_4O_2$	Fufural
19,53	110	$C_6H_6O_2$	2-furancarboxyaldehyde-5-(methyl)
21,15	60	$C_2H_4O_2$	Acedic Acid
39,94	126	$C_6H_6O_3$	5-Hydroxymethyl-2-furaldehyde
37,88	116	$C_6H_{12}O_2$	Hexanoic acid
37,57	152	$C_{10}H_{16}O$	Monoterpenes
39,17	414	$C_{29}H_{50}O$	Phytosterol
45,31	222	$C_{13}H_{14}N_2O_3$	Flavonoids
58,77	144	$C_6H_8O_4$	2,3-Dihydro-3,5-Dihyroxy-6-Methyl-4H-Pyran-4-One
60,54	326	$C_{21}H_{42}O_2$	Ethyl nonadecanoate

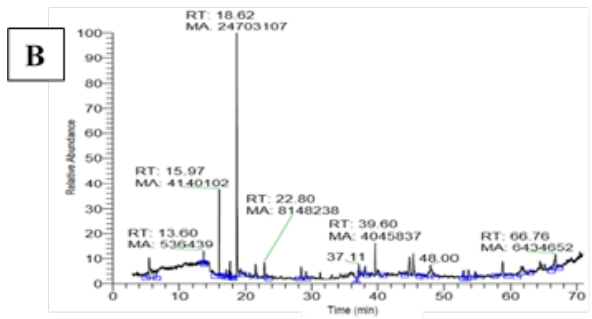

RT	M.Wt	M.F.	Compound Name
11,49	222	$C_{13}H_{14}N_2O_3$	Flavonoids
16,38	96	$C_5H_4O_2$	Fufural
19,53	110	$C_6H_6O_2$	2-furancarboxyaldehyde-5-(methyl)
21,15	60	$C_2H_4O_2$	Acedic Acid
39,94	126	$C_6H_6O_3$	5-Hydroxymethyl-2-furaldehyde
37,88	116	$C_6H_{12}O_2$	Hexanoic acid
40,25	414	$C_{29}H_{50}O$	Phytosterol
42,61	412	$C_{29}H_{48}O$	Phytosterol
45,61	152	$C_{10}H_{16}O$	Monoterpenes
56,35	536	$C_{40}H_{56}$	Vitamin E
58,77	144	$C_6H_8O_4$	2,3-Dihydro-3,5-Dihyroxy-6-Methyl-4H-Pyran-4-One

Figure 3. GC-MS chromatograms of green fruit (A) and leaf (B) extracts.

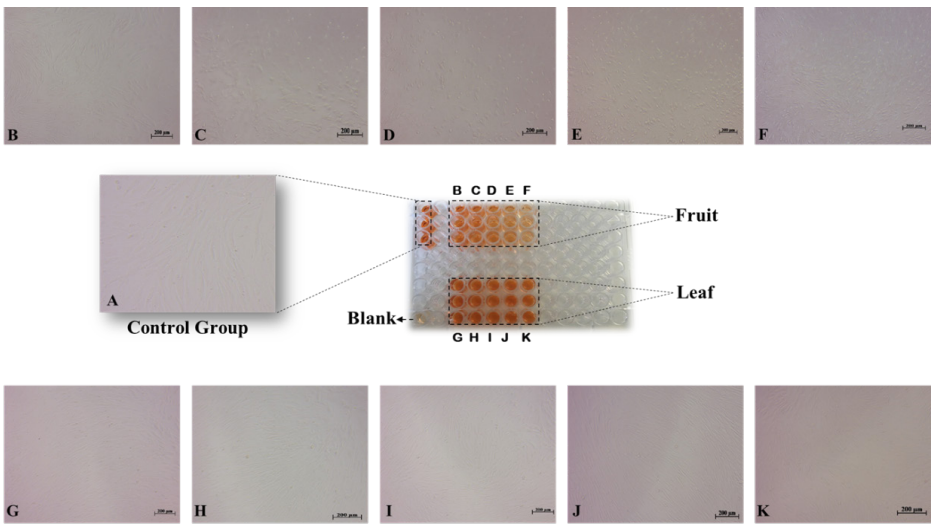

Figure 4. Experimental setup for XTT assay and inverted phase-contrast microscopy images of hAMSCs that were treated with various concentrations of the extracts. Un-treated hAMSCs as control (A), microscopic images of green fruit extract (B, C, D, E and F) and leaf extract (G, H, I, J and K) as dose-depended concentrations (Black scale bar: 200 μm).

monoterpenes can inhibit microbial proliferation and prevent dehydration, etc. [24,25]. Finally, the active substance/s that cause cell apoptosis were not specified because of the huge chemical composition of the green fruit extract.

Cytotoxicity

Human adipose-derived MSCs were treated with aqueous leaf and green fruit extracts, and the cell viability was determined via the XTT assay often used in the identification of cytotoxicity levels (Figure 4). The colorimetric assay depends on the reduction of tetrazolium salts (XTT) to orange colored formazan products by living cells (metabolically active). Cell viability measurements obtained from the XTT assay are represented in Figure 5.

M. azedarach L. green fruit extracts showed dose dependent cytotoxic effect on hAMSCs. The IC_{50} value for green fruit extract was found to be 728.05 μg/well, whereas no value could be determined for the leaf extract because it did not show any cytotoxic effect against the

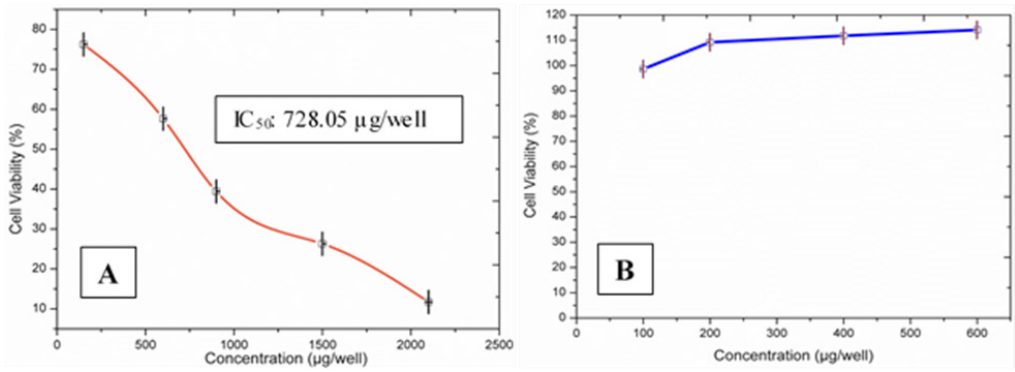

Figure 5. Cell viability assessment of green fruit (A) and leaf (B) extract.

hAMSCs. Green fruit extracts inhibited the cell proliferation as shown in Figure 5A. Although the TPC and antioxidant capacities of leaf extracts were higher than that of the green fruit extract (Figure 2), surprisingly, the green fruit extract showed a remarkable cytotoxic effect on hAMSCs in contrast to leaf extract (Figure 5B). The absence of similar studies in the literature limits our interpretation about these results. It is noteworthy in mentioning that the underlying reason of cytotoxicity is not related to the TPC or antioxidant capacity, but probably, to the presence of a chemical compound.

CONCLUSION

Plants have been used as alternative medicine for therapeutic purposes since the beginning of mankind. Therefore, the identification of extraordinary chemical contents is crucial for their use in the healthcare industry. Nowadays, hMSCs, hAMSCs in particular, are utilized in the treatment of many types of diseases. Exploring novel agents or substances from medicinal plants for proliferation, differentiation or maintenance of hMSCs may present and lead to new opportunities in tissue engineering and regenerative medicine applications. *M. azedarach* L. leaf and green fruit extracts were prepared and applied to hAMSCs with the aim of evaluating their cytotoxicity levels, which in turn is the preliminary phase in understanding the potential effect of these extracts on hAMSCs.

The green fruit extract was found to be highly cytotoxic in contrast to leaf extract. We believe further studies on *M. azedarach* L. extracts should be designed in order to gain a better understanding of the main underlying causes of the cytotoxicity or proliferation of hAMSCs.

Conflict of interest

The authors declare that they have no conflict of interest.

Acknowledgements

The authors acknowledge the financial support of the Çanakkale Onsekiz Mart University, Scientific Research Projects Coordination Unit (Project ID. FBA-2015-549). We would also like to thank the Çanakkale Onsekiz Mart University, Science and Technology Application & Research Center for their support regarding the GC-MS analyses. Finally, we would like to thank Prof. Kaan C. Emregul for his comments and language proofreading.

References

1. S.S. Handa, S.P.S. Khanuja, G. Longo, D.D. Rakesh, Extraction technologies for medicinal and aromatic plants, J. Nat. Prod., 5 (2008) 440.
2. B. Biswas, K. Rogers, F. Mclaughlin, D. Daniels, A. Yadav, Antimicrobial activities of leaf extracts of guava (*Psidium guajava* l.) on two gram-negative and gram-positive bacteria, Int. J. Microbiol., (2013) 1-6.
3. M. Azam, A. Mamun-Or-Rashid, N. Towfique, M. Sen, S. Nasrin, Pharmacological potentials of *Melia azedarach* L., A review, Am. J. Biosci., 1 (2013) 44-49.
4. I. Khan, M. Yasinzai, Z. Mehmood, I. Ilahi, Comparative study of green fruit extract of *Melia azedarach* linn. with its ripe fruit extract for antileishmanial, larvicidal, antioxidant and cytotoxic activity, Asian J. Nat. Appl. Sci., 2 (2014) 442-454.
5. C. Carpinella, C. Ferrayoli, G. Valladares, M. Defago, S. Palacios, Potent limonoid insect antifeedant from *Melia azedarach*, Biosci. Biotechnol. Biochem., 66 (2002) 1731-1736.
6. T. Akihisa, X. Pan, Y. Nakamura, T. Kikuchi, N. Takahashi, M. Matsumoto, E. Ogihara, M. Fukatsu, K. Koike, H. Tokuda, Limonoids from the fruits of *Melia azedarach* and their cytotoxic activities, Phytochemistry, 89 (2013) 59-70.

7. K. Sangeetha, S. Rajarajan, In vitro antiviral activity of indian medicinal plants to asian and east central south african lineage of Chikungunya virus, Int. J. Pharm. Sci. Res., 6 (2015) 692-697.
8. B. Asokan, B. Rajkumar, S. Balamuruganvelu, S. Jaikumar, In vivo antidiabetic activity of ethanolic flower extract *Melia azedarach* L., Acta Biomed. Sci., 2 (2015) 215-217.
9. S. Sultana, H.M. Asif, N. Akhtar, M. Waqas, S.U. Rehman, Comprehensive review on ethanobotanical uses, phytochemistry and pharmacological properties of *Melia azedarach* linn., Asian J. Pharm. Res Heal. Care, 6 (2014) 26-32.
10. J. Yu, Y. Wang, Z. Deng, L. Tang, Y. Li, J. Shi, Y. Jin, Odontogenic capability: bone marrow stromal stem cells versus dental pulp stem cells, Biol. Cell, 99 (2007) 465-474.
11. H. Jin, Y. Bae, M. Kim, S.-J. Kwon, H. Jeon, S. Choi, S. Kim, Y. Yang, W. Oh, J. Chang, Comparative analysis of human mesenchymal stem cells from bone marrow, adipose tissue, and umbilical cord blood as sources of cell therapy, Int. J. Mol. Sci., 14 (2013) 17986-18001.
12. Y.E. Arslan, M.M. Hız, T. Sezgin Arslan, The use of decellularized animal tissues in regenerative therapies, Kafkas Univ. Vet. Fak. Derg., 21 (2015) 139-145.
13. I. Jun, Y. Bin Lee, Y.S. Choi, A.J. Engler, H. Park, H. Shin, Transfer stamping of human mesenchymal stem cell patches using thermally expandable hydrogels with tunable cell-adhesive properties, Biomaterials, 54 (2015) 44-54.
14. M.T. Sutton, D. Fletcher, S.K. Ghosh, A. Weinberg, R. van Heeckeren, S. Kaur, Z. Sadeghi, A. Hijaz, J. Reese, H.M. Jane, D.P. Lennon, A.I. Caplan, T.L. Bonfield, Antimicrobial properties of mesenchymal stem cells: therapeutic potential for cystic fibrosis infection, and treatment., Stem Cells Int., 2016 (2016) 1-12.
15. V.L. Singleton, J.A. Rossi, J. Jr, Colorimetry of total phenolics with acid reagents, Am. J. Enol. Vitic., 16 (1965) 144-158.
16. E. Erten, T. Arslan Sezgin, B. Derkus, Y.E. Arslan, Detergent-free decellularization of bovine costal cartilage for chondrogenic differentiation of human adipose mesenchymal stem cells in vitro, RSC Adv., 6 (2016) 94236-94246.
17. Y.E. Arslan, T. Sezgin Arslan, B. Derkus, E. Emregul, K.C. Emregul, Fabrication of human hair keratin/jellyfish collagen/eggshell-derived hydroxyapatite osteoinductive biocomposite scaffolds for bone tissue engineering: From waste to regenerative medicine products, Coll. Surf. B Biointerf., 154 (2017) 160-170.
18. A.V. Khân, A.A. Khan, I. Shukla, In vitro antibacterial potential of *Melia azedarach* crude leaf extracts against some human pathogenic bacterial strains, Ethnobot. Leafl., 12 (2008) 439-445.
19. J. Kubola, S. Siriamornpun, Phenolic contents and antioxidant activities of bitter gourd (*Momordica charantia* L.) leaf, stem and fruit fraction extracts in vitro, Food Chem., 110 (2008) 881-890.
20. G. Zengin, C. Sarikurkcu, P. Uyar, A. Aktumsek, S. Uysal, M.S. Kocak, R. Ceylan, *Crepis foetida* L. subsp. rhoeadifolia (Bieb.) Celak. as a source of multifunctional agents: Cytotoxic and phytochemical evaluation, J. Funct. Foods, 17 (2015) 698-708.
21. R. Apak, K. Güçlü, M. Özyürek, S.E. Karademir, Novel total antioxidant capacity index for dietary polyphenols and vitamins C and E, using their cupric ion reducing capability in the presence of neocuproine: CUPRAC Method, J. Agric. Food Chem., 52 (2004) 7970-7981.
22. S.D. Çekiç, K.S. Başkan, E. Tütem, R. Apak, Modified cupric reducing antioxidant capacity (CUPRAC) assay for measuring the antioxidant capacities of thiol-containing proteins in admixture with polyphenols, Talanta, 79 (2009) 344-351.
23. H. Aoudia, B.D. Oomah, F. Zaidi, R. Zaidi-Yahiaoui, J.C.G. Drover, J.E. Harrison, Phenolics, antioxidant and anti-inflammatory activities of *Melia azedarach* extracts, Int. J. Appl. Res. Nat. Prod., 6 (2013) 19-29.
24. N.G. Ntalli, S. Vargiu, U. Menkissoglu-Spiroudi, P. Caboni, Nematicidal carboxylic acids and aldehydes from *Melia azedarach* fruits, J. Agric. Food Chem., 58 (2010) 11390-11394.
25. A. Sen, A. Batra, Chemical composition of methanol extract of the leaves of *Melia azedarach* L., Asian J. Pharm. Clin. Res., 5 (2012) 42–45.

The Study of Genetic Parameters Ecologically Stable Mulberry Silkworms Breeds on Different Conditions

Çevresel Dayanıklı Dut İpekböceği Türlerinin Farklı Koşullarda Genetik Parametrelerinin Öğrenilmesi

Research Article

Famil Nasibov and Turane Mamadova*
Livestock Scientific Research Institute, Goy-Gol district, Azerbaijan.

ABSTRACT

For the first time by adaptive selection have created new high viable and productive hybrid lines suitable for the climatic conditions of Ganja-Gazakh region. Experiments were carried out in 2 different conditions. Thus the results of the studies prove that on the basis of a 3 year adaptive selection, each of the created 4 lines, with the exception of 1-2, technological performance and productivity are on high rate. According to the envorimental resistance of the material as well as its first selection, the second generation, is significantly more productive than regionalized highly productive Mayak-3 type.

Key Words
Mulberry silkworm, hybrid, test, genotype, coefficient of ecological stability, environmental tolerance.

ÖZ

Uyarlanabilir seçimle ilk defa Gence-Gazah iklim koşulları için uygun olan yeni, yüksek uyarlanabilir ve verimli melez hatları oluşturulmuştur. Deneyler 2 farklı koşul da gerçekleştirilmiştir. Bu çalışmaların sonucunda, 3 yıllık adaptatif seleksion sürecinde oluşturulan dört hattın her biri hariç tüm biyolojik, teknolojik ve verimlilik göstergelerine sahiptir. Ayrıca çevresel dayanıklılığına göre çok verimli Mayak-3 türünü içermektedir. Yeni türler sadece kuru kozanın ipekliliği dışında kozaların tüm biyolojik ve teknolojik yönden Azerbaycan Cumhuriyetinin yeni oluşturulan dut ipekböceği türleri ve melezleri için konulan tüm sınırlara cevap vermektedir.

Anahtar Kelimeler
İpekböceği, melez, test, genotip, ekolojik stabilitik katsayısı, çevresel dayanıklı.

Article History: Received: Nov 07, 2017; Revised: Jan 02, 2017; Accepted: Feb 13, 2017; Available Online: Feb 21, 2018.

DOI: 10.15671/HJBC.2018.222

Correspondence to: T. Mamadova, Livestock Scientific Research Institute, Goy-Gol district, Azerbaijan.
Tel: (+994) 556446591 Fax: (+994) 556446591 E-Mail: turana.mamadova@mail.ru

INTRODUCTION

Artificial selection is one of the most important and powerful tools for creating new breeds and improving existing breeds in the modern selection of agricultural animals, including mulberry silkworm. The effectiveness of the selection depends largely on the correct assessment of the pedigree value of the selected breeds [1]. As a result of genetic studies, it was determined that the inheritance coefficient, selector differential, variation coefficient, phenotypic and genotypic correlation coefficients and other genetic parameters should be used for the proper evaluation of the genotype [2,3]. It should be noted that the mulberry silkworm's genotypes should have a complex selection, taking into account productivity and environmental sustainability. There fore, considering these two characteristics, it is necessary to determine the selection criteria that will lead to an effective result.

Only some sort of commodities and silk products are obtained from mulberry silkworm breed and hybrids. But the quantity and quality of the raw-silk products are affected by a number of quantitative indicators of economic value by this or that degree [4,5]. The cocoon products, the ability of the survival of the worms, opening ability of dry cocoon, raw silk output, the degree of tolerance of sex or a hybrid to various infectious diseases and the effective use of spent food have a stronger influence on the amount of raw silk product(s) than other features and characteristics [6,7].

The inseparable and total length of the silk wire opening from the cocoon, the metric number and the inequality have a significant effect on the quality of raw silk products. The genetic improvement of each of these symptoms and signs ultimately leads to an increase in the quantity and quality of raw silk products [8-10].

The results of hundreds of special investigations and selection studies that have been carried out in the last 50 to 60 years have clarified that genetic parameters allow to characterize the genetic structure of the selection patterns by quantitative characteristics, to evaluate the effects of genotype and ambient conditions on the development and formation of quantitative signs and other important selective issues to solve. They, in turn, significantly improve the efficiency of selective work by improving the efficiency of selection methods, more optimal planning of selection programs and shorter and better quality of implementation.

MATERIALS and METHODS

Materials

As the material of selection was taken thesegenus Mayak-2, Chine-21 and Ukraine-1. In the process of selection we conducted experiments in 2 different conditions in unconditional and conditional conditions. In the experiments in unconditional conditions, silkworms are fed on the basis of agro-technical regulations adopted in our country. In experiments carried out in pessimal conditions, the worms in the first three years are also fed under optimal conditions, and in the last 2 years-in conditional conditions, using 2 ecofactors. Prepared selective material was fed in summer and autumn and the main lines were selected and separated.

In our research, the range of breeding lines for years and generations was 16-32 families. In order to study the adaptive ability of the selection lines and to determine the environmental stability ratios, representative control populations have been created and used in every generation. The volume of control populations consisted of 3-4 repeats of 150-200 worms per generation.

The mass of the live cocoon, which is the most important ingredient of the live silkworm, was used in the selection process as the leading selection criteria for improving adaptive ability. 3-way selection was applied on selection lines. In the first and second stages - the selection of the family, and the third one - individual selection.

In summer, hybrids of the above-mentioned genes were fed optimally until the end of the third year. At the third age, each family is divided into 2 half-families. From the first day of the fourth year to the end of the fodder, the first half-families of each family are fed in optimal conditions, and

the second half-families- in pessimal conditions. Average mass prices of a living cocoon and threadof a cocoon in every half-family ($X_{oş}$ və$X_{pş}$) and based on these prices the average prices of each family by both signs from two environments (X_{or}), environmental sustainability coefficient (ES_i) and selection index ($Sİ_i$) are determined by the following formula of B. H. Abbasov:

$$ES_i = X_i^{-pş} / X_i^{-oş} \quad (1)$$

$$Sİ_i = ES_i (X_i^{-pş} + X_i^{-pş}) / 2 \quad (2)$$

where:

$X_i^{-pş}$ - the average value of the evaluated sign of genotype in pessimal conditions;

$X_i^{-oş}$ - the average value of the evaluated sign of the genotype in optimal conditions

We should analyze several aspects to further characterize the environmental sustainability, biological, technological and productivity indicators of newly created breeds. 30 Females, 30 males were taken from materials bred both in optimal and pessimal conditions for setting biological and technological indicators of the newly created sexes.

The weight and silkiness of the wet cocoon were determined separately. The coefficient of ecological stability and phenotypic parameters of variability according to the received indicators are separately determined depending on the gender of the main signs of reproduction of each sex and is compared with the corresponding parameters of the signs of the Mayak-3.

RESULTS and DISCUSSION

The phenotypic variability parameters of the main breeding characteristics of new breeds, mean square displacements (σ) and coefficients of variation (Cv) are much lower in both optimal and pessimal conditions compared to the control ones (Tables 1 and 2). Another important fact is that many economic values, in particular the phenotypic and paratypic variability of the biological symptoms of all living creatures, as well as silkworm breeds, increase as a result of deteriorating environmental conditions.

The discussion of biological and technological parameters of the newly created breeds with the genus Mayak-3 is shown in the first table. Table 1 shows that, in comparison with the type of control «Mayak-3», the weight change of a wet cocoon on the Chinese-21 line x-Mayak-2 is 2.73 absolute percent, the coefficient of variation in the weight of the cocoon thread increased by 3.0 percent.

It is also visible from the table, that the coefficient of variation in the age range of new breeds increased by 0.12-0.32%. The reason for this fact is that these new species have high environmental sustainability. This is also confirmed by the ecological sustainability of the breeds. Thus, the coefficient of stability of the cocoon mass in Mayak-3 is 0.926 and in new breeds is 0.969-0.970, the ecological stability of the threadmass in the control breed is 0.916, and in new breeds 0.974-0.985 mg (Table 2).

Thus, the results of the research prove that each of the four lines that we created with a 3-year adaptive selection, with the exception of 1-2, significantly exceed in all biological, technological and production indicators, as well as environmental sustainability, their first selection material, namely, the second generation, as well as the high-yielding genus Mayak-3, widespread in our country.

It should be noted that newly created breeds, except the silkiness of the dry cocoon, correspond to all the progressive limits imposed on the newly created silkworm breeds and hybrids in the Republic of Azerbaijan for all biological and technological indicators.

CONCLUSIONS

It is clear that for both reasons the ecological sustainability of the Mayak-3 control breed is average, and in new breeds it is high. Thus, a comparative analysis of the phenotypic variability parameters or the environmental stability coefficients also indicate that the new breeds are superior to the regionalized Mayak-3 genus due to the resistance of the main selection features.

Table 1. Average cocoon thread prices of control and new breeds in optimal and pessimal conditions, parameters of variability and coefficients of ecological stability.

Sex	Optimal condition			Pessimal condition			ES
	X±m	σ	CV	X±m	σ	CV	
			Mayak-3 (control)				
♀	2.50±0.038	0.207	8.27	2.34±0.050	0.273	11.68	0.936
♂	2.10±0.031	0.169	8.03	1.92±0.035	0.194	10.07	0.914
Average	2.30±0.034	0.188	8.15	2.13±0.042	0.234	10.88	0.926
			Chine-21 x Mayak-2 (F_{10})				
♀	2.46±0.026	0.144	5.86	2.37±0.026	0.144	6.08	0.963
♂	2.00±0.020	0.110	5.49	1.95±0.021	0.114	5.83	0.975
Average	2.23±0.23	0.127	5.68	2.16±0.024	0.129	5.96	0.969
			Mayak-2 x Chine-21 (F_{10})				
♀	2.46±0.030	0.163	6.63	2.37±0.029	0.161	6.78	0.963
♂	2.08±0.024	0.134	6.42	2.03±0.024	0.132	6.49	0.976
Average	2.27±0.027	0.148	6.52	2.20±0.026	0.146	6.64	0.969
			Mayak 2 x Ukraine-1 (F_{10})				
♀	2.63±0.029	0.157	5.98	2.54±0.029	0.157	6.19	0.966
♂	2.13±0.023	0.124	5.80	2.08±0.022	0.121	5.81	0.976
Average	2.38±0.026	0.140	5.89	2.31±0.026	0.139	6.00	0,970
			Ukraine-1 x Mayak-2 (F_{10})				
♀	2.52±0.026	0.142	5.63	2.44±0.026	0.142	5.80	0.968
♂	2.12±0.020	0.108	5.06	2.06±0.021	0.113	5.47	0.972
Average	2.32±0.023	0.125	5.36	2.25±0.024	0.128	5.64	0.970

Table 2. Average cocoon thread prices of control and new breeds in optimal and pessimal conditions, parameters of variability and coefficients of ecological stability.

Sex	Optimal condition			Pessimal condition			ES
	X±m	σ	CV	X±m	σ	CV	
				Mayak-3 (control)			
♀	551±7.7	42.0	7.63	501±10.0	54.8	10.95	0.909
♂	519±6.6	36.2	6.98	479±8.4	46.2	9.4	0.923
Average	535±7.1	39.1	7.30	490±9.2	50.5	10.30	0.916
				Chine-21 x Mayak-2 (F_{10})			
♀	552±6.6	36.0	6.51	540±6.6	36.3	6.72	0.978
♂	520±5.4	29.5	5.67	516±5.6	30.8	5.96	0.992
Average	536±6.0	32.7	6.09	528±6.1	33.5	6.34	0.985
				Mayak-2 x Chine-21 (F_{10})			
♀	555±6.9	37.7	6.80	541±6.9	38.0	7.02	0.975
♂	525±6.1	33.7	6.42	515±6.1	33.7	6.54	0.981
Average	540±6.5	35.7	6.61	528±6.5	35.8	6.78	0.978
				Mayak-2 x Ukraine-1(F_{10})			
♀	582±7.2	39.5	6.78	565±7.1	39.1	6.91	0.971
♂	554±6.6	36.2	6.54	541±6.6	36.0	6.65	0.976
Average	568±6.9	37.8	6.66	553±6.8	37.5	6.78	0.974
				Ukraine-1 x Mayak-2 (F_{10})			
♀	562±5.6	30.6	5.44	550±5.8	31.6	5.74	0.979
♂	530±4.8	26.2	4.95	522±5.0	27.7	5.30	0.985
Average	546±5.2	28.4	5.20	536±5.4	29.6	5.52	0.982

References

1. N.M. Hasanov, S.K. Gojayeva, V.R. Aliyeva, The main biological indicators of silkworm breeds stored in the Gene Pool of the Silk Institute, AzNII Scientific News, Baku, 19 (2012) 50-55.
2. B.H. Abbasov, Study of ecological stability of the breed of silkworm and hybrids for raw silk products Azerbaijan Agrarian Sci., 3-4 (2001) 60-63.
3. D.Grekov, E.Kipriotis, P.Tzenov, Sericulture training manual, Greece, Komotini, (2005) 320.
4. V.I. Vlasov, V.N. Novostavsky, Modeling the evaluation of producers during developing the breeding programs, Cytology and Genetics., 3 (1979) 210-212.
5. Y. Nacheva, P. Tzenov, N. Petkov, Study on the heterosis and its components in hybrids between mono bivolitine and polivolitine strains of silkworm (*Bombyx mori* L.) with reference to the weight characteristic, Bulgarian J. Agric. Sci., 6 (2004) 741-744.
6. M. Kazuei, K. Masahiro, Shin S. et al., The genome sequence of silkworm, *Bombyx mori* DNA Resarch 11 (2004) 27-35
7. E.J. Reed, L.L. Bianchini, C. Viney, Sample selection, preparation methods, and the apparent tensile properties of silkworm (*B. mori*) cocoon silk, Biopolymer., 6 (2012) 397-407.
8. V.S. Grachev, Use of selection and genetic parameters in selection of highly productive dairy cattle, Ch. Zootechnician, 9 (2006) 24-25.
9. A. Dzneladze, N.Stepanishvili, A. Giorgadze et al., Mulberry silkworm perspective breeds with very long and finne cocoon thread, Proc. of International Conference, Sericulture challenges in the 21st Centure. Bulgaria, Vratza, (2007) 183-188.
10. A. Dzneladze, N. Stepanishvili, A. Giorgadze, et al Mulberry silkworm perspective breeds with very long and finne cocoon thread, Proc. of International conference: Sericulture shallenges in the 21st Centure, Bulgaria, Vratza, (2007) 183-188.

Some Characteristic Properties of Chestnut and Rhododendron Honeys in Turkey

Türkiye'deki Kestane ve Ormangülü Ballarının Bazı Karakteristik Özellikleri

Research Article

Nazlı Mayda[1*], Aslı Özkök[2], Kadriye Sorkun[1,2]

[1]Hacettepe University, Science Faculty, Biology Department, Beytepe, Ankara, Turkey.

[2]Hacettepe University, Bee and Bee Products Applications and Research Center (HARÜM), Beytepe, Ankara, Turkey

ABSTRACT

Chestnut (*Castanea sativa* Mill.) and Rhododendron (*Rhododendron* spp. L.) (mad honey) honeys are produced generally in Black Sea Region in Turkey and both of them are the special honeys because of their organic component content and known their high antioxidant capacity. In the first step of this study we researched the melissopalynological differentiation of the chestnut and rhododendron honeys and then in the second step we determined the chemical compounds and sugar content of the rhododendron, chestnut and mixed chestnut&rhododendron honeys. For this purpose total 18 honey samples were collected from 4 different districts from Black Sea Region of Turkey and melissopalynological analyses were done by microscope. Chemical composition and sugar content (fructose&glucose) were determined by High Performance Liquid Chromatograpy (HPLC) and Gas Chromatography-Mass Spectrometry (GC-MS). After melissopalynological anaylses were obtained 10 monofloral chestnut, 2 monofloral rhododendron and 6 mixed chestnut&rhododendron honeys. As a result of sugar analysis with HPLC, F/G rates were found between 1.17 and 1.80. GC-MS chemical substance analyses of honeys revealed alcohols, aldehydes, ketones, aliphatic acids and their esters, carboxylic acids and their esters and flavanonoids.

Key Words

Chestnut honey, rhododendron honey, mellissopalynological analysis, sugar analysis, chemical compounds.

ÖZ

Türkiye'de genellikle Karadeniz bölgesinde üretilen kestane (*Castanea sativa* Mill.) ve ormangülü (*Rhododendron* spp. L.) (delibal) balları içerdiği organik bileşenler ve yüksek antioksidan seviyeleri ile bilinen önemli ballardır.Bu çalışmanın ilk aşamasında kestane ve ormangülü ballarının melissopalinolojik farklılıkları araştırılmış, ikinci aşamasında ise ormangülü, kestane ve kestane ormangülü karışık balların şeker içerikleri ve kimyasal bileşenleri belirlenmiştir. Bu amaçla Türkiye'nin Karadeniz Bölgesinde, 4 farklı yerden toplamda 18 bal örneği toplanmıştır ve mikroskop ile melissopalinolojik analizleri yapılmıştır. Kimyasal bileşim ve şeker içeriği (fruktoz&glikoz) HPLC ve GC-MS ile belirlenmiştir. Melissopalinolojik analizler sonrasında 10 balın monofloral kestane balı, 2'sinin monofloral ormangülü ve 6'sının da kestane ormangülü karışık ballar olduğu saptanmıştır. HPLC ile yapılan şeker analizleri sonucunda F/G oranının 1.17 ve 1.80 arasında olduğu, GC-MS kimyasal analizleri sonucunda da balların alkoller, aldehidler, ketonlar, alifatik asit ve esterleri, carboksilik asit ve esterleri ile flavanoidleri içerdiği ortaya çıkarılmıştır.

Anahtar Kelimeler

Kestane balı, deli bal, melissopalinolojik analizler, şeker analizleri, kimyasal bileşikler.

Article History: Received: Feb 02, 2017; Revised: Feb 08, 2017; Accepted: Feb 09, 2017; Available Online: Feb 21, 2018.

DOI: 10.15671/HJBC.2018.223

Correspondence to: N. Mayda, Department Of Biology, Hacettepe University, Ankara, Turkey.

Tel: +90 3127807161 Fax: +90 3122992028 E-Mail: nazli.mayda@gmail.com

INTRODUCTION

Chestnut (*Castanea sativa* Mill.) and Rhododendron (*Rhododendron* spp. L.) (mad honey) honeys are found generally in Black Sea Region in Turkey and both of them are the special honeys for their organic component content and known their high antioxidant activity.

Chesnut plant is one of the best sources of nectar and pollen for honeybees. Chestnut honey with dark color and bitter taste, can stay in a liquid state for a long time because of its slow crystallization rate [1,2].

Mad honey, produced by honeybees from the nectars of *Rhododendron* genus (*R. ponticum* and *R. luteum*) flowers. *R. ponticum* and *R. luteum* plants, which are belongs to Ericaceae family, grow mainly in the Black Sea Region of Turkey, Japan, Nepal, Brazil, Europe and some parts of North America [3]. This honey's taste is bitter because of its slightly sharp taste and most of them contains toxins which are called grayanotoxins and they can be toxic when their consumption. So people use generally "Mad Honey" name for this honey due to subsequent consumption effects. On the other hand this honey is widely used in indigenous medicine [2].

In *Rhododendron* genus, 208 compounds have been isolated, composed of mostly flavonoids and diterpenoids [4]. Most of those diterpenoids are grayane-type diterpenoids, polyhydroxylated cyclic hydrocarbons that do not contain nitrogen [5]. It is reported that mad honey intoxication is largely associated with lipid-soluble grayanotoxins (GTXs) similar to the alkaloids veratridine, acotinine and batrachotoxin [6]. GTXs tend to bind to the activated state of sodium channels and cause persistent activation at resting membrane potential. They lead to blockage of sodium channel inactivation and shift of the voltage dependence of activation to more negative potentials [2,7].

In this study we researched the melissopaynological differentiation of the chestnut and rhododendron honeys and then we determined the chemical compounds and sugar content of the rhododendron, chestnut and mixed chestnut rhododendron honeys

MATERIALS and METHODS

Collection of Honey Samples

Honey samples were provided by beekeepers. Total 18 honey samples were collected from 4 different districts [Bartın (n=10); Kastamonu (n=1); İstanbul (n=1); Düzce (n=6)] from Black Sea Region of Turkey (Figure 1). Pollen analysis was performed to authenticate the botanical origin of chestnut and rhododendron honeys.

Microscopic Analysis of Honeys

For microscopic analysis Wodehouse (1935) [8] and Sorkun (2008) [9] methods were accepted and honey preparations were examined by Olympus CX41 microscope.

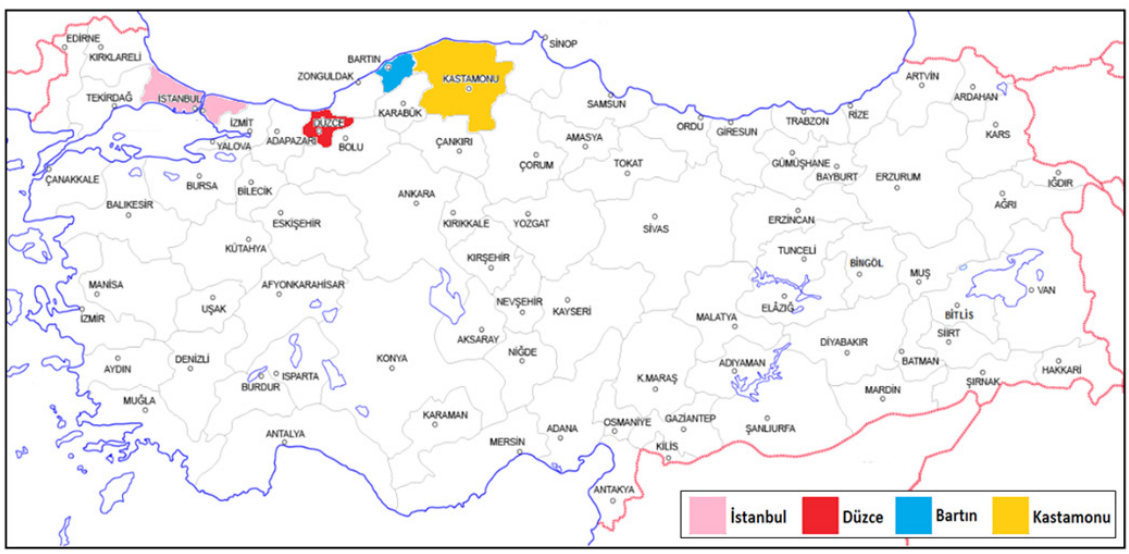

Figure 1. The regions where honey samples were collected.

Preparates from Honey Samples

Preparates to identify in 10 grams of honey are obtained as follows:

500 grams of stock honey was well stirred with a sterile glass stick and 10 grams of it was separated for obtain preparats. Then the sample and 20 ml distilled water mixed in a tube and left in a water bath of 45°C for 30-45 minutes. Then this melted honey mixture was centrifuged in 3500 rpm for 45 minutes. Water in centrifuged tubes was removed and tubes were left upside down on a drying mat for full drainage. The material was taken from the bottom of the tube and plated on a lam with basic fucsin-glycerin gelatin mixture.

Basic fucsin-glycerin-gelatine mixture and honey were taken with the edge of a sterile needle was transferred to a microscope slide and put on a hotplate set at 40°C. When the gelatine was melted, 18×18 mm cover slips were placed on the samples. Pollen slides were researched with Olympus CX41 microscope and immersion objective (x100) was used for identification of pollens. During microscopic studies all the area, which is 18x18 mm, was checked. 200 pollen was counted for every sample and determined pollen types according to their botanical origin.

Relevant sources were used in the identification of the pollen were from Persano Oddo and Piro (2004) [10], Özkök Tüylü and Sorkun (2007) [11] and Sorkun (2008) [9] as well as reference preparats

Determination of the Botanical Originals of Honey Samples

The determination of the botanical origin is based on the relative frequencies of nectariferous species' pollen types. The frequency classes of pollen grains were given as predominant (>45%), secondary pollen (15–45%), important minor pollen (3–15%) and minor pollen (<3%) [12].

GGenerally a honey can be defined as unifloral if the "characteristic" pollen (e.g. *Brassica* in rape honey) exceeds 45%. These are general guidelines but many pollen types are underrepresented (*Robinia pseudoacacia*, *Citrus* spp., *Tilia* spp.) or overrepresented (*Castanea sativa*, *Eucaliptus* spp.). For instance, to characterize acacia honey as unifloral, R. *pseudoacacia* pollen must be over 15%, citrus must have at least 10% of *Citrus* spp. pollen while, for chestnut honey, a content of 70-90% of *Castanea* pollen is required to classify honey as unifloral [12-14].

High Performance Liquid Chromatography (HPLC) Sugar Analysis

Bogdanov and Baumann (1988) [15] method and HPLC (Agilent 1200 Series) were used for the determination of fructose and glucose at honey samples. According to this method 5 g honey was weighed into a beaker and dissolved in 40 ml water. Pipetted 25 ml of methanol into a 100 ml volumetric flask and transferred the honey solution quantitatively to the flask. Filled to the mark with water. Poured through a membrane filter and collected in sample vials. Also fructose (2 g) and glucose (1.5 g) standards were prepared same way. 80 volumes of acetonitrile to 20 volumes of water mix was used as mobil phase. Flow rate was 1.3 ml/min at constant temperature of 30°C.

Gas Chromatography-Mass Spectrometry (GC-MS) Chemical Compounds Analysis

GC-MS was used for chemical compound analysis of the honey samples. 5 g honey dissolved in 5 ml methanol and mixed for 1 minute by vortex. Next centrifuged at 3500 rpm for 15 minutes. Then upper phase was filtered to vials and 1 μl solution injected to GC-MS. A GC 6890N from Hewlett-Packard (Palo Alto, CA, USA) coupled with mass detector (MS 5973 Hewlett-Packard) was used for the analysis of honey samples. Experimental conditions of GC-MS system were as follows: DB 5MS column (30 mx0.25 mm and 0.25 μm of film thickness) was used and flow rate of mobile phase (He) was set at 0.7 ml/min. In the gas chromatography part, temperature was kept at 150°C with 10°C/min heating ramp. After this period, temperature was kept at 150°C for 2 minutes. Finally, temperature was increased to 280 with 20°C/min heating ramp and then kept at 280°C for 49 minutes and chemical substances of the honey samples were identified by using standard Nist Libraries available in the data acquisition system of GC-MS.

RESULTS and DISCUSSION

After melissopalynological anaylsis were obtained 10 monofloral chestnut, 2 monofloral rhododendron and 3 mixed chestnut&rhododendron honeys (Table 1) (Figure 2 and 3).

According to Turkish Food Codex (2012) [16] and Codex Alimentarius Committee on Sugars (2001) [17] sum of the fructose and glucose should be not less than 60g/100g and ratio of fructose to glucose should be between 1.0% and 1.85% for chestnut honeys. White (1978) [18] reported that the ratio of Fructose and Glucose in honey varied from 1.0 to 1.2 and this ratio could also change depending on the nutrition the beekeper has made during the spring. Manzanares et al. (2017) [19] with 42 chestnut honeys, they reported that F 37.5%-44.1%, G 23.2%-30.9%, F + G 63.3%-74.8% and F/G 1.29- 1.78. Also Can et al. (2015) [20] found the values respectively, F 38.44%, G 19.35%, F+G 57.79%, F/G 1.98%, at chestnut honey. In our results we found Fructose between 29.20% and 42.99%, Glucose between 18.25% and 31.15%, F+G between 49.18% and 73.02% and ratio of F/G between 1.30% and 1.80% at chestnut honey samples. It was found Fructose 36.91% and 37.45%, Glucose 26.52% and 28.86%, F+G between 63.43% and 66.30% and ratio of F/G 1.31% and 1.38% at rhododendron honey samples. In our study, it was determined Fructose between 31.03% and 38.79%, Glucose between 23.26% and 32.61%, F+G between 55.99% and 71.00% and ratio of F/G 1.17% and 1.52% at chestnut&rhododendron honey samples (Table 2, Figure 4). Consequently, codex and other studies have been found to be in accordance with our results of sugar analysis.

GC-MS chemical substance analyses of honeys revealed alcohols, aldehydes, ketones, aliphatic acids and their esters, carboxylic acids and their esters and flavonoids (Table 3). Bonago et al. reported that, hydrocarbons (n-Heptacosane, n-nonacosane, n-tricosane, n-pentacosane, and n-hentriacontane, etc), carboxylic acid and esters, were present in the chestnut honeys as a result of the chemical analysis. The same authors reported that in their another studies with unifloral chestnut honey, honeys contained 50 kinds of volatile components [21,22]. In recent years researchers determined furan derivatives in higher amounts in chestnut honey [1,23-25]. Also we found furan derivatives in this study especially in chestnut honey samples (C1,C5,C6,C7,C8,C9).

Radovic et al., (2001) [25] found furfural, which is an aromatic aldehyde, before in acacia honey. It was also determined in lime and lavender honey by Cuevas-Glory et al., (2007) [26]. In this study we

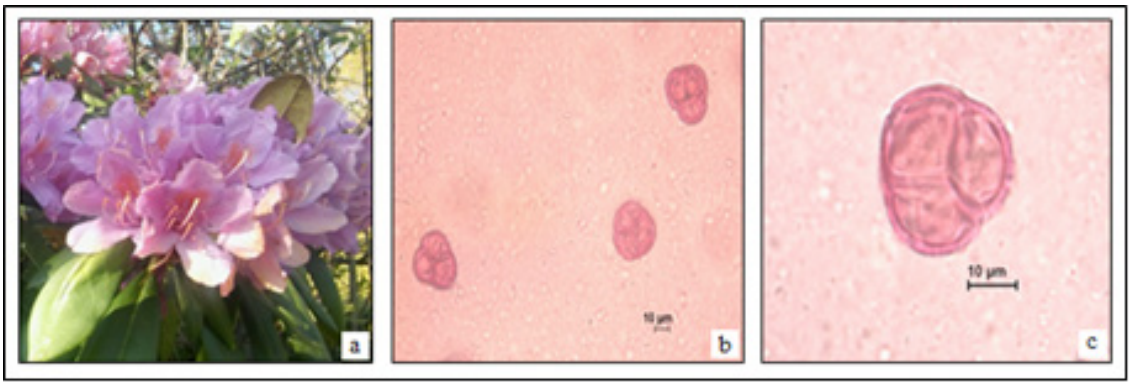

Figure 2. a. *Rhododendron ponticum*, b-c.pollen photos of *Rhododendron* spp.

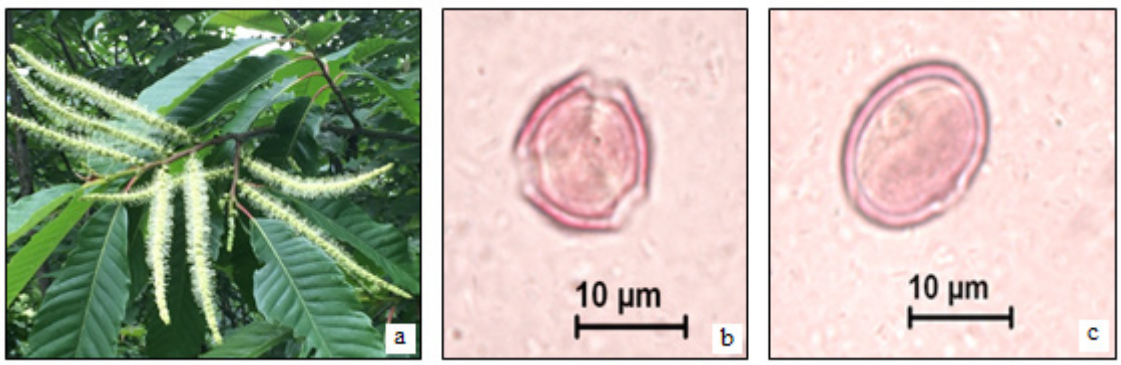

Figure 3. a.*Castanea sativa*, b-c.polar and equatorial view of *Castanea sativa* pollen.

Table 1. Melissopalynologic analysis of honey samples.

Honey sample	Total Pollen Number (TPN)	Predominant type of pollen (>45%)	Secondary pollen (15-45%)	Important Minor Pollen (3-15%)	Minor Pollen (<3%)	Region	Honey type
1	722419	*Castanea sativa* (97.5%)	-	-	*Rumex* sp. (1%) *Rosaceae* (1%) *Fabaceae* (0.5%)	Bartın	Chestnut
2	110844	*Castanea sativa* (97.7%)	-	-	*Brassicaceae* (1.7%) *Fabaceae* (0.4%)	Bartın	Chestnut
3	511271	*Castanea sativa* (97.5%)	-	-	*Rosaceae* (1.5%) *Asteraceae* (0.5%) *Rumex* sp. (0.5%)	Bartın	Chestnut
4	37626	*Castanea sativa* (91.5%)	-	*Ericaceae* (7.42%)	*Asteraceae* (1%)	Bartın	Chestnut
5	8733	*Castanea sativa* (90%)	-	*Ericaceae* (4.5%) *Rosaceae* (4.5%)	-	Bartın	Chestnut
6	292364	*Castanea sativa* (83.7%)	-	*Rosaceae* (8.86%)	*Ericaceae* (2.95%) *Lamiaceae* (2.46%) *Cistaceae* (1.97%)	Bartın	Chestnut
7	162796	*Castanea sativa* (92.5%)	-	-	*Rosaceae* (3%) *Lamiaceae* (2%) *Apiaceae* (1%) *Cistaceae* (0.5%) *Chenopodiaceae* (0.5%) *Poaceae* (0.5%)	Bartın	Chestnut

Table 1. Melissopalynologic analysis of honey samples (continue).

Honey sample	Total Pollen Number (TPN)	Predominant type of pollen (>45%)	Secondary pollen (15-45%)	Important Minor Pollen (3-15%)	Minor Pollen (<3%)	Region	Honey type
8	63113	*Castanea sativa* (97%)	-	-	*Cistaceae* (1%) *Ericaceae* (0.5%) *Rosaceae* (0.5%) *Salix* sp. (0.5%) *Apiaceae* (0.5%)	Bartın	Chestnut
9	58975	*Castanea sativa* (97.5%)	-	-	*Cistaceae* (1.5%) *Ericaceae* (1%)	İstanbul	Chestnut
10	398568	*Castanea sativa* (98.5%)	-	-	*Rosaceae* (0.5%) *Apiaceae* (0.5%) *Rumex* sp. (0.5%)	Kastamonu	Chestnut
11	4778	*Ericaceae* (50%)	*Castanea sativa* (38.8%)	*Poaceae* (11.1%)	-	Bartın	Rhododendron
12	118658	*Ericaceae* (48.4%)	*Castanea sativa* (33.3%) *Salix* sp. (15.15%)	-	*Onobrychis* sp. (1.21%) *Cistaceae* (0.6%)	Bartın	Rhododendron
13	14729	-	*Rosaceae* (22%) *Castanea sativa* (20%) *Salix* sp. (18%) *Papaveraceae* (17%)	*Fabaceae* (7%) *Ericaceae* (7%) *Brassicaceae* (7%)	-	Düzce	Chestnut& Rhododendron
14	888	*Castanea sativa** (48%)					

Table 1. Melissopalynologic analysis of honey samples (continue).

Honey sample	Total Pollen Number (TPN)	Predominant type of pollen (>45%)	Secondary pollen (15-45%)	Important Minor Pollen (3-15%)	Minor Pollen (<3%)	Region	Honey type
15	76039	*Castanea sativa** (68%)	-	*Ericaceae* (14.5) *Asteraceae* (9.5)	*Fabaceae* (2.8) *Rosaceae* (2.5) *Apiaceae* (2.7)	Düzce	Chestnut& Rhododendron
16	1728	-	*Castanea sativa* (30%) *Ericaceae* (23.9%)	*Fabaceae* (14.1%) *Cistaceae* (14.1%) *Liliaceae* (9.8%)	*Centaurea* sp. (2.8%) *Rosaceae* (2.8%) *Hedysarum* sp. (1.4%) *Asteraceae* (1.4%) *Brassicaceae* (1.4%)	Düzce	Chestnut& Rhododendron
17	4142	*Castanea sativa** (58%)	-	*Cistaceae* (9.6%) *Ericaceae* (8%) *Fabaceae* (8%) *Apiaceae* (5.6%) *Salix* sp. (4.3%) *Rosaceae* (4%)	*Campanulaceae* (1.6%) *Onobrychis* sp. (0.8%)	Düzce	Chestnut& Rhododendron
18	5186	*Castanea sativa** (52.7%)	*Rosaceae* (15.2%) *Salix* sp. (20.8%)	*Ericaceae* (4.2%) *Fabaceae* (4.1%)	*Liliaceae* (1.3%) *Poaceae* (1.3%)	Düzce	Chestnut& Rhododendron

* Chestnut honey, a content of 70-90% of Castanea pollen is required to classify honey as unifloral.

Table 2. HPLC sugar analysis results of honey samples.

Honey Sample	Honey type	Fructose (%)	Glucose (%)	F+G (%)	F/G (%)
C1	Chestnut	33.64±2.87	19.14±2.37	52.78±4.54	1.76±0.19
C2	Chestnut	37.81±2.76	29.12±5.22	66.96±7.56	1.30±0.15
C3	Chestnut	30.92±3.95	18.25±2.63	49.18±6.36	1.71±0.09
C4	Chestnut	29.20±2.94	24.71±4.76	53.93±7.37	1.21±0.14
C5	Chestnut	36.68±0.80	29.52±3.02	66.20±3.32	1.24±0.13
C6	Chestnut	41.86±1.33	31.15±3.72	73.02±5.04	1.30±0.12
C7	Chestnut	42.99±2.20	23.76±1.77	66.75±3.68	1.80±0.09
C8	Chestnut	40.47±4.62	25.57±5.75	66.04±10.31	1.6±1.18
C9	Chestnut	33.62±4.48	23.38±4.44	57.00±0.65	1.49±0.42
C10	Chestnut	33.04±3.27	22.90±3.24	55.94±4.52	1.46±0.27
R11	Rhododendron	37.45±2.05	28.86±4.22	66.30±2.53	1.31±0.25
R12	Rhododendron	36.91±5.09	26.52±1.66	63.43±5.76	1.38±0.20
CR13	Chestnut&Rhododendron	35.41±0.83	23.26±0.86	58.67±1.19	1.52±0.07
CR14	Chestnut&Rhododendron	38.39±3.44	32.61±1.49	71.00±4.08	1.17±0.10
CR15	Chestnut&Rhododendron	38.79±1.12	27.62±1.90	66.41±1.66	1.40±0.12
CR16	Chestnut&Rhododendron	33.23±0.41	25.00±0.86	58.23±1.19	1.32±0.04
CR17	Chestnut&Rhododendron	31.56±1.07	25.13±0.68	56.7±1.17	1.25±0.05
CR18	Chestnut&Rhododendron	31.03±0.85	24.96±1.07	55.99±1.83	1.24±0.03

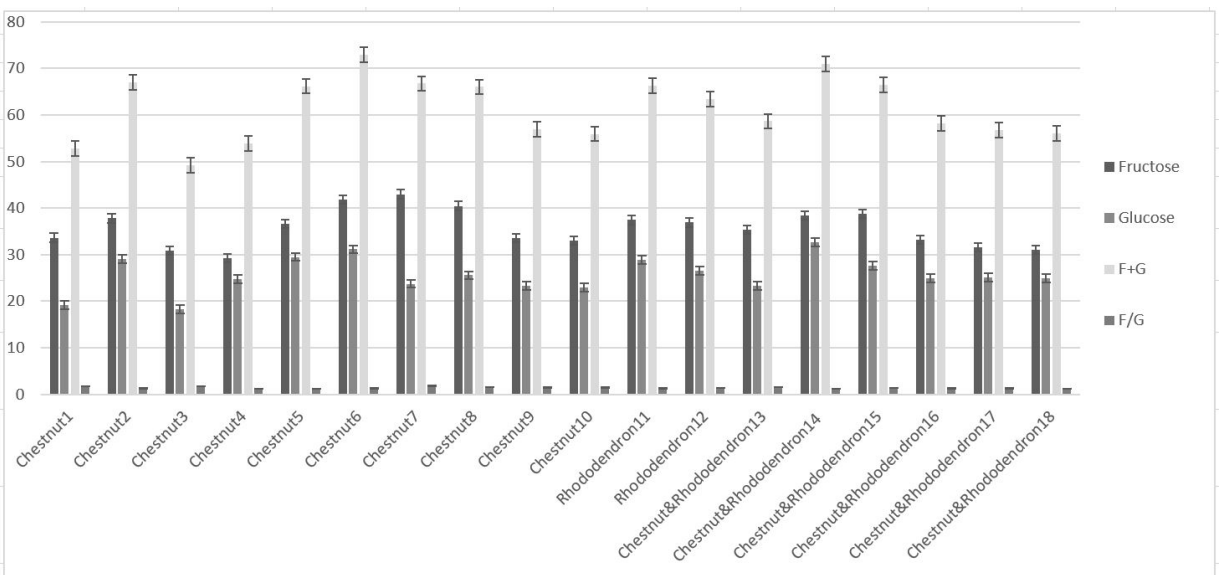

Figure 4. HPLC sugar analysis results of honey samples.

Table 3. GC-MS analysis results of honey samples.

Sample No	C1	C2	C3	C4	C5	C6	C7	C8	C9	C10	R11	R12	CR13	CR14	CR15	CR16	CR17	CR18
Alcohols																		
2,4-Hexadiyne-1,6-diol	-	-	-	-	-	-	-	-	-	-	-	-	-	-	-	0.91	-	-
2-Furan-methanol	1.78	-	-	-	3.52	0.02	1.07	0.89	-	-	-	-	-	-	-	-	-	-
3-Furan-methanol	-	-	-	-	0.70	-	-	-	1.35	-	-	-	-	-	-	-	-	-
2-Pyridinemethanol,3-hdroxY	-	-	-	-	-	-	1.43	-	-	-	-	-	-	-	-	-	-	-

Sample No	C1	C2	C3	C4	C5	C6	C7	C8	C9	C10	R11	R12	CR13	CR14	CR15	CR16	CR17	CR18
Aldehydes																		
3-Fural-dehyde	-	-	-	-	-	-	2.30	-	-	-	5.11	-	-	1.73	-	-	-	-
Furfural	3.85	3.04	5.38	-	0.84	0,03	0.42	0.39	-	-	-	-	-	-	-	-	-	-
2-Furan-carbo-xalde-hyde, methyl	0.57	-	0.98	0.55	-	-	0.43	0.40	0.33	0.41	0.97	-	-	-	-	-	-	-
5-Acetoxymethyl-2-furaldehyde	-	-	-	-	-	-	-	-	-	-	1.75	-	-	-	-	-	-	-
Benzaldehyde,2-hydroxy-5-methoxy	-	-	-	-	-	-	-	0.91	-	-	-	-	-	-	-	-	-	-

Sample No	C1	C2	C3	C4	C5	C6	C7	C8	C9	C10	R11	R12	CR13	CR14	CR15	CR16	CR17	CR18
Ketones																		
Ethanone, 1-(1H-pyrazol-4-yl)	-	-	-	-	-	3.03	-	-	-	-	-	-	-	-	-	-	-	-
1-(5-Methylfuran-2-yl)-2-2	-	-	-	-	-	-	-	-	-	-	-	-	-	8.21	-	-	-	-
3-Methyl-2-furoic acid	-	-	-	1.46	-	2.55	1.70	1.79	-	-	-	1.58	-	-	-	-	-	-

Table 3. GC-MS analysis results of honey samples. (continued)

Sample No	C1	C2	C3	C4	C5	C6	C7	C8	C9	C10	R11	R12	CR13	CR14	CR15	CR16	CR17	CR18
Aliphatic Acids and Their Esters																		
Cyclopentaneacetic acid	-	-	-	-	-	-	-	-	-	-	-	-	-	-	-	0.34	-	-
Nonanoic acid	-	-	-	-	1.31	-	-	-	-	-	-	-	-	-	-	-	-	-
Hexanoic acid, 6-bromo	-	-	-	-	-	-	-	-	-	-	-	-	-	-	1.25	-	-	-
n-Decanoic acid	-	-	-	-	-	-	-	-	-	-	-	7.71	-	-	-	-	-	-
Methyl 4-pentynoate	-	-	-	-	-	-	-	-	-	-	-	-	-	-	-	5.10	8.82	9.69
Octanoic acid	-	-	-	-	-	-	-	-	-	0.62	-	-	-	-	-			

Sample No	C1	C2	C3	C4	C5	C6	C7	C8	C9	C10	R11	R12	CR13	CR14	CR15	CR16	CR17	CR18
Carboxylic Acids and Their Esters																		
1,3-Butadiene-1-carboxylic acid	-	-	-	-	-	-	-	-	-	-	-	-	-	-	-	-	0.21	-
Carbonocyanidic acid, ethyl ester	-	-	-	-	-	-	-	-	-	-	-	0.27	0.13	0.39	-	-	-	-
Spirohexane-1-carboxylic acid, ethyl ester	-	-	-	-	-	-	-	-	-	1.21	-	-	-	-	-	-	-	-

Sample No	C1	C2	C3	C4	C5	C6	C7	C8	C9	C10	R11	R12	CR13	CR14	CR15	CR16	CR17	CR18
Flavonoids																		
1-Propene, 3-(2-cyclopentenyl)-2-m ethyl-1,1-diphenyl-	-	-	-	-	-	-	-	-	-	-	-	-	-	-	-	-	0.01	-
4H-Pyran-4-one, 3,5-dihydroxy-2-methyl-	-	-	-	-	3.14	-	-	3.16	0.98	-	-	-	-	-	-	-	-	-
4H-Pyran-4-one,2,3-dihydro-3,5-dihydroxy-6-methyl-	-	-	-	-	-	2.55	-	-	-	-	-	3.82	2.00	-	-	-	-	-
2H-Pyran, 3,4-dihydro	-	-	-	-	-	-	0.14	-	1.02	-	-	0.03	-	-	-	-	-	-
1-Propene, 1-chloro-2-methyl	0.89	-	-	-	-	-	-	-	-	-	-	-	-	-	-	-	-	-

found furfural in seven samples of the ten chestnut honeys (C1,C2,C3,C5,C6,C7,C8) (Table 3).

Flavanoids are important compounds because of their antioxidant effects. Flavanones are one of the most important groups of the flavonoids. Yu et al., 2013 and Özkök et al., 2016 [27,28] determined 2,3-dihydro-3,5-dihydroxy-6-methyl-4H-pyran-4-one (DDMP) flavanones which is a strong antioxidant in the pine honey samples. Also we found DDMP in the C6, R12 and CR13 samples (Table 3).

In this study, the chemical composition of chestnut and rhododendron honeys and their sugar content were investigated and it was determined that they could show changes depending on the botanical origins of honey.

ACKNOWLEDGEMENTS

We would like to thank Turkish Association of Beekeepers (TAB) and beekeepers who helped us for providing samples during our fieldwork.

References

1. E. Alissandrakis, P.A. Tarantilis, C. Pappas, P.C. Harizanis, M. Polissiou, Investigation of organic extractives from unifloral chestnut (*Castanea sativa* L.) and eucalyptus (*Eucalyptus globulus* Labill.) honeys and flowers to identification of botanical marker compounds, LWT-Food Sci. Tech., 44 (2011) 1042-1051.
2. S. Silici, A.T. Atayoglu, Mad honey intoxication: a systematic review on the 1199 cases, Food Chem. Toxic., 86 (2015) 282-290.
3. P. Stevens, *Rhododendron* L. Flora of Turkey and the East Aegean Islands, 6 (1978) 90-94.
4. Y. Qiang, B. Zhou, K. Gao, Chemical constituents of plants from the genus Rhododendron, Chem. & Biod., 8 (2011) 792-815.
5. K.F. Lampe, Rhododendrons, mountain laurel, and mad honey, Jama, 259 (1988) 2009-2009.
6. S. Cestèle, W.A. Catterall, Molecular mechanisms of neurotoxin action on voltage-gated sodium channels, Biochimie, 82 (2000) 883-892.
7. T. Narahashi, I. Seyama, Mechanism of nerve membrane depolarization caused by grayanotoxin I. J. Phys., 242,2 (1974) 471-487.
8. R.P. Wodehouse, Pollen grains: Mcgraw-Hill Book Company, Inc; New York; London, 1935.
9. K. Sorkun, Türkiye'nin Nektarlı Bitkileri, Polenleri ve Balları: Palme Yayıncılık, Türkiye, 2008.
10. L.P. Oddo, R. Piro, É. Bruneau, C. Guyot-Declerck, T. Ivanov, J. Piskulová, H. Russmann, Main European unifloral honeys: descriptive sheets, Apidologie, 35 (2004) S38-S81.
11. A.Ö. Tüylü, K. Sorkun, The investigation of morphologic analysis of pollen grains which are economically important and collected by *Apis mellifera* L., Hacettepe J. Bio. Chem., 35 (2007) 31-38.
12. F. Corvucci, L. Nobili, D. Melucci, F.V. Grillenzoni, The discrimination of honey origin using melissopalynology and Raman spectroscopy techniques coupled with multivariate analysis, Food Chem., 169 (2015) 297-304.
13. A.G. Sabatini, L. Bortolotti, G.L. Marcazzan, Conoscere il miele: Avenue media, 2007.
14. A. Terrab, A.G. González, M.J. Díez, F.J. Heredia, Characterisation of Moroccan unifloral honeys using multivariate analysis, European Food Res. Tech., 218 (2003) 88-95.
15. S. Bogdanov, E. Baumann, Bestimmung von Honigzucker mit HPLC, Mitt Geb Lebensmittelunters Hyg, 79 (1988) 198-206.
16. Türk Gıda Kodeksi Bal Tebliği, 2012/58 C.F.R. (2012).
17. Codex Standard 12. Revised Codex Standard for Honey, Standards and Standard Methods, 11 C.F.R. 2001.
18. J.W. White Jr, Honey., In Advances in food research, 24 (1978), 287-374.
19. A.B. Manzanares, Z.H. García, B.R. Galdón, E.M. Rodríguez-Rodríguez, C.D. Romero, Physicochemical characteristics and pollen spectrum of monofloral honeys from Tenerife, Spain, Food Chem., 228 (2017) 441-446.
20. Z. Can, O. Yildiz, H. Sahin, E.A. Turumtay, S. Silici, S. Kolayli, An investigation of Turkish honeys: their physico-chemical properties, antioxidant capacities and phenolic profiles, Food Chem., 180 (2015) 133-141.
21. G. Bonaga, A.G. Giumanini, The volatile fraction of chestnut honey. J. Api. Res., 25 (1986) 113-120.
22. G. Bonaga, A.G. Giumanini, G. Gliozzi, Chemical composition of chestnut honey: analysis of the hydrocarbon fraction J. Agricult. Food Chem., 34 (1986) 319-326.
23. A. Bouseta, S. Collin, J.P. Dufour, Characteristic aroma profiles of unifloral honeys obtained with a dynamic headspace GC-MS system, J. Api. Res., 31 (1992) 96-109.
24. C. Guyot, A. Bouseta, V. Scheirman, S. Collin, Floral origin markers of chestnut and lime tree honeys, J. Agricult. Food Chem., 46 (1998) 625-633.
25. B. Radovic, M. Careri, A. Mangia, M. Musci, M. Gerboles, E. Anklam, Contribution of dynamic headspace GC–MS analysis of aroma compounds to authenticity testing of honey, Food Chem., 72 511-520.
26. L.F. Cuevas-Glory, J.A. Pino, L.S. Santiago, E. Sauri-Duch, A review of volatile analytical methods for determining the botanical origin of honey, Food Chem., 103 (2007) 1032-1043.
27. X. Yu, M. Zhao, F. Liu, S. Zeng, J. Hu, Identification of 2,3-dihydro-3,5-dihydroxy-6-methyl-4H-pyran-4-one as a strong antioxidant in glucose–histidine Maillard reaction products, Food Res. Int., 51 (2013) 397–403.